Instituto de Astrofísica de Andalucía
Consejo Superior de Investigaciones Científicas

Programa de Doctorado en
Física y Ciencias del Espacio (B09.56.1)
Universidad de Granada

CO_2 retrievals in the Mars daylight thermosphere from 4.3 μm limb emissions

Sergio Jiménez-Monferrer

Memoria presentada para optar al grado de
Doctor en Ciencias Físicas

Directores:
Dr. Miguel Á. López-Valverde
Científico Titular del CSIC
Dr. Bernd Funke
Científico Titular del CSIC

Tutor:
Dr. Emilio J. Alfaro Navarro
Investigador Científico del CSIC

Granada, Spain 30th August 2019

Editor: Universidad de Granada. Tesis Doctorales
Autor: Sergio Jiménez Fonferrer
ISBN: 978-84-1306-337-9
URI: http://hdl.handle.net/10481/57443

To Belén, Aiden and Ellery

Agradecimientos

Y cuando las tinieblas se cernían sobre él, la encontró, dormida, envuelta en una luz tenue, sin foco definido...

Llegados a este punto, es habitual recordar a los compañeros de viaje. Es lícito y comprensible poner en valor las ayudas recibidas, intangibles o materiales. En este caso, en este viaje, es particularmente lícito. Particularmente comprensible.

Gracias Miguel Ángel por haber confiado en mí desde el primer momento, y en mis capacidades con el paso del tiempo. Gracias Bernd por tu distante cercanía, y tu dedicación incondicional. Gracias Maya por ayudarme a dar los primeros pasos, y gracias Francisco por enseñarme a correr. Gracias Manuel por tu cariñosa rigurosidad. Y gracias Emilio por tu filosófica tutela. Amplío mi agradecimiento a todos los miembros del Instituto de Astrofísica de Andalucía por acogerme en su seno estos cuatro años, en particular a Antxon, Salva, Alicia, Eva, Antonio, Brittany, Ana, Emilio, Álex, Ana Karla y Manuel.

Sin pasado, no hay futuro. Ni presente. Lo que soy es consecuencia de lo que he sido, del entorno en el que he sido. Gracias José Carlos por estimular mi ambición, gracias Iván por tu genialidad y apoyo, gracias Alberto por tu bondadosa ironía, gracias Jon por recordarme cada día lo importante que es la humildad. Chema, Manel, Feli, simplemente gracias.

Sin juegos, el camino acaba griseando. Gracias Diego, Vicente, Víctor, Migue, Carlos, Eva, Davitín, David, Alícia, Alzina, Salvatore, Dani, Amparo, y Pedro por tantos ratos agradables y los que, espero, están por llegar. Gracias Manolo por hacerme llegar el *Mighty Pen*, tan útil para escribir estas líneas.

Sin formación... sin formación persiste el ingenio. No obstante, se trata de una parada obligatoria en el trayecto. Gracias Alfonso, Luis, Laura, Fabià, Miguel Ángel, Rapul, Pitu, Amparo y Leugim. Recuerdo aquellos días con agradable nostalgia.

Este viaje de fantasía requiere también detenerse donde la imaginación se defiende de la realidad. Gracias Dr. y Dra. Mumu, Oruga, Deglutor, Bosón, Capataz, Caballero Pato, Chomp, Bancoso, Eli, Zorrojo, Mapache Digestivo, Despojo y Reno. Sí, Reno. Gracias a todos los guardianes que dedican su existencia a cuidar de los sueños. Gracias Flogis por crear conmigo. Gracias P. L. y Trol. Gracias Boogie por hacer la vida irrealmente divertida. Gracias Tokio, Ruedas y Moléculas por poner a funcionar la factoría, gracias Anyell por enseñarme a perdonar, y gracias Bugger por mostrarme algunos entresijos del idioma. Gracias Zoel por hacerme entender el poder del cambio. Gracias Señor Que por librarnos de incómodas tareas. Gracias Techo por tantas reflexiones. Gracias Bahh por relativizar los problemas. Gracias Escalera Luccini por salvarme la vida.

Se acerca el destino y lo mejor está por llegar. Mamá, Papá, Carlos, gracias por traerme al mundo y ayudarme a entenderlo, por acompañarme en mi viaje hacia este yo. Gracias abuelos, abuelas y resto de familia por llegar donde ellos no alcanzaron. Gracias Ricardo y Ana, Albertina, Javi, Teresa y Óscar por hacer lo propio al otro lado del espejo. Gracias Klaus, Deneb y Áster por vuestra efímera pero inolvidable compañía.

Finalmente, gracias Aiden y Ellery por mostrarme una vida diferente, por vuestro obsesivo empeño en sacar este trabajo adelante. Gracias por no necesitar un motivo para dar un motivo, gracias por vuestros inocentes ojos, pequeños gremlins... Belén, gracias por trazar el camino conmigo, más allá del abismo. Para toda la vida.

La arropó y la abrazó, y la acunó como si fuera de su propia estirpe.

Resumen

Marte es un mundo vasto y complejo. Un planeta rojizo, debido a su superficie, ampliamente cubierta por polvo y rocas de óxido férrico. Marte tiene una atmósfera tenue, principalmente compuesta por dióxido de carbono (CO_2), con circulación atmosférica y patrones climáticos, como la Tierra. Sin embargo, tiene destacadas oscilaciones diurnas de viento, debido a una excursión térmica considerable. Las oscilaciones tienen un efecto en todas las capas de la atmósfera, y ejercen una influencia apreciable sobre el resto de la circulación atmosférica global de Marte.

En la última década, varias misiones han viajado al *Planeta Rojo* y algunas más han sido aprobadas para ser lanzadas en los próximos años. Dos de estas misiones han sido diseñadas, construidas y operadas por/desde Europa, y son especialmente relevantes para esta Tesis:

- Mars Express, lanzada en junio de 2003, llegó a Marte en diciembre del mismo año. Estaba formada por dos módulos, un orbitador y una sonda de exploración en superficie, pero la comunicación con la sonda se perdió durante el descenso. El orbitador completó su misión nominal con éxito y, de hecho, continua operativo en el momento de escribir este trabajo. Entre otros, Mars Express lleva dos instrumentos importantes para el tema de esta Tesis, PFS (Planetary Fourier Spectrometer) y OMEGA (Observatoire pour la Minéralogie, l'Eau, les Glaces et l'Activité). Para este estudio se ha hecho un uso exhaustivo de las emisiones de CO_2 observadas en geometría limbo por OMEGA, dada su excelente cobertura vertical.

- ExoMars, enviado en dos fases o misiones distintas. La primera fase, ExoMars Trace Gas Orbiter, se lanzó en 2016 y, tras más de un año de aerofrenado y ajuste de su órbita, comienza ahora a producir los

> primeros resultados científicos. En su carga se incluyen dos instrumentos también relevantes para este trabajo, NOMAD (Nadir and Occultation for Mars Discovery) y ACS (Atmospheric Chemistry Suite). La segunda misión, programada para 2020, consistirá en un módulo de aterrizaje, encargado de depositar un vehículo de exploración en la superficie marciana.

Como hilo conductor entre estas dos misiones, el proyecto europeo UPWARDS (Understanding Planet Mars With Advanced Remote-sensing Datasets and Synergistic Studies) arrancó en 2015, en el marco del programa de investigación e innovación Horizonte 2020 de la Unión Europea. UPWARDS tenía como objetivo componer una imagen global de Marte, desde el subsuelo hasta la alta atmósfera. El proyecto UPWARDS abarcaba el desarrollo de nuevas herramientas científicas para el análisis de datos orbitales, como los que se esperan de ExoMars, así como el estudio de datos existentes no explotados, como los proporcionados por Mars Express. El trabajo presentado en esta Tesis ha sido parcialmente financiado por UPWARDS.

A pesar de la importancia de la termosfera, por ejemplo, para el proceso de escape atmosférico, es quizá la región menos conocida de la atmósfera marciana. La mayor parte de la información que tenemos sobre estas alturas proviene de fuentes muy dispersas e inconexas entre sí. Entre ellas, unos pocos perfiles tomados *in situ* durante el descenso de algunas misiones, como Viking 1 y 2, las maniobras de aerofrenado de las misiones Mars Global Surveyor y Mars Reconnaissance Orbiter, el instrumento SPICAM a bordo de Mars Express, y los instrumentos a bordo de la misión MAVEN. Estas medidas permitieron obtener perfiles de densidad y temperatura, y estudiar la variabilidad estacional y geográfica de la termosfera. Según estas observaciones y las simulaciones numéricas de las mismas, la termosfera de Marte es una región compleja y dinámica, fuertemente acoplada a las capas inferiores. En concreto, los efectos causados por las tormentas de polvo y la variabilidad térmica en la baja atmósfera se propagan hacia arriba, llegando hasta la termosfera. Para comprender esta región hace falta, por lo tanto, una visión global de la atmósfera, desde las interacciones con la superficie hasta los intercambios de especies con la exosfera.

Los datos termosféricos previamente descritos presentan una cobertura temporal y geográfica limitada. Algunos efectos importantes, como la influencia de la actividad solar, son difíciles de entender con los datos disponibles. La mayoría de ellos, excepto las medidas de aerofrenado, se concentran en la parte nocturna del planeta, lo que deja la termosfera diurna prácticamente inexplorada. Durante el día es cuando se producen las emisiones atmosféricas no térmicas más fuertes en el infrarrojo. Estas emisiones infrarrojas ofrecen una interesante oportunidad para el sondeo remoto a dichas alturas en los planetas terrestres.

De hecho, existen observaciones termosféricas de Marte en el infrarrojo, pero esos datos no han sido explotados suficientemente hasta la fecha, debido a la complejidad de su interpretación física, y la dificultad numérica de la inversión matemática necesaria. Estas observaciones fueron obtenidas por dos instrumentos a bordo de Mars Express, OMEGA y PFS. Se espera que su análisis proporcione un conocimiento más amplio y profundo sobre la termósfera diurna a las alturas de su máxima sensibilidad.

En el Grupo de Atmósferas Planetarias Terrestres (GAPT) del Instituto de Astrofísica de Andalucía (IAA), se dispone de amplia experiencia en emisiones atmosféricas no térmicas, de modelos para la atmósfera marciana, así como de herramientas para la inversión de tales emisiones. Especies moleculares como el CO_2 producen fuertes emisiones no térmicas en el infrarrojo en las capas más altas de la atmósfera. A esas alturas, la densidad es tan baja y las colisiones entre moléculas tan escasas que no se puede seguir considerando que existe equilibrio termodinámico local (ETL). La desviación de ETL ocurre frecuentemente en el hemisferio diurno cuando la radiación solar excita dichas especies en las bandas ro-vibracionales del infrarrojo cercano y medio (entre 1 y $10\,\mu$m). Las emisiones producidas contienen información sobre las densidades de las especies emisoras y, por lo tanto, contribuyen a la obtención de perfiles de densidad y temperatura en la alta atmósfera. Las observaciones de esta naturaleza vienen típicamente marcadas por ciertas dificultades. En primer lugar, la emisión de capas tan tenues es baja, de manera que las observaciones en geometría limbo, en las que se integra la emisión a lo largo de un camino grande en el detector, es extremadamente útil. Además, en comparación con alturas inferiores, donde la temperatura determina la emisión, hay una problemática inherente a las condiciones de no ETL, al no ser correcta esta aproximación. Esta adversidad se soluciona con el uso de códigos de inversión que incluyen un modelo de no ETL para el cálculo directo (herramienta fundamental del problema inverso). Finalmente, la ausencia de medidas locales de las magnitudes atmosféricas implicadas, que son necesarias para iniciar y guiar la inversión, se solventa asumiendo ciertas condiciones *a priori*, predichas por simulaciones numéricas en 3D mediante el uso de modelos globales de circulación en Marte de vanguardia.

Hemos analizado las emisiones infrarrojas de CO_2, en la región alrededor de 4.3 μm, obtenidas por OMEGA en geometría limbo en la termosfera diurna de Marte, con el objetivo de inferir información sobre parámetros atmosféricos fundamentales, como densidad y temperatura. Estas emisiones se producen por fluorescencia de la radiación solar por parte del CO_2 y es necesario incorporar condiciones de no ETL. Hemos realizado la calibración radiométrica de los datos proporcionados por OMEGA, limpiado los espectros disponibles, incluyendo el uso de técnicas de agrupamiento, y generado perfiles verticales de radiancia para cada conjunto de datos orbitales. La distribución y la geometría de los espectros obtenidos por OMEGA son altamente heterogéneas, dando lugar a proyecciones muy diferentes en el limbo de la atmósfera marciana. Por este motivo, se estableció una serie de criterios geométricos para facilitar una posterior comparación consistente entre los resultados de las inversiones.

Tras generar los perfiles verticales de radiancia, hemos aplicado un esquema de inversión no ETL basado en un esquema ampliamente validado para la Tierra, que adaptamos a condiciones marcianas. En este trabajo se presenta la configuración de la inversión, y una discusión sobre los perfiles de densidad de CO_2 invertidos. También se formó un total de 742 perfiles a partir de las 47 órbitas de OMEGA con observaciones en geometría limbo previamente seleccionadas. La convergencia alcanzada para el conjunto de todos los datos fue del 94 %, resultado que puede considerarse muy satisfactorio.

A partir de las densidades de CO_2 invertidas, derivamos perfiles de temperatura, asumiendo equilibrio hidrostático. Para ello, usamos un algoritmo desarrollado a tal efecto. Para el 60 % de las órbitas analizadas, encontramos un mínimo en el perfil de temperaturas a 140–150 km, lo que indica una termosfera más fría que la del modelo empleado, el LMD-MGCM. Por el contrario, en el 30 % de las órbitas se obtuvo una termosfera más caliente que la predicha por el modelo.

Se incorpora también un estudio exhaustivo de sensibilidad del esquema de inversión. Hemos encontrado que, en general, la incertidumbre debida a la calibración de la ganancia instrumental y la inherente al error de la inversión son de especial importancia, mientras que la influencia de las temperaturas en la atmósfera de referencia usada como *a priori*, tomada de nuestro modelo de circulación general (GCM, por sus siglas en inglés), es menor. Según nuestro estudio, los perfiles de CO_2 se pueden derivar con una precisión de aproximadamente 20 % y una resolución vertical de unos 15 km entre 120 y 160 km de altura tangente, .

Finalmente, hemos comparado los perfiles de densidad y temperatura obtenidos con las predicciones del LMD-MGCM y con los resultados proporcionados recientemente por otros instrumentos que estudian la termosfera marciana. En general, no se observan correlaciones claras de las discrepancias datos-modelo obtenidas con ninguna dimensión temporal o espacial, ni mediante un estudio global, ni cuando se analizan subconjuntos de datos de OMEGA más homogéneos, es decir, con geolocalizaciones restringidas. Hay una única excepción, el ángulo cenital solar, que afecta a la emisión atmosférica. La mayoría de las observaciones provenientes de otros experimentos, como medidas *in situ* de NGIMS o remotas de IUVS (ambos a bordo de MAVEN) tienen incertidumbres del mismo orden que las presentadas en este trabajo. Los resultados de dichos experimentos también ponen de manifiesto diferencias importantes cuando se comparan al LMD-MGCM o a otros modelos de circulación general. Dicha comparación global con las simulaciones numéricas indica una variabilidad atmosférica en consonancia con la encontrada también en nuestros datos de OMEGA. Este resultado apunta a la necesidad de validación de modelos globales a alturas termosféricas. La termosfera de Marte es, de hecho, una región compleja y dinámica.

Abstract

Mars is a vast and complex world. It is a terrestrial planet with a reddish appearance, due to a surface mostly covered by ferric oxide dust and rocks. Mars has a faint atmosphere mainly composed of carbon dioxide (CO_2), with atmospheric circulation and weather patters, like Earth. It has, however, remarkable diurnal oscillation of winds, due to a considerable thermal excursion. These oscillations have an effect on all the layers of the atmosphere, exerting a appreciable influence over the global atmospheric circulation on Mars.

In the last decade, several spacecrafts and rovers have visited the *Red Planet*, and a few more are approved for the next years. Two of these missions were designed, built and operated entirely at/from Europe, and are of special relevance for this Thesis:

- Mars Express, launched in June 2003, arrived at Mars in December of the same year. It consisted on two modules, an orbiter and a rover, but the rover was lost due to communication problems during the descent. The orbiter successfully completed its nominal mission and, in fact, is still operational at the time of writing. Among others, Mars Express carries two instruments important to the topic of this Thesis, PFS (Planetary Fourier Spectrometer) and OMEGA (Observatoire pour la Minéralogie, l'Eau, les Glaces et l'Activité). This work makes extensive use of the CO_2 emissions observed in limb geometry by OMEGA, given its excellent vertical coverage.

- ExoMars, delivered in two different phases or missions. The first stage, ExoMars Trace Gas Orbiter, was launched in 2016 and, after more than a year of aerobraking and orbit insertion, is currently producing the first scientific results. Its payload also includes two

instruments relevant to this work, NOMAD (Nadir and Occultation for Mars Discovery) and ACS (Atmospheric Chemistry Suite). The second mission, scheduled for 2020, will consist on a lander, responsible for delivering a rover to the Martian surface.

As a unifying thread between these two missions, the European project UPWARDS (Understanding Planet Mars With Advanced Remote-sensing Datasets and Synergistic Studies) kicked off back in 2015, within the scope of the European Union's research and innovation programme Horizon 2020. UPWARDS aimed at composing a global image of Mars, from the subsurface to the higher atmosphere. The project took into account the development of new scientific tools for spacecraft data analysis, like those expected from ExoMars, and the study of existing unexploited data, like those provided by Mars Express. The work presented in this Thesis was partly supported by UPWARDS.

Despite the importance of the thermosphere, for instance, to the atmospheric escape to space, this is maybe the less known region of the Martian atmosphere. Most of the information we have of these altitudes comes from very disperse and unconnected sources. Among them,a few *in situ* profiles taken during the descent of some missions, like Viking 1 and 2, the aerobraking manoeuvres by the Mars Global Surveyor and Mars Reconnaissance Orbiter spacecrafts, the SPICAM instrument on board Mars Express, and the instruments on board the MAVEN mission. These measurements allowed to obtain density and temperature profiles, and to study the seasonal and geographical variabilities of the thermosphere. According to these observations and their numerical simulations, the thermosphere of Mars is a complex and dynamic region, strongly coupled to lower layers. Concretely, the effects caused by the dust storms and the temperature variability in the low atmosphere are propagated upwards up to the thermosphere. To understand this region, it is therefore necessary a global view of the atmosphere, from its interactions with the surface, to the exchanges of species with the exosphere.

The thermospheric data previously described have a limited temporal and geographical coverage. Some important issues, like the influence of solar activity, are difficult to understand from the available data. Most of them, except aerobraking measurements, concentrate in the night side of the planet, leaving the diurnal thermosphere almost unexplored. It is in the dayside thermosphere where the strongest infrared atmospheric non-thermal emissions are produced. These infrared emissions offer an interesting possibility for remote sounding at these heights in all terrestrial planets.

There are indeed thermospheric observations of Mars in the infrared, but they have not been sufficiently exploited so far, due to the complexity of the physical interpretation and the numeric difficulty of the required mathematical inversion. These observations were acquired by two instruments on board Mars Express, OMEGA and PFS. Their analysis is expected to provide a wider and deeper understanding of the dayside thermosphere at the maximum sensitivity altitudes.

In the Group of Terrestrial Planetary Atmospheres (GAPT, for its Spanish acronym) at the Instituto de Astrofísica de Andalucía (IAA), a large experience on non-thermal atmospheric emissions, physical models for the Mars atmosphere, and tools for the inversion of such emissions are available. Molecular species, like CO_2, produce strong non-thermal emissions in the infrared in the higher layers of the atmosphere. At those altitudes, the density is so low and molecular collisions are so rare that local thermodynamic equilibrium (LTE) conditions no longer apply. The departure from LTE typically occurs in the diurnal hemisphere when such species are excited by solar radiation in the rotational-vibrational bands in the near and medium infrared (between 1 and 10 μm). The emissions produced contain information on the densities of the emitting species, and therefore contribute to the extraction of density and temperature profiles in the higher atmosphere. Some difficulties arise with this type of observations. First, the emission of these tenuous layers is low, so the observation in limb geometry, where the emission of a large atmospheric path is integrated on the detector, is extremely helpful. Besides, inherent difficulties arise when dealing with non-LTE conditions, as this approximation is not valid. This issue is solved by the use of inversion codes including a non-LTE model in the forward calculation (fundamental tool of the inverse problem). Finally, the lack of local measurements of the atmospheric magnitudes involved, needed to start and guide the retrieval, is overcame by the assumption of *a priori* conditions predicted by 3-D numerical simulations by state-of-the-art Global Circulation Models of Mars.

We analysed limb infrared CO_2 emissions, in the region around 4.3 μm, obtained by OMEGA in the daylight thermosphere of Mars, in order to infer information on fundamental atmospheric parameters, like density and temperature. These emissions are caused by CO_2 fluorescence of solar radiation, and the investigation needs to take into account non-LTE conditions. We performed a radiometric calibration on the data provided by

OMEGA, cleaned the available spectra, including the use of clustering techniques, and generated radiance vertical profiles for each orbital dataset. The distribution and geometry of the spectra acquired by OMEGA are highly heterogeneous, leading to very different projections in the limb of the Martian atmosphere. For this reason, a series of geometric criteria was established in order to allow for an easier and consistent comparison among the results of the retrievals.

Once the radiance vertical profiles were generated, we applied a non-LTE retrieval scheme based on a extensively validated scheme working for Earth, which we adapted to Martian conditions. In this work we present information on the inversion set up, and a discussion on the retrieved CO_2 density profiles. A total of 742 profiles were formed from the 47 OMEGA orbits with limb observations previously selected. The convergence rate achieved considering the entire dataset was 94%, which is considered as very satisfactory.

From the retrieved CO_2 densities, we derived temperature profiles, assuming hydrostatic equilibrium. For this, we made use of an algorithm developed for that task. For 60% of the orbits analysed we found a minimum in the temperature profile at 140–150 km, indicating a thermosphere colder than that of the model used, the LMD-MGCM. On the opposite side, a thermosphere warmer than that predicted by the model was obtained in 30% of the orbits.

An extensive sensitivity study of the retrieval scheme was also carried out. We found that, in general, the uncertainty due to the instrumental Gain calibration and that caused by the retrieval noise error itself are of primary importance, while the influence of the temperatures in the reference atmosphere used as *a priori*, provided by our General Circulation Model (GCM), is minor. According to our study, CO_2 profiles can be derived with a precision of around 20% and a vertical resolution of around 15 km between 120 and 160 km tangent altitude.

Finally, we compared the density and temperature profiles obtained to the predictions of the LMD-MGCM and to the results recently provided by other instruments studying the Martian thermosphere. In general, no clear correlation of the data-model discrepancies obtained with any temporal or spatial dimension is observed, neither from a global study nor when a more homogeneous subset of OMEGA observations, i.e., at constrained geolocation, is analysed. There is one exception, the solar zenith angle, which affects the atmospheric emission. Most observations from other instruments, like *in situ* or remote measurements by NGIMS and by IUVS (both on board MAVEN), respectively, have uncertainties of the order of those presented in this work. The results from these experiments also bring to light important differences when compared to the LMD-MGCM or other General Circulation Models. This global comparison with numeric simulations indicates an atmospheric variability in line with that found in our OMEGA data. This result points to the necessity of validation of global models at thermospheric altitudes. The thermosphere of Mars is, indeed, a complex and dynamic region.

Contents

List of Figures

List of Tables

No one would have believed in the last years of the nineteenth century that this world was being watched keenly and closely by intelligences greater than man's and yet as mortal as his own.

Herbert George Wells

1

Introduction

Abstract

This introductory chapter is devoted to give a general overview of the main characteristics of Mars and its atmosphere, some of the open problems nowadays, and the motivation and goals of the present Thesis research. A review of the space missions to Mars leads the reader to the fundamentals of the current knowledge of the atmospheric conditions of the planet, with an emphasis put on the higher atmosphere or thermosphere. At this point, we briefly discuss the difficulties for sounding this region remotely, even when the infrared emissions of carbon dioxide (CO_2), the strongest at these altitudes, are used. A short review of the spectroscopy of the CO_2 molecule is then introduced, giving way to a brief description of global circulation models, valuable tools to understand the distribution and dynamics of species in the atmosphere, focusing on the model used in this work as a reference, the LMD-MGCM. Finally, the motivation of this dissertation and its main objectives are exposed.

1.1. Planet Mars

Two hundred and thirty million kilometres away on average, Mars is the fourth planet from the Sun in our Solar System. Mars is commonly known as the *Red Planet* due to the iron pigments present in its rocks and dust, which gives the surface a reddish hue in Earth's night sky. Focusing on the blood-red appearance of the planet, both Greeks and Romans named it after their respective god of war, Ares and Mars. The planet's two small moons, Phobos and Deimos, were named by Romans after the two horses that the god of war used to pull his chariot. Wars, blood, fear, little green men and death rays were usual companions of Mars through the centuries in the social imaginary. A world that we know today is cold and dry, exposed to intense ultraviolet radiation due to the lack of a protective ozone layer (Forget et al., 2008). Outside Earth, however, Mars is the planet most hospitable for life we know of, and every space mission to our neighbour keeps providing us surprises, making the Mars exploration more interesting than ever.

Galileo Galilei was the first to telescopically observe the *Red Planet*. Given the proximity to Earth, and mainly because it is further from the Sun, Mars is a planet rather easy to observe (Anguita, 1998). That allowed Tycho Brahe to perform precise observations and his measurements helped Johannes Kepler to formulate the laws of planetary motion. Mars describes an elliptical orbit around the Sun, with a perihelion of 1.38 AU (Astronomical Unit, around 150 million kilometres) and an aphelion of 1.66 AU, taking approximately two Earth years to complete an orbit. Giovanni Domenico Cassini, in 1666, observed spots in the Mars surface and deducted a rotation period of 24 hours and 40 minutes, surprisingly close to the currently accepted one (24 hours and 37 minutes), and very similar to Earth's day duration. Mars has an axial tilt of roughly 25 deg, similar to Earth's axis inclination, and thus it has cyclical seasons. Both planets have ice caps at the poles too. Table 1.1 summarises the main characteristics of Mars, compared to Earth's.

Although all these similarities could indicate the portrayal of a twin planet of Earth, a common view during the nineteenth century, significant differences also arise when comparing the planets upon closer inspection. Mars is small, with a diameter half the size of Earth's. With this size and a lower density, Mars has only one tenth of Earth's mass and a gravity field one third as strong. The Martian atmosphere is thin in comparison with Earth's, and is mainly composed of carbon dioxide (CO_2), like Venus'. Its atmospheric pressure is extremely low, about one hundredth of that on Earth. The existence of liquid water on the surface is not possible in these conditions for a significant amount of time. Several planetary missions, however, have provided evidence on the presence of liquid water below the planetary surface.

	Mars	Earth
Orbit distance (average)	228 million km	150 million km
Orbit eccentricity	0.093	0.017
Length of year	687 days	365 days
Tilt of axis	24.9 deg	23.4 deg
Length of day	23 hours 56 minutes	24 hours 37 minutes
Equatorial diameter	6792 km	12756 km
Mass	6.4×10^{23} kg	6.0×10^{24} kg
Surface gravity	$3.71\ \mathrm{m\,s^{-2}}$	$9.81\ \mathrm{m\,s^{-2}}$
Escape velocity	$18.1\ \mathrm{km\,h^{-1}}$	$40.3\ \mathrm{km\,h^{-1}}$
Surface temperature	130 – 300 K	185 – 330 K
Surface pressure	0.006 atm	1 atm
Atmospheric constituents	CO_2 (95%), N_2, Ar	N_2 (78%), O_2 (21%)

Table 1.1: Mars facts compared to Earth.

1.2. Space exploration

The combination of the orbits of Earth and Mars establish the existence of privileged slots every second year, when the planets are closer to each other. These are the ideal times for the arrival of the space probes to Mars, because the travel time is shortest and the conditions for communication with Earth during orbit insertion become optimal (Anguita, 1998).

Although the first missions to Mars date from the early 1960s, it took until 1965 before the first successful flyby (Mariner 4) and until 1972 before the first orbiter (Mariner 9) and lander (Mars 3) missions reached the planet. The history of space exploration of Mars is sprinkled with mission failures. As a matter of fact, roughly only half of the delivered missions to Mars have achieved partial or total success (Forget et al., 2008). Table 1.2 summarises the successful missions up to the first months of 2019, according to NASA (NASA, 2019).

Given the high expectations created by the lack of close observations

Missions to Mars				
Year	Country	Mission	Type	Results
1964	US	Mariner 4	F	Returned 21 images
1969	US	Mariner 6	F	Returned 75 images
1969	US	Mariner 7	F	Returned 126 images
1971	USSR	Mars 2	O	No useful data
1971	USSR	Mars 3	O, L	8 months of poor data
1971	US	Mariner 9	O	Returned 7329 images
1973	USSR	Mars 5	O	Returned 60 images
1973	USSR	Mars 6	F, L	Occultation experiment
1975	US	Viking 1	O, L	First successful landing mission
1975	US	Viking 2	O, L	16000 images, atmosphere and soil
1988	USSR	Phobos 2	O, L	Successful orbital observations
1996	US	Mars Global Surveyor	O	More images than all missions to date
1996	US	Mars Pathfinder	L, R	First rover on another planet
2001	US	**Mars Odyssey**	O	High resolution images of Mars
2003	ESA	**Mars Express**	O, L	Orbiter imaging Mars in detail
2003	US	MER Spirit	R	Operated for 2208 sols
2003	US	MER Opportunity	R	Operated for 5351 sols
2005	US	**MRO**	O	More than 26 Tb of images
2007	US	Phoenix	L	Returned more than 25 Gb of data
2011	US	**Curiosity**	R	Exploring Mars' habitability
2013	India	**MOM**	O	Surface, mineralogy and atmosphere
2013	US	**MAVEN**	O	Studying Martian atmosphere
2016	ESA/RU	**ExoMars TGO**	O, L	Orbiter studying Martian atmosphere
2018	US	**InSight & MarCO**	F, L	EDL with help of MarCO CubeSats

Table 1.2: Partial and total successful missions to Mars. Year corresponds to launch date and type refers to F: Flyby, O: Orbiter, L: Lander, R: Rover. EDL stands for entry, descent and landing. Operational missions in 2019 are highlighted in bold font.

and by the human imagination, disappointment reigned when the first probes approached the planet: no canals, no Martians, no water and lots of craters in a dead-looking environment. In this introduction, we will focus on missions directly impacting on the knowledge of the atmosphere of Mars, condensing the main historical findings, as described by Forget et al. (2008), to a few paragraphs.

Indirect analysis of the atmosphere, as captured by the first flybys over the *Red Planet* in 1965, indicated a surface pressure of less than 7 millibars, much more tenuous than expected. In the early 1970s the first artificial satellite was successfully put in orbit around Mars (Mariner 9). The spacecraft arrived when a great dust storm was underway and the whole surface was obscured. Mariner 9 could examine the surface, the atmosphere, the polar caps and the clouds in different spectral bands. In 1976, the Viking probes were the first to successfully land on the planet, and their on board experiments led the scientist to officially conclude that no life was found, although unanimity was lacking.

The cuts in the space exploration budgets, the focus on other Solar System bodies and the series of failed missions caused two decades of low activity coming from Mars' surroundings, with the exception of the partial success achieved by Phobos 2 in 1989. Two last achievements arrived before the end of the century, Mars Global Surveyor and Mars Pathfinder, both launched in 1996. Mars Global Surveyor lasted for ten years and observed, among other discoveries, local magnetic fields, footprints of past liquid water, and water ice (Albee et al., 2001). Regarding the atmosphere, one of its instruments, TES, supplied the thermal structure up to about 40 km, including weather patterns, like the repetition of dust storms or dust devils, and the basic picture of the so called water-cycle, an annual exchange between the poles and the atmosphere. On the other hand, the Pathfinder lander carried inside a small rover, *Sojourner*, that became the first human vehicle moving through the Martian surface.

The golden years of the Mars robotic exploration were to come with the 21th Century. Besides conducting its own scientific observations (like hydrogen distribution maps and radiation environment records), Mars Odyssey serves as a communication link between robots on the planet surface and Earth since 2001 (Kornfeld et al., 2008; Zeitlin et al., 2010). The Spirit and Opportunity rovers far outlasted their nominal longevity (90 days), exploring the planet during 7 and 14 years, respectively. They found strong evidence of past liquid water, used the Argon abundance as a tracer of atmospheric dynamics, and measured the frequency and dynamics of dust devils, among other findings (Andrews-Hanna et al., 2007; Lemmon et al., 2015).

On Christmas night of 2003, Mars Express entered Mars' orbit, becoming the first successful mission to Mars by the European Space Agency (ESA). Mars Express revolutionised many areas of Mars' science, in particular, the knowledge of the upper atmosphere of Mars, which is the target region in this Thesis, and is still operative in 2019 (Mars Express, 2019). Mars Express contributed, for example, to the discovery of water ice and polar ice caps made of CO_2 and water (Bibring et al., 2004a), and the controversial detection of methane in the atmosphere (Formisano et al., 2004). One of the instruments on board the spacecraft, OMEGA, will be the object of study in Chapter 3, as it provided the spectral measurements used throughout this work.

Mars Reconnaissance Orbiter (MRO), operational since 2006, and the Phoenix lander, arrived in 2008, continued unveiling the watery past of the planet, and extended the systematic mapping of the Martian atmospheric temperatures up to about 80 km, below the thermosphere. The last rover to land on Mars (and yet the only one currently alive), Curiosity, is probably the most famous space explorer. We know that Ancient Mars could have supported living microbes, as key ingredients for life were found by Curiosity (Grotzinger et al., 2014). Besides, the discovery of organic carbon and the detection of a background level of methane leave the conjectures about ancient Mars and the expectation towards its future as open as ever.

In the last years, two other relevant missions, from the atmospheric point of view, arrived at the *Red Planet*, MAVEN and ExoMars. MAVEN confirmed that the loss of hydrogen to space is related to the solar wind (Jakosky et al., 2018), and supplied new density and temperature measurements at thermospheric altitudes, most of them still under investigation (Jain et al., 2015; Evans et al., 2015). ExoMars Trace Gas Orbiter (TGO), within the first months of science production, has refuted the methane findings of Mars Express and Curiosity (Korablev et al., 2019a) and is expected to study also the upper atmosphere using the technique of solar occultation, a very effective way to sound very low gas abundances, and previously used by Mars Express on a few occasions. Finally, InSight, a mission devoted to the deep interior of the planet, recorded the sounds of Martian winds for the first time in 2018.

Several missions are under development for the next launch slot. Hope Mars Mission (UAE), Mars 2020 (USA), ExoMars 2020 (ESA, Russia), 2020 Chinese Mars Mission (China) and Mars Terahertz Microsatellite (Japan) are planned to be launch in 2020. Additionally, Mars Orbiter Mission 2 (India) should be launched in 2022 and Martian Moons Exploration (Japan) in 2024.

1.3. The atmosphere of Mars

Although the Martian atmosphere may seem dense when seen from Earth, due to the obscuration of the surface by the airborne dust particles, it is extremely thin in comparison with that of our planet. This is a major characteristic which affects most aspects of the current Mars climate. The pressure at the surface is less than one hundredth of Earth's atmospheric pressure. The tenuous Martian atmosphere is mainly composed of carbon dioxide (CO_2), with minor contributions of nitrogen, argon and traces of other gases. Since CO_2 is not a greenhouse gas as strong as Earth's water vapour, the greenhouse effect on Mars is small, about 5 K, one sixth the average value on Earth (Haberle, 2013).

The atmosphere of Mars was denser in the past, probably much denser, enough to support large oceans of water (Parker et al., 1993). Perhaps it also contained more greenhouse gases. The planet seems to have lost most of the atmosphere due to the impact of huge objects in its early years, reactions with the surface and escape to space (Hunten et al., 1987; Zharkov, 1996). The low gravity makes Mars a not very efficient planet at retaining its atmosphere when dealing with impacts of meteorites, thermal escape or solar wind erosion. Mars lacks a magnetic field like that on Earth, and even CO_2 molecules can be ejected into space after colliding with ions strongly accelerated by the solar wind (Forget et al., 2008).

Despite the thin atmosphere, Mars has well-defined weather patterns, like cold fronts and cyclones at synoptic scales, with an atmospheric circulation, including Hadley cells and descending branches at high latitudes, driven by the same forcings as on Earth. The Martian global winds are mainly produced by thermal contrasts and by the rotation of the planet, yielding general patterns similar to those observed on Earth. However, because of the extreme temperature differences between day and night, the diurnal oscillation of winds is remarkable. These oscillations have an effect on all the layers of the atmosphere, exerting a considerable influence over the global atmospheric circulation on Mars (Forget et al., 2008). Winds on Mars are a key ingredient of a peculiar characteristic of this atmosphere, its large amount of airborne dust, including dust storms. They appear and grow frequently in regions of massive winds (Taylor, 2010) and, in certain regions and seasons, can become global and cover the entire planet.

1.3.1. Seasonal cycles

In 1784, sir William Herschel measured the axial tilt of Mars and the growth and shrinking of its polar caps. These observations led him to conclude that Mars had seasons, just like Earth (Figure 1.1). Indeed, Mars is a planet of changes, with three remarkable seasonal cycles: CO_2, water and dust. We will summarise the main features of these dominant cycles; more details can be found in Read et al. (2004) and in Forget et al. (2008).

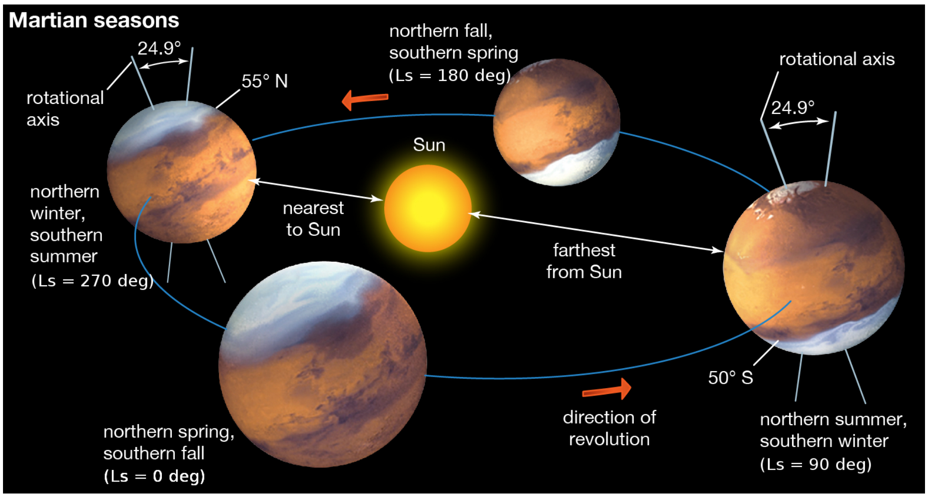

Figure 1.1: The seasons of Mars, a result of the planet's inclination of 24.9 deg (Encyclopædia Britannica, 2019). As the seasons change, the polar caps alternately grow and shrink.

CO_2 cycle. During autumn and winter in the polar regions, the low temperatures reached permit the condensation of CO_2 (around 150 K in the typical Martian low pressures). On the other hand, the CO_2 sublimates again in spring and summer. Because CO_2 is the main constituent of the atmosphere, this seasonal condensation and sublimation of CO_2, which varies the atmospheric mass by about 30%, produces important effects. This includes the transport of heat, momentum and atmospheric trace constituents that intervene in clouds formation (both water and CO_2

particles, this second type of cloud being a unique feature on Mars; on Earth, CO_2 never condenses in the atmosphere since temperatures do not get that low) (Sánchez-Lavega, 2011). In other words, the atmosphere itself freezes over. While this strong seasonal change is clearly visible at the surface, at thermospheric altitudes the cycle is not as strong, or is not well characterised, possibly because the also variable thermal structure counters its effect. Most CO_2 ice in the northern polar cap disappears during summer, while in the south pole a remnant of solid CO_2 stays throughout all the year, in equilibrium with the atmosphere. The eccentric orbit of Mars translates into a warmer but shorter summer in the southern hemisphere (near perihelion), turning it into a more stable location for ice formation and for ice long-term presence. On Mars, water ice clouds occur much less frequently than on Earth, whose closest counterpart are cirrus clouds, being the winter poles, in the seasonal darkness, the cloudiest regions. Regarding CO_2 clouds, these form in the polar autumn and winter during the condensation period, possibly in the form of snow on top of dust grains. At lower latitudes, CO_2 clouds have also been found, but tend to be tenuous and at high altitudes, 80 to 100 km, where atmospheric waves permit occasional cold pockets (Taylor, 2010; Spiga et al., 2012).

Water cycle. The abundance of water vapour on the Martian atmosphere varies due to the exchange with ground reservoirs and to the meridional transport. During the northern summer, the Sun sublimates the water cap on the north pole and the water vapour is transported to other latitudes by the atmospheric circulation. Due to the low temperatures in the polar regions, water clouds can form with a small amount of water in the air. They are thin, infrequent and usually upstaged by clouds of CO_2. In these conditions, frost can also appear at the surface. This way, the water cycle gets partially closed. In the south pole, the ice cap is so cold that retains the frozen water and would, eventually, empty the reservoirs in the north pole. This north-to-south transference arises the possibility of an inverse cycle at some point in the past (Forget et al., 2008). Water ice clouds are also observed at low latitudes, specially during aphelion at some locations and local times, associated to cold patches, and seem to have an impact on the global circulation (Sánchez-Lavega et al., 2018). In total, the amount of water present in both atmosphere and polar caps is about 20% of the volume required to fill the ancient Martian ocean basins, if that is indeed what they are. The rest of water needed should be either hidden below the surface, where it could be liquid, or have been lost to space (Taylor, 2010). There is some evidence of large amounts of water ice at mid and high latitudes in the subsurface (Putzig et al., 2014; Orosei et al., 2015; Wilson et al., 2018).

Dust cycle. Dust particles cover the surface of Mars and provide the atmosphere with small suspended particles, an effect particularly notorious during the dust storms, when dust can extend up to altitudes above 50 km (Haberle et al., 1982). The particles in suspension affect the opacity of the atmosphere and increase its temperature, and they cool the surface significantly if the amount of suspended dust is large. Dust in Mars may also be lifted in the form of *dust devils*, a strong whirlwind that can reach tens of metres in width and several kilometres in altitude. They usually occur in the Martian afternoon, after maximum insolation, and play a key role in providing dust to the atmosphere (Basu et al., 2004; Kahre et al., 2006). During northern spring and summer (southern autumn and winter), only a few number of dust storms occur, while northern autumn and winter (southern spring and summer) are the seasons of major dust storms. Sometimes, typically every second year, they reach a planetary scale and can last up to several months (Martin, 1974). In the last year there have been two episodes of quasi global dust storms (NASA, 2019).

The dust, water and CO_2 cycles are actually linked, as each one affects the others. Water ice clouds alter the circulation and winds, hence the dust lofting. And dust warming affects the condensation. On the other hand, dust grains are needed for the nucleation of ice (Vandaele et al., 2019).

1.3.2. Vertical temperature structure

The atmosphere of a planet is usually separated, for its study, into layers parallel to the surface, because the strongest variation of the temperature occurs with height. For the case of Earth, the layers are as follows:

- *Troposphere*: this is the lowest part of the atmosphere, between 0 and 11–16 km, where most weather phenomena take place. The temperature decreases with altitude due to the convective regime that dominates the layers in contact with the (usually) warmer ground.

- *Stratosphere*: in this layer, extending from about 15 to about 50 km, dominated by radiative transport, the temperature raises with altitude, due to the absorption of ultraviolet solar radiation by ozone.

- *Mesosphere*: in this region, between 50 and 85 km, the temperature slightly decreases with altitude, due to radiative cooling to space, mainly by CO_2, O_3 and H_2O.

- *Thermosphere*: the temperature raises again with altitude in this region, due to absorption of ultraviolet and X-ray solar radiation, reaching very high values, which gives the name to this layer. It extends from 85 to above 500 km. The heating sources are partially compensated by thermal conduction and by radiative cooling of CO_2 and NO. Also at these altitudes the energetic solar radiation, at diverse spectral ranges in the UV and X-ray frequencies, ionises the neutral species, giving rise to ionospheric layers, peaking at diverse altitudes. Further, diffusion of species dominates over atmospheric turbulence, which produces a distinct vertical gradient of composition with altitude, with light species more abundant at higher levels.

The upper boundaries of these atmospheric layers are called, respectively, *tropopause*, *stratopause*, *mesopause* and *thermopause*. The region above the thermopause is called *exosphere*, where the extremely low pressure makes collisions between atoms and molecules a rare event, and thus the loss of species into space by thermal motions is possible on Earth. The troposphere is commonly known as the *lower atmosphere*, the stratosphere and the mesosphere together are frequently called the *middle atmosphere*, and everything between the mesopause and the outer space is usually called the *upper atmosphere*.

Figure 1.2 compares the vertical temperature profiles of Venus, Earth and Mars. The convective region, or troposphere, is much more extended on Mars and Venus, partially because none of these planets presents any stratospheric layer, as their ozone content is very small. However, on Mars, in the presence of a large amount of airborne dust, an isothermal layer or even a thermal inversion similar to a stratosphere is possible. On Mars, the convective region thus gives way to the radiation dominated mesosphere at ~ 45 km. In the large Martian mesosphere, extending up to ~ 120 km, the global temperature keeps falling, at a lower rate, determined by radiative cooling to space, until temperatures become nearly constant. This is an average behaviour and the thermal profile at any spe-

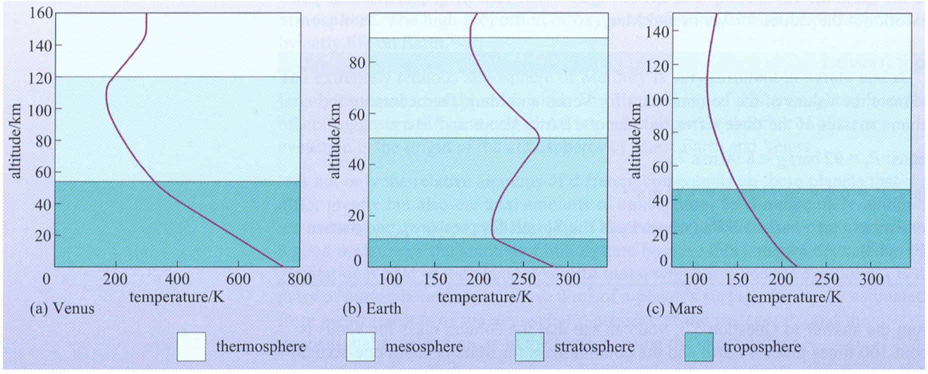

Figure 1.2: Vertical temperature structure of Venus (left), Earth (middle) and Mars (right) (Beatty et al., 1999). Notice the different vertical scales.

cific location shows a more dynamic nature, with oscillations both local (condensation, waves propagating from below) and global (general circulation). The thermosphere of Mars is characterized by an increase in temperature, but, like on Venus, efficient cooling by CO_2 does not allow large temperature gradients to occur, or not as large as on Earth.

1.3.3. Upper atmosphere

The Martian upper atmosphere or thermosphere is very unknown, compared to lower altitudes, but the available data show a complex and dynamic region, strongly coupled with lower layers. Concretely, the effects of dust storms, of wave patterns, and of high temperature variations in the lower atmosphere can be transferred to the thermosphere. Several reviews of the Mars upper atmosphere describe a number of open issues and ongoing debates (Bougher et al., 2015; Gérard et al., 2017; López-Valverde et al., 2018). They seem to agree that a global mapping is necessary to understand the state of the upper atmosphere, its interactions with lower layers, and the exchanges with the exosphere above, where species can scape to space. Improved modelling of the physics and those interactions is also necessary.

Regarding the available data at thermospheric altitudes, and before MAVEN, most observations came from remote sounding of airglow emissions, in addition to the entry profiles and aerobraking tracks of a few missions. They were, like the SPICAM project, mostly focused on the nightside hemisphere. In the dayside thermosphere, the most intense effects of the solar radiation are produced in either a direct way (heating from ultraviolet absorption by CO_2) or an indirect way (atmospheric expansion of the lower region due to absorption by dust). Similarly, it is in the dayside thermosphere where the strongest infrared atmospheric emissions (non-thermal, by CO_2) are produced (López-Valverde and López-Puertas, 1994b). These infrared emissions offer an interesting possibility for remote sounding at these heights in all terrestrial planets (López-Puertas and Taylor, 2001).

There are indeed thermospheric observations of Mars in the infrared, but they have not been sufficiently exploited so far, due to the complexity of the physical interpretation and the difficulty of the required inversion. These observations were acquired by two instruments on board Mars Express (MEx), OMEGA and PFS. Their analysis is expected to provide a wider and deeper understanding of the dayside thermosphere (López-Valverde et al., 2011).

One of those difficulties arises because, at high altitudes, the extremely low density makes collisions between atoms and molecules very rare. In these conditions, the so called *local thermodynamic equilibrium* (LTE) approximation is no longer valid at describing the molecular state populations responsible for these emissions and, therefore, the emissions themselves. Instead, all the molecular processes involved in the excitation and relaxation of the states need to be considered in detail.

Under LTE conditions, the temperature alone determines the molecular state populations. If the temperature is low, very few molecules are expected to be found in states higher than the ground; if the temperature is high, the opposite becomes true. When collisions are reduced in number due to the density decay with altitude, the rates of excitation or de-excitation by radiation are comparable to (or larger than) those produced by collisions.

When the LTE approximation is valid, since the population of the upper states is dictated by the temperature, the emission depends on the atmospheric density only via the number of molecules in the ground state, which is always known to a good approximation. However, under non-LTE, there is an additional dependence via the population of the upper states, which can be a complex non-linear function of the ground state density.

In this work, we will focus on limb observations of dayside radiances emitted in the upper atmosphere of Mars by CO_2 under non-LTE conditions.

1.4. The CO_2 molecule

The Martian atmosphere is mainly composed by carbon dioxide (95%), the atmospheric species with the strongest infrared emissions in the thermosphere, with small contributions of nitrogen (2.7%) and argon (1.6%). Traces of other compounds (oxygen, carbon monoxide, water vapour, hydrogen and other noble gases) are also present. As seen before, the global amount of CO_2 in the atmosphere, and hence the atmospheric pressure, strongly varies among seasons, up to 30%. This is because CO_2 can condense on the surface in winter polar regions and sublimate back to the atmosphere during summer. The variability of CO_2 in the upper atmosphere is more complex, as many other processes participate. In this Thesis we derive CO_2 abundances at thermospheric altitudes from remote observations.

Carbon dioxide is a triatomic linear molecule, composed by two oxygen atoms with a carbon atom between them, and its spectroscopy is very well known. In this section, we follow Herzberg (1945), Banwell (1972) and Goody and Yung (1989) to present a short review of this molecule spectroscopy.

For a N-atomic linear molecule, the degrees of vibrational freedom can be calculated as $3N-5$. Thus the CO_2 molecule geometry yields to four fundamental vibrations, also known as *normal modes of vibration*. Figure 1.3 shows the normal vibrations for the CO_2 molecule, where only three vibrational frequencies are specified, because ν_2 actually consists of two vibrations. The motions involved in the two *bending* modes are identical in all senses but the direction, leading to the same value for the vibrational frequency. Modes related this way are referred to as *degenerated*.

A vibrational mode is infrared active only if there is a dipole change during the vibration. This is not the case for the *symmetric stretching* (Figure 1.3, a), where the dipole moment remains equal to zero, and thus this mode is infrared inactive. On the contrary, the *antisymmetric stretching* and both *bending* modes are infrared active. For polyatomic molecules, the vibrations which imply a dipole change can be either parallel or perpendicular, according to the alignment of the change with respect to the axis of rotational symmetry of the molecule. This distinction is important because the selection rules obtained by the Schrödinger equation depend on the type of vibration.

The selection rule for parallel vibrations is found to be

$$\Delta J = \pm 1 \qquad \Delta v = \pm 1, \pm 2, \pm 3, \ldots \tag{1.1}$$

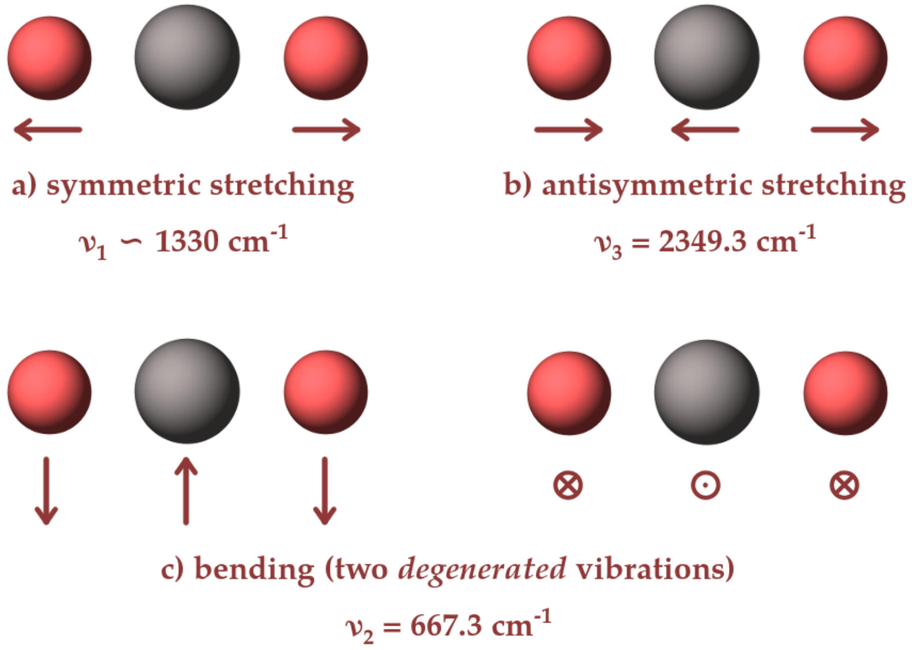

Figure 1.3: CO_2 vibrational modes. The stretching modes are parallel vibrations, while the bending modes are perpendicular.

where J and v are, respectively, the rotational and vibrational quantum numbers. This selection rule gives way to spectra with two branches, called P and R, with lines about equally spaced on each side, and without a central branch, called Q.

For perpendicular vibrations, the selection rule can be written as

$$\Delta v = \pm 1 \qquad \Delta J = 0, \pm 1 \tag{1.2}$$

which implies that a vibrational change could take place without a simultaneous rotational transition. In fact, transitions with $\Delta J = 0$ correspond to a central Q branch, present in this type of vibrations.

The *bending* vibrations, in the 15 μm region, are important for radiative cooling, and interactions by radiative and collisional processes are included in our non-LTE model as described in Chapter 2. On the other hand, the *antisymmetric stretching* mode, around 4.3 μm, is important for heating by solar pumping during daytime. Here we will briefly introduce the emission spectra produced in this spectral region, as it is the subject of study throughout this work.

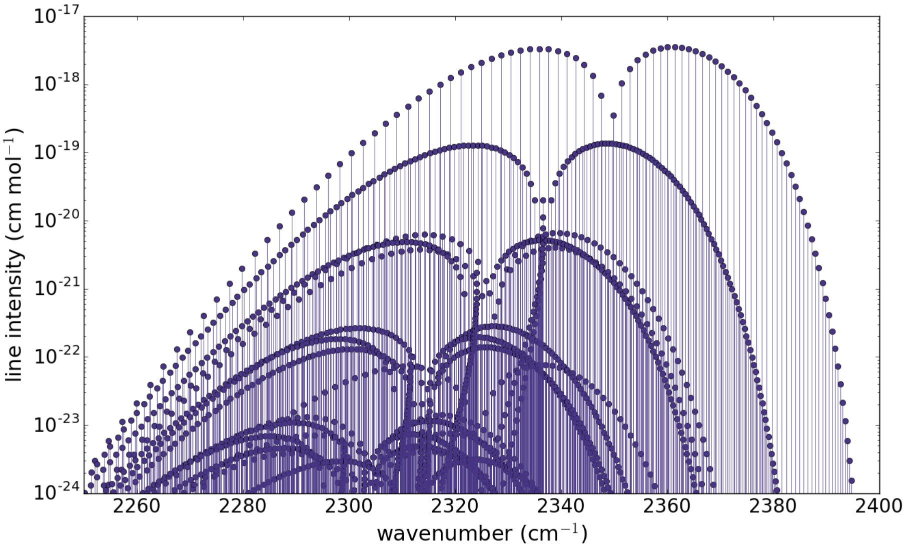

Figure 1.4: CO_2 spectral lines for all bands in the $2250 - 2400\,\mathrm{cm}^{-1}$ interval. A logarithmic representation is chosen to plot together several emission bands.

Figure 1.4 shows all the emission lines of the CO_2 molecule in the $2250 - 2400\,\mathrm{cm}^{-1}$ region, with a line intensity of $10^{-24}\,\mathrm{cm}^{-1}(\mathrm{mol\,cm}^{-2})^{-1}$ or higher. The spectral data for this figure and throughout the rest of the work were obtained from the HITRAN online database (Rothman et al., 2013). Several bands of very different intensities are observed in the plot (note the logarithmic scale in the vertical axis). All the bands have P (left) and R (right) branches, as expected for parallel vibrations (Equation 1.1), and are slightly shifted with respect to each other.

It is usual to define the vibrational state of a CO_2 molecule as (v_1, v_2, v_3), considering the three vibrational modes previously presented. We may simplify this expression writing (v_d, v_3), with $v_d = 2v_1 + v_2$, because a change of one quantum in the *symmetric stretching* vibrational state is equivalent, from the energetic point of view, to a change of two quanta in the *bending* vibrational state ($\nu_1 = 2\nu_2$).

The transitions of the form $\Delta v_3 = \pm 1$, are called *fundamental* when the lower state is the ground, that is, when $v_d = 0$ and $v_3 = 1$. If $v_d > 0$, we observe the so called *hot bands*, which are named according to the value of v_d. This way, we have *first hot* bands for $v_d = 1$, *second hot* bands for $v_d = 2$, and so on.

Usually the fundamental band (FB) is the strongest, because it corresponds to emissions of the lowest, and hence most populated, excited level. In Figure 1.5 the FB is plotted alone, with a linear scale in the vertical axis. However, this general rule may not apply for arbitrary atmospheric conditions, like extreme non-LTE situations, where it it even possible that some high energy states present larger populations (and emissions) than lower states. In this situation, called *population inversion* (López-Valverde and López-Puertas, 1994b; López-Valverde et al., 2016), the contribution to the total emission of weaker transitions may become important. In the upper thermosphere, optically thin for the FB due to the low density, this is the dominant emission. On the contrary, in the lower thermosphere and the mesosphere, where the FB emission is rapidly self absorbed, the SH (second hot) bands (Figure 1.6) stand out. A detailed description is given in Chapter 2.

1.5. Mars General Circulation Models

A General Circulation (or Global Climate) Model (GCM) is a numerical implementation of the physical equations that describe atmospheric circulation, and other basic physics and chemistry assumed for the atmosphere, like the ideal gas law and the energy conservation, for each of the boxes of a discrete grid. Global models simulate the state of the atmosphere, including the processes relevant to the meteorology, in a three dimensional space (altitude, longitude and latitude), after discretisation on a given grid, and at a given time step, which define the model resolution. They can be used to reproduce observations, which would then validate the model, or to predict the atmospheric behaviour of regions with poor observational coverage. Global numeric models can be complex and powerful, depending on the number of variables and processes they incorporate, although they have inherent limitations for several reasons. One of them is due to the natural unpredictability of atmospheres, given the chaotic and turbulent behaviour of the non-linear atmospheric equations (González-Galindo, 2006). To lessen the effects of the day-to-day variability, difficult to predict, it is usual to perform temporal averaging of the GCM results. Problems also arise when treating subgrid-scale dynamics (Houghton, 1977), i.e., the phenomena in a spatial scale smaller than the grid size of the models. Further, even the known physics can contribute with a complex time-consuming function, so they are incorporated in a parametrised, simplified manner. For these reasons, spatially and temporarily constrained calculations of GCMs are usually not fully

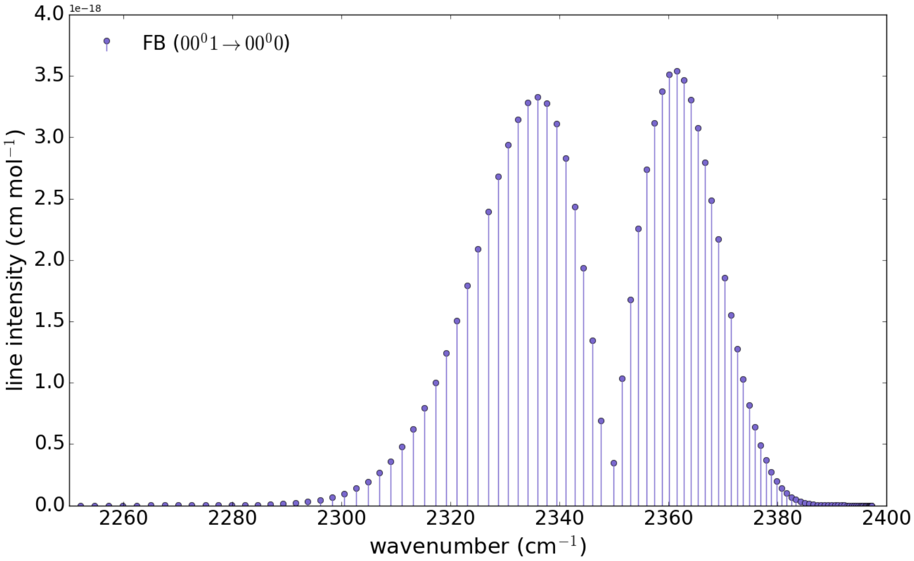

Figure 1.5: Intensities of the CO_2 spectral lines for the fundamental band of the v_3 mode of vibration in the 2250 – 2400 cm^{-1} interval.

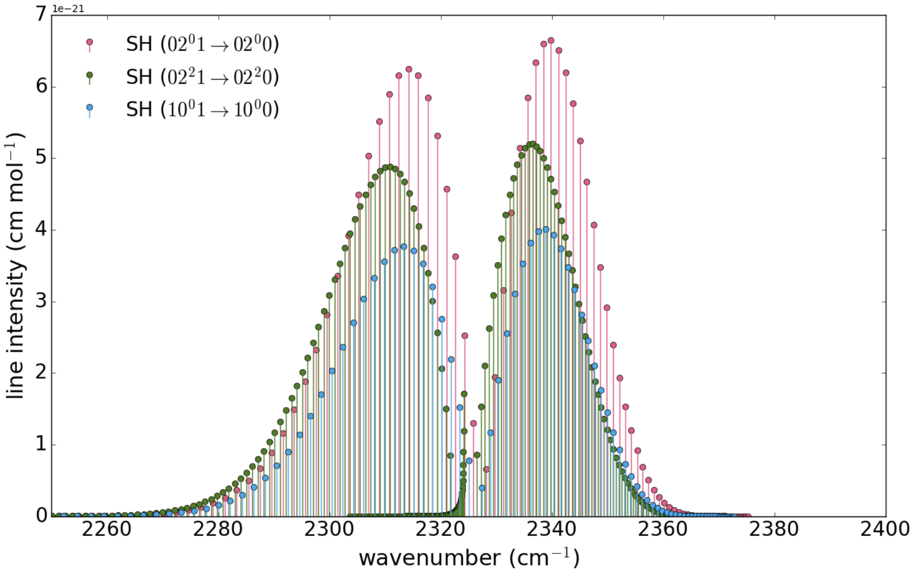

Figure 1.6: Intensities of the CO_2 spectral lines for the second hot bands of the v_3 mode of vibration in the 2250 – 2400 cm^{-1} interval.

trustworthy, and it is recommended to study only general features, at the climatic level, with them.

In the case of Mars, GCMs are inheritors of Earth GCMs, with a large development history. Mars global circulation modelling started in the 60s (Leovy and Mintz, 1969) and continued adding relevant processes, mathematical power, ambition and applications. Nowadays, large-scale motions, CO_2 and water cycles, turbulent and molecular diffusion, NLTE processes, photochemistry, radiative transfer, collisions, conduction, convection, heating and cooling rates, gravity waves or dust are typical modules of a Martian GCM.

A very important aspect in the development of a GCM is its validation and tuning with available data. For the particular case of the Martian upper atmosphere, the lack of data to contrast the predictions of the models imposes an additional difficulty (González-Galindo et al., 2008). This is the case of the abundance and variability of CO_2 in the thermosphere, where it is a key component of the energy budget, of the ionospheric reactions, and the source of reactive species like atomic oxygen, but the GCM predictions are still largely non validated with systematic observations.

Description of the model

In this work, we used the Mars GCM developed at the Laboratorie de Météorologie Dynamique, LMD-MGCM (Forget et al., 1999; González-Galindo et al., 2015) in two different ways. First, for characterising the atmospheric conditions (temperature, pressure and abundance profiles) of the geolocations corresponding to the OMEGA measurements (Chapter 4). In other words, to build an *a priori* climatology and a first guess input for the inversion problem. Secondly, when comparing the results of our inversions with model predictions (Chapter 8), with the goal of validating the model on the one hand and guiding the physical interpretation of our results on the other.

The LMD-MGCM is able to simulate in a self-consistent way the full atmospheric range, from the surface to the exobase, located in Mars between 200 and 300 km, depending on diverse conditions, like season, solar activity and thermal structure. The version of the model used includes an improved parametrisation of the CO_2 15 μm cooling, a modification of the solar variability scheme (able to handle the observed day-to-day variability of the UV solar flux), a variable and realistic dust load in the lower atmosphere (retrieved from TES and THEMIS nadir observations and estimated from MCS limb observations), an extended photochemical scheme, and the radiative effects of water ice clouds (see González-Galindo et al. (2015) and references therein).

The simulations were specifically performed for this work on a 64 × 48 horizontal grid, corresponding to a resolution of 3.75 deg latitude and 5.625 deg longitude. The vertical layering is uneven, with higher resolution in the lower layers. In the upper atmosphere, the vertical resolution is of about 7 km. When vertical profiles were needed at the location and time of one specific observation of OMEGA, they were obtained at the closest point of the GCM grid, and using monthly averages. Simulations for the period from 2002 to 2011, corresponding to five Martian years (MY26, MY27, MY28, MY29 and MY30), were used, and the temporal standard deviation (STD) of the model output at a given point during those periods was taken as a measure of the reference atmosphere uncertainty at that location.

1.6. Motivation and objectives

Scientific motivation. As seen in previous sections, the Martian thermosphere is a complex region, strongly coupled with lower layers, and not observationally explored in a systematic way. Several instruments on board Mars Express have improved their limb-pointing capabilities to perform observations at high altitudes (above 50 km) in the Martian atmosphere. This is the case of the strong emissions, due to solar fluorescence of CO_2, observed by OMEGA and PFS, in the spectral range around 4.3 μm (Formisano et al., 2006; López-Valverde et al., 2011; Piccialli et al., 2016). These emissions have not been fully exploited so far, i.e., not used to derive both temperature and CO_2 density. Retrieving these parameters from non-LTE solar fluorescence is a challenging task. However, if non-LTE effects were properly incorporated into an inversion scheme, an entirely new set of observations of the dayside of Mars would be available at thermospheric altitudes. This could improve our understanding of the thermospheric state and its variability, and should help to validate and enhance the performance of global models at these altitudes.

Non-LTE retrievals of CO and CO_2 from IR emissions at high altitudes have been commonly undertaken in the case of Earth' atmosphere (Jurado-Navarro et al., 2016; Funke et al., 2009; Kaufmann et al., 2002; Mertens et al., 2009), and have recently been performed also for the Titan (López-Valverde et al., 2005; Adriani et al., 2011; García-Comas et al.,

2011) and Venus (Gilli et al., 2015; Peralta et al., 2016) atmospheres. The retrievals on Venus were performed for CO from VIRTIS/Venus Express measurements, assuming optically thin conditions, or from a nadir down-looking geometry, with a fixed and broad emission layer, which simplifies the inversions. However, CO_2 is a minor species on Earth, unlike the case of Mars. The application of a non-LTE retrieval in a limb geometry which addresses optically thin and thick conditions, from the emission of the dominant species of the atmosphere is an entirely new problem in terrestrial atmospheres.

Both OMEGA and PFS provide datasets of these emissions, whose full exploitation was a target within the scope of the European project UPWARDS (Understanding Planet Mars With Advanced Remote-sensing Datasets and Synergistic Studies), an integral study of Mars in preparation for Exomars (UPWARDS, 2019). OMEGA provides simultaneous 2-D imaging and spectra of the CO_2 emissions, with a relatively small field of view, allowing to study the altitude variation of the 4.3 μm emission (Piccialli et al., 2016). On the other hand, PFS has a larger field of view, although with a better spectral resolution. This dissertation focuses on the OMEGA dataset.

Objectives of this Thesis. The main goal of this work is the retrieval of CO_2 densities in the upper atmosphere of Mars (120–180 km, approximately) from daytime observations by OMEGA in the 4.3 μm region in the limb of the planet. We combined state-of-the-art non-LTE models and line-by-line retrieval techniques. From the retrieved CO_2 density profiles, we derived temperature profiles assuming hydrostatic equilibrium. An extensive sensitivity study was also performed. Finally we studied the spatial and temporal distribution of the CO_2 densities and temperatures obtained, by comparing them to global atmospheric models and results from other instruments sounding Mars' atmosphere.

The research consisted on a series of stages or partial objectives:

- Study and familiarisation with the radiative transfer equation and non-LTE conditions in planetary atmospheres. For this stage, a generic versatile model, GRANADA, was adapted to Martian conditions.
- Familiarisation with line-by-line radiance codes, able to incorporate the non-LTE situations previously described. A forward model called KOPRA, perfectly coupled to GRANADA, was used to per-

form direct calculations and generate synthetic spectra.

- Study, cleaning and calibration of limb observations provided by the OMEGA instrument on board Mars Express. The concrete objective was to form radiance vertical profiles, with realistic error bars, suitable for comparison with the non-LTE simulations produced by the forward model aforementioned.
- Application of the retrieval scheme to OMEGA data. The inversion code selected (RCP) was previously applied to retrieve CO_2 in Earth's mesosphere and is coupled to GRANADA and KOPRA. This step required iterative solutions working for the Martian case, sensitivity tests with a full error analysis, and the study of *Jacobians* and *averaging kernels* obtained during the retrievals.
- Estimation of temperature profiles from the retrieved densities, assuming hydrostatic equilibrium.
- Interpretation and comparison of the retrieved densities with predictions by a cutting-edge General Circulation Model, the LMD-MGCM, and with the results obtained from observations performed by other instruments. Conclusions on validation of the LMD-MGCM are also presented.

Outline. Chapter 2 summarises the fundamentals of atmospheric stratification and radiative transfer, describes the forward and inverse models, and presents the retrieval scheme developed and applied in this work. Chapter 3 gives an overview of the Mars Express mission and the OMEGA instrument, presenting the limb dataset selected. Chapter 4 explores the content of a typical OMEGA dataset and goes through its calibration and preprocessing. In Chapter 5 the main retrieval results obtained for the complete set are shown and analysed. Chapter 6 is devoted to the derivation of temperature profiles from the retrieved CO_2 densities, assuming hydrostatic equilibrium. Chapter 7 inspects the sensitivity of the inversion to the use of a different *a priori* CO_2 density profile and to the main uncertainty sources of the forward model. Chapter 8 compares the retrievals of the entire OMEGA dataset analysed to a General Circulation Model and to the results from other instruments found in the literature. Finally, Chapter 9 summarises this work, enunciates the main conclusions, and suggests future applications and extensions or improvements of the retrieval scheme.

There's no sort of use in knocking, and that for two reasons. First, because I'm on the same side of the door as you are; secondly, because they're making such a noise inside, no one could possibly hear you.

Charles Lutwidge Dodgson

2

Radiative transfer and inverse problem on Mars

Abstract

This chapter is focused on the theory of the main physical processes involved in a planetary atmosphere. These processes are important for a complete understanding of an atmosphere and for developing accurate forward models, essential to perform the retrievals. Some basic thermodynamics concepts are presented first, to then derive and solve the radiative-transfer equation (RTE), considering local and non-local thermodynamic equilibrium (LTE and non-LTE, respectively) conditions. An special treatment of the non-LTE calculation is included, because, under these conditions, the RTE is coupled to the statistical equilibrium equation (SEE). Afterwards we present the forward and inverse problems, and introduce the main features of our CO_2 non-LTE model. This includes a description of the main vibrational levels and radiative transitions of the model, and a brief update on its radiative and collisional processes. We finally describe the computational codes used in this work to perform retrievals in non-LTE conditions (KOPRA, GRANADA, and RCP), and present the complete retrieval scheme for the Martian atmosphere.

2.1. Atmospheric stratification

In this section we use some basic thermodynamics to develop simple equations for the vertical structure of an atmosphere. These concepts are essential to handle atmospheric profiles, both before the retrieval (preprocessing in Chapter 4) and after it (temperature derivation in Chapter 6).

The density of a planetary atmosphere falls with altitude, because it is under the planet's gravitational field. The assumption of static equilibrium is usually reasonable as vertical motion is very small (Houghton, 1977). In this scenario, we may describe the hydrostatic equilibrium as

$$dp = -g\rho dz, \tag{2.1}$$

where p and ρ are, respectively, the pressure and density at an altitude z, and the gravity, g, is approximately constant within the atmospheric region, small compared with the radius of the planet.

Consider the equation of state of an ideal gas,

$$\rho = \frac{pM_r}{RT}, \tag{2.2}$$

where M_r is the molecular weight of the gas at temperature T, and R is the gas constant. Combining equations 2.1 and 2.2 and integrating from the ground to a given altitude, z, we obtain

$$p = p_0 e^{-\int_0^z dz/H}, \tag{2.3}$$

where $H = RT/gM_r$ is known as the *scale height*, i.e., the increase in altitude necessary to reduce the pressure by a factor e (Houghton, 1977).

Noting that $\rho = 1/V$, where V stands for volume, and differentiating Equation 2.2, we get

$$pdV + Vdp = \frac{R}{M_r}dT = (c_p - c_v)dT, \tag{2.4}$$

because $c_p - c_v = R/M_r$ for a perfect gas, being c_p and c_v the specific heat at constant pressure and at constant volume, respectively.

In hydrostatic equilibrium, we shall assume that gravitational and buoyancy forces are balanced and can be excluded from the First Law of Thermodynamics, applied to a small change to a closed system, and thus,

$$dq = c_v dT + pdV, \tag{2.5}$$

where dq is the quantity of heat, equal to 0 if no heat enters or leaves the closed system. For this assumption, Equations 2.4 and 2.5 together lead to

$$\frac{dT}{dz} = -\frac{g}{c_p} = -\Gamma_d, \tag{2.6}$$

where Γ_d is the *adiabatic lapse rate* for a dry atmosphere, a magnitude accounting for the temperature gradient in the atmosphere, and an indicator of the atmosphere stability (Andrews, 2010).

2.2. Basics of radiative transfer and non-LTE

In this section we derive the radiative-transfer equation for a general case, and write a particular expression for observations in limb geometry. For this, we mainly follow Andrews (2010).

The interaction between radiation and atmospheric gases plays a key role in the configuration of the atmospheric conditions. In the absence of clouds, scattering can be neglected in the infrared, and thus we will consider absorption and emission processes only at this point. Solar photons are absorbed at certain discrete frequencies by molecules, which are promoted to a higher energy level,

$$\Delta E = h\nu, \tag{2.7}$$

where ΔE is the energy gap between the low and high levels involved in the transition, ν is the frequency of absorption, and h is Planck's constant. The excited state after the transition can relax either re-emitting a photon of the same energy, or by collisions, transferring ΔE to other forms of energy. For instance, vibrational-thermal (V-T) collisions lead to local *heating* of the atmosphere. The transference of photon energy to heat is called *quenching*. Photons may also be emitted by the inverse process to absorption, producing a local *cooling* of the atmosphere. In the infrared, ΔE corresponds to a difference between the energies of pairs of vibrationally or rotationally excited states of the emitting molecule, rather than the energy of a pure electronic transition.

2.2.1. The radiative-transfer equation

We consider interactions of two kinds between radiation and matter, extinction and emission, depending on the direction of the energy transference. Lambert's law states that the absorption which occurs when radiation, L_ν, goes through matter is proportional to the mass of absorber, $n_a ds$, and to the incident radiation itself. Thus,

$$dL_\nu = -e_\nu n_a L_\nu ds, \tag{2.8}$$

where n_a is the number density of absorbing molecules or atoms, ds is the path travelled, and e_ν is the extinction coefficient, including both absorption and scattering. For emission, we have

$$dL_\nu = j_\nu n_a ds, \tag{2.9}$$

where j_ν is the emission coefficient, which includes scattering too.

Under strict thermodynamic equilibrium, the gas inside an isothermal cavity (a cavity with walls maintained at a uniform temperature) is in equilibrium with its walls. The radiation emitted through a hole cut in the cavity behaves as *black-body* radiation and depends only on frequency and temperature. The spectral energy density of a black-body at temperature T is given by Planck's law and the spectral radiance (power per unit area, per unit solid angle, per unit frequency interval) is called the *Planck function*:

$$B_\nu(T) = \frac{2h\nu^3}{c^2(e^{h\nu/(k_B T)} - 1)}, \tag{2.10}$$

where c is the speed of light and k_B is Bolztmann's constant. Equation 2.10 can be expressed per unit wavelength interval, noting that $\lambda = c/\nu = 1/\tilde{\nu}$, where λ is the wavelength and $\tilde{\nu}$ is the wavenumber, commonly used in spectroscopy,

$$B_\lambda(T) = \frac{2hc^2}{\lambda^5(e^{hc/(\lambda k_B T)} - 1)}. \tag{2.11}$$

Integrating Equation 2.11 over all wavelengths, we obtain the well-known black-body radiance,

$$B(T) = \pi^{-1}\sigma T^4, \tag{2.12}$$

where σ is the Stefan-Boltzmann constant.

Also under thermodynamic equilibrium, it can be shown that the energy levels are populated following the Bolzmann distribution,

$$\frac{n_i}{n_j} = \frac{g_i}{g_j} e^{-(E_i - E_j)/(k_B T)}, \tag{2.13}$$

where n_i and n_j are, respectively, the number of molecules in the states with energies E_i and E_j, and with statistical weights, or degeneracies, g_i and g_j.

If thermodynamic equilibrium applies, Kirchhoff's law states that extinction and emission coefficients are related by the Planck function,

$$B_\nu = \frac{j_\nu}{e_\nu}. \tag{2.14}$$

When the thermodynamic equilibrium assumption ceases to be valid, this relation is generalised by defining the source function as

$$J_\nu = \frac{j_\nu}{e_\nu}. \tag{2.15}$$

Combining equations 2.8, 2.9 and 2.15, we obtain

$$\frac{dL_\nu(s', \mathbf{s})}{ds} = -e_\nu n_a (L_\nu(s', \mathbf{s}) - J_\nu(s', \mathbf{s})) \tag{2.16}$$

for a radiation field present at s' at an arbitrary direction, $\mathbf{s}$.

Equation 2.16 is known as the radiative-transfer equation (RTE), as derived by Schwarzschild and Milne in the early part of the 20th century (Chandrasekhar, 1960). By integrating this equation over all solid angles, we may write the heating rate as

$$h_\nu(s') = 4\pi e_\nu n_a (\bar{L}_\nu(s') - \bar{J}_\nu(s')) \tag{2.17}$$

where $\bar{L}$ and $\bar{J}$ are, respectively, the radiance and the emission averaged over all solid angles.

As seen above, for planetary atmospheres in the infrared, neglecting the scattering processes is usually a good assumption, making the extinction coefficient equal to the absorption coefficient, $e_\nu = k_\nu$.

Writing e_ν and n_a in Equation 2.16 as a function of distance, we can obtain a formal solution of the radiative-transfer equation. Consider first the *optical thickness* between two points, s_0 and s, along the direction $\mathbf{s}$. The optical thickness, $\bar{\tau}_\nu$, is a dimensionless parameter accounting for the absorption of radiation across the optical path (Figure 2.1) defined as

$$\bar{\tau}_\nu(s_0, s) = \int_{s_0}^{s} k_\nu(s') n_a(s') ds', \tag{2.18}$$

where $\bar{\tau}_\nu$ is a positive quantity, since $s > s_0$.

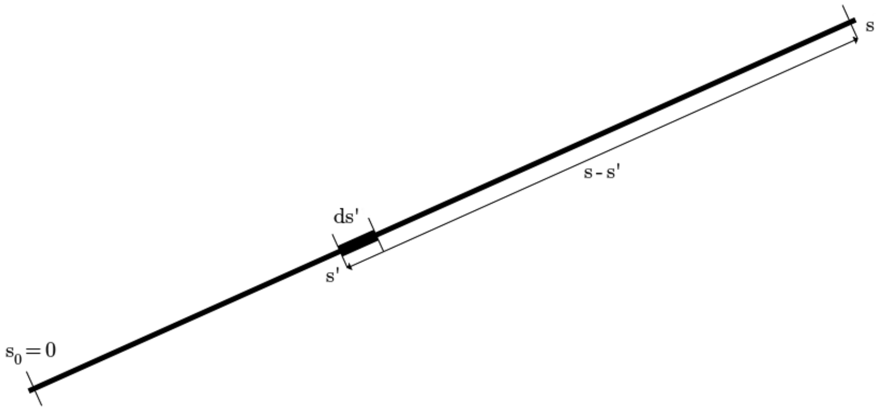

Figure 2.1: Optical path between points s' and s along the direction $\mathbf{s}$.

The radiative-transfer equation at point s' can thus be written as

$$\frac{dL_\nu(s',\mathbf{s})}{d\bar{\tau}_\nu} = L_\nu(s',\mathbf{s}) - J_\nu(s',\mathbf{s}), \tag{2.19}$$

where the change of sign in the right-hand term is a consequence of the arbitrary choice of the origin of $\bar{\tau}_\nu$ at the top of the atmosphere (TOA).

After multiplying Equation 2.19 by the integrating factor $e^{-\bar{\tau}_\nu}$, we can integrate it from s, where $\bar{\tau}_\nu = 0$, to s_0, obtaining

$$L_\nu(s,\mathbf{s}) = L_\nu(s_0,\mathbf{s})e^{-\bar{\tau}_\nu(s_0,s)} + \int_0^{\bar{\tau}_\nu(s_0,s)} J_\nu(s',\mathbf{s})e^{-\bar{\tau}_\nu(s',s)}d\bar{\tau}_\nu. \tag{2.20}$$

Equation 2.20 has a simple physical interpretation. The radiance, L_ν, reaching s is composed of two terms. The first term is the contribution at s_0, attenuated by an exponential factor due to extinction over the distance $s - s_0$. The second term, the integral, is the sum of emissions from all the elements ds' at different positions, s', along the path, each of them attenuated by extinction over the remaining distance, $s - s'$ (Figure 2.1).

The radiance measured by an instrument is obtained from the integral over frequency of the product of the radiances emitted by the atmosphere and the instrumental response function, $F(\nu)$,

$$L(x_{obs}) = \int_{\Delta\nu} L_\nu(x_{obs})F(\nu)d\nu, \tag{2.21}$$

where $L_\nu(x_{obs})$ is the *monochromatic radiance* at the observation point, x_{obs}, and $\Delta\nu$ is the spectral width of the instrument, i.e., the frequency range where the response function is different from zero.

Limb observations

All the atmospheric emissions analysed in this work were taken in limb geometry by the instrument OMEGA on board Mars Express (Figure 2.2).

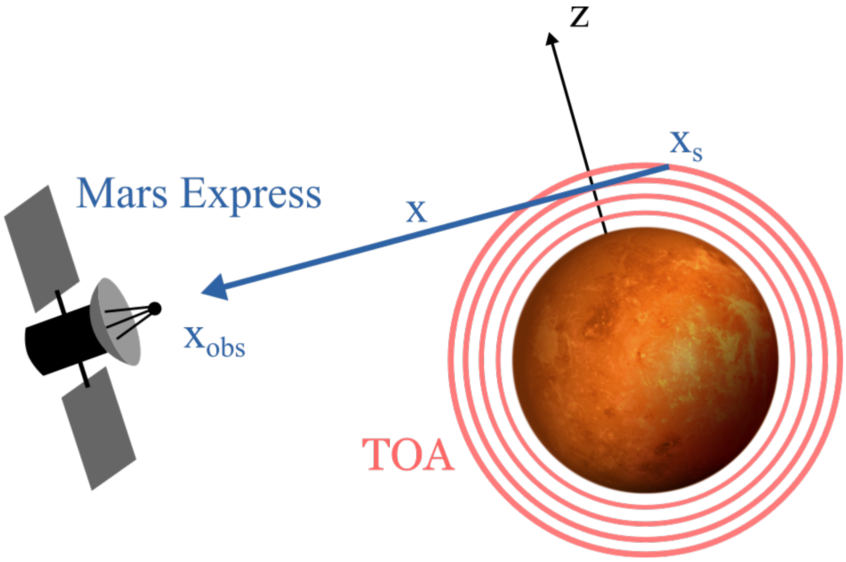

Figure 2.2: Mars limb observation geometry.

For limb observations, the monochromatic radiance is calculated from

$$L(x_{obs}) = \int_{x_s}^{x_{obs}} J_\nu(x) \frac{d\mathcal{T}_\nu(x)}{dx} dx, \qquad (2.22)$$

where x is the position along the limb path, from x_s, the furthest point of the path in the atmosphere, to x_{obs}, the observation point (Figure 2.2), and $\mathcal{T}$ is the *monochromatic transmittance* (López-Puertas and Taylor, 2001), defined as

$$\mathcal{T}(x, x_{obs}) = e^{\int_x^{x_{obs}} k_\nu(x') n_a(x') dx'}. \qquad (2.23)$$

2.2.2. Notion of local thermodynamic equilibrium

Mars' atmosphere is not in strict thermodynamic equilibrium. However, in the lower atmosphere, where the pressure is high, the redistribution of the kinetic energy of molecules occurs much faster than the redistribution with other energy forms, such as radiation or internal energy

(López-Puertas and Taylor, 2001). A Maxwellian distribution of molecular velocities can thus be assumed for a local kinetic temperature,

$$T = \frac{2E_k}{3k}, \tag{2.24}$$

where E_k is the mean kinetic energy of the gas. We consider that a given state is in *local thermodynamic equilibrium* (LTE) when its population is provided by Boltzmann's law at this local kinetic temperature (López-Puertas and Taylor, 2001), i.e., when the mean time between collisions for a given molecule is much shorter than the lifetime for radiative decay. It then follows that the source function, J_ν, is described by the Planck function, B_ν, at the local kinetic temperature. It should be remarked that LTE may prevail for a form of energy and not for all of them at the same time. In particular, rotational levels might be in LTE while vibrational levels are not, and the same situation is usual for different vibrational levels, with LTE conditions applying to some of them, but not to all.

In strict thermodynamic equilibrium, the radiative field is blackbody radiation ($L_\nu = B_\nu$) and the source function is given by the Planck function ($J_\nu = B_\nu$). In LTE the source function is still given by the Planck function, but the radiance, L_ν, can differ from B_ν. For this reason, LTE, unlike strict TE, is compatible with a net gain or loss of radiative energy by the gas. In other words, it is compatible with a non-zero heating rate. The only requirement is that collisions should be fast enough to transfer the net absorbed or emitted radiative energy into kinetic energy (López-Puertas and Taylor, 2001).

2.2.3. Notion of non-local thermodynamic equilibrium

When thermal collisions are not enough to keep a Boltzmann distribution of populations, i.e., a distribution determined by the local kinetic temperature, *non-local thermodynamic equilibrium* (non-LTE) considerations need to be taken into account. The concept of non-LTE was introduced in the context of stellar atmospheres by Milne (1930). In atmospheric context, non-LTE conditions typically apply at high altitudes (low pressures) and for the shorter wavelength bands (more energetic). Some typical processes contributing to non-LTE are:

- Non-thermal collisional processes, like vibrational-vibrational energy transfer (V-V), or electronic to vibrational energy transfer (E-V). For example, the exchange of v_3 quanta between different CO_2 isotopes is very important to understand the CO_2 emission at $4.3\,\mu$m.

- Radiative processes, like spontaneous emission to space, or absorption of solar or atmospheric radiations, among others.
- Chemical excitation by exothermic recombination, or photochemical reactions, to mention a couple of typical examples.

2.2.4. The problem of the source function for non-LTE

Equation 2.20, which involves macroscopic quantities, solves the RTE and can thus be used to simulate the atmospheric emissions, but only if the source function is known. For example, under LTE conditions the source function is described by the Planck function, which is known if the temperature is given. However, when we need to consider non-LTE conditions, the source function is unknown and, therefore, needs to be computed before obtaining the radiation field. Its calculation can be more complicated if many microscopic processes become relevant. For that reason, it is necessary to solve the RTE together with the equation that describes the source function, the *statistical equilibrium equation* (SEE).

The non-LTE source function depends on the number density of the populations of the upper and lower energy levels of the transition involved. In addition, the absorption coefficient is given by the parameters introduced at microscopic levels in Einstein's formulation. In non-LTE, the populations of the energetic levels are no longer governed by the kinetic temperature. It is convenient to introduce the concept of *vibrational temperature*, T_v, to describe them (López-Puertas and Taylor, 2001). These temperatures, when introduced in Equation 2.13, give the excited populations, in a functional form identical to LTE, playing the role of the kinetic temperature. Thus, we may write

$$\frac{n_v}{n_0} = \frac{g_v}{g_0} e^{-(E_v)/(k_B T_v)}, \tag{2.25}$$

where n_v and n_0 are, respectively, the number densities of the upper and lower vibrational states, g_v and g_0 are their respective *degeneracies* (statistical weights), and E_v is the energy difference of the transition. It then follows that if the vibrational temperature of a level differs from the local kinetic temperature, the level is in vibrational non-LTE. An equivalent expression can be derived for non-LTE due to rotational transitions. Non-LTE situations also occur for electronic transitions, which, although present at planetary atmospheres too, they usually are related to astrophysical environments (Thomas, 1965).

As mentioned above, the source function of a gas in non-LTE cannot be described solely by the Planck function. The statistical equilibrium equation expresses the balance between the microscopic processes and provides information on the source function. The RTE is thus coupled to the SEE in non-LTE, and both equations need to be solved simultaneously.

Einstein's coefficients for a two-level simplified approach, being 1 the lower level and 2 the upper level, are related by

$$\frac{A_{21}}{B_{21}} = \frac{2h\nu_0^3}{c^2} \qquad \text{and} \qquad \frac{B_{12}}{B_{21}} = \frac{g_2}{g_1}, \tag{2.26}$$

where ν_0 is the frequency of the vibrational transition or band centre, and Einstein's coefficients, A_{21}, B_{21} and B_{12}, are proportional, respectively, to the rate of spontaneous emission, to the rate of induced emission, and to the rate of absorption. The two-level assumption is plausible for bands which do not extend over a wide spectral interval, i.e., if there is only one dominant transition connecting the upper state to lower states (López-Puertas and Taylor, 2001).

For a general case of radiation-matter interaction, the net rate of emitted photons (emission minus absorption) is proportional to the change in the radiance of the radiative field. The change of the radiance along a distance ds, over a solid angle $d\omega$, is given by

$$\frac{dL_\nu}{ds}\frac{d\omega}{h\nu} = (n_2 A_{21} + n_2 B_{21} L_\nu - n_1 B_{12} L_\nu)\frac{d\omega}{4\pi}, \tag{2.27}$$

where the factor $1/h\nu$ in the first term is introduced to convert the energy units of L_ν into number of photons, and the factor $d\omega/(4\pi)$ in the right hand term accounts for the number of photons produced in $d\omega$ (López-Puertas and Taylor, 2001).

The absorption coefficient and the source function can now be written, using the Einstein relations, as

$$k_\nu = \frac{h\nu}{4\pi}\frac{n_1}{n_a}B_{12}\Big(1 - \frac{g_1 n_2}{g_2 n_1}\Big), \tag{2.28}$$

$$J_\nu = \frac{2h\nu^3}{c^2}\Big(\frac{g_2 n_1}{g_1 n_2} - 1\Big)^{-1}. \tag{2.29}$$

To calculate the population ratio, n_2/n_1, we need to consider all the processes contributing to populate and depopulate the vibrational levels involved. A detailed description for the derivation of the SEE can be found in López-Puertas and Taylor (2001), and here we enumerate the terms introduced by processes of different kinds:

- *Radiative processes.* The rate of absorption is $B_{12}n_1\bar{L}_{\Delta\nu}$ and the rate of emission is $A_{21}n_2 + B_{21}n_2\bar{L}_{\Delta\nu}$. For both cases, $\bar{L}_{\Delta\nu}$ is the mean radiance averaged over the spectral band.
- *Thermal collisional processes.* The number of molecules de-excited from level 2 to level 1 by vibrational-thermal (V-T) collisions is $l_t = k_t[M]$, where k_t is the collisional thermal rate and M is any air molecule. The number of molecules excited from level 1 to level 2 is $p_t = k'_t[M]$, where k'_t is the inverse collisional rate.
- *Non-thermal processes.* The specific production rate of level 2 molecules, p_{nt}, comprises the contributions of vibrational-vibrational (V-V), electronic-vibrational (E-V) and chemical recombination processes, at rates k_{vv}, k_{ev} and k_c, respectively. The specific loss rate of level 2 molecules, l_{nt}, is only contributed by V-V processes at rate k'_{vv}.

Combining all the processes described above, we obtain the statistical equilibrium equation for a two-level system as

$$\frac{n_2}{n_1} = \frac{B_{12}\bar{L}_{\Delta\nu} + p_t + p_{nt}}{A_{21} + B_{21}\bar{L}_{\Delta\nu} + l_t + l_{nt}}. \tag{2.30}$$

From equations 2.26, 2.29 and 2.30, we can derive a new expression for the source function, centred at ν_0, for the two-level approximation (Goody and Yung, 1989; López-Puertas and Taylor, 1989),

$$J_{\nu_0} = \frac{\bar{L}_{\Delta\nu} + \epsilon_1 B_{\nu_0}}{1+\epsilon_2}, \tag{2.31}$$

where ϵ_1 and ϵ_2 are given by

$$\epsilon_1 = \frac{p_t + p_{nt}}{A_{21}}\frac{g_1}{g_2}\left(e^{\frac{h\nu}{kT_k}} - 1\right) \quad \text{and} \quad \epsilon_2 = \frac{l_t + l_{nt}}{A_{21}}\left(1 - \frac{p_t + p_{nt}}{l_t + l_{nt}}\frac{g_1}{g_2}\right). \tag{2.32}$$

Equation 2.31 calculates the non-LTE source function taking into account the contribution of the microscopic processes, including the radiation field. We can now solve the RTE (Equation 2.20) together with the SEE (Equation 2.30) to obtain both the source function and the radiation field (or its divergence, the heating rate).

2.2.5. Solution of the non-LTE problem

There are some particular non-LTE cases in which the source function, the population of the energy levels and the heating/cooling rates can be obtained using simple equations with a reasonable accuracy, without solving the complete RTE, as described by López-Puertas and Taylor (1989). This way, when radiative processes are important only as a loss mechanism because the absorption of radiation can be neglected, we may consider the *weak radiative field* approximation in Equation 2.20. This is the case of two usual scenarios, known as escape to space and cooling to space. On the other hand, the formulation is also simplified when a source supplying radiation from outside the non-LTE region dominates over the radiative exchange between layers. In this case we may use the so called *strong external field* approximation . The two usual scenarios of this simplification are solar radiation and thermal emission from the lower boundary. Finally, when collisions with molecules having non-LTE populations, chemical recombinations or photochemical reactions dominate the excitations sources, simplified expressions may also be applied. The solution of the RTE for all these particular cases can be found in López-Puertas and Taylor (2001).

When no approximations are valid, we need to solve the RTE, coupled to the SEE, in a general case, considering the exchange of photons between atmospheric layers, the variation of the absorption coefficient with frequency due to vibration-rotation lines, the local thermal and non-thermal processes, and the collisional coupling between some vibrational levels. This generic case is the one solved in this Thesis, and in previous studies in the GAPT team at the Instituto de Astrofísica de Andalucía (IAA) (López-Valverde and López-Puertas, 1994a; López-Valverde et al., 2008).

The Curtis matrix method

A common mathematical approach is the Curtis matrix method, which solves the RTE by expressing the heating rate at a given altitude, h_i, in terms of the source function for other atmospheric layers, J_j, and the heating rates at the lower, $h_{l,i}$, and higher, $h_{u,i}$, boundaries of the atmospheric region under consideration (Curtis, 1956). Thus

$$h_i = \sum_j \mathcal{C}_{i,j} J_j + h_{l,i} + h_{u,i} \qquad \text{for} \quad 2 \leq i \leq N-1, \tag{2.33}$$

where $\mathcal{C}_{i,j}$ are the elements of the Curtis matrix, and only depend on the transmission properties of the atmosphere (López-Puertas and Taylor, 2001). The Curtis elements form an $N \times N$ matrix, being N the number of atmospheric layers. The diagonal elements represent the cooling to space, while the non-diagonal elements give the net heating rates between layers.

The dimension of the Curtis matrix is usually reduced to $(N-2) \times (N-2)$, assuming boundary conditions for the source function in the surface (Planck function at surface kinetic temperature) and in the top of the atmosphere (incoming solar radiation, neglecting radiation from outer space). This procedure solves some instability issues when inverting the matrix.

If we write Equation 2.33 in matrix form, we have

$$\mathbf{h} = \mathcal{C}\mathbf{J} + \mathbf{h_b}, \tag{2.34}$$

where $\mathcal{C}$ is the Curtis matrix, of order $(N-2) \times (N-2)$, and $\mathbf{h}$, $\mathbf{J}$ and $\mathbf{h_b} = \mathbf{h_l} + \mathbf{h_u}$ are vectors, with components ranging from 2 to $N-1$.

The source function can be written in matrix form too, and thus

$$\mathbf{J} = \mathbf{B} + \mathcal{D}\mathbf{h}, \tag{2.35}$$

where $\mathcal{D}$ is a diagonal matrix, also of order $(N-2) \times (N-2)$, and $\mathbf{B}$ is a vector with components ranging from 2 to $N-1$. The elements of the matrix $\mathcal{D}$ are given by

$$D = \frac{1}{4\pi S n_a \epsilon}, \tag{2.36}$$

where S, known as *band strength*, and ϵ are defined as

$$S = \int_{\Delta\nu} k_\nu d_\nu \qquad \text{and} \qquad \epsilon = \frac{l_t}{A_{21}}\Big(1 - e^{-h\nu_0/(k_B T)}\Big). \tag{2.37}$$

The solution of the coupled system described by equations 2.34 and 2.35 leads to a simultaneous solution of RTE and SEE, with

$$\mathbf{h} = (\mathcal{I} - \mathcal{C}\mathcal{D})^{-1}(\mathcal{C}\mathbf{B} + \mathbf{h_b}) \qquad \text{and} \qquad \mathbf{J} = (\mathcal{I} - \mathcal{D}\mathcal{C})^{-1}(\mathbf{B} + \mathcal{D}\mathbf{h_b}), \tag{2.38}$$

where $\mathcal{I}$ is the unit matrix.

The RTE–SEE coupled system can also be faced by solving iteratively both equations, alternating the RTE calculations, involving all atmospheric layers, with SEE calculations, involving all the energy levels. The main disadvantage of these methods, usually known as *Lambda iterations*, is the slow convergence, specially for optically thick conditions. Some strategies have been used to accelerate convergence, by avoiding the full calculation of radiative transfer in each iteration (Kutepov et al., 1991; Rybicki and Hummer, 1991). Both methods of calculation can be combined by including the Curtis solutions of the RTE into the Lambda iterations, in order to speed up convergence.

2.3. Inverse problem in atmospheric sounding

In order to develop a non-LTE inversion scheme of infrared emissions for Mars, and to analyse its results, it is convenient to recall some basic notions of forward modelling and the inverse method, and other key concepts associated to the resolution and error propagation associated to this methodology. This revision follows Rodgers (2000).

Remote sensing allows to derive fundamental atmospheric parameters, like composition or temperature, via global-coverage observations. The derivation is usually done, however, indirectly, as the actual observations are based on measurements which have some dependence on these fundamental quantities. For example, the target parameters of this study are the CO_2 abundance and the temperature in the higher atmosphere of Mars, but they will be inferred from spectral radiances emitted by CO_2 molecules, following radiative or collisional interactions. In this situation, the so called forward problem would reproduce the radiances emitted by whichever processes occurring for given atmospheric conditions, and can be expressed as

$$\mathbf{y} = \mathrm{F}(\mathbf{x}), \tag{2.39}$$

where $\mathbf{y}$ is a vector of measurements (in our case, a set of observed limb spectra at certain altitudes, in a given spectral range and resolution), with dimension M (number of tangent heights where observations are available), $\mathbf{x}$ is a vector of retrieval parameters, with dimension N (number of tangent heights where CO_2 is inverted), and F is the non-linear function representing the formal solution of the radiative transfer equation.

On the contrary, the inverse problem works the other way round, and can be written as

$$\mathbf{x} = \mathrm{f}(\mathbf{y}). \tag{2.40}$$

Usually the radiative-transfer problem is linearised with respect to a reference state, $\mathbf{x_0}$, and a term, ϵ, is included to account for all the instrumental errors, both random and systematic, so we have

$$\mathbf{y} = \mathrm{F}(\mathbf{x_0}) + \mathrm{K}(\mathbf{x} - \mathbf{x_0}) + \epsilon, \tag{2.41}$$

where K is the so called *Jacobian* matrix or *weighting function* matrix, of order $M \times N$, in which each element is the partial derivative of a forward model element with respect to a state vector element, i.e.,

$$K_{ij} = \frac{\partial F_i(\mathbf{x})}{\partial x_j}, \text{ with } i = 1 \ldots \mathrm{M} \text{ and } j = 1 \ldots \mathrm{N}. \tag{2.42}$$

The Jacobian matrix gives thus the sensitivity of the measurements with respect to a given parameter, or to a given parameter at a given altitude.

The measurement errors are normally represented by a covariance matrix, $\mathrm{S_y}$, with elements

$$S_{ij} = \langle (\epsilon_i - \langle \epsilon_i \rangle)(\epsilon_j - \langle \epsilon_j \rangle) \rangle, \tag{2.43}$$

where ϵ_i and ϵ_j are the errors of the individual measurements i and j.

The solution of the inverse problem is normally achieved by an iterative process, given the usually high non-linearity of the equations. The iteration, to obtain the solution at step $k+1$ from step k, can be written as

$$\mathbf{x_{k+1}} = \mathbf{x_k} + \left[\mathrm{K}^T \mathrm{S_y}^{-1} \mathrm{K}\right]^{-1} \times \left[\mathrm{K}^T \mathrm{S_y}^{-1} (\mathbf{y} - \mathrm{F}(\mathbf{x}))\right]. \tag{2.44}$$

A stable solution of the inversion and a convergent iteration normally requires additional considerations. First, when $M < N$, the equations are described as under-determined, the inverse problem becomes ill-posed, and its solution is very sensitive to noise propagation. Secondly, the rank of K, p, represents the actual number of linearly independent rows within the state space. If this subspace is of lower dimension than the state space ($p < N$), there is a *null space* where the solution can take any value, because it is not really determined by the measurements. That happens, for example, when the altitude range of interest is not effectively covered by the instrument. The value of p is a very important information in a retrieval process, as it tells about how many measurements actually provide information on the retrieval parameter. For a reasonable solution of the state vector in the null space, some *a priori* information, $\mathbf{x_a}$, is frequently required. In our case we will use specific runs of the LMD Mars General Circulation Model (González-Galindo et al., 2015), adapted to the time and location of the OMEGA limb measurements, as *a priori*. All inverse problems incorporate a *regularisation matrix*, R, which is equivalent to include additional information to fill the gaps, and provide a character of continuity to the measurements (Jurado-Navarro, 2015). Several authors propose to use diverse regularisation methods and test the quality of the solutions obtained. For an *optimal estimation* method, which is a frequent statistical methodology for solving Equation 2.44, Rodgers (2000) propose the use of the covariance matrix of the *a priori* information, $\mathrm{S_a}$, as the regularisation matrix, when such *a priori* information can be well evaluated. The optimal estimation method provides the best trade-off between the retrieval random errors and the degrees of freedom, i.e., the number of independent pieces of information contained in the measurements. An alternative is to use one of the diverse Tikhonov regularisation methods (zeroth, first or second order), where a parameter is used to weight the measurements versus the *a priori* information. The main advantage of the Tikhonov regularisation of orders greater than zero is to guarantee the independence of the solution from the absolute value of the *a priori*. We adopted here a 1st-order Tikhonov regularisation, which is appropriate when the solution is expected to follow the *a priori* shape.

It is convenient to avoid strong non-linearities during the iteration process by assuring a *linear* behaviour, i.e., sufficiently small changes in $\mathbf{x}$ in each step. For this purpose, we use a Levenberg-Marquardt damping (Levenberg, 1944; Marquardt, 1963). In practice, this is done by including a damping term, $\lambda\mathrm{I}$. The parameter λ varies during the iterations, as it is chosen depending on the value of a χ^2-type functional, a measure of the goodness of the retrieval at each iteration step, the closer to unity the better. χ^2 is defined as

$$\chi^2 = \Big[\mathbf{y} - \mathrm{F}(\mathbf{x})\Big]^T \mathrm{S_y^{-1}} \Big[\mathbf{y} - \mathrm{F}(\mathbf{x})\Big] + (\mathbf{x} - \mathbf{x_a})^T \mathrm{R}(\mathbf{x} - \mathbf{x_a}). \qquad (2.45)$$

Considering all these terms, the iterative solution to the inverse method may be written as

$$\mathbf{x_{i+1}} = \mathbf{x_i} + \Big[\mathrm{K}^T\mathrm{S_y^{-1}}\mathrm{K} + \mathrm{R} + \lambda\mathrm{I}\Big]^{-1} \times \Big[\mathrm{K}^T\mathrm{S_y^{-1}}(\mathbf{y} - \mathrm{F}(\mathbf{x})) - \mathrm{R}(\mathbf{x_i} - \mathbf{x_a})\Big], \qquad (2.46)$$

and is solved in this work with a tool called *Retrieval Control Program* (RCP, von Clarmann et al. (2003)), which is described below.

Rodgers (2000) defines the gain matrix, G, as the inverse transformation of the Jacobian (Equation 2.42), i.e., it expresses how the measurements, $\mathbf{y}$, map into the retrieved parameters, $\mathbf{x}$. From Equation 2.46, the definition of the gain matrix is

$$\mathrm{G} = \Big[\mathrm{K}^T\mathrm{S_y^{-1}}\mathrm{K} + \mathrm{R}\Big]^{-1}\mathrm{K}^T\mathrm{S_y^{-1}}. \qquad (2.47)$$

From the gain matrix, a useful definition in retrieval theory follows, that of the *averaging kernel* matrix, $\mathrm{A} = \mathrm{GK}$. The averaging kernels describe how the true profile maps into the parameter space, and is frequently used to characterise the quality of the retrievals. In an ideal case, if the retrieved values coincided with the true ones, A would be equal to the identity matrix. In practice, the averaging kernel matrix always shows a broad diagonal structure with maximum values lower than 1. This is the case, for example, when the retrieval grid is finer than the measurement grid, which is a common situation. The full width at half maximum (FWHM) of either the rows or the columns of A provide the actual vertical resolution of the sounding instrument. Besides, the trace of A represents the degrees of freedom.

We will apply all these notions to the inversion results in following chapters.

2.4. Inversion tools and adaptation to Mars

2.4.1. Forward and non-LTE models

The forward model, $\mathrm{F}(\mathbf{x})$, is an essential piece of every inversion process. It basically consists on a precise line-by-line radiative transfer calculation with a careful handling of geometrical conditions, ray-tracing and instrumental line shape, among others. Under non-LTE conditions, it additionally requires the simulation of the energy state populations of the species responsible for the emissions. This is performed with a dedicated non-LTE model, developed for the species at work, and which is coupled to the line-by-line model.

At the IAA, our team has been developing and applying non-LTE inversion methods to Earth's atmosphere observations, in collaboration with the Karlsruhe University, during the last two decades.

The forward model adopted for the present study combines a generic non-LTE radiative transfer algorithm, the *Generic RAdiative traNsfer AnD non-LTE population Algorithm* (GRANADA) (Funke et al., 2012), with a well tested line-by-line radiative transfer model, the *Karlsruhe Optimized and Precise Radiative transfer Algorithm* (KOPRA) (Stiller, 2002).

KOPRA was developed at the Institut für Meteorologie und Klimaforschung, IMK (Karlsruhe, Germany). Originally suited to simulate infrared measurements by the instrument MIPAS (Stiller, 2002), KOPRA is able to handle many other sounding geometries from satellite or balloon observations, taking into account the field of view and the spectral response of the given instrument.

KOPRA aims at solving the integrated RTE (Equation 2.20), assuming the Curtis-Godson approximation (Curtis, 1952; Godson, 1953). To do it, KOPRA calculates the infrared monochromatic radiances using a line-by-line technique and also provides the Jacobian matrix computed in a quasi-analytical mode. The radiative-transfer model is based on a layer-by-layer approach, with calculation of the partial gas columns and the Curtis-Godson means for each path segment of the line of sight. For the calculation of this line of sight, KOPRA takes into account the oblateness of the planet (Jurado-Navarro, 2015). The spectral lines are modelled using a Voigt profile, i.e., convolving the Lorentz and Doppler line shapes. Spectroscopic information is usually taken from the HITRAN database (Rothman et al., 2013) although KOPRA can also handle other spectroscopic databases.

KOPRA can also be used to perform sensitivity tests of simulated radiances (see Chapter 7) by using its large versatility (for instance, in the definition of vibrational bands, of included gases and isotopes, of reference atmosphere profiles, of the spectral resolution or of the grid of tangent heights).

The information on the non-LTE populations of the molecular states is provided by GRANADA, the non-LTE model, which was implemented at the IAA. GRANADA calculates the non-LTE state populations of molecular rotational, vibrational and electronic levels (Funke et al., 2012), and their derivatives with respect to the non-LTE retrieval parameters. The code expresses the non-LTE populations as ratios with respect to the populations in LTE, or as vibrational (or rotational) temperatures. GRANADA is also able to compute the heating and cooling rates of the involved vibrational bands, information used by KOPRA to calculate the infrared radiance of the non-LTE emissions. GRANADA incorporates a generalised scheme for all molecules, used for populations of CO_2, O_3, CO, NO, NO_2, H_2O, CH_4, HCN, among others. It also allows for user-defined configurations like, for example, states and transitions, the altitude range, iteration strategies or processes definitions.

The algorithm solves the SEE (Equation 2.30) locally, taking into account radiative, collisional and chemical productions and losses, for all the energy levels considered, and the RTE (Equation 2.16) for all the bands connecting these levels in a discrete atmosphere at given altitude levels. The RTE–SEE coupled system cannot be solved analytically and requires a numerical solution. GRANADA uses the Curtis matrix and the Lambda iteration methods (or a combination of both) to achieve a solution iteratively. For a detailed description, see Funke et al. (2012).

GRANADA can be used to perform sensitivity tests of the vibrational temperatures to changes in the collisional rates or in the profiles of the reference atmosphere. It also provides non-LTE corrections of the Jacobians calculated by KOPRA, by taking into account the dependency of the non-LTE populations on the retrieved parameters.

The set-up of GRANADA for Earth conditions was updated by Jurado-Navarro (2015), for the derivation of CO_2 densities and non-LTE parameters in the terrestrial upper atmosphere.

The flexibility of GRANADA, and its numerical implementation into KOPRA, allowed for a rather direct adaptation of the terrestrial CO_2 non-LTE scheme to the Martian atmosphere. CO_2 non-LTE populations calculated with GRANADA were compared to those calculated with another non-LTE model for CO_2 atmospheres also developed in our group (López-Valverde and López-Puertas, 1994b; Roldán et al., 2000; López-Valverde et al., 2016), and good agreement was found. Small differences in some state populations could be attributed to the different radiative transfer and set of vibrational states included. A detailed manuscript describing and comparing both models was under preparation at the time of writing.

Next we will revisit the main characteristics of the GRANADA model and present the changes applied to the radiative and collisional processes, in order to adapt the code from Earth to Mars.

Selection of the set of CO_2 vibrational levels

Let us start with a reminder on the chosen notation. The vibrational state of the CO_2 molecule was defined in Section 1.4 as (v_1, v_2, v_3) or, in a compressed form, (v_d, v_3), with $v_d = 2v_1 + v_2$. In these expressions, v_i is the quantum number associated to the mode of vibration i. The Herzberg notation, $v_1 v_2^l v_3$, where l is the vibrational angular momentum associated to the degenerated bending mode (see Section 1.4), is also used in this Thesis to represent the vibrational state.

Figure 2.3 shows the vibrational excited levels and the radiative transitions included in the model for the isotope $^{12}C^{16}O_2$ (626 hereinafter), the most abundant at normal atmospheric conditions.

A reduced number of transitions was considered for the other five most abundant CO_2 isotopes, $^{13}C^{16}O_2$ (636), $^{16}O^{12}C^{18}O$ (628), $^{16}O^{12}C^{17}O$ (627), $^{16}O^{13}C^{18}O$ (638) and $^{16}O^{13}C^{17}O$ (637). These vibrational levels are

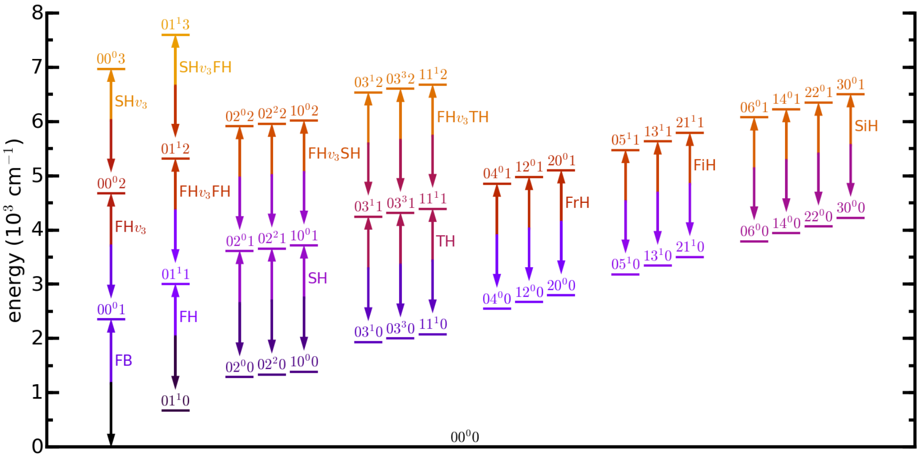

Figure 2.3: CO_2 vibrational levels and radiative transitions included in the model for the 626 isotopologue. Only transitions in the 4.3 μm region are shown. For clarity, vibrational levels of the form $v_1v_2^lv_3$, with $l > 0, 1$ and $v_d = 2v_1 + v_2 \geq 4$ are omitted. The nomenclature used for the vibrational bands is the same as in Table A.1.

included due to the fast V-V coupling with the 626 isotope and their important contribution to the radiative cooling (López-Valverde and López-Puertas, 1994a). Our CO_2 model for Mars iteratively solves the SEEs, including collisional and radiative processes, for the CO_2 isotopes and also for two vibrational states of CO, since both molecules are coupled via collisional V-V exchanges (López-Valverde and López-Puertas, 1994b).

All the individual transitions included for each of the CO_2 isotopes are summarised in Table A.1 (Appendix A). In total, 95 CO_2 vibrational bands, 17 of them with full radiative transfer among atmospheric layers, are included, considering all six isotopes (66 in the region around 4.3 μm, 17 of them with full radiative transfer). Similarly to Earth observations in wide spectral ranges at 4.3 μm (López-Puertas et al., 1986), weak transitions from a large number of states do contribute to the total emission.

Vibrational temperatures

The vibrational temperature introduced in Equation 2.25 is an intuitive measurement of the non-LTE population of an energetic level, as it clearly visualises the departure from non-LTE when compared to the kinetic temperature.

Figure 2.4 shows the vibrational temperature for nine of the most relevant excited levels, for Martian conditions, during daytime. 00^01 is the upper level of the fundamental band at 4.3 μm, 01^11 and 01^10 are, respectively, the upper and lower levels of the first hot band. The upper (02^01, 02^21 and 10^01) and lower (02^00, 02^20 and 10^00) levels responsible of the second hot bands are also shown. The colour palette of Figure 2.3 is maintained for easier identification of the levels

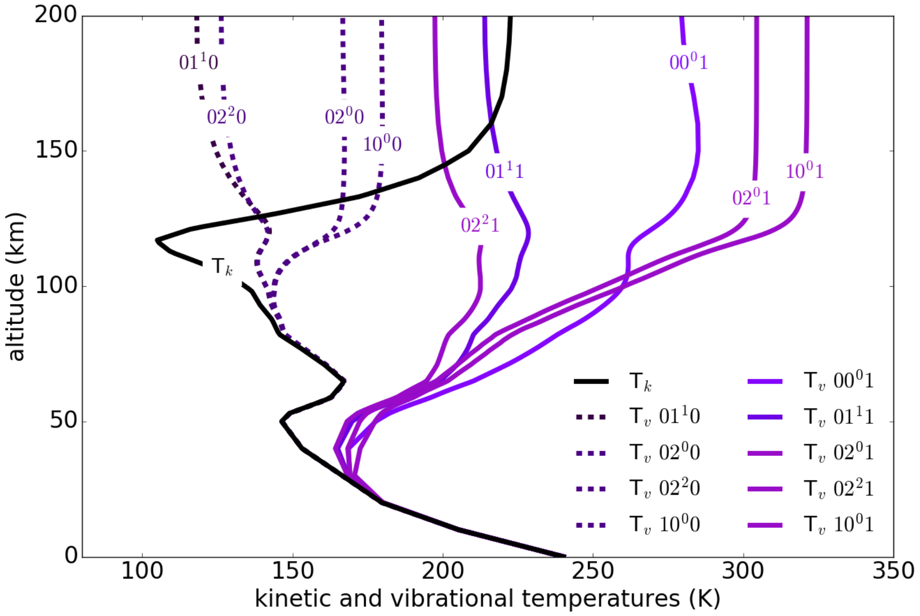

Figure 2.4: Vibrational temperatures of nine vibrational states of the 626 CO_2 isotope, the main one. The kinetic temperature is shown in black, for reference. Colours are the same as in Figure 2.3.

Vibrational temperatures larger than the kinetic one indicate populations larger than in LTE. This is the case for all the states with strong solar absorption during daytime, like the first excited state of CO_2 in the asymmetric stretching mode, 00^01, responsible for the strong fundamental band of this vibrational mode around 4.3 μm. Hence its vibrational temperature is very large above 60 km, indicating a larger population than in LTE. In contrast, the states emitting at 15 μm, such as 02^00, 02^20, 10^00 and 01^10 are not directly pumped by solar absorption, but higher energy states are able to relax to these lower states by spontaneous emission. At high altitudes these states show populations depleted from LTE, i.e., vibrational temperatures smaller than the kinetic temperature, due to the strong emission to space by 01^10 in the fundamental band and the strong V-V coupling of the other v_2 states to this one (López-Valverde and López-Puertas, 1994b).

Contribution of vibrational bands

Figure 2.5 shows a simulation using our non-LTE forward model, i.e., KOPRA and GRANADA, of the contribution of the most relevant bands to the CO_2 limb emission around $4.3\,\mu$m at tangent altitudes of 70, 90, 110, 130, 150 and 170 km, for an arbitrary reference atmosphere, as seen by the OMEGA instrument, that is, using the OMEGA spectral resolution and field of view.

In the uppermost altitudes, above 160 km, the pressure is very faint, and hence optically thin conditions generally apply to all the emission bands. In this situation, the stronger fundamental bands at $4.3\,\mu$m dominate. That is clearly seen in (f), where almost all the emission comes from the fundamental bands of the 626 and 636 isotopes, which present a slightly shifted spectrum from each other. As we lower the altitude of observation, the atmosphere becomes optically thicker and thicker for all the emissions. This effect is more relevant for the stronger bands of the more abundant isotopes, which are rapidly self-absorbed. Thus, the contribution of the 626 fundamental band starts to lose relevance below 160 km, while the relative contribution of the fundamental emission of the 636 stays the same (e, d). The second hot bands, with their lower states depleted, as seen above, slightly weaken, but gain relative weight on the total emission, and quickly become the main radiative component, when the fundamental bands are strongly absorbed (d). They even become almost the only bands responsible of emission at 110 km, considering the contributions from all the isotopes (c). In the lower atmosphere, below 100 km, the pressure is larger, and most of the stronger bands are in optically thick conditions. For that reason, the total emission is considerably affected by the contributions of the 626 fourth hot bands, and even the second hot bands of minor isotopes, like 628, at 70 km (a).

CO_2 collisional exchanges in the Mars atmosphere

The main collisional processes involving CO_2 in GRANADA are deeply explained in Funke et al. (2012) and Jurado-Navarro (2015). In this section we present the most relevant updates to adapt the code to the Martian conditions, taking as a reference the work on non-LTE modelling of the

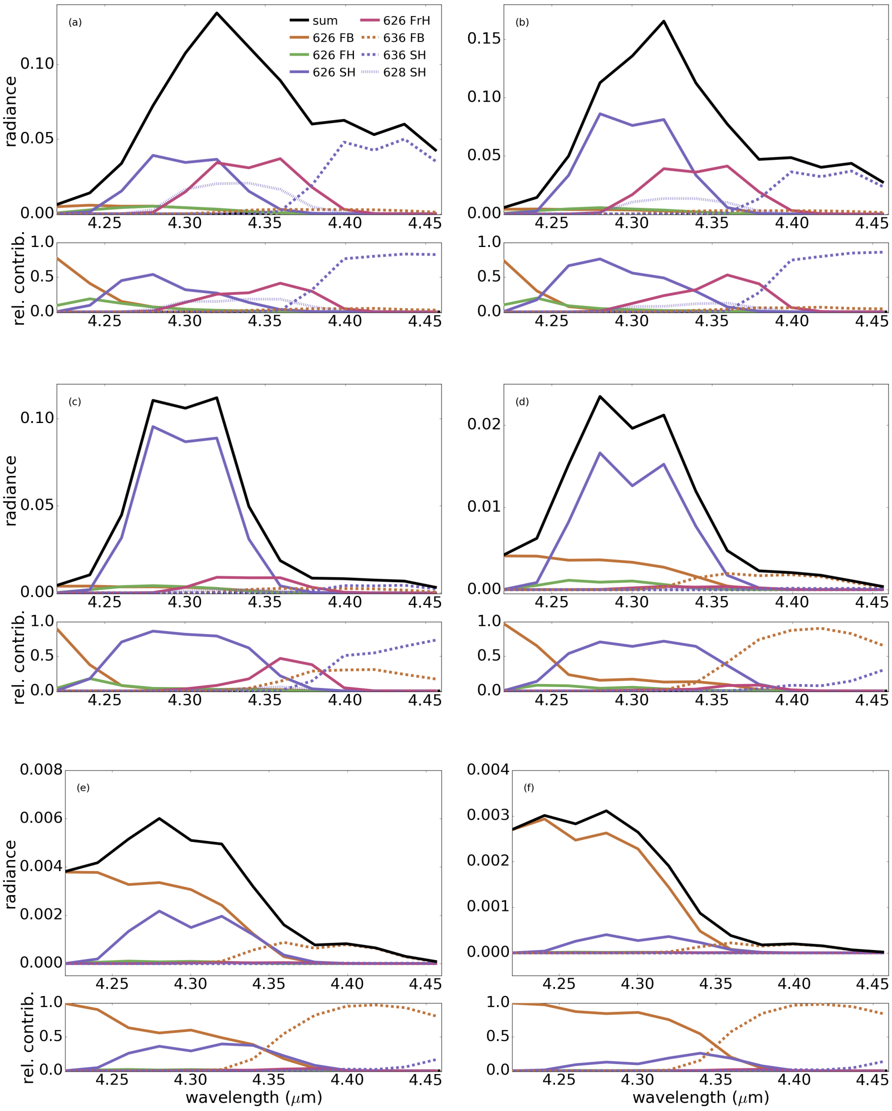

Figure 2.5: Band contributions to CO_2 emission at 4.3 μm. Figure a) corresponds to an altitude of 70 km, b) to 90 km, c) to 110 km, d) to 130 km, e) to 150 km and f) to 170 km. The most relevant bands (FB, FH, SH and FrH for isotope 626, FB and SH for 636, SH for 628) are displayed. The sum of the contributions from all the bands included in the model is shown in black at all altitudes. The bottom panel of each sub-figure represents the relative contributions to the total emission. The nomenclature used for the vibrational bands is the same as in Table A.1. *All*: Radiance units are $Wm^{-2}sr^{-1}\mu m^{-1}$.

infrared emissions in the atmosphere of Mars done by López-Valverde and López-Puertas (1994a) (tables 3 and 4). We will refer to this publication as MARVEN, because it describes a model used in the IAA to characterise the atmospheres of Mars and Venus. Many of the collisional exchanges in GRANADA and MARVEN obviously coincide, but the most recent work by Jurado-Navarro (2015) includes an update on some rates based on more recent laboratory measurements and on his own derivation from analysis of MIPAS observations of Earth non-LTE emissions. The impact of these updates in collisional relaxation rates is normally small. Like in MARVEN, we distinguish between collisions where there is no change in the vibrational state of one of the colliding molecules (vibrational-thermal or V-T) and collision with both molecules changing their excitation state (vibrational-vibrational or V-V).

VT1. These processes correspond to the redistribution of the vibrational energy of the asymmetric v_3 mode into that of the v_1 and v_2 modes in vibrational-thermal collisions.

$$\mathrm{CO}_2^i(0,0^0,1)+\mathrm{M}\rightleftharpoons \mathrm{CO}_2^i(0,\nu_2,0)+\mathrm{M}+\Delta E^i, \tag{2.48}$$

where M is the colliding molecule (CO_2, N_2, CO or $O(^3P)$), i represents the involved isotope, and ΔE^i is the energy emitted or absorbed in the process. For all CO_2 isotopes, VT1 collisions with N_2 and $O(^3P)$ are included as in MARVEN's table 3. When the colliding molecule is CO_2 or CO, the collisional rates are updated, following Jurado-Navarro (2015), as follows:

- k_1 for collisions with other CO_2 molecule is now calculated by a linear fit between 10.58 x 10^{-15} and 7.17 x 10^{-15} $\mathrm{cm^3 s^{-1}}$ for the temperature ranging from 163 to 301 K. The collisional rates for the higher excited transitions are obtained as $k_{1b}=0.18k_1$ ($v_2=2$) and $k_{1c}=0.82k_1$ ($v_2=3$).
- k_3 and k_{3c} ($v_2=3$) for collisions with CO are now calculated by a linear fit between 10.58 x 10^{-15} and 7.17 x 10^{-15} $\mathrm{cm^3 s^{-1}}$ for the temperature ranging from 163 to 301 K.

VT2. VT2 processes refer to the thermal (de)-excitation of the bending-symmetric levels. Only interactions by single v_2 quantum exchanges are considered. The case of $v_2=1$ is the most important, since the upper

($v_2 = 2, 3$) levels are more significantly influenced by V-V than by V-T processes.

$$\mathrm{CO}_2^i(0, v_2, 0) + \mathrm{M} \rightleftharpoons \mathrm{CO}_2^i(0, \nu_2 - 1, 0) + \mathrm{M} + \Delta E^i, \tag{2.49}$$

where M is the colliding molecule (again, CO_2, N_2, CO or O(^{3}P)). For all CO_2 isotopes, VT2 collisions with CO_2, N_2, CO or O(^{3}P) are included as in MARVEN's table 3.

VT4. This process does not directly involve CO_2 molecules; however, CO and O(^{3}P) molecules are important for other V-T processes (VT1 and VT2), as described in López-Valverde and López-Puertas (1994a).

The process have been included as in MARVEN's table 3,

$$\mathrm{CO}(v) + \mathrm{O}(^3\mathrm{P}) \rightleftharpoons \mathrm{CO}(v - 1) + \mathrm{O}(^3\mathrm{P}) + \Delta E, \tag{2.50}$$

with the same collisional rate. CO is also important for V-V processes, and therefore a CO model needs to be coupled to the CO_2 model.

VV2. These processes account for the rearrangement of the v_3 vibrational mode into the v_1 and v_2 modes of the four major CO_2 isotopes (626, 636, 628, 627). They are described as

$$\mathrm{CO}_2^i(v_3) + \mathrm{CO}_2 \rightleftharpoons \mathrm{CO}_2^i(v_2 + 2, v3 - 1) + \mathrm{CO}_2(0, 1^1, 0) + \Delta E_i \tag{2.51}$$

for the deactivation, mainly, of $(0, 0^0, 1)$ isotopic levels via collisions with the main isotope only, and

$$\mathrm{CO}_2(v_3) + \mathrm{CO}_2^i \rightleftharpoons \mathrm{CO}_2(v_2 + 2, v3 - 1) + \mathrm{CO}_2^i(0, 1^1, 0) + \Delta E_i, \tag{2.52}$$

for the excitation of the $(0,1^1,0)$ levels of minor isotopes due, mainly, to the relaxation of the highly populated $(0,0^0,1)$ state of the major isotope. These VV2 processes are incorporated using the rate constants presented in MARVEN.

VV4. Finally, VV4 processes consider intermolecular V-V exchanges between CO_2 and CO. They are the most important collisional processes for the population of CO(1), although not very relevant for the deactivation of the CO_2 states. The processes

$$\mathrm{CO}_2(v_3) + \mathrm{CO} \rightleftharpoons \mathrm{CO}_2(v_3 - 1) + \mathrm{CO}(1) + \Delta E, \tag{2.53}$$

are included, following MARVEN's description.

2.4.2. The retrieval processor

As mention above, equation 2.46 is iteratively solved by the so called Retrieval Control Program (RCP). The iterative procedure starts from an initial guess. During the inversion, RCP repeatedly uses the spectra and Jacobians calculated by KOPRA, and the non-LTE populations for the given atmospheric state at the current step, provided by GRANADA (see Figure 2.6). The measurement covariance matrix is calculated by RCP from the noise equivalent spectral radiance of the measurements. Convergence is reached when the change of the retrieval parameters with respect to the previous iteration is smaller than a given fraction of the noise retrieval error.

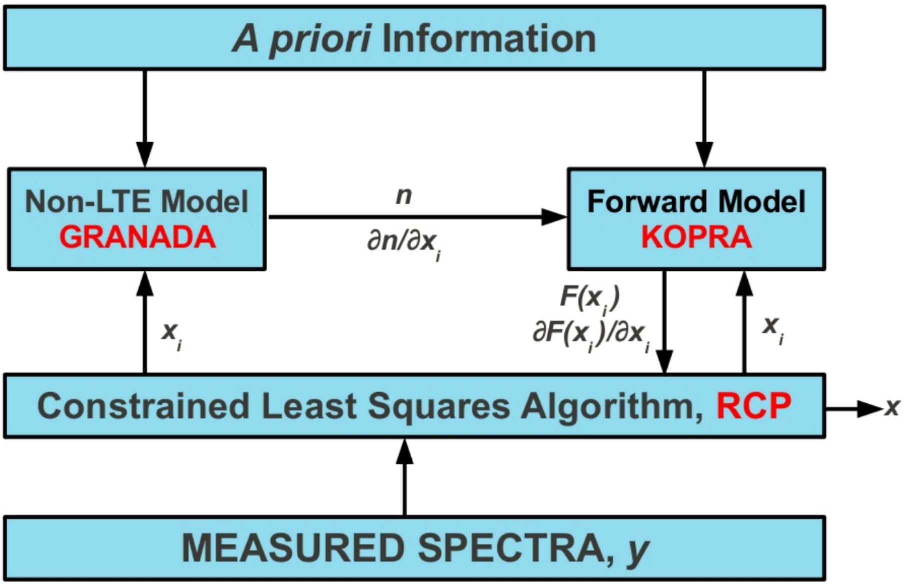

Figure 2.6: The IMK-IAA non-LTE retrieval scheme. x_i is the vector of the retrieval parameters at each iteration step, x is the output vector of retrieval parameter, and n are the non-LTE populations from GRANADA. KOPRA calculates the simulated spectra, $\mathrm{F}(\mathbf{x_i})$, and the Jacobians, $\partial\mathrm{F}(\mathbf{x_i})/\partial\mathbf{x_i}$ at each iteration. Reprinted from Jurado-Navarro (2015)

RCP is a constrained least squares algorithm for retrieving the atmospheric parameters, conceived and developed at IMK with the non-LTE section implemented by the IAA team. The regularisation matrix can be read in or built from a combination of Tikhonov-type terms of different orders, allowing the adaptation to any particular retrieval problem. The RCP code uses a Levenberg-Marquardt damping for stability (see Section 2.3), which is forced to be zero in the last iteration. All the convergence parameters are user defined, in order to optimise the retrieval performance. The inputs to RCP are:

- measured spectra or synthetic spectra generated by a given forward model (like KOPRA),
- initial guess, and
- *a priori* information of the quantities to be retrieved.

The main outputs are the retrieved parameters (like CO_2 abundances), in addition to diagnostics, such as the averaging kernels, the noise error covariance matrix or the vertical resolution.

2.5. Mars non-LTE retrieval scheme

The main characteristics of our inversion scheme are summarized in Jurado-Navarro (2015). There, the retrieval of CO_2 abundances from MIPAS spectra in Earth's upper atmosphere was successfully tackled. The retrieval scheme is formed by the combination of the three algorithms described above, after adaptation to Mars conditions. Like a general non-LTE retrieval scheme, it follows these five steps (see Figure 2.6):

- the *a priori* information is introduced in KOPRA and GRANADA,
- GRANADA calculates the non-LTE populations,
- KOPRA uses the non-LTE populations to compute the outgoing radiances and the Jacobians,
- the simulated spectra and the measured (or synthetic) spectra are passed to the RCP for iteration,
- if the result does not satisfy the convergence criterion, the result is sent back to KOPRA and GRANADA for recalculation, otherwise the retrieved data are obtained.

Retrievals for both synthetic and measured spectra were performed under Martian conditions with the OMEGA instrumental characteristics. Below 120 km we found strong non-linearities typical of a very optically thick regime, where both the non-LTE CO_2 populations as well as the limb radiances strongly depend on the target, i.e., on the CO_2 density. This leads to non-convergence in many cases. For that reason, the CO_2 profiles were regularised by means of a Tikhonov-type smoothing with a strong diagonal constraint below 100 km, in order to force the retrieved CO_2 to be close to the climatological density (*a priori*) at those altitudes. Above 100 km, the constraint was optimised to obtain stable calculations with a precision high enough to allow for meaningful retrieved CO_2 abundances above 120 km.

For here am I sitting in a tin can. Far above the world.
Planet Earth is blue and there's nothing I can do.
David Robert Jones

3

Mars Express and OMEGA

Abstract

This chapter is dedicated to the OMEGA instrument on board the Mars Express (MEx) mission to Mars, and, in particular, to its limb observations in the infrared. First, a general overview of the MEx mission objectives is given. Then the main features and scientific goals of the OMEGA instrument are presented. To conclude, we enumerate the limb dataset studied in this work, showing the distribution of the orbits across the planet and listing their exact location.

3.1. The Mars Express mission

Launched on June 2, 2003, Mars Express (MEx), so called because of the rapid and streamlined development time, represents ESA's first visit to another planet in the Solar System. In this section, we present the main characteristics and science highlights of MEx. For a full description of the mission and details of the findings, please refer to the MEx website (Mars Express, 2019).

Since the start of the science operations back in 2004 until today, still operational, the durable orbiter has given scientists an entirely new view of Mars, and is helping to answer fundamental questions about the geology, atmosphere, surface environment, history of water and potential for life on Mars.

The spacecraft follows a highly elliptical orbit around the planet, varying the distance to it from 330 km (pericentre) to 10530 km (apocentre). The payload of MEx consists on seven instruments originally designed to study most aspects of the planet, including its atmosphere and climate, and the mineralogy and geology of the surface and subsurface, during at least one Martian year. However, as of August 2019 the mission is still operational and providing very useful measurements of the surface and the atmosphere of Mars. The spacecraft also provides relay communication services between Earth and various landers deployed on the surface. Figure 3.1 shows an artist's impression of Mars Express with the planet atmosphere in the background, observed in a limb geometry.

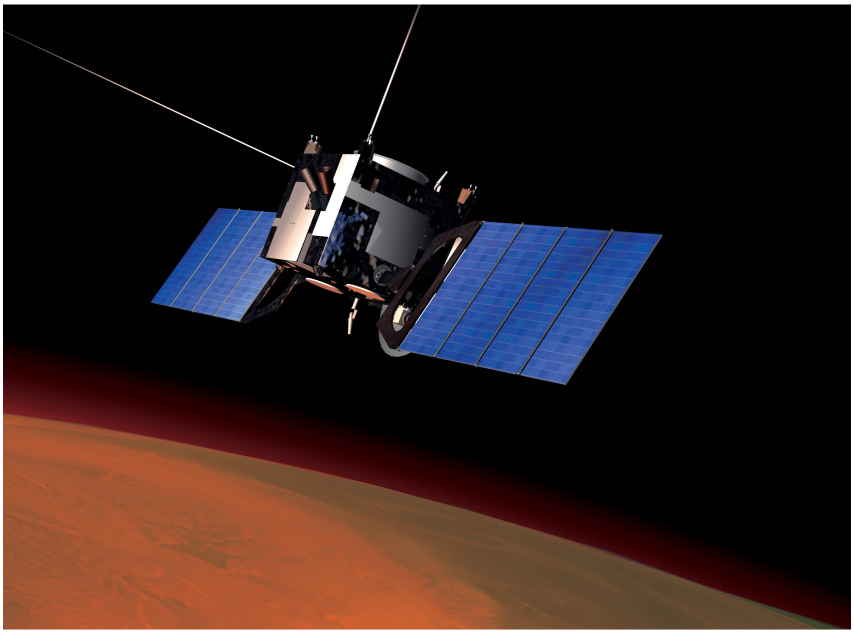

Figure 3.1: Artist's impression of Mars Express in orbit around Mars. Illustration by Medialab (Mars Express, 2019).

The mission included a lander, Beagle-2, that was successfully released before the orbit insertion, but was declared lost as no further contact was established after release. In January 2015, the Mars Reconnaissance Orbiter captured some images of Beagle-2 in which the lander appeared to have partially deployed on the surface.

Mars Express has achieved a good number of discoveries. Among them, we may emphasise the evidence of liquid water on Mars, the controversial detection of methane in the atmosphere, the identification of recent glacial landforms, the sounding of the polar regions, the evidence of recent and episodic volcanism, an updated estimation of the current rate of atmospheric escape, the identification of localised auroras on Mars, the observation of a meteoric layer in the Martian ionosphere, the unambiguous detection of carbon dioxide clouds, and the unprecedented exploration of Phobos (Mars Express, 2019). More insight reviews of the different MEx instruments achievements can be found in many special issues devoted to this mission, like Science (2005), Encrenaz and Sotin (2005), Neukum et al. (2010) or JGR (2018).

3.2. The OMEGA instrument

The data used in this work were remotely acquired by the Observatoire pour la Minéralogie, l'Eau, les Glaces et l'Activité (OMEGA) on board Mars Express. OMEGA is an imaging spectrometer with three spectral channels covering the 0.36 to 5.08 μm spectral range, with a variable spectral resolution.

It was originally developed to determine, as its primary goal, the mineral content of the Martian surface and the molecular composition of the atmosphere. While most of the time OMEGA works in nadir mode to carry out the mineralogical characterisation of the Martian surface, some atmospheric observations using limb geometry are also performed. Some OMEGA features, objectives and calibration processes are summarised here whereas a full description of the instrument and its ground calibration can be found in Bibring et al. (2004b). Figure 3.2 shows a picture of the OMEGA infrared channel.

3.2.1. Scientific goals

The scientific objectives of the OMEGA instrument are listed next, according to Bibring et al. (2004b).

Mineralogy.

- Identify the minerals of the major geological units to study the evolution of Mars caused by internal activity, meteoritic impacts and interaction with the atmosphere.

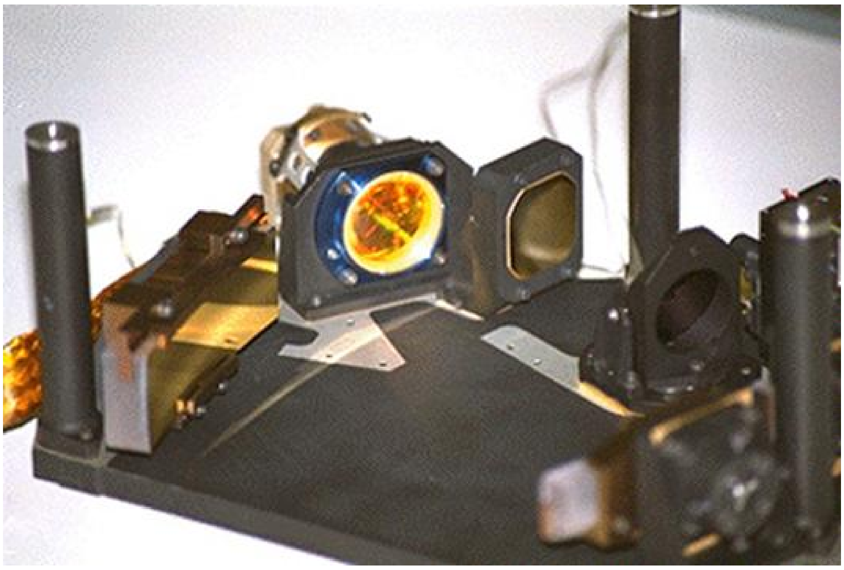

Figure 3.2: OMEGA infrared channel prior to integration into the instrument (Mars Express, 2019).

- Increase the sensitivity for detecting constituents with restricted geographical extension.
- Map mineralogical boundaries between geological units, to understand Mars' hemispherical asymmetry.
- Identify the composition of deposits and reveal possible gradients in the hydration minerals near features associated with fossil water flows.
- Monitor features associated with wind transportation.

Polar caps and frosts.

- Determine the spatial evolution of the two polar caps, by observing CO_2 and H_2O to discriminate between the permanent ice and the seasonal frosts.
- Identify dust within the polar ices to reveal the transportation processes.
- Identify the sites where most of the water resides, as they are expected to be the most favourable sites for past organic activity, and could asses water resources for future manned exploration.

Atmospheric evolutionary processes.

- Measure the ground pressure and local pressure variations.
- Monitor the CO and H_2O (minor constituents) partial pressures for each resolved pixel.
- Infer the thermal profile from the inversion of the strong CO_2 band at 4.3 μm.
- Measure the aerosol content.
- Confirm and study the spatial variation of fluorescence emission in CO_2 at 4.3 μm.

3.2.2. Instrument features

OMEGA comprises three spectrometers, one for the VNIR (visible and near infrared range) channel, and two for the SWIR (short wavelength infrared range) channel. Their spectral ranges are shown in Table 3.1. The main optical and detection capabilities of the instrument are listed next (Bibring et al., 2004b).

- *Imaging*: 128 contiguous IFOVs of 1.2 mrad each, corresponding to less than 350 m surface sampling when closer to the planet.
- *Spectral*: 352 (or 400, depending on the summing mode chosen for the visible channel) contiguous *spectels* (i.e. spectral elements) to acquire the entire spectrum from 0.36 to 5.08 μm for each resolved pixel (96 (or 144) to cover the VNIR channel, and 128 for each of the SWIR sub-channels).
- *Photometric*: SNR $>$ 100 over the full spectral range, allowing the identification of percentage absorptions and thermal variations.

Table 3.1 summarises the main characteristics of the VNIR and SWIR channels (Bonello et al., 2005; Mars Express, 2019).

The target of this research, the CO_2 4.3 μm emission falls within the range of the SWIR L sub-channel, also known as long wavelength infrared range (LWIR) channel, which covers from 2.52 to 5.08 μm with a resolution of about 20 nm. This channel consists of a 200 mm Cassegrain telescope with a fore-optics to provide cross-track scanning, a beam splitter (all elements shared with the SWIR C sub-channel), and an actively cooled detector array (Bibring et al., 2004b). While the spectral resolution is not

	VNIR channel	**SWIR C channel**	**SWIR L channel**
Telescope	2x Gauss objective	Cassegrain	
Scanning mode	Push Broom	Whisk Broom	
Detector size	384×288 pixels	128 pixels (linear)	
Pixel size	$23 \times 23\,\mu\text{m}^2$	$90 \times 120\,\mu\text{m}^2$	
Field of view	154 mrad (8.8 deg)	154 mrad (8.8 deg)	
Instantaneous FoV	1.2 mrad	1.2 mrad	
Spectral range	$0.36 - 1.08\ \mu$m	$0.92 - 2.69\ \mu$m	$2.52 - 5.08\ \mu$m
Spectral resolution	7.5 nm	14 nm	20 nm
Signal-to-noise ratio	> 100	> 100	
Radiometric sensitivity	$< 20\%$ (absolute), $< 1\%$ (relative)		
Dynamic range	12 bits	12 bits	

Table 3.1: Main characteristics of OMEGA's VNIR and SWIR channels.

high, the main advantage of OMEGA is its fine spatial sampling, which translates into an altitude resolution of around 1 to 9 km when looking at the limb from the Mars Express orbit. The Level 0-1 data products consist of three-dimensional *qubes*, with two spatial and one spectral dimensions, where the second spatial dimension for the images is provided by the MEx spacecraft along-track motion.

3.3. Selection of limb observations

In this work, we created a large dataset of vertical Level 2 radiance profiles and performed retrievals for them. They were created from Level 1 calibrated radiances pertaining to a total of 47 OMEGA *qubes*. The generation of these Level 2 profiles is described in Chapter 4.

Most of the datasets used in this Thesis correspond to nadir orbits, with a strip acquired in limb geometry (target of opportunity), selected from a larger sample of 98 *qubes* containing limb observations, provided by the OMEGA team. They are listed next, sorted according to their acquisition date.

Martian Year 26: 0044_1.

Martian Year 27: 0285_0, 0330_2, 0647_1, 0961_0, 0964_0, 0965_0, 0966_0, 0967_0, 0970_0, 0971_0, 0973_0, 0975_0, 0978_0, 0979_0, 0982_0, 0989_0, 0998_0, 1001_0, 1002_0, 1008_0, 1012_0, 1023_0, 1084_0, 1402_0, 1619_4, 1880_1, 2547_2.

Martian Year 29: 5851_0, 6020_1, 6071_1, 6104_1, 6126_1, 6146_0, 6586_0.

Martian Year 30: 7554_4, 7586_4, 7597_4, 7604_4, 7619_4, 7679_0, 7686_0, 7697_0, 7701_0, 7708_0, 7715_0, 7718_0.

The distribution of the spectra geolocation of the selected orbits is shown in Figure 3.3, in four different geometric projections: latitude versus longitude, solar longitude, solar zenith angle and local time.

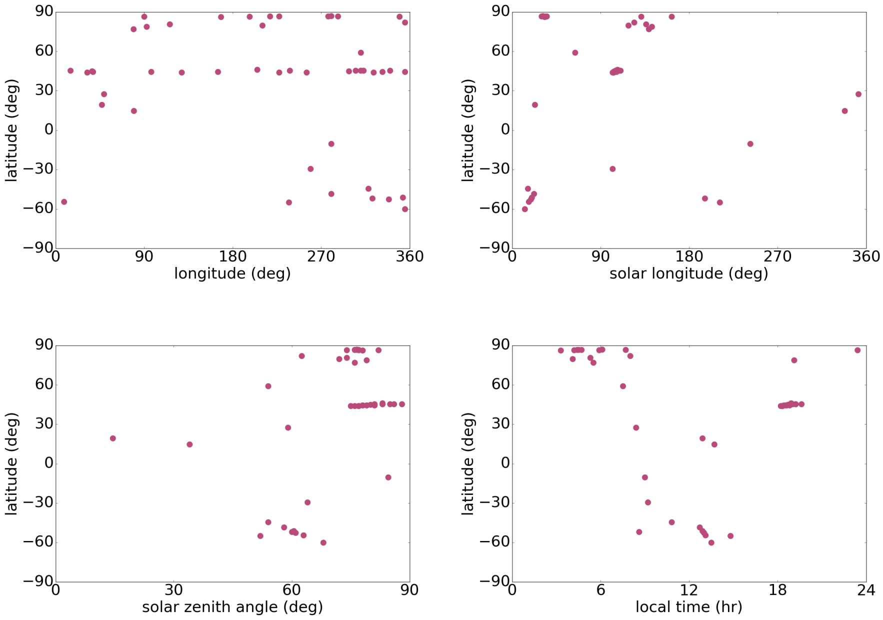

Figure 3.3: Coverage of the 47 OMEGA *qubes* analysed in this work. Each point corresponds to the center of the limb observations of a data *qube*. *Top left*: Latitude versus longitude. *Top right*: Latitude versus solar longitude. *Bottom left*: Latitude versus solar zenith angle. *Bottom right*: Latitude versus local time.

The coverage of the planet atmosphere is not rich enough to allow for a global atmospheric study. There are, however, some interesting regions, where the population of available observations is denser and variability studies are possible (longitudinal variations for a fixed latitude, seasonal variations for a fixed latitud, or latitudinal variations within specific seasons, i.e., with a fixed solar longitude). These scenarios are studied in Chapter 8, where the retrievals are compared with global circulation models and other instruments observations.

Table 3.2 details the latitude, longitude, solar zenith angle and solar longitude of the 47 OMEGA data *qubes*. Columns regarding profile formation and convergence will be explained later (chapters 4 and 5).

Table 3.2: Geolocation of the limb observations center and profile information for the entire set of orbits analysed. ΔLat is the latitude step between adjacent profiles within a *qube*. Columns for latitude (Lat), longitude (Lon), solar zenith angle (SZA), solar longitude (L_s) and latitude step (ΔLat) are all in degrees. # profiles is the number of vertical radiance profiles built for each *qube*. The last column shows the percentage of convergence obtained for the application of the retrieval to these profiles.

Geolocation and convergence of the limb observations

Orbit	Lat	Lon	SZA	L_s	# profiles	ΔLat	# converged
0044_1	14.8	79.3	34.0	338	11	0.02	11 (100%)
0285_0	-44.5	317.8	54.0	16	30	0.06	30 (100%)
0330_2	19.5	47.0	14.5	23	24	0.10	24 (100%)
0647_1	59.0	310.0	54.0	64	12	0.09	7 (58%)
0961_0	44.0	255.0	75.0	102	8	0.06	4 (50%)
0964_0	44.0	323.0	76.0	103	6	0.10	5 (83%)
0965_0	44.0	227.0	77.0	103	7	0.10	3 (43%)
0966_0	44.0	128.0	77.0	103	6	0.10	3 (50%)
0967_0	44.0	32.0	77.0	103	6	0.10	5 (83%)
0970_0	44.5	97.0	78.0	103	7	0.10	7 (100%)
0971_0	44.5	355.0	78.0	103	9	0.08	9 (100%)
0973_0	44.5	165.0	79.0	104	8	0.10	8 (100%)
0975_0	44.5	332.0	79.0	104	10	0.09	10 (100%)
0978_0	45.0	37.0	80.0	104	10	0.10	10 (100%)
0979_0	45.0	298.0	81.0	104	10	0.10	10 (100%)
0982_0	45.5	15.0	81.0	105	10	0.10	10 (100%)

continued on next page

Table 3.2 – continued from previous page

Orbit	Lat	Lon	SZA	L_s	# profiles	△Lat	# converged
0989_0	44.5	38.0	81.0	106	10	0.12	8 (80%)
0998_0	45.5	238.0	83.0	107	10	0.15	10 (100%)
1001_0	45.5	305.0	83.0	107	10	0.15	10 (100%)
1002_0	46.0	205.0	83.0	107	10	0.15	6 (60%)
1008_0	45.5	340.0	85.0	108	12	0.15	10 (83%)
1012_0	45.5	310.0	86.0	109	10	0.15	8 (80%)
1023_0	45.5	313.0	88.0	110	10	0.20	7 (70%)
1084_0	79.8	210.0	72.0	118	30	0.02	30 (100%)
1402_0	86.6	349.6	82.0	162	10	0.02	10 (100%)
1619_4	-51.8	322.0	60.0	196	20	0.03	20 (100%)
1880_1	-10.3	280.0	84.5	242	6	0.09	4 (67%)
2547_2	27.5	49.0	59.0	352	30	0.05	30 (100%)
5851_0	-29.3	259.0	64.0	102	16	0.02	16 (100%)
6020_1	82.0	355.0	62.5	124	24	0.40	23 (96%)
6071_1	86.5	90.0	74.0	131	30	0.08	30 (100%)
6104_1	80.7	116.0	74.0	136	30	0.03	30 (100%)
6126_1	76.9	79.0	76.0	139	30	0.02	30 (100%)
6146_0	78.9	92.5	79.0	142	30	0.02	26 (87%)
6586_0	-55.0	237.0	52.0	211	20	0.05	20 (100%)
7554_4	-60.0	355.0	68.0	13	24	0.12	24 (100%)
7586_4	-54.5	8.5	63.0	17	16	0.20	16 (100%)
7597_4	-52.5	338.5	61.0	19	16	0.20	15 (94%)
7604_4	-51.2	353.0	60.5	20	16	0.20	15 (94%)
7619_4	-48.5	280.0	58.0	22	8	0.25	8 (100%)
7679_0	86.7	287.0	76.0	30	20	0.03	20 (100%)
7686_0	87.0	280.0	76.5	31	20	0.03	20 (100%)
7697_0	86.7	227.0	77.0	32	20	0.03	19 (95%)

continued on next page

Table 3.2 – concluded from previous page

Orbit	Lat	Lon	SZA	L_s	# profiles	$\triangle$Lat	# converged
7701_0	86.3	168.0	78.0	33	20	0.02	20 (100%)
7708_0	86.6	197.0	77.0	34	20	0.03	20 (100%)
7715_0	86.7	218.0	76.5	34	20	0.03	16 (80%)
7718_0	86.8	277.0	76.0	35	20	0.03	17 (85%)

end of the table

Without a past you can't have a future.

Michael Andreas Helmuth Ende

4

Atmospheric profiles and OMEGA data preprocessing

Abstract

In this chapter, we briefly describe the extraction of vertical profiles from the LMD-MGCM, in order to characterise the atmospheric conditions of locations where the retrievals are performed. We also need these profiles for a geometric correction during the calibration of the OMEGA dataset. The calibration and preprocessing are detailed by following the analysis of a particular OMEGA orbit (0330_2) as an example. The preprocessing includes the cleaning of the data *qubes*, the generation of 2-D radiance vertical profiles, and the determination of the noise equivalent spectral radiance for every cell in the grid. Finally, the general criteria followed to generate the radiance vertical profiles are exposed.

This chapter extends section 2 of Jiménez-Monferrer et al. (2019).

4.1. Atmospheric profiles from the LMD-MGCM

Here we describe the climatology used based on temperature, pressure and abundance profiles, as taken from specific runs of the LMD Mars GCM (González-Galindo et al., 2015), for MY26, MY27, MY29 and MY30 (see sections 1.5 and 3.3 for details).

The profiles were extracted from NetCDF files, using an IDL script supplied by the LMD-MGCM team. We coupled this routine to a script, which reads all OMEGA locations from a single file, to accelerate and automatise the extraction for future revision and extension. The profiles were extracted alongside the standard deviation around every point, in order to allow for instructive comparisons between observations and model, i.e., accounting on the uncertainties of both of them (Chapter 8). The *qubes* have an extension in latitude and longitude close to a grid point of the model and the retrieval results are not very sensitive to the input profiles, as will be shown in Chapter 7.

The climatology was first utilised to compute forward calculations, needed in the calibration process (see next section), and then as the atmospheric conditions (*a priori* knowledge, in the case of the inverted magnitude) to perform the retrievals. These retrievals were perform for both synthetic spectra, i.e., generated by a forward model, for test purposes, and real measurements, as observed by OMEGA.

Figure 4.1 shows the input temperature and pressure profiles corresponding to orbit 0330_2 (latitude 19.5 deg, longitude 47.0 deg, solar zenith angle 14.5 deg, and solar longitude 23.0 deg), observed on 2004/04/23 (MY27), as provided by the LMD-MGCM. Figure 4.2 shows the main volume mixing ratio (vmr) profiles for the same geolocation.

4.2. Calibration and preprocessing

Chapter 3 introduced the main features of the OMEGA instrument on board Mars Express and enumerated the *qubes* analysed in this work. A total of around one hundred OMEGA limb dayside *qubes*, covering from 2004 to 2010 (Martian Years 26-30), are available. For this work, 47 of these orbits were fully analysed, from the spacecraft acquisition, going through the calibration and cleaning of the datasets, and the vertical and latitudinal binning to form the radiance profiles, prior to finally retrieve the CO_2 abundances and subsequently derive the temperature profiles.

The CO_2 emission measured by OMEGA in the infrared falls around $4.3\,\mu$m. In this work we analyse the radiance observed in the range from 4.22 to $4.46\,\mu$m. Concretely, we have measurements on 13 discrete wavelengths, namely 4.2199, 4.2407, 4.2605, 4.2801, 4.3003, 4.3199, 4.3399, 4.3595, 4.3793, 4.3993, 4.4180, 4.4369, $4.4563\,\mu$m. During the 16 years of the Mars Express mission to date, as time went by, some of the spectral points suffered from ageing and started to provide wrong data. Hence, for

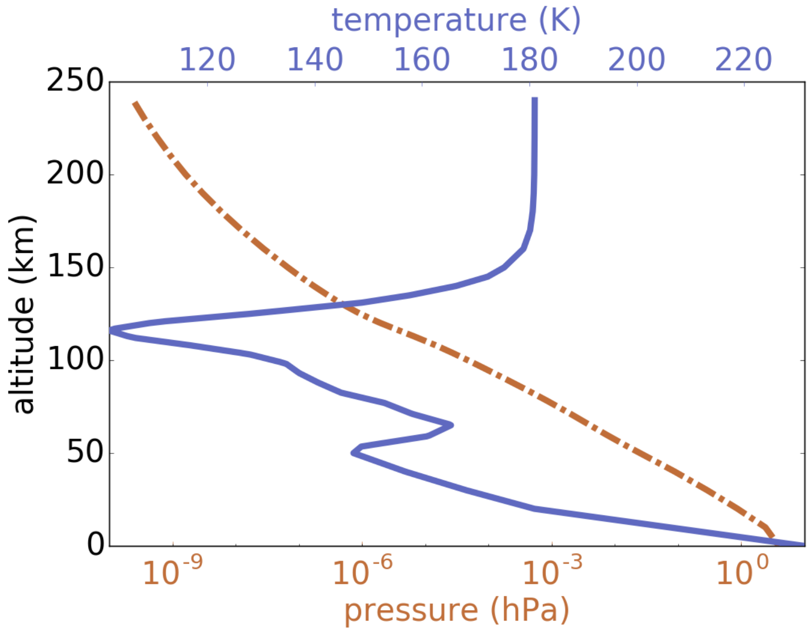

Figure 4.1: Temperature (solid) and pressure (dashdotted) of the input profile, as taken from the LMD-MGCM for the *qube* 0330_2 (MY27).

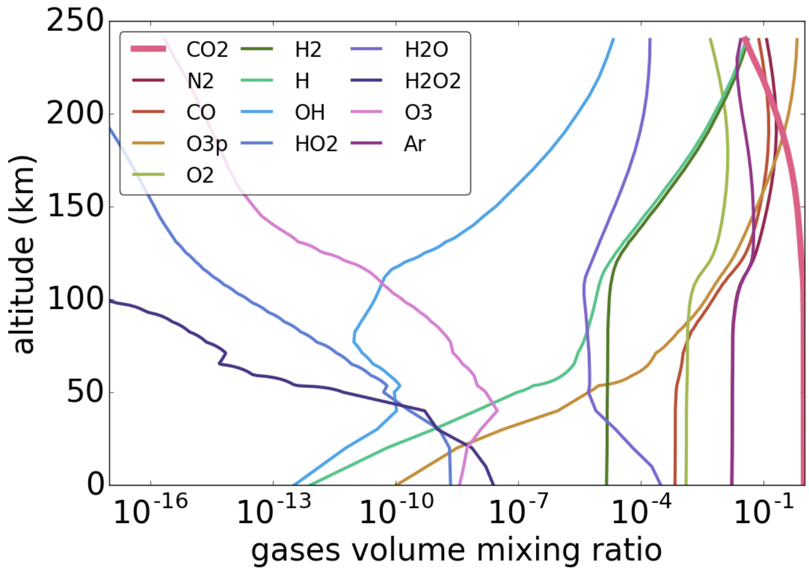

Figure 4.2: *A priori* vmr of CO_2 and abundance of other species included in the LMD-MGCM for the *qube* 0330_2 (MY27).

the later orbits analysed (higher numbered orbits), we relied only on 11 or 9 wavelength measurements, instead of the maximum of 13. Concretely, from orbit 1619_4 on data for 11 wavelengths were available (between 4.2199 and 4.4180 μm), and observations after orbit 7554_4 (included) only offered 9 valid wavelengths (between 4.2199 and 4.3793 μm).

4.2.1. Calibration and cleaning of the dataset

OMEGA data are presented in *qubes*, a 3-D dataset with the two spatial dimensions of the field of view plus the spectral dimension. We started the OMEGA data analysis using the level 0 (non-calibrated) observations publicly available at the ESA Planetary Science Archive (PSA, 2019). Figure 4.3 shows the distribution of the available spectral data according to their altitude, longitude, latitude and solar zenith angle, for the case of the 0330_2 data *qube*.

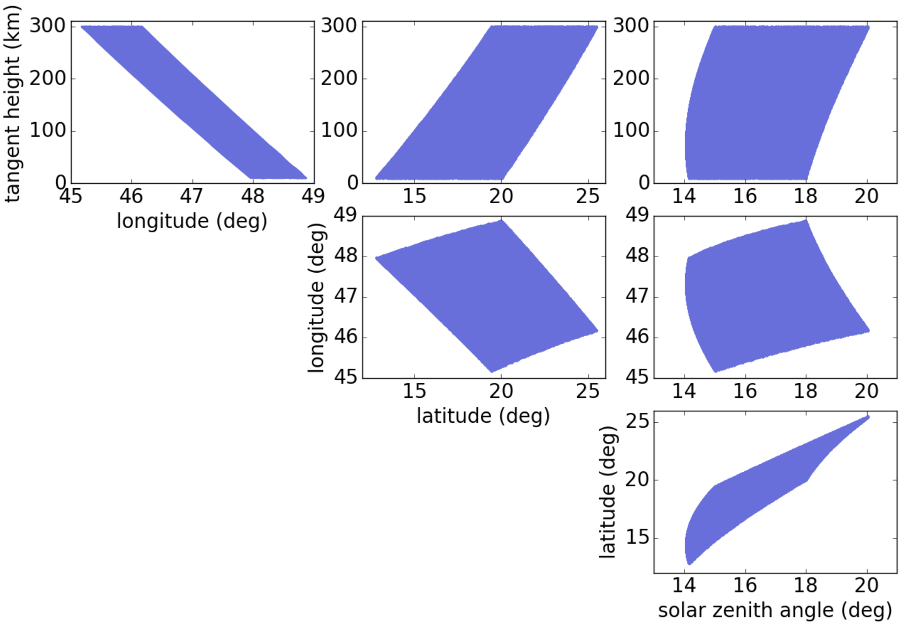

Figure 4.3: Location of the limb spectral data for the OMEGA orbit 0330_2 in different planes: LON-ALT, LAT-ALT, SZA-ALT, LAT-LON, SZA-LON and SZA-LAT. Each individual point (not resolvable in the figures) corresponds to a complete spectrum, totalling 20801 spectra.

The calibration and cleaning of all the 47 orbits were done by the following steps:

- First we needed to change the calibration pipeline provided by the OMEGA team, because a hard cut was applied to data below an arbitrary value. This cut is not expected to affect measured radiances where the signal is strong, but causes an undesired critical effect on limb observations at high altitudes, where the signal is close to zero. Figure 4.4 shows the cut at different wavelengths for orbit 0330_2. As can be seen, all measurement points below a given radiance where assigned a fixed value. That is the reason behind the accumulation of data in the lower boundary of the observed radiances.

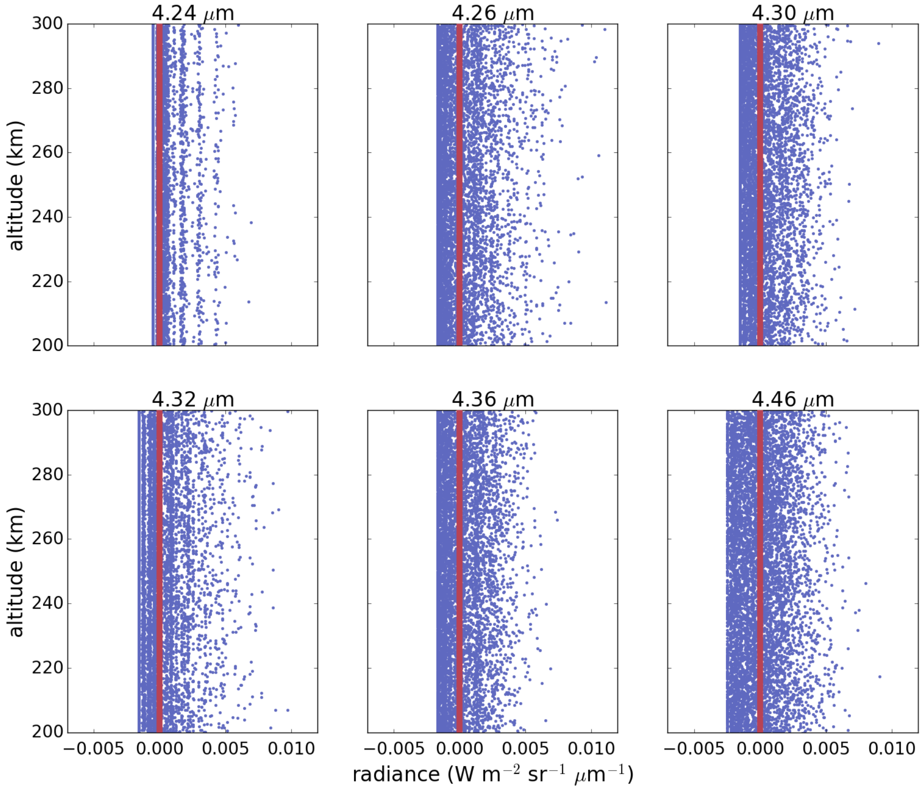

Figure 4.4: Radiance vertical profiles of orbit 0330_2 between 200 and 300 km. The red lines represent the zero radiance level.

- Then we performed a geometric correction for the altitude registration of the SWIR L channel, as described in Equation 1 in Piccialli et al. (2016). This correction introduces a vertical shift with an orbitdependant sign. To decide the sign of the shift, we compared the corrected spectra with the prediction of our forward model, calculated for the atmospheric conditions extracted from the LMD-MGCM at the time and the location of the observed orbit (Figure 4.5). We also introduced an empirical modification as described by Jouglet et al. (2009) to correct for variations in the calibration level with respect to its nominal value before launch. See more details in Audouard et al. (2014).

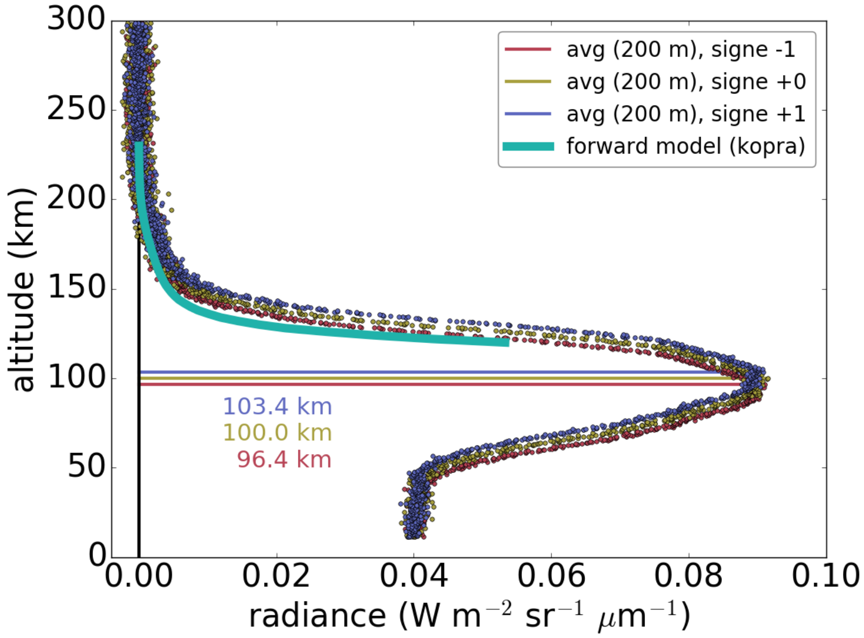

Figure 4.5: Radiance vertical profiles of orbit 0330_2 after applying the SWIR L shift correction with different signs, compared with the forward model prediction for atmospheric conditions of the LMD-MGCM. The vertical profiles are averaged using a bin of 200 m. The numbers in the plot refer to the altitude of the peak. For orbit 0330_2, the sign selected for the shift correction is -1 (see Piccialli et al. (2016)), as it gives a closer value to the forward model calculation.

- Then we corrected in wavelength, with a shift of one spectel, i.e., one spectral grid point (except orbit 1023_0, where no correction was applied, and orbit 2547_2, where a shift of two spectels was introduced), by inspecting all spectral shapes between 4.2 and 4.4 μm, because there is a known shift of this magnitude affecting most of the spectra. This was done by adjusting the spectral position of the well-known contribution of several narrow CO_2 bands around 4.3 μm (López-Valverde and López-Puertas, 1994b). This wavelength shift is illustrated in Figure 4.6.

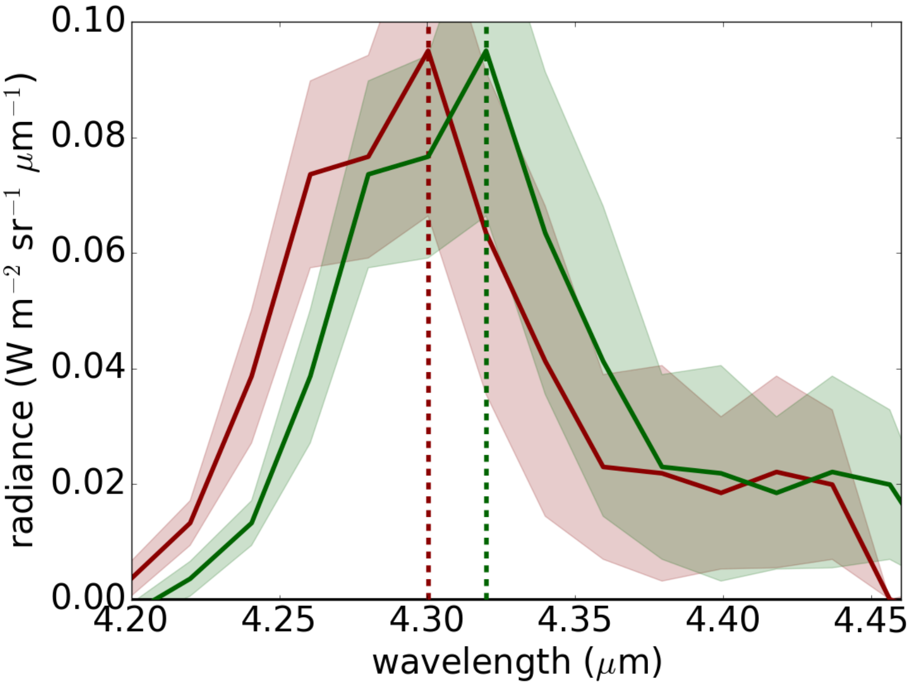

Figure 4.6: Wavelength correction for orbit 0330_2. All the available spectra from 80 to 130 km are averaged together to shape the observed radiance emission, with the standard deviation shown as a shaded region. Reddish (greenish) colours are used before (after) the correction takes place. Note the radiance peak is found at 4.32 μm after the spectral shift, as expected (Figure 2.5 (b, c and d panels)).

- Afterwards we analysed the spectra using a clustering algorithm (k-means, with 15 clusters, MacQueen (1967)), in order to easily detect singular spectra (spurious, instrumentally affected or influenced by a local perturbation) and reject outliers and corrupted spectra. The groups resulting from clustering were accepted or discarded according to the spectral shape of their centroid, i.e., non-physical shapes (far from the expected spectral shape at the given tangent height, according to the non-LTE model) were eliminated. Figure 4.7

shows the spectra of the centroids and Figure 4.8 the distribution of the data into the 15 groups.

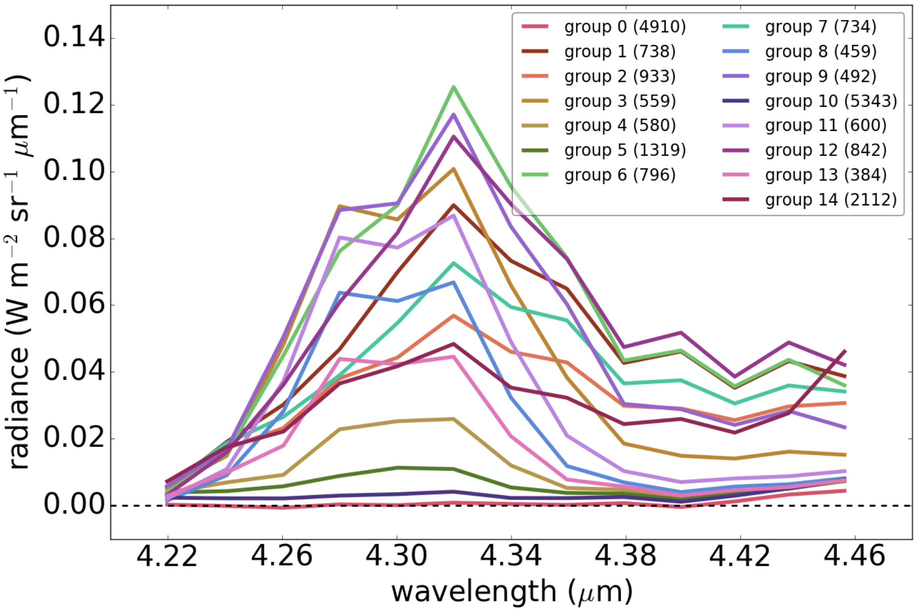

Figure 4.7: Spectra of cluster centres (k = 15) for orbit 0330_2. Colours correspond to cluster identifiers, and the numbers in parentheses refer to the number of spectra in the group. The spectral shape of the cluster centres allows to accept or discard groups of spectra easily.

Once the data were calibrated and cleaned, the radiance vertical profiles were built as described in the following section.

4.2.2. Generation of radiance vertical profiles

Dataset 0330_2 will continue serving as a thread of how the vertical radiance profiles were built for each orbit. As shown in Figure 4.3, for a given observation, latitude and longitude coverages are linked. To avoid large variations in the horizontal dimension, we forced averaging close in latitude (ΔLat = 0.1 deg). This, together with the small variation in solar zenith angle, guarantees homogeneous non-LTE conditions. In general, between 6 and 30 profiles per data *qube* are produced, all extending from 50 km to about 200–250 km. The actual number depends on the 2-D limb projection of the dataset. Figure 4.9 shows the location of the 24 profiles

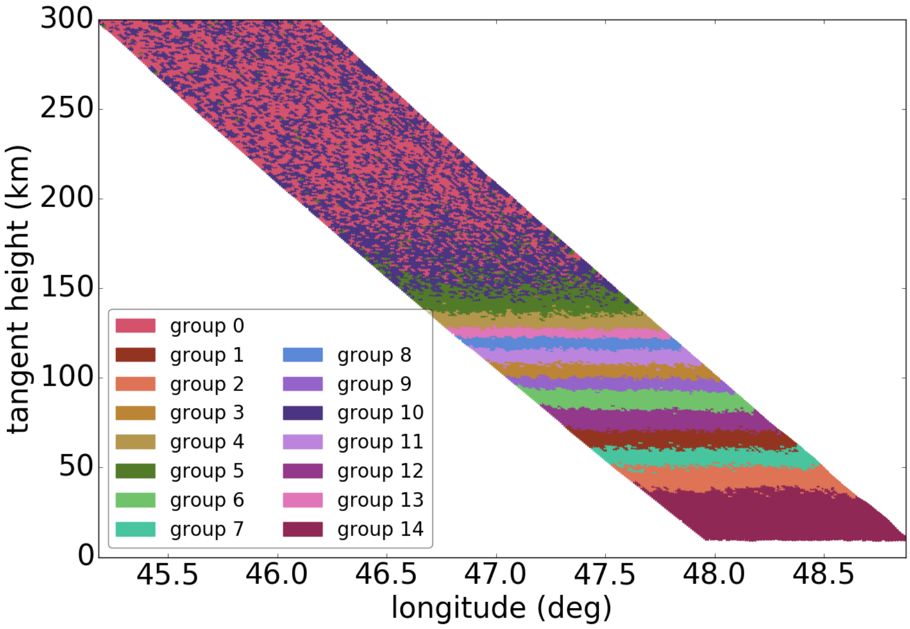

Figure 4.8: Distribution of the spectra into different groups after clustering. Colours correspond to cluster numbers. The grouping mainly follows a distribution as a function of tangent height, as expected for non-LTE radiation. See text for details.

generated for orbit 0330_2, separated by 0.1 deg in latitude. For all the profiles in this orbit, a uniform spacing of 2 km in tangent height was used to define each altitude–latitude bin. A different vertical binning was used in a reduced number of (more noisy) orbits. This issue will be addressed later in this chapter.

For every vertical profile, its zero-radiance level (or deep space radiance offset) and its noise level (or noise equivalent spectral radiance) were computed. Both were estimated by combining all the data above 250 km, where the radiance is expected to be zero on average. Each data *qube* reaches a different altitude, and hence the amount of data above that 250 km limit varies from orbit to orbit, but we observed that this limit is, in general, high enough to guarantee that the signal is dominated by instrumental noise. A small number of orbits do not reach those altitudes or present spurious spectra above a certain altitude value. For these cases, the zero-radiance and noise levels are determined as high as possible. For all the vertical profiles, the mean of the radiances measured above that tangent height was used to correct for the signal bias at all altitudes, while

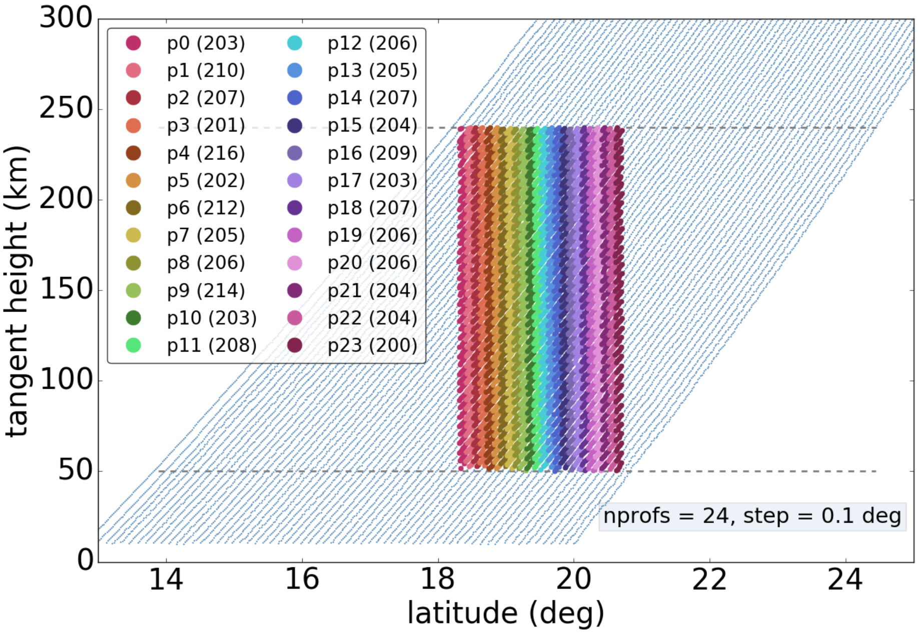

Figure 4.9: Geolocation of the 24 vertical profiles for orbit 0330_2. Different colours correspond to individual vertical profiles, and the number in parentheses accounts for the total spectra belonging to each profile. The pale blue dots in the background correspond to the geolocation of the OMEGA observations, like in Figure 4.3.

the noise level, i.e., the standard deviation, $noise_{TOA}$, was later used to obtain the noise for every cell.

Figure 4.10 shows the measurement noise for every profile in orbit 0330_2, on an altitude–latitude cross section. Each profile consists on a series of cells 2 km wide in the vertical and 0.1 deg large in latitude. The measurement error for each cell is the maximum of

- the standard error of the spectra in the cell, or
- the measurement noise at the top of the atmosphere, $noise_{TOA}$, divided by the square root of the number of spectra in the cell.

If a cell contains only one spectrum, the maximum of the noise value of the neighbour cells is used.

Figure 4.11 shows the averaged radiance vertical profiles and Figure 4.12 the averaged spectra at different tangent heights, both with noise values, for profile #20 of the OMEGA orbit 0330_2, after correcting the

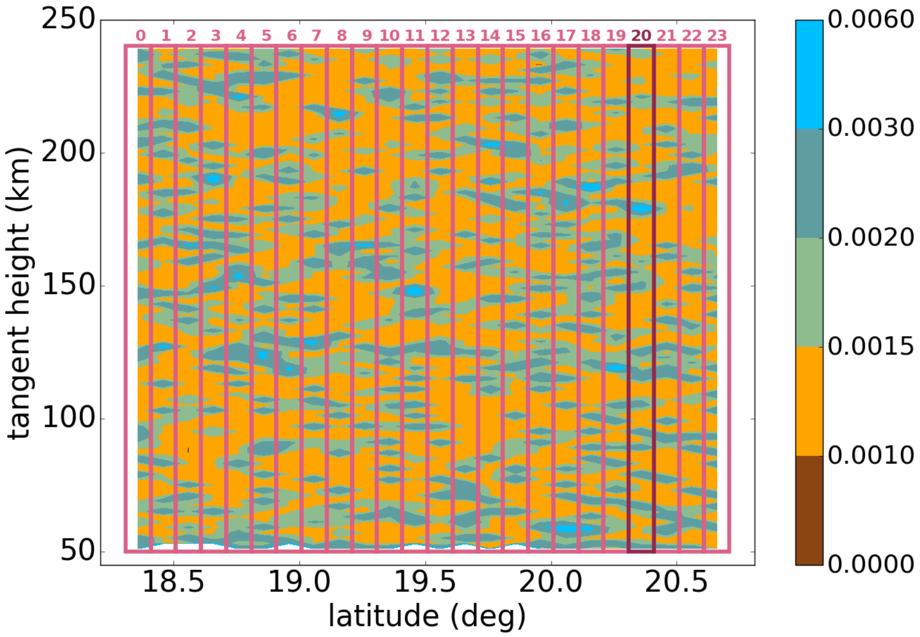

Figure 4.10: Calculated measurement error ($\mathrm{Wm^{-2}sr^{-1}\mu m^{-1}}$) for the 24 vertical profiles, at 4.30 μm. Profile #20 is highlighted in dark red. See text for details.

radiances for the deep space offset. The measurement errors obtained in these cells at all tangent heights are similar to the noise deduced from the space views. The fact that the measurement error is comparable or smaller than the noise means that our binning in the horizontal dimension is appropriate, in the sense that it does not introduce any significant variability in the radiances.

4.3. Remarks on the radiance vertical profiles

In Figure 4.9 we showed the 24 vertical profiles extracted from orbit 0330_2. Here we explain the criteria followed to extract the vertical profiles from the complete set of OMEGA observations selected. All the formed radiance vertical profiles can be consulted in Appendix B. The distribution and geometry of the spectra acquired by OMEGA are highly heterogeneous, leading to very different footprints or projections on the Martian atmosphere. For this reason, we needed to establish a series of criteria in order to homogenise the sample, i.e., to allow for an easier com-

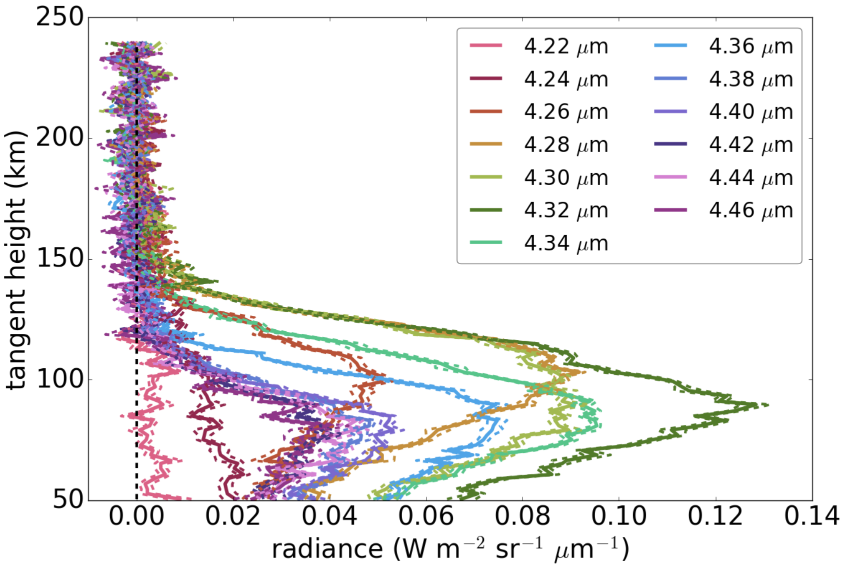

Figure 4.11: Spectral radiances at different wavelengths for profile #20 of the OMEGA orbit 0330_2, after correcting the spatial offset. The dashed lines represent the measurement noise. The spectra correspond to latitudes between 20.31 and 20.41 deg. Different colours are used for different wavelengths.

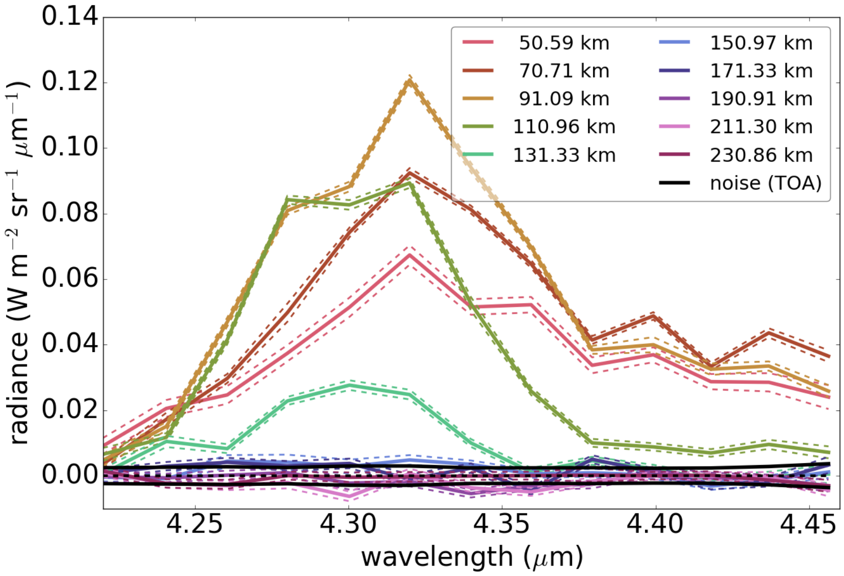

Figure 4.12: Spectra with measurement noise (dashed) for the same profile as Figure 4.11. Colours correspond to different tangent heights.

parison of the results of the retrievals, and we summarise them here, along with some example figures.

- **Tangent height:** as a general rule, a minimum altitude of 50 km is set. For the higher boundary, the selection depends on two traits related to the orbit. On the one hand, the OMEGA observations are available up to different maximum altitudes depending on the trajectory of the Mars Express spacecraft. For instance, *qube* 0970_0 only offers measurements up to a tangent altitude varying from 180 to 220 km (Figure 4.13). Besides, some orbits exhibit a considerable amount of spurious data above a given altitude, and then this altitude was chosen to be the upper limit. On the other hand, the atmospheric conditions provided by the LMD-MGCM are also limited to an inconstant altitude, as the vertical parameter used in the model is the atmospheric pressure, not the altitude (Forget et al., 1999). We chose the minimum of the limits associated to observations and model as the upper boundary for each orbit, varying from 190 to 300 km.
- **Altitude binning:** when possible, a vertical step of 2 km was chosen for the generation of the profiles. For *qubes* with convergence problems,

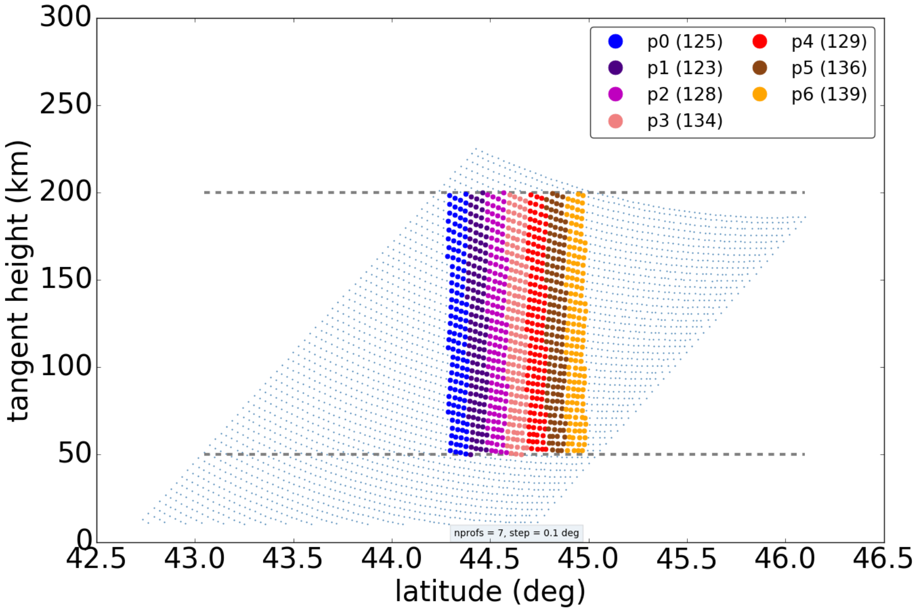

Figure 4.13: Same as Figure 4.9, for orbit 0970_0.

due to higher variability in the radiance vertical profiles, the binning was widened, up to 4 km. That was the case for 7 of the 47 orbits: 0970_0 (Figure 4.13), 1023_0, 7554_4, 7586_4, 7597_4, 7604_4 and 7619_4.

- **Latitude binning and number of profiles:** as stated before, the vertical profiles were formed averaging spectra taken close in latitude, to avoid large variations in the horizontal dimension. Considering the altitude constraints, the 2-D projection of the available data, and a sufficiently small latitudinal step (always smaller than 0.5 deg), we generated as many profiles as possible, always trying to guarantee a minimum number of spectra inside every cell in the grid. This way, we obtained between 6 and 30 profiles per orbit, with a latitudinal binning varying from 0.02 to 0.4 deg. It is important to note, at this point, the situation found on a few orbits, which directly impacted the convergence rate of the retrievals. Due to a steering effect, individual cells of some profiles contain spectra taken at different shots, whoch are later averaged together. This problem is present on profiles 9, 10 and 11 of orbit 0647_1 (Figure 4.14). Orbits 1619_4, 1880_1, 5851_0 and 6146_0 are also affected by this issue.

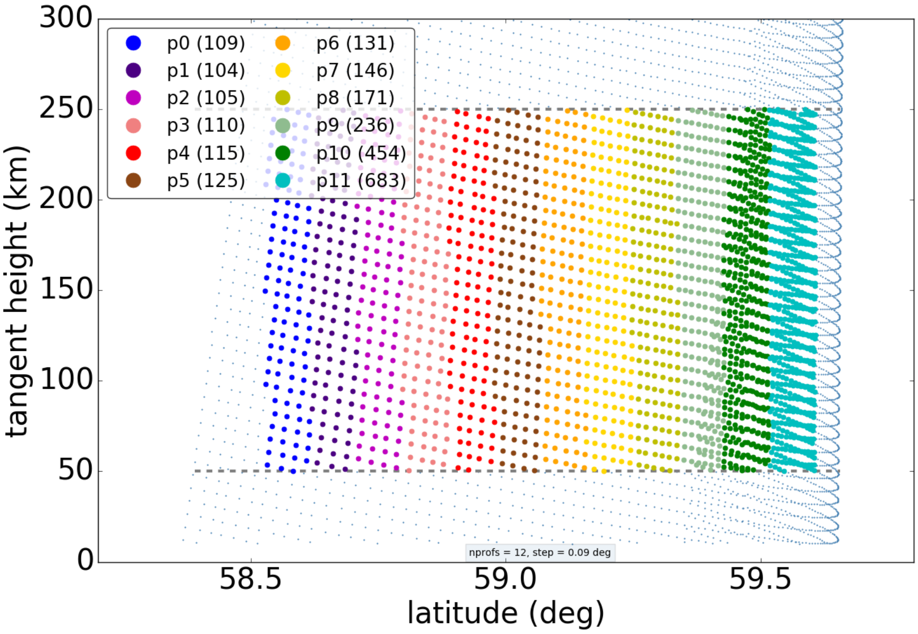

Figure 4.14: Same as Figure 4.9, for orbit 0647_1.

- **Regularisation:** the characteristics inherent to each of the orbits are extremely variable. We found different atmospheric conditions depending on the time and location of the observations, the radiances measured highly differ for different orbits due to the spacecraft distance to the planet, there is a different amount of spectra per cell, and hence a different measurement noise, among other dissimilarities. If the retrievals were performed using the same regularisation matrix for all the profiles, the averaging kernels, and thus the vertical resolution, obtained would strongly depend on the orbit. For this reason, the regularisation matrix was modified (all its elements multiplied by a constant factor) for each orbit, to guarantee a similar vertical resolution for all the cases, making it possible to directly compare the results.

To finish this section, three more examples are provided, just to expose the varied casuistry of the vertical profiles generation. Figures 4.15, 4.16 and 4.17 show, respectively, the profiles formed for orbits 0044_1, 1402_0 and 6586_0.

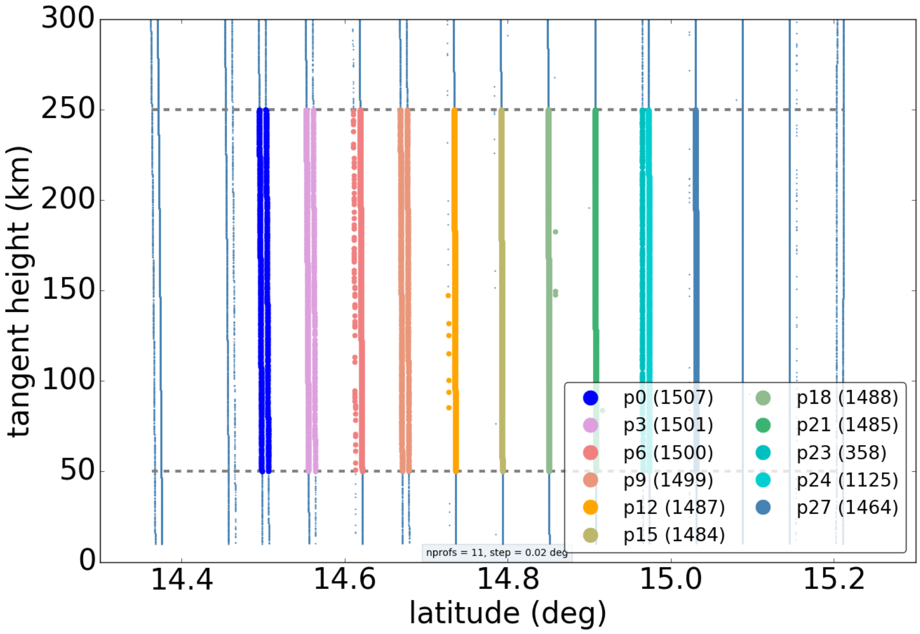

Figure 4.15: Same as Figure 4.9, for orbit 0044_1.

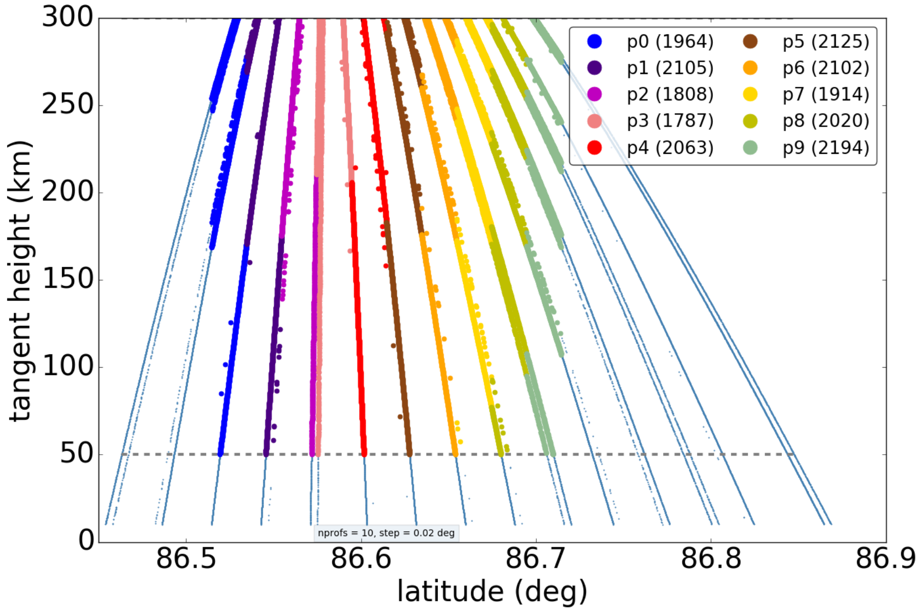

Figure 4.16: Same as Figure 4.9, for orbit 1402_0.

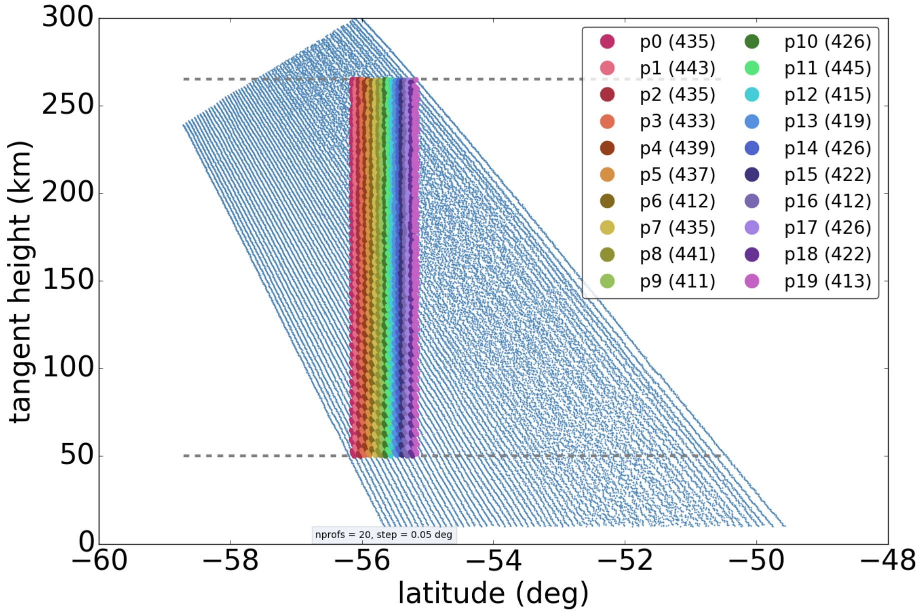

Figure 4.17: Same as Figure 4.9, for orbit 6586_0.

We have no need of other worlds. We need mirrors. We don't know what to do with other worlds. A single world, our own, suffices us; but we can't accept it for what it is.

Stanisław Herman Lem

5

Inversion of CO_2 at thermospheric altitudes

Abstract

In this chapter we apply the retrieval scheme presented in Chapter 2 to one vertical profile (#20) of a given OMEGA *qube* (0330_2). We detail the selected input parameters for the inversion and show the density profiles obtained after it, the spectral residuals of the best fit and some extra diagnostics results. We then apply the retrieval scheme to all the profiles generated from the OMEGA subset analysed (totalling 742). Finally, we report on the global convergence rate achieved (94%) and discuss the possible causes behind non-convergent profiles.

This chapter extends section 4 of Jiménez-Monferrer et al. (2019).

5.1. Retrieval of profile #20 of orbit 0330_2

In order to test and fine tune the application of the retrieval scheme to the OMEGA datasets, we first focused on a few profiles. In this section, we describe the behaviour of the inversion taking as an example one individual radiance vertical profile, #20, of data *qube* 0330_2. Once the performance of the inversion was satisfactory, it was globally applied to the entire dataset.

5.1.1. Key retrieval parameters

Input parameter	Value(s) chosen and references
OMEGA orbital datasets	47 *qubes* from MY26 to MY30 (Section 3.3)
A priori CO_2 abundances	LMD-MGCM at tangent point (Section 4.1)
Atmospheric conditions	LMD-MGCM at tangent point (Section 4.1)
Instantaneous FoV	1.2 mrad (Section 3.2)
Spectral resolution	27 nm (Section 3.2)
Selected wavelenghts	13 wavelengths from 4.22 to 4.46 μm (Section 4.2)
Tangent altitude range	120–180 km (Section 5.1)
Regularisation	1st-order Tikhonov (Section 2.3)
Maximum relative error	0.01
Non-LTE model	GRANADA adapted to Mars (Section 2.4)
RTE–SEE solution	Curtis-Godson approximation (Section 2.4)
CO_2 isotopes	626, 636, 628, 627, 638 and 637 (Appendix A)
CO_2 ro-vibrational bands	95 bands (Appendix A)
Spectroscopic database	HITRAN 2012 (Rothman et al., 2013)

Table 5.1: Main retrieval input parameters used for CO_2 density inversions in Mars. RTE and SEE stand for radiative-transfer equation and statistical equilibrium equation, respectively.

Table 5.1 summarises the main input parameters selected to perform the CO_2 density retrievals. A description of some of these the parameters can be found in previous chapters and in Appendix A. It should be noted that we assume a spectral resolution (in terms of FWHM) of 27 nm instead of the nominal 20 nm (Chapter 3). This is because a better global fit is generally achieved by assuming 27 nm for the instrumental response (see the sensitivity study in Chapter 7).

5.1.2. Retrieved absolute and relative density profiles

Figures 5.1 and 5.2 illustrate the CO_2 abundance obtained during the retrieval of profile #20 of orbit 0330_2, shown in absolute and relative terms, respectively. The direct outcome of the inversion process is the absolute density of CO_2 and this is shown in Figure 5.1, together with the *a priori*. In order to build a relative abundance, or volume mixing ratio (vmr), the absolute density is required. Some caution is needed for this because a simple, direct extraction of the atmospheric density from the LMD-MGCM is not appropriate. This is because the CO_2 is the major constituent of the Mars atmosphere and the retrieval profile, different to the *a priori*, will in general be inconsistent with the model values.

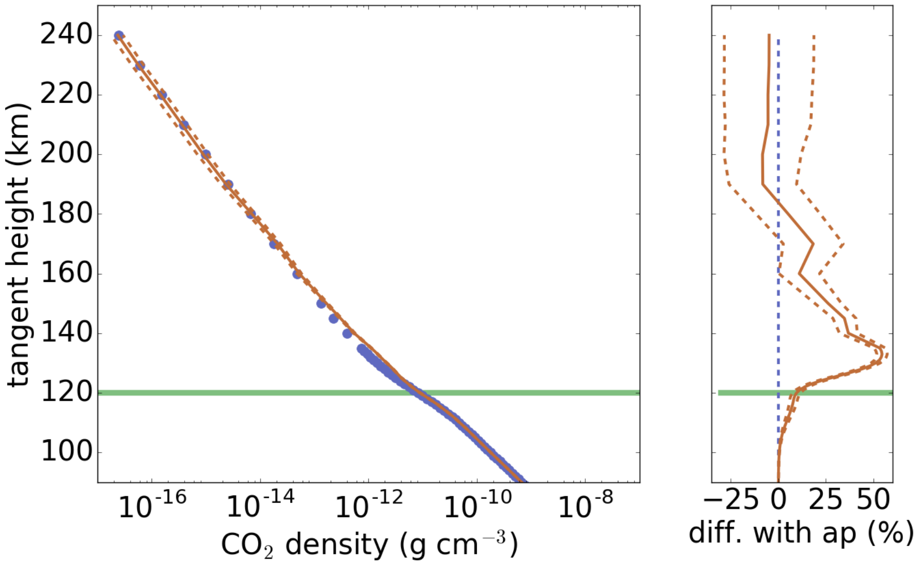

Figure 5.1: *Left*: Retrieved CO_2 density for profile #20 of orbit 0330_2 (orange line, with noise error in dashed lines), compared with the *a priori* profile (blue dots). *Right*: Relative difference of the retrieved CO_2 density with respect to the *a priori*. *Both*: The green line at 120 km represents the lower boundary of the retrievals. Only results above that line are relevant.

We obtained the total density by adding to the retrieved CO_2 density (Figure 5.1) the individual densities of the remaining minor constituents taken from the LMD-MGCM. On the other hand, Figure 5.2 shows the relative abundance of CO_2 as volume mixing ratio, the magnitude commonly used to best illustrate vertical variations of species abundances.

In general, below 120 km we found strong non-linearities in a very optically thick regime, where both the non-LTE CO_2 populations as well as the limb radiances strongly depend on the CO_2 density. This dependence leads to non-convergence in many cases. For that reason, the CO_2 profile is regularised by means of a 1st-order Tikhonov matrix (Section 2.3, with

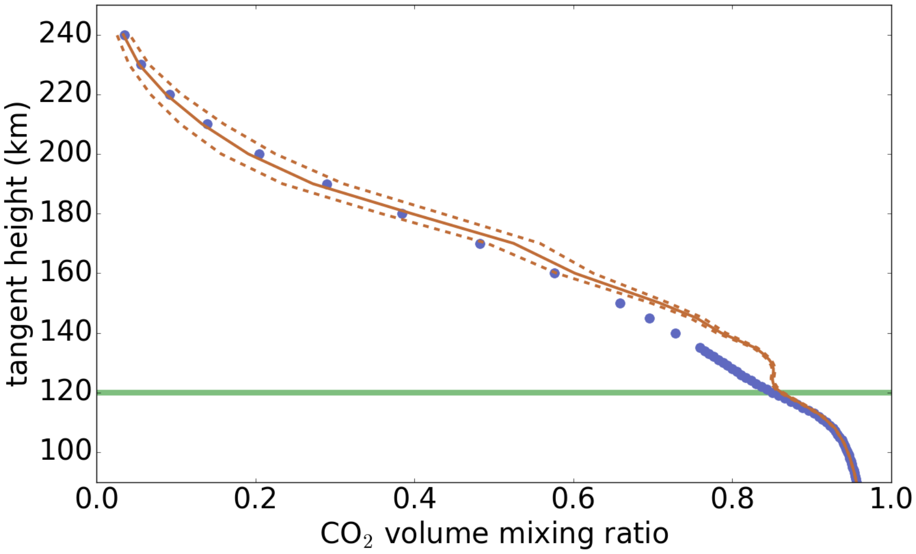

Figure 5.2: Same as Figure 5.1 (left), with the CO_2 abundance expressed as vmr. The total density was updated taking into account the abundance of the remaining gases from the GCM. See text.

a strong diagonal constraint below 100 km, in order to force the retrieved CO_2 to be close to the climatological density (*a priori*) in the lower mesosphere. Above 100 km, the values are chosen as a trade-off between a reasonable retrieval noise error and an acceptable vertical resolution, high enough to allow for meaningful retrieved CO_2 abundances above 120 km. The retrieved density is hence meaningful only between 120 and 180 km. Below 120 km the retrieval process is strongly regularised, and the uppermost altitudes are dominated by noise, as can be seen in figures 4.11 and 4.12.

We obtained what seem typical profiles at these altitudes, and close to the *a priori* CO_2 profile, with differences smaller than 50% at all altitudes of interest, and smaller than 20% above 150 km. The differences above about 180 km are within the retrieval noise. The vmr profile shows more clearly the largest difference with the a priori, around 130 km.

5.1.3. Best fit and residuals

In the retrieval process the convergence is achieved when the difference in the radiance between two consecutive iterations is smaller than a fraction of the retrieval noise error.

Figure 5.3 shows the spectra obtained at different tangent heights from the last iteration of the retrieval, compared with the measured spectra. In Figure 5.4 the simulated radiance profiles in the last step are compared with the observations. This is done at four wavelengths, i.e., four profiles are shown. In the same figure, the output radiance from the first run, that is, our forward model (KOPRA) applied to the input atmosphere, is also shown.

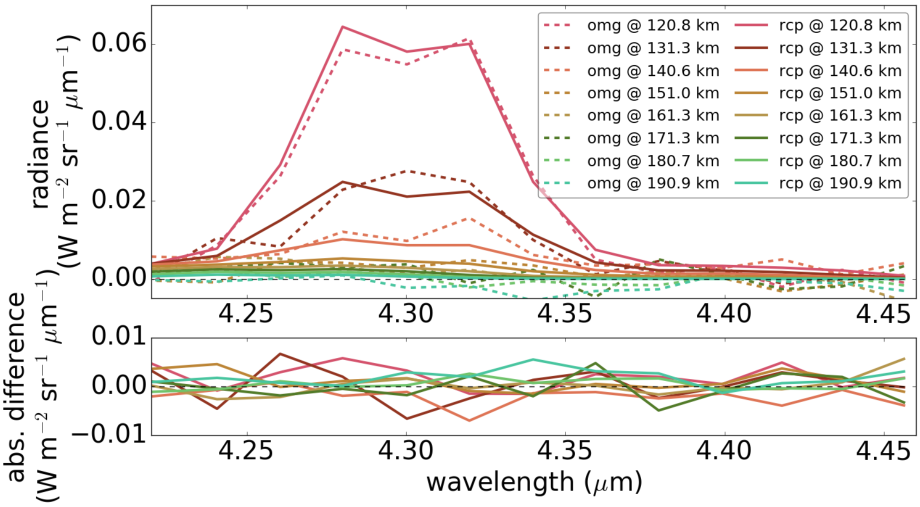

Figure 5.3: *Top*: Best fit spectra for the profile #20 of the OMEGA orbit 0330_2 (*rcp*, solid), compared with observations (*omg*, dashed), at different tangent heights. *Bottom*: Differences between best fit and OMEGA. The measurement noise is about 0.002 $\mathrm{W m^{-2} sr^{-1} \mu m^{-1}}$ and slightly varies with altitude, as can be seen in figures 4.11 and 5.4.

The best fit spectra in Figure 5.3 present a double-peak shape below 130 km and centred around 4.30 μm, which tends to disappear above about 140 km. This behaviour is typical in a CO_2 atmosphere, with a limb emission dominated by the fundamental band of the main isotope at high altitudes, but with large contributions from its two second hot bands (both centred at 4.30 μm) at lower altitudes, where the fundamental band is optically thick (Piccialli et al., 2016; López-Valverde et al., 2011; Gilli et al., 2009). Differences between the best fit and the measurements are slightly larger than the noise (Figure 5.4), and present a quasi-random spectral shape at all altitudes. This behaviour is observed throughout the

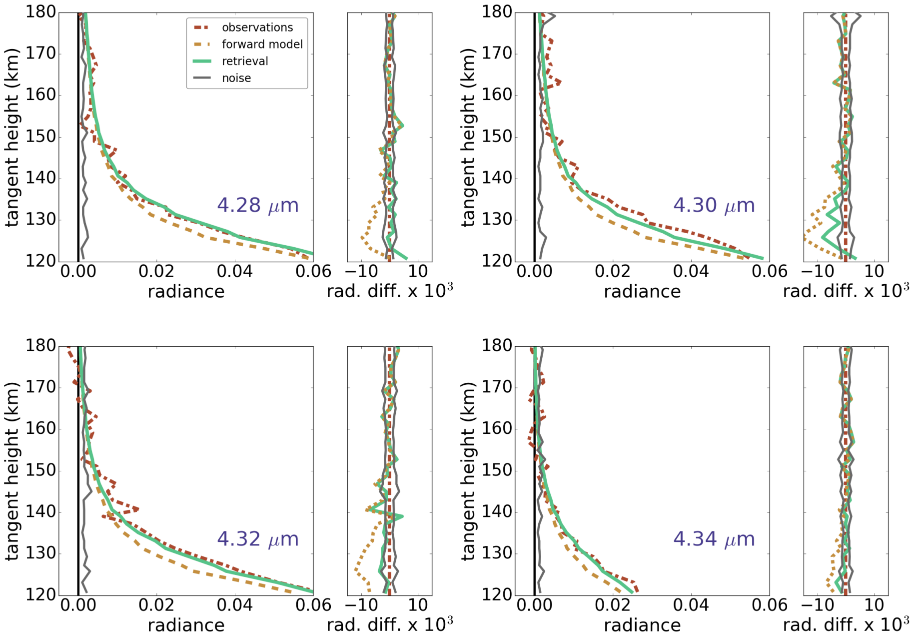

Figure 5.4: [All panels] *Left*: Best fit for profile #20 (solid), compared with observations (dashdotted) and with simulations of the forward model after the first step of the iteration (dashed). *Right*: Differences with the observations. Measurement noise is added for reference (grey solid lines). All radiance units are in Wm^{-2}sr$^{-1}\mu$m^{-1}.

whole spectral range, inside and outside the major emission, which occurs between 4.25 and 4.35 μm.

The most peculiar difference in this profile is obtained at a tangent height of 131 km, where the measured spectra shows only a single maximum, at 4.30 μm. This may indicate an atmosphere colder than the assumed thermal profile, where the double peak shape on the second hot bands is expected to approach a single maximum shape centred around 4.30 μm. A joint retrieval of CO_2 and temperatures might improve the fit in the future, but is beyond the scope of the present study. Since the temperature uncertainties are not the dominant source of retrieval errors (see Chapter 7), the CO_2 densities obtained in such a joint retrieval are expected to be similar to the present results.

Figure 5.5 shows the averaging kernels for both rows and columns. The full width at half maximum of either the columns or the rows of the averaging kernels provides the actual vertical resolution of the retrieved

CO_2, indicating a value of about 15 km between 120 and 160 km. This is coarser than the vertical sampling of the instrument for this orbit, about 3.37 km. This is also larger than the vertical binning used, 2 km, which indicates that a thicker binning of the data is possible. At higher altitudes, the averaging kernels are wider, as expected, since the non-LTE source function of all major bands is constant with altitude in the optically thin regime. Consequently, the emission only depends on the density of CO_2, which strongly decreases with altitude, both because pressure falls and its vmr also decreases.

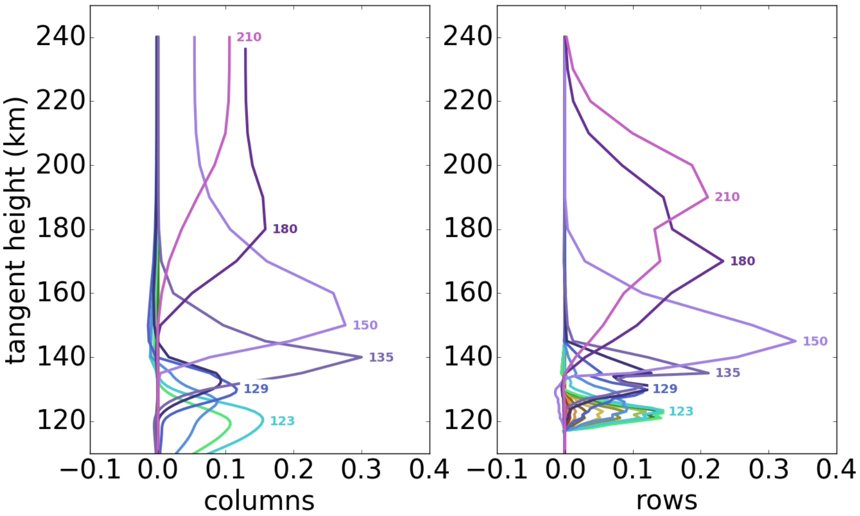

Figure 5.5: Averaging kernels resulting from the retrieval process. Different colours represent different averaging kernels and the numbers are the corresponding altitudes in km. For clarity, only one every three columns (or rows) is being represented in the figure.

The trace of the averaging kernel matrix gives the number of independent pieces of information, i.e., the degrees of freedom. This is between 4 and 5 in the whole altitude range of this particular profile. The results for vertical resolution and degrees of freedom presented here are typical values of all the CO_2 retrievals performed in this Thesis.

5.2. Retrievals of all the profiles of orbit 0330_2

Following the same steps described in previous sections, we retrieved the CO_2 density for the 24 profiles of orbit 0330_2. Since the dispersion in latitude, longitude and local time is very small (much smaller than the LMD-MGCM grid), we assumed the same *a priori* (and first guess) CO_2 profile and the same reference atmosphere for the thermal structure and the abundance of minor gases. The results are shown in Figure 5.6.

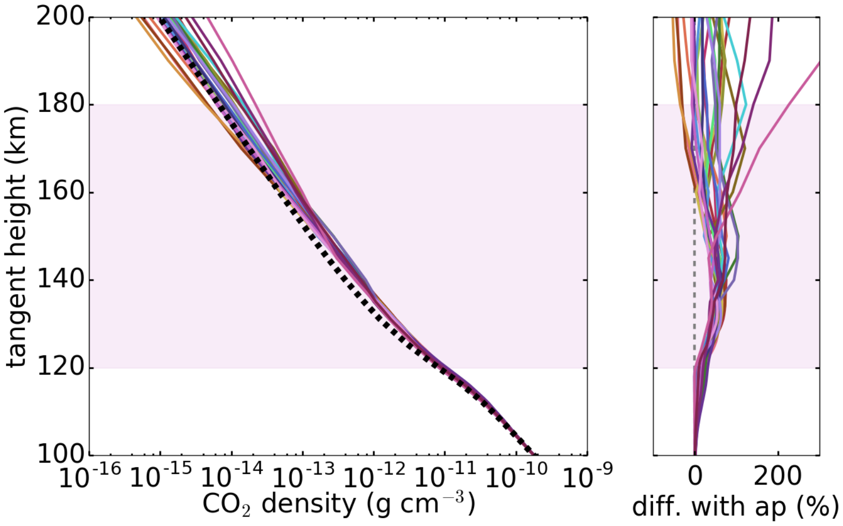

Figure 5.6: *Left*: Densities retrieved for all the profiles in orbit 0330_2, each of them with a different colour (solid), and *a priori* density (dashed). *Right*: Relative differences with the *a priori* density. The retrieved quantities contain measurements information only in the shaded region.

The inspection of figures 4.11, 4.12 and 5.6 shows that, below a CO_2 density value of about $10^{-14}\,\mathrm{gcm}^{-3}$, or above 180 km in this reference orbit, the atmospheric emission is similar or smaller than the OMEGA noise level, i.e., the noise error dominates the error analysis. This will also be shown in Chapter 7. This density limit was confirmed for all the orbits analysed in this study, and allowed us to determine a reliability zone, i.e., the altitude range where the retrieved magnitudes contain information on the measurements. This region goes from 120 km to the upper limit imposed by the noise level, which depends on the data *qube* and usually varies between 180 and 190 km. For all the portrayed profiles, this altitude interval is shown as a shaded region.

Figure 5.6 shows a behaviour common to most orbits studied here (Appendix B), that the dispersion in the individual CO_2 profiles within each orbit is relatively small. This is not surprising, given the small geographical extension of most *qubes* in latitude, longitude and local time. The dispersion increases with altitude, specially above about 160 km, following the larger relative noise in the data.

In this orbit we obtained a CO_2 abundance larger than the *a priori* in all the profiles, specially between 125 and 150 km, with averaged maximum differences around 75% at 135 km.

5.3. Retrievals for all the limb orbits

5.3.1. Convergence analysis

Table 3.2 details the number of profiles formed and their latitudinal width, and the convergence rate achieved for the 47 OMEGA data *qubes*, alongside with the location of the observations. A mean number of 16 radiance vertical profiles per orbit were formed, totalling 742 profiles. The number of successful retrievals was 694, obtaining a global 94% convergence rate, which is considered as very satisfactory.

The reasons behind non-convergent retrievals are diverse. A detailed inspection of the non-convergent retrievals throws no insight on the potential correlation of convergence and the location of the dataset (latitude, longitude or solar longitude). Most of the unsuccessful inversions are located where the concentration of observations is larger, so non-convergent retrievals are distributed across the whole dataset. No correlation was found between the non success of the inversions and the thermal structure of the atmosphere or the distance of the retrieved profiles to the *a priori* either.

We found some correlation with the solar zenith angle, as expected, because the larger the solar illumination, the lower the non-LTE emission and hence the signal-to-noise ratio. This way, almost all of the orbits with a radiance peak below 0.05 $\mathrm{Wm^{-2}sr^{-1}\mu m^{-1}}$ at 4.30 μm (see Appendix B) found convergence problems for at least one of their vertical profiles. Another reason in a few cases is the geometric projection of the radiance measurements. The binning used usually implies observations sufficiently close in space, but some orbits exhibit spectra from more distant locations, due to a steering effect. This usually leads to useless vertical profiles.

5.3.2. Vertical profiles and retrievals

The radiance vertical profiles at 4.30 μm and the retrieved densities for the entire set of 47 OMEGA orbits are included in Appendix B. In addition, for a global overview of the results obtained by the retrievals and their comparison with models, please refer to Section 8.1. Here three particular cases are selected, together with orbit 0330_2 studied above, in order to illustrate the casuistry of the retrievals. All the information on the geolocation of the data can be consulted in Table 3.2.

Orbit 1023_0

Orbit 1023_0 was observed during the northern summer (solar longitude 110 deg, latitude 45.5 deg). This case was selected because of its extremely high solar zenith angle (88 deg). In this situation, the solar excitation is weak and the radiances emitted are low. In Figure 5.7 (top right panel), the huge dispersion among radiance profiles for contiguous locations (see profiles formed in the top left panel) is clear, and the radiance peak at 4.30 μm varies around 0.01–0.02 $\mathrm{Wm^{-2}sr^{-1}\mu m^{-1}}$. Besides, the radiance profiles are quite noisy, even though the vertical binning for this orbit was enlarged to 4 km. For these reasons, the retrieved CO_2 for the profiles which successfully achieved convergence (7 out of 10) also present a large dispersion (bottom left panel, with the mean CO_2 density profile highlighted in solid blue). The (poor) spectral fit to the observations, at four different tangent heights from 120 to 180 km, is shown in the bottom right panel for one of the vertical profiles formed (#8). The comparison with the model will be addressed later in Chapter 8.

Orbit 7701_0

Orbit 7701_0 was selected due to its proximity to the pole, during northern springtime (solar longitude 33 deg, latitude 86.3 deg). As can be seen in Figure 5.8 (top left panel), 20 vertical profiles densely populated (the numbers inside the parentheses account for the total number of spectra available in each profile) were formed. The peak radiance at 4.30 μm is about 0.035 $\mathrm{Wm^{-2}sr^{-1}\mu m^{-1}}$ for all the profiles (top right panel), and the dispersion among them is much smaller than for orbit 1023_0. The retrieved CO_2 densities indicate the high thermosphere (above 140 km) is denser than in the model for almost all the vertical profiles (bottom left panel). The fit in radiances for a selected profile (#5) is shown in the bottom right panel, where the reduced number of available wavelengths due to ageing is also visible.

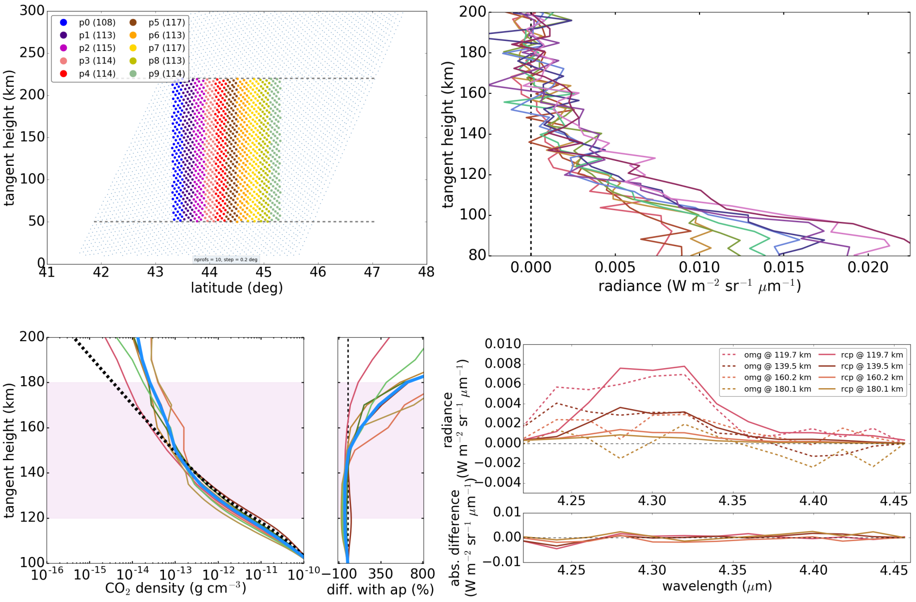

Figure 5.7: Vertical profiles (top left), radiances for all profiles at 4.30 μm (top right), retrieved densities for all profiles and differences with *a priori* (bottom left), and residuals for best-fit radiances of profile #8 and differences with omega observations (bottom right), for orbit 1023_0. See text for details.

Orbit 1619_4

To conclude this section, we chose orbit 1619_4 because it is located in the southern hemisphere of Mars, also in springtime there (solar longitude 196 deg, latitude −51.8 deg). Again, 20 vertical profiles were generated from the projected distribution of spectra in the atmosphere (Figure 5.9, top left panel). The radiances corresponding to these profiles present small dispersion, reaching a radiance peak slightly over 0.06 $\mathrm{Wm^{-2}sr^{-1}\mu m^{-1}}$ (top right panel). The retrieved CO$_2$ densities show an oscillation of roughly 40 km wavelength (bottom left panel), probably due to the effect of a gravity wave. This issue will be revisited in Section 8.2, along with the comparison of the results with the measurements of other instruments sounding the Martian thermosphere. The radiance fit in the bottom right panel of the figure shows good agreement with the data above 150 km, with important differences only in the proximity to the lower boundary, where the effects of the strong regularisation below 120 km are more intense.

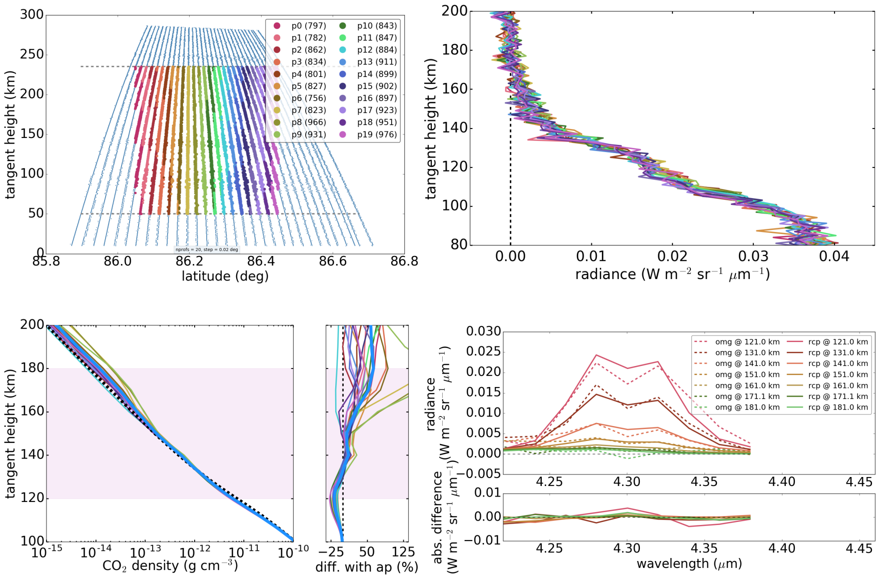

Figure 5.8: Same as Figure 5.7 for orbit 7701_0. The bottom right panel shows the best-fit radiances for profile #5.

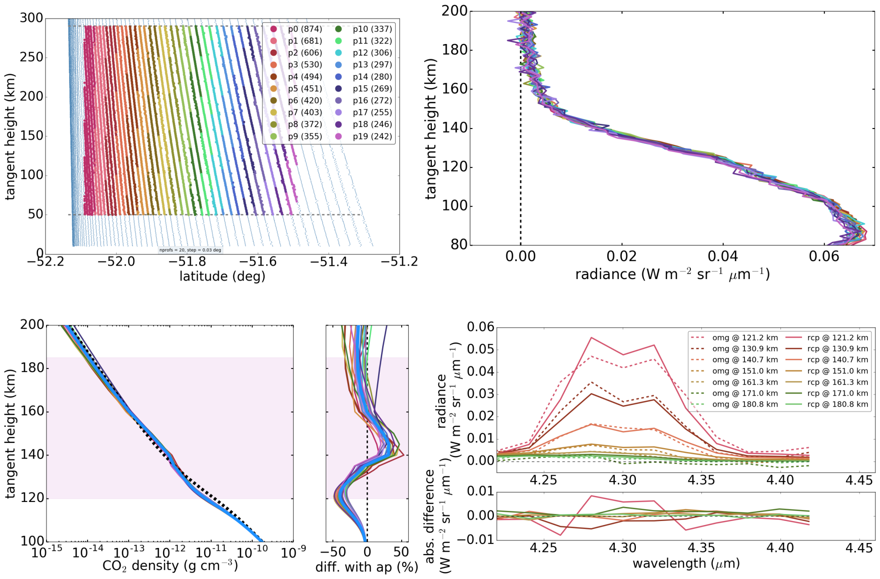

Figure 5.9: Same as Figure 5.7 for orbit 1619_4. The bottom right panel shows the best-fit radiances for profile #17.

Destruction is a form of creation.

Richard Kelly

6

Temperatures from inverted CO_2 profiles

Abstract

A custom algorithm to derive temperature profiles from the retrieved densities, assuming hydrostatic equilibrium, is presented in this chapter. First, we show the formulation behind the algorithm, and then apply it to derive the temperature distribution of the atmosphere for the particular case of profile #20 of orbit 0330_2. Later, we discuss the results of the derivation temperatures for all the OMEGA subset selected. Finally, the application of the algorithm (and its validation) to dayglow emissions in the ultraviolet frequency range is presented.

This chapter extends section 4 of Jiménez-Monferrer et al. (2019).

The CO_2 non-LTE emissions measured with the geometry and spectral resolution of the OMEGA instrument do not contain much direct information on the atmospheric thermal structure. For this reason, even simultaneous retrievals of CO_2 and temperature, not tackled in this work, will possibly not succeed to this end. An alternative method is followed in this Thesis, by applying the hydrostatic approximation to the CO_2 inverted profiles. This is a common approach extensively used in planetary atmospheres, and in particular in the Mars upper atmosphere when either densities (Forget et al., 2009) or airglow radiances (Leblanc et al., 2006; Bougher et al., 2017) are observed but a rigorous direct inversion of the temperature is not possible.

6.1. Algorithm to derive temperature profiles

Here we present an implemented algorithm to derive temperatures from the retrieved CO_2 density profiles, by assuming hydrostatic equilibrium, based on the expression of Theon and Nordberg (1965). The algorithm was also used to derive temperature profiles from the Martian dayglow as measured by SPICAM and as simulated by the LMD-MGCM (see Section 6.4).

At a given altitude, z_i, corresponding to layer i, we may write the temperature of a gas, T_i, as

$$T_i = \frac{\int_{z_0}^{z_i} \rho g dz}{\rho_i \frac{R}{M_r}} + \frac{\rho_0}{\rho_i} T_0, \tag{6.1}$$

where T_0 is the temperature at the top of the atmosphere (TOA), ρ is the gas density, M_r is the gas molar mass, R is the gas constant, g is the gravity, and z is the altitude (the variable of integration), and the integration is extended from the TOA, z_0, to layer i.

This expression is strictly valid when CO_2 is in diffusive equilibrium, i.e., above the homopause, located in Mars around 125 km. It can also be valid in the homosphere if the molar mass, M_r, and the density, ρ, are given for the whole atmosphere, and if it is assumed to be in hydrostatic equilibrium there. Using values from the LMD-MGCM, we have tested the validity of this expression from the exosphere to the ground, with negligible errors in the transition region around the homopause.

In Equation 6.1, T_i is obtained via an iteration process starting at TOA. In other words, we derive the temperature at each altitude except at TOA, where it has to be prescribed. Besides, this method is very sensitive to density gradients. At each layer, once ρ is known (taken from the individual CO_2 density profiles retrieved from OMEGA), all inputs are determined except T_0. We calculated this value from the density gradient between the two higher altitudes in each of the CO_2 profiles.

The uncertainty of the derived temperature was computed by the quadratic sum of two components: (i) First, a purely random contribution, calculated by generating 200 arbitrary density profiles close to the retrieved CO_2 density. This is done by adding random variations at each altitude, around the CO_2 densities. For simplicity, we chose density fluctuations of 20%, found to be typically representative of the CO_2 noise error (Chapter 7). Then the 200 temperature profiles were obtained and their dispersion computed. (ii) Secondly, a systematic contribution of unknown sign due to the downwards propagation of a ±40 K uncertainty on the temperature at the TOA. This uncertainty value is arbitrary and intended to reproduce the large model uncertainties in the uppermost thermosphere of Mars. We found that this second component is significant only above 140 km, approximately.

Figure 6.1 shows a demonstration of this algorithm, i.e., the result of the hydrostatic derivation of the temperature from a CO_2 density profile, taken from the LMD-MGCM for atmospheric conditions corresponding to the geolocation of the OMEGA 0044_1 *qube*. The obtained temperature is compared with that predicted by the model with an excellent agreement.

The temperature assumed at TOA may not be close to the actual value (although it obviously does in this example). However, the downwards

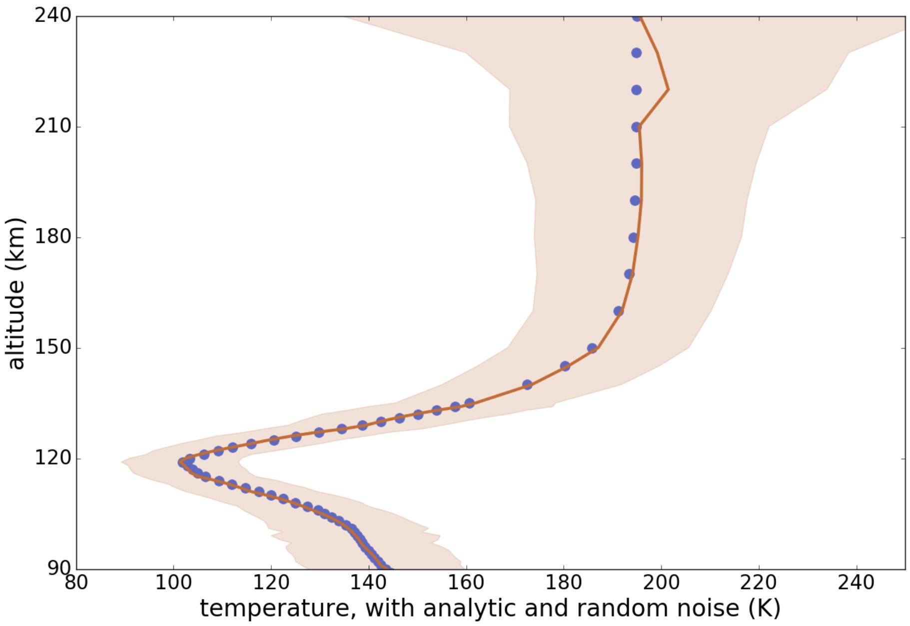

Figure 6.1: Temperature derived from a hydrostatic adjustment applied to the CO_2 density taken from the LMD-MGCM (solid orange line). The temperature provided by the LMD-MGCM is shown with blue dots. The shaded region is the estimated total error (see text for details).

calculations rapidly approach the true (hydrostatic) profile. Although in this example the estimated error propagates down to the ground, the derived temperature uncertainty becomes negligible below a given altitude for the retrieved CO_2 profiles, due to the strong regularisation forced in the lower region of the atmosphere, as can be seen, for instance, in Figure 6.2.

6.2. Temperatures for orbit 0330_2

We first derived the temperatures associated to the density profile in Figure 5.1, left panel (profile #20), under the hydrostatic assumption. The results obtained are shown in Figure 6.2, together with their uncertainties, as a shaded region.

The temperature obtained for profile #20, is remarkably close to the LMD-MGCM reference profile, considering its uncertainty. This gets larger above about 190 km, the region where the OMEGA noise dominates

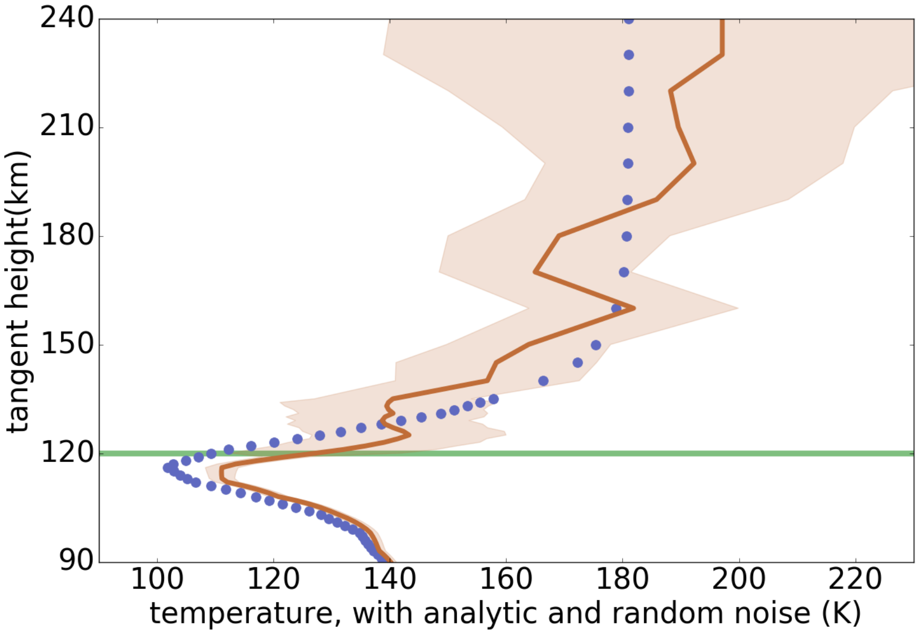

Figure 6.2: Temperature derived from a hydrostatic adjustment applied to the retrieved CO_2 density (solid orange line). The temperature provided by the LMD-MGCM is shown with blue dots. The shaded region is the estimated total error (see text for details). The green line at 120 km represents the lower boundary of the retrievals.

the inversion of CO_2 and the information content is therefore very small. Let us recall that the LMD-MGCM thermal structure is not used in our derivation of temperature but only in the retrieval of CO_2, via the *a priori* and the dependence of radiative transfer on the kinetic temperature (a secondary effect).

Following the process described above, temperature profiles were derived for the 24 retrieved CO_2 profiles of the orbit 0330_2 (Figure 5.6, left panel), and they are depicted in Figure 6.3. The average of the temperatures derived for all the profiles is shown as a solid blue line.

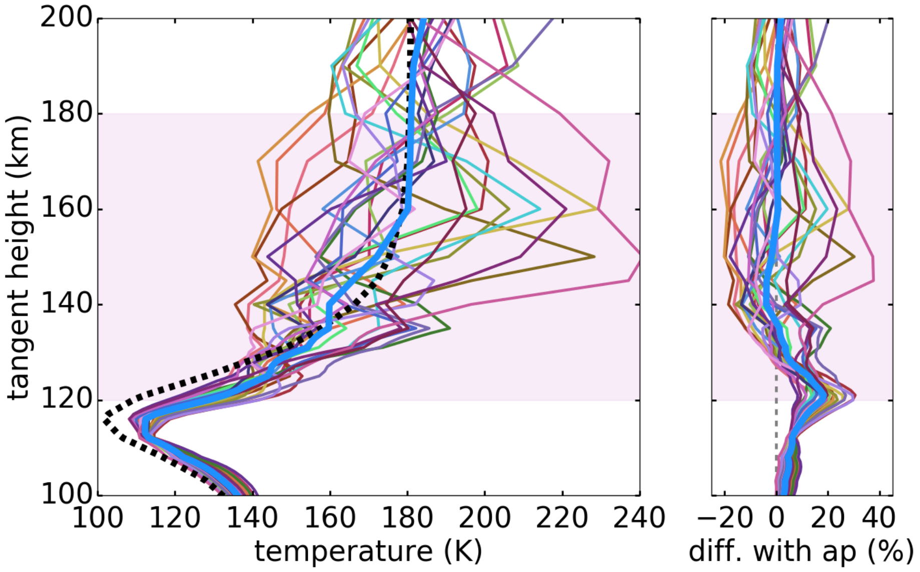

Figure 6.3: Temperatures derived for all the profiles in orbit 0330_2, each of them with a different colour (solid). Their relative differences with the input temperature (dashed) are also shown. The range of altitudes with meaningful CO_2 inversions (120–180 km) is shown as a shaded region. The average temperature of all the profiles in the orbit is represented by a thick blue line.

The average temperature is very close (within 30%) to the LMD-MGCM above about 130 km. However note that the temperatures in all the profiles present a positive bias around 120 km. This is the very bottom of the region of interest, and should be looked upon with caution, as this is surely an artefact of the strong regularisation applied there, during the inversion of CO_2, i.e., produced by a forced gradient in the CO_2 densities. These densities are, in all the 24 profiles, larger than the climatology around 130 km (see Figure 5.6), and therefore, present a tendency to the climatological value at the bottom of the inversion range, 120 km, which produces an artificial density gradient.

All the individual temperature profiles of *qube* 0330_2 have similar uncertainties to the profile #20 (Figure 6.2). The dispersion observed in Figure 6.3 increases with altitude from 120 to about 160 km, and then decreases at higher altitudes, due to the selection of T_0. Because the temperature at TOA is calculated from the CO_2 density gradient at the higher altitudes available for each profile, the values of T_0 for all the profiles in the same orbit tend to be close to each other. This is specially true for orbit 0330_2, where the variation in T_0 is within only 2 K. For orbits with higher variability in the CO_2 density gradient, the dispersion in T_0 reaches values around 20 K, and this effect, the decrease of temperature dispersion with altitude, is not so obvious.

6.3. Temperatures for selected orbits

As mentioned in previous chapters, the temperature profiles are not directly retrieved from the OMEGA observations, but derived from the retrieved CO_2 densities, assuming hydrostatic equilibrium. All the CO_2 density profiles are available in Appendix B. Here we focus on two additional profiles in order to illustrate the types of thermal structures obtained in this work. In addition to the study of these two profiles, a few general results are also discussed. For a more global study of the derived temperatures and their comparison with the LMD-MGCM, please refer to Chapter 8.

Similarly to the result obtained for profile #20 of orbit 0330_2 (Figure 6.2), most of the $\sim$ 750 temperature profiles obtained in this work present a systematic bias at 120 km, more or less prominent depending on the orbit. This is an artefact produced by an excessive gradient in the density, due to the strong regularisation introduced below the retrieval boundary, as stated before.

The large dispersion in the derived temperature among the individual temperature profiles of orbit 0330_2 (Figure 6.3) is not a general rule. Rather, the difference among individual temperatures of the same orbit are small, typically like those shown in figures 6.4 and 6.5, which show the two cases selected here, orbits 7708_0 and 7686_0, respectively. Notice that the constant value of the temperatures from 190 to 200 km derived for *qube* 7708_0 (Figure 6.4) is due to boundary effects, as, for this particular orbit,

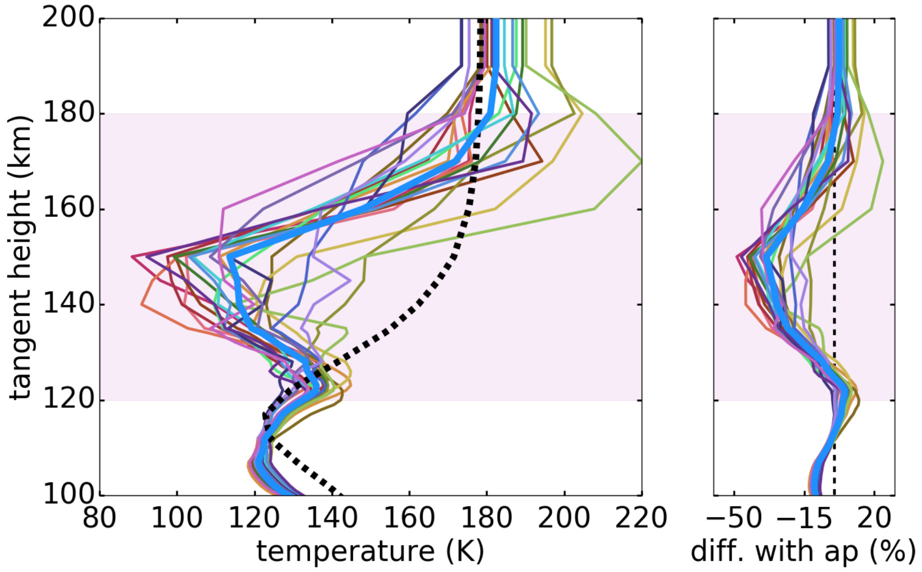

Figure 6.4: Same as Figure 6.3, for orbit 7708_0.

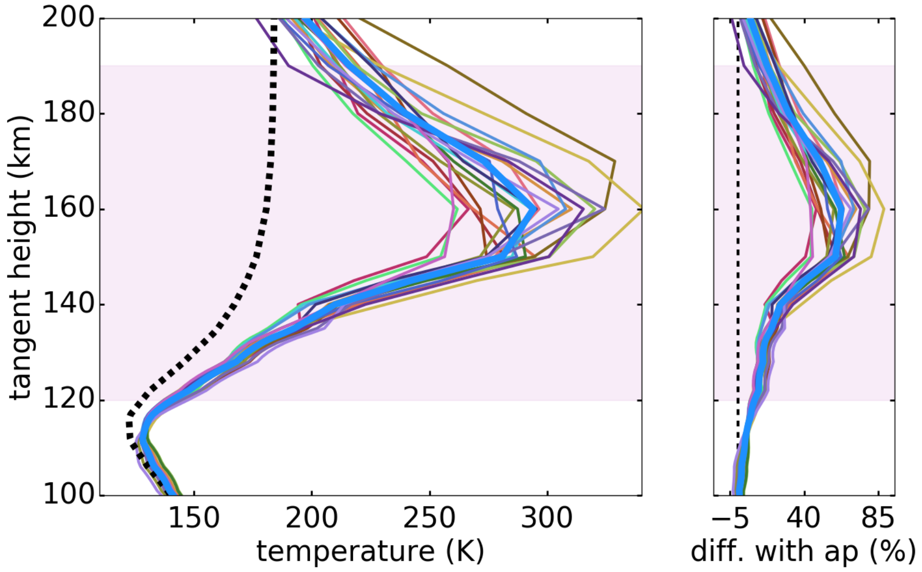

Figure 6.5: Same as Figure 6.3, for orbit 7686_0.

the radiance vertical profiles, and hence the retrievals, were extended only up to 200 km, about 30 km lower than our average TOA.

In 28 out of the 47 orbits (60%), including 7708_0 (Figure 6.4), a second minimum in the temperature profile is found at about 150 km, sometimes a bit lower, at about 140 km. This very cold thermosphere is not reproducible under usual climatic scenarios by the LMD-MGCM (this issue will be addressed later in Chapter 8). On the contrary, 14 orbits (30%), including 7686_0 (Figure 6.5), exhibit a larger value of the temperature around 150 km, pointing to a warmer thermosphere than that predicted by the model. The cases selected therefore illustrate two common results in the lower thermosphere. There are five orbits remaining, for which the fit between the derived temperatures and the model is fine within a ±10% tolerance. This is true throughout the whole retrieval range of altitudes, excluding the bias at 120 km, due to regularisation.

The radiance vertical profiles and the inverted densities for these particular cases (0330_2, 7708_0 and 7686_0), and for the whole dataset, are available in Appendix B.

6.4. Application to SPICAM dayglow emissions

The implemented algorithm to derive temperature profiles, assuming hydrostatic equilibrium, has also been tested and applied to the determination of thermospheric temperatures from dayglow emissions on Mars (González-Galindo et al., 2019). In other words, we applied Equation 6.1 to radiances instead of densities. This is an approximation which only makes sense if the radiances are linearly dependent on the densities, i.e., in an optically thin regime. This has been applied extensively to observations on Mars (see references in González-Galindo et al. (2019)).

Our objective is dual. On the one hand, we aim at deriving information on the thermal structure from SPICAM UV observations. On the other hand, we want to test the usual assumptions behind the application of Equation 6.1 to the observed UV radiances, including a quantitative evaluation of the errors associated to these hypotheses.

These assumptions have traditionally included (i) the neglect of the dissociative recombination of CO_2^+ and the electron impact excitation of CO for Cameron bands production, and (ii) the derivation of temperatures from the scale height of the emission in the isothermal region (upper thermosphere) and in the optically thin region for UV solar radiation.

This is an ongoing work, combining observations and GCM model results. Here we describe the application of the algorithm to UV radiances simulated with the LMD-MGCM, and its validation.

First, we extracted profiles of the Volume Emission Rate (VER) of the CO_2^+ UV doublet and the Cameron bands from the LMD-MGCM, recently extended to simulate these dayglow emissions (González-Galindo et al., 2018). We also extracted CO_2 number density and temperature profiles from the model. The extraction was performed at a set of 10000 locations randomly distributed in season, latitude, longitude and local time (between 6 am and 6 pm), with a non-uniform distribution in solar zenith angle (see González-Galindo et al. (2019) for details). Solar minimum conditions appropriate for the SPICAM dataset were assumed for the simulation spanning one Martian Year.

The temperature profiles derived (using Equation 6.1) from the limb-integrated VER of both CO_2^+ UV doublet and Cameron bands, and from the CO_2 density profile, were compared to the temperature profile of the model at the same location, as a measure of the quality and accuracy of this measurement (Figure 6.6).

As discussed above, the temperature derived from the CO_2 density profile reproduces very well the actual temperature profile, with differences always below 2 K. The temperature derived from the CO_2^+ UV doublet gives differences less than 5 K between about 160 and 230 km, and less than 2.5 K between 175 and 225 km. However, the temperature derived from the Cameron bands is clearly above, with differences always larger than 15 K.

The traditional derivation of temperatures from the scale height of the UV emissions is essentially equivalent to our derivation, but the study presented here demonstrates that its application to the Cameron bands is incorrect, giving a significant bias towards too warm values. Even the derivation of temperatures from the CO_2^+ UV doublet is not very precise, with small positive biases in the 175–225 km range, but larger errors outside these altitudes. These results are being applied to a revision of temperatures from SPICAM VER measurements by our team (González-Galindo et al., 2019).

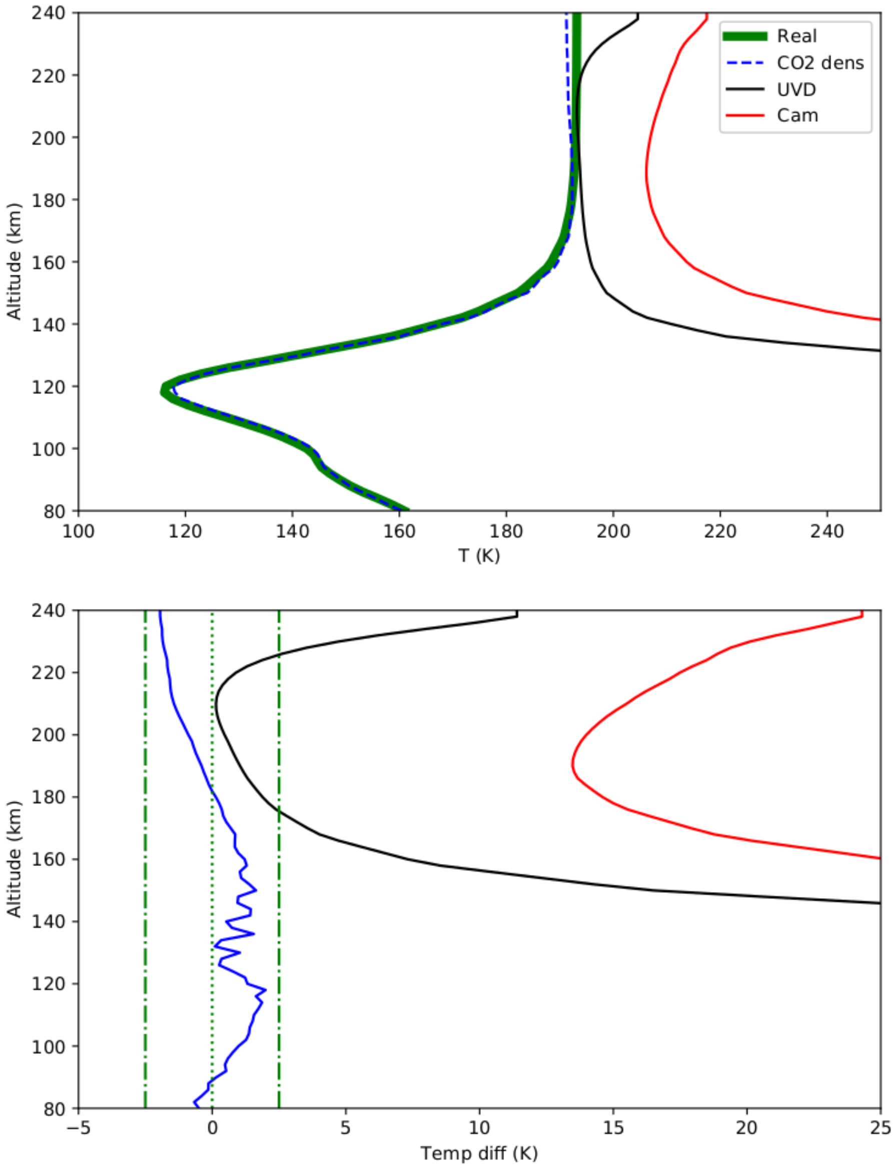

Figure 6.6: *Top*: Temperature profile extracted from the LMD-MGCM (green thick line) and derived from the LMD-MGCM CO_2 density profile (dashed blue line), and the CO_2^+ UV doublet (black line) and Cameron bands (red line) limb-integrated profiles, as simulated by the LMD-MGCM. *Bottom*: Differences between the derived temperature profiles and the actual one. The green dashed-dotted lines represent a deviation of ±2.5 K. Reprinted from González-Galindo et al. (2019).

What's worse? Thinking you're being paranoid or knowing you should be?

Shane Carruth

7

Sensitivity studies

Abstract

This chapter goes in depth through the retrieval by analysing its sensitivity to the uncertainty in the forward model parameters and to variations in the *a priori*. A discussion on the total retrieval uncertainties closes the journey for profile #20 of orbit 0330_2. A total uncertainty in the retrieved CO_2 densities between 20% and 35%, depending on the altitude, is estimated.

This chapter extends section 5 of Jiménez-Monferrer et al. (2019).

7.1. Sensitivity to forward model parameters

A series of sensitivity tests were conducted in order to estimate the impact of the known uncertainties in several forward model parameters on the retrieved CO_2. As it is customary, this was done by introducing perturbations in those parameters and observing the changes in the inverted CO_2. The error in the retrieved CO_2, ϵ_i, associated to the uncertainty of a given parameter, ϵ_p, can be described by

$$\epsilon_i = \frac{\partial x}{\partial p}\epsilon_p, \tag{7.1}$$

where x is the target variable of the retrieval and p is the parameter being modified. The partial derivative in Equation 7.1 is actually a matrix of dimension $N \times N$, where N is the number of points in the vertical grid used in the inversion. The changes in the parameter, ∂p, are ideally introduced at one altitude at a time and the changes in density, ∂x, are evaluated at all altitudes. In all the tests performed, $\partial x / \partial p$ is largest at the altitude where the perturbation is introduced. Therefore, for simplicity and to accelerate the calculation, in this study we introduced perturbations for the entire altitude range simultaneously.

We present here both random and systematic uncertainties. A note regarding the systematic errors is convenient. The most important sources of these errors are related to the pointing and to the observed spectral shifts. These were addressed (corrected) during the calibration and preprocessing of the observations (see Chapter 4). Such a correction is not perfect and it is the remaining component after these corrections what is named here as systematic error, and it is assumed to portrait an stochastic nature. In this work, we consider all the parameter errors, ϵ_i, as independent and therefore can be combined quadratically, together with the noise error component, ϵ_{noi}, to obtain the total error, ϵ_{tot}.

$$\epsilon_{tot}^2 = \sum_i \epsilon_i^2 + \epsilon_{noi}^2 \tag{7.2}$$

Table 7.1 summarises the perturbations in the most relevant parameters that were identified and studied for profile #20 of orbit 0330_2. The retrieved densities for all these perturbations were compared with the nominal inversion, `NOM`, to obtain the values, ∂x, in Equation 7.1. The contributions of all the individual sensitivity tests to the total retrieval uncertainty and a global discussion is presented next and in Section 7.3.

For clarity, the sensitivity retrievals are grouped in five categories.

Perturbations in the reference temperature profile

A first group of tests was focused on the perturbations in the atmospheric thermal structure, which was extracted from the LMD-MGCM (González-Galindo et al., 2015) for Martian Year 27. A complete description of the model and the profiles can be found in Section 1.5 and Chapter 4. To perturb this variable, we used the maximum of the GCM-supplied uncertainties in temperature and of the uncertainty obtained in the derivation of the temperature assuming hydrostatic equilibrium (Figure 6.2). This criterion, applied to the profile #20, implies that the temperature is decreased and increased by 15 K at all altitudes (tests `TMP1` and `TMP2`, respectively, in Table 7.1).

Sensitivity tests		
Test	**Perturbed parameter**	**Notes**
`NOM`	nominal	prof#20 (0330_2)
`TMP1`	GCM temperature profile decreased, 15 K	$T_{GCM} - 15$ K
`TMP2`	GCM temperature profile increased, 15 K	$T_{GCM} + 15$ K
`SHF1`	radiance offset, -2.5×10^{-5} $Wm^{-2}sr^{-1}\mu m^{-1}$	$-1/2$ $stderr_{TOA}$
`SHF2`	radiance offset, $+2.5 \times 10^{-5}$ $Wm^{-2}sr^{-1}\mu m^{-1}$	$+1/2$ $stderr_{TOA}$
`SHF3`	pointing offset, $-1/4 \times$ FoV	-0.84 km
`SHF4`	pointing offset, $+1/4 \times$ FoV	$+0.84$ km
`SHF5`	spectral shift, $-1/5$ spectel	-2 cm^{-1}
`SHF6`	spectral shift, $+1/5$ spectel	$+2$ cm^{-1}
`SFL`	solar flux increased by 1%	sf $\times 1.01$
`IGN1`	instrumental gain decreased by 10%	gain $\div 1.10$
`IGN2`	instrumental gain increased by 10%	gain $\times 1.10$
`FOV1`	instantaneous field of view decreased to 1.0 mrad	$iFOV_{nom} = 1.2$ mrad
`FOV2`	instantaneous field of view increased to 1.4 mrad	$iFoV_{nom} = 1.2$ mrad
`ILS1`	FWHM (ILS) decreased to 25 nm	$FWHM_{nom} = 27$ nm
`ILS2`	FWHM (ILS) increased to 29 nm	$FWHM_{nom} = 27$ nm
`KVV1`	collisional rate halved	$k_{VV} \times 0.50$
`KVV2`	collisional rate doubled	$k_{VV} \times 2.00$

Table 7.1: Summary of the perturbed parameters for the sensitivity tests presented in this work. See text for details.

Shifts in measured radiance, pointing and spectral calibration

Three parameter errors associated to the data acquisition were explored. First, in tests `SHF1` and `SHF2` the radiance profile was, respectively, reduced and increased by half of the standard error of the mean at the TOA, approximately $5{\times}10^{-5}$ $Wm^{-2}sr^{-1}\mu m^{-1}$. This was included at all altitudes in order to account for possible radiometric calibration biases and for the uncertainty in the space offset. Secondly, all spectra were shifted in altitude to estimate the effects of possible misalignment in pointing (cases `SHF3` and `SHF4`). The offset was chosen to be ±0.25 times the field of view projected at the tangent point and expressed in kilometres.

This is because we repeated the retrieval three times, one for the nominal pointing and two with offsets in the nominal pointing of ±0.5 times the field of view, and then chose the inversion giving the best fit. And third, regarding the spectral calibration (tests `SHF5` and `SHF6`), we assumed an accuracy of 1/5 of the spectel width, approximately $\pm 2\,\mathrm{cm}^{-1}$, following the description in Bibring et al. (2004b) for the ground calibration goals of the OMEGA instrument.

Sensitivity to the solar flux and to the instrumental Gain

According to the recent inversion of CO_2 densities in Earth's mesosphere from MIPAS observations by Jurado-Navarro (2015), an uncertainty of 1% in the solar fluxes may be considered conservative around $4.3\,\mu$m. Here we assumed a solar flux 1% larger than the nominal one (test `SFL`). On the other hand, regarding the instrumental Gain, we made an assumption based on several ideas discussed by Bibring et al. (2004b) and Vincendon et al. (2015, and personal communication), and on comparisons with TES (Thermal Emission Spectrometer, on board Mars Global Surveyor). Before delivery, the photometric calibration goal was to achieve an accuracy better than 1% spectel-to-spectel (relative) and better than 20% in absolute terms. However, this last value seems very conservative because, when compared to TES, OMEGA shows a gain accuracy better than 3% in absolute terms in a nadir geometry (Vincendon et al., 2015). Tests `IGN1` and `IGN2` in Table 7.1 implement an intermediate instrumental Gain uncertainty of ± 10%.

Figure 7.1 shows the retrieved densities for tests `SHF3`, `SHF6`, `TMP1` and `IGN1`. These four perturbations are among the most important of the whole set of sensitivity tests, as pointed in Table 7.2. Each one produces a relative variation in the retrieved density up to 20%.

Sensitivity to the FoV and to the ILS

Retrievals were done by perturbing the spatial and spectral resolutions. For the first of these studies, labelled `FOV1` and `FOV2`, we changed the instantaneous Field of View (FoV) from the nominal 1.2 mrad to 1.0 mrad and 1.4 mrad, respectively. These variations follow the suggestions of Bonello et al. (2005) and Bellucci et al. (2006), during their study of the OMEGA instrument performance. On the other hand, regarding the Instrumental Line Shape (ILS) and following Bonello et al. (2005), the

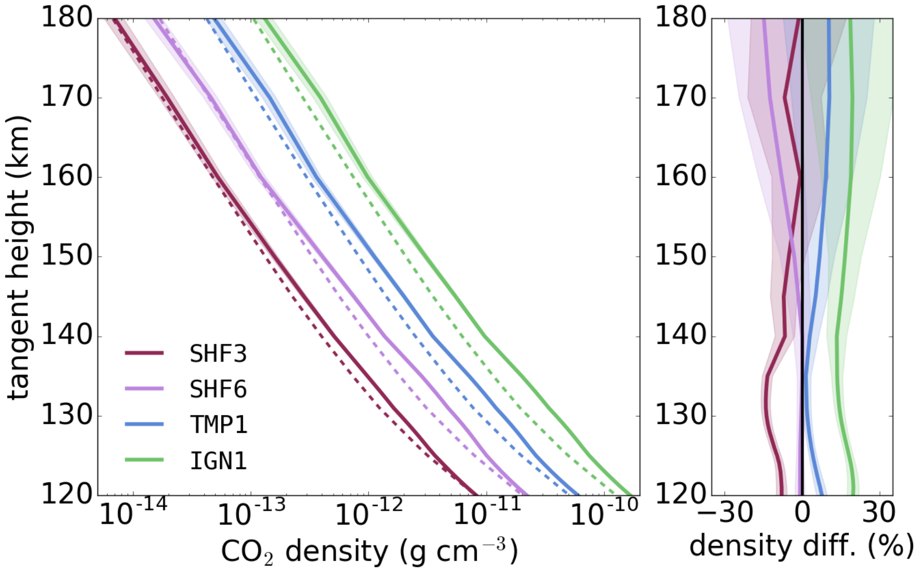

Figure 7.1: *Left*: Retrieved CO_2 density profiles for the four sensitivity tests `SHF3`, `SHF6`, `TMP1` and `IGN1`, with their *a priori* (dashed) and noise (shaded). Except for `SHF3`, the profiles are shifted for clarity. *Right*: Relative differences with respect to `NOM`.

FWHM of the ILS was decreased from 27 nm to 25 nm in `ILS1` and increased to 29 nm in `ILS2`.

Sensitivity to variations in the collisional rates

In the last group of perturbations, we introduced variations in some vibrational-vibrational collisional rates of the non-LTE model (part of the forward model). Tests `KVV1` and `KVV2` include perturbations (up and down) by a factor 2 in the exchanges of one v_3 quanta among vibrational states of the same and/or different CO_2 isotopes. This collisional process can be described as

$$CO_2 + CO_2(\nu_3) \rightleftharpoons CO_2(001) + CO_2(\nu_3 - 1) + \Delta E, \tag{7.3}$$

where ΔE is a small amount of vibrational energy released during the collision.

Although the number of possible perturbations that can be introduced in the non-LTE model is very large, this V-V collisional exchange was expected to give the largest uncertainty and impact. However, our retrievals showed that the impact on the retrieved CO_2 of these changes is very small. Other collisional processes were also examined in detail, confirming their negligible contribution to the total error.

The best fit for the radiance after each of the sensitivity tests is similar to the nominal case and is not shown for that reason. No large differences are expected because of the compensation of the CO_2 abundance introduced by the retrieval process. When a larger value of the radiance is needed, the resulting retrieval tends to provide more CO_2 to match the observed spectra, and vice versa.

7.2. Sensitivity to *a priori* CO_2 abundances

To test the retrieval sensitivity to this input parameter, we performed two retrievals of profile #20 of orbit 0330_2 with two very different *a priori* density profiles, those for orbits 0044_1 and 0647_1, as extracted from the LMD-MGCM at their given locations. The abundances obtained in the inversions are shown in figures 7.2 and 7.3, respectively, compared to the nominal retrieval (see Chapter 5). The volume mixing ratio is shown instead of the density for an easier comparison.

In the case of 0044_1, corresponding to a quite denser atmosphere, the retrieved abundances are slightly larger than in the nominal case, but only at the highest altitudes. As can be seen in the right panel of Figure 7.2, the relative differences between the nominal and the modified *a priori* profiles is about 50% in the 120-180 km range, but the retrieved CO_2 remains fairly the same (within the noise error uncertainties, smaller than 10%), and very close to the nominal retrieval.

When the more rarefied 0647_1 atmosphere is assumed as the *a priori*, the retrieved abundances are slightly below those of the nominal case, but clearly within the uncertainty values, with maximum deviations of about 2% in the entire interval of altitudes.

This result of a low sensitivity to the *a priori* was observed in all the converged retrieved that were analysed.

7.3. Total retrieval uncertainties

Table 7.2 summarises the most relevant sensitivity tests performed and their impact in the total uncertainty matrix at 120, 140, 160 and

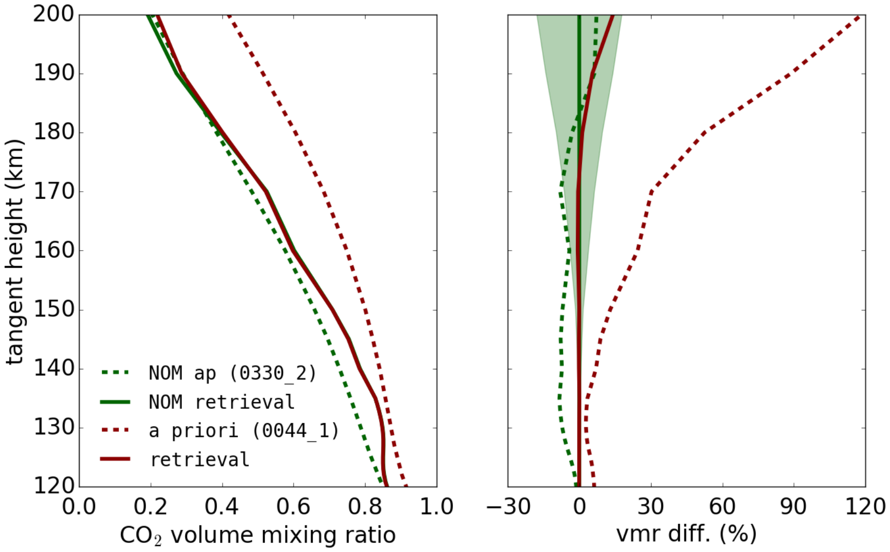

Figure 7.2: *Left*: *A priori* (dashed red) and retrieved (solid red) CO$_2$ profiles considering the atmospheric conditions corresponding to orbit 0044_1, compared to the *a priori* (dashed green) and retrieved (solid green) CO$_2$ for the nominal case. *Right*: Relative differences with respect to the nominal retrieved CO$_2$. The noise error computed for the nominal case is shown as a shaded region.

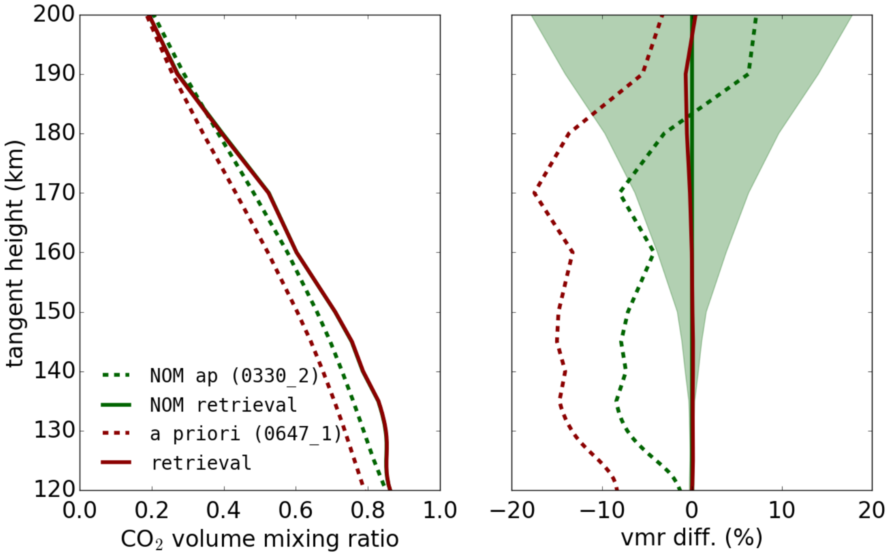

Figure 7.3: Same as Figure 7.2 but considering the atmospheric conditions corresponding to orbit 0647_1.

180 km. The noise error, directly obtained during the retrieval process, is also added to the table and to the total uncertainty. Both positive and negative errors are listed, although in most cases they are approximately symmetric. When they are not symmetric, the mean of their absolute values is taken in the computation of the total error. As mentioned above, all the perturbations in the table were considered to be independent to each other, and thus they were quadratically combined to obtain the total values.

Sensitivity results						
Parameter	**Uncertainty**	**Related tests**	**@120 km**	**@140 km**	**@160 km**	**@180 km**
GCM temperature	±15 K	`TMP1` and `TMP2`	−6% +8%	−3.5% +3%	−8% +9%	−9% +10%
radiometric calibration	±1/2 $\text{stderr}_{\text{TOA}}$	`SHF1` and `SHF2`	±0.1%	±0.3%	±1.7%	+3.4% −3.2%
pointing	±1/4 FOV	`SHF3` and `SHF4`	+5% −8%	**+15%** **−7%**	+18% −0.7%	+20% −1.2%
spectral calibration	±2 cm^{-1}	`SHF5` and `SHF6`	−0.8% −0.3%	+0.1% −0.7%	−8% +7%	**−15%** **+16%**
solar flux	±1%	`SFL`	∓1.7%	∓1.2%	∓1.8%	∓1.8%
instrumental gain	±10%	`IGN1` and `IGN2`	**−16%** **+20%**	**−12%** **+14%**	**−17%** **+19%**	**−16%** **+19%**
instantaneous field of view	±0.2 mrad	`FOV1` and `FOV2`	∓0.6%	+0% +0.2%	−0.1% +0%	∓0.1%
instrumental line shape	±2 nm	`ILS1` and `ILS2`	+1.4% −1.6%	+0.6% −0.7%	±0.3%	+0.7% −0.8%
collisional rate	÷/× 2.0	`KVV1` and `KVV2`	+1.8% −1.0%	−0.5% +0.3%	−1.0% +0.7%	−0.8% +0.6%
noise error	-	`NOM`	±1.9%	±3.4%	±10%	**±16%**
total error	-	-	±**20**%	±**18**%	±**27**%	±**33**%

Table 7.2: Summary of the sensitivity tests and their impact on the total uncertainties at tangent heights 120, 140, 160 and 180 km. The percentage of variation is obtained for each sensitivity test by comparing the retrieved densities with those of the nominal case, at the indicated tangent altitudes. The dominant parameters at each altitude are highlighted in red.

In the lower thermosphere, below 150 km, the most relevant uncertainties arise from the instrumental gain and the pointing, with moderate values, around 20% for the worst case. The selection of the input temperature is also important in this region. Since CO_2 presents its strongest emission at these altitudes, the measurement noise has a minor impact. At higher tangent heights, above 150 km, the noise error dominates, together with the instrumental gain, over the rest of uncertainties. In the upper thermosphere, the spectral calibration and, to a small extent, the pointing and the input temperature, become also important.

In general, except at the higher thermosphere, the influence of the uncertainties associated to the input temperature can be considered as minor. This, together with the small sensitivity to the *a priori* CO_2 abundance, reinforces the confidence on the retrieval scheme presented in this work. In addition, the possible remaining radiometric offset has a rather low impact on the retrieval after the corrections introduced (see Chapter 4). The inversion also shows robustness against unknown variations in the determination of the field of view, the instrumental line shape, the solar flux variability, and the non-LTE collisional rates.

Have you ever thought you would like to be a man?

Isaac Asimov

8

Comparison with models and previous measurements

Abstract

In this chapter we compare the results of the inversions to the LMD-MGCM, including extreme climatic scenarios, for both atmospheric dust and solar forcing. We also inspect particular regions of the planet, where more observations are available, allowing for spatial or temporal studies. Then we compare our retrievals with previous measurements by other instruments sounding the upper atmosphere of Mars, finding consistency in both variability and total error obtained. For one of them, ExoMars TGO, we present a demonstration consisting on simulations for solar occultation geometries, and recent spectra obtained by the NOMAD LNO channel in the limb.

8.1. Comparison with the LMD-MGCM

In this section, we compare our results to the LMD-MGCM. This is a widely validated self-consistent description of the whole atmospheric range, from the ground to the exobase, has a user-friendly access and permits custom runs. In addition, our team at the IAA actively participates in its development and we are therefore familiar with its performance, merits and limitations. There are, however, other Martian GCMs which permit simulations of the upper Martian atmosphere and which deserve to be mentioned at this point.

- Coupled MGCM-MTGCM. This model is formed by the coupling of to independent models, a lower-atmosphere code, the NASA Ames Mars MGCM (Haberle et al., 1999), and a code specially developed for the upper atmosphere, the Mars Thermospheric General Circulation Model of NCAR-Michigan University (Bougher et al., 2006). The non-LTE 15 μm cooling scheme is implemented in this model based upon detailed 1-D non-LTE calculations for the Mars atmosphere (López-Valverde et al., 1998). The primary limitation of the coupled MGCM-MTGCM framework is that linking two separate codes across an interface is not seamless. This is being addressed by the ongoing development and validation of a new framework from the ground to the exosphere, the Mars Global Ionosphere-Thermosphere Model, M-GITM (Bougher et al., 2015).
- UCL MarsTIM. The University College London Martian Thermosphere Ionosphere Model is based on a previous GCM for the thermosphere of Titan (Müller-Wodarg et al., 2000). The energy balance in the model includes the IR heating and cooling rates in non-LTE, calculated following López-Valverde and López-Puertas (2001).
- Canadian GM3. The Global Mars Multiscale Model of York University, Toronto (Moudden and McConnell, 2005) is the adaptation to Mars of the Global Environmental Multiscale (GEM) model, developed at the Meteorological Service of Canada for weather forecasting purposes. This model reaches 160 km and, in the upper atmosphere, non-LTE effects are taken into account using the parametrisation developed by López-Valverde and López-Puertas (2001).
- Max Planck Institute GCM. This redesigned version of the terrestrial Cologne Model of the Middle Atmosphere (Hartogh et al., 2005; Medvedev and Yiğit, 2012) extends also up to 160 km. In the upper atmosphere, an optimised version of the exact non-LTE code of Kutepov et al. (1998) and Gusev and Kutepov (2003), employing the method of accelerated lambda inversion, is implemented.

In addition to the 15-μm cooling rate parametrisation, other factors of relevance at thermospheric altitudes are also different among these models. Notably, their assumptions on escape, diffusion, gravity wave propagation and UV solar absorption efficiency.

A dedicated effort to perform an ambitious comparison among all these codes is missing (López-Valverde et al., 2018; Bougher et al., 2018). However, a couple of quantitative comparisons were performed in the past. One of them is the study by González-Galindo et al. (2010), devoted to compare the global simulations of thermal and wind fields at thermospheric altitudes between the LMD-MGCM and the MTGCM of the Michigan University. This study found significant differences locally, likely due to the dust loading of the lower atmosphere and to the upward propagation of waves. A second study, by Medvedev et al. (2015), tried to shed light on the comparative cooling by radiation (CO_2 emission to space at $15\,\mu$m) versus gravity wave dissipation at thermospheric altitudes. They concluded these two cooling sources needed a revision in order to reproduce the cold temperatures found by SPICAM in the lower atmosphere (Forget et al., 2009). One possibility to increase the CO_2 cooling is by augmenting the amount of atomic oxygen in the simulations. The ways to increase the gravity wave cooling were not clear, but a review of its current parametrisation in GCMs is possibly needed.

8.1.1. Cautions and limitations

The distribution of the OMEGA limb observations analysed (Figure 3.3 and Table 3.2) is far from ideal for a complete study of the thermosphere of Mars. However, direct comparisons with General Circulation Models are always possible given their usually fine grid. In addition, the total number of OMEGA observations permit some statistical evaluation of the goodness of the retrievals, and to suggest possible future extensions to identify discrepancies with the model.

Also, it is possible to determine a few special locations where a significant amount of OMEGA data do permit the analysis of spatial and temporal trends and variations. This will be discussed in Section 8.1.4.

Besides the coverage limitation, the comparison to a Global Circulation Model and/or instruments cannot be considered faultless for two additional reasons. On the one hand, we do not know the thermal structure below 120 km, because our retrievals are restricted to the Martian thermosphere. As stated in previous chapters, the thermosphere is coupled to the lower layers, so the lack of information below 120 km imposes an important limitation. On the other hand, the amount and distribution of the suspended dust is also unknown, and this is a major factor leading to variability in the Martian atmosphere.

An important consideration when comparing data with models is to take into account their uncertainties. Regarding the LMD-MGCM, two sources of uncertainty were considered. First, the interpolation from the grid points of the model to the actual location and time of the observations. Since the model grid and time steps are small and the variations between adjacent points are usually linear, our linear interpolation is believed to introduce only marginal errors. The second source is the inherent uncertainty associated to the model results (Lewis et al., 1999). The gridded values of the model are averages in time and space, and therefore they hide small scale variability and sub-grid processes, besides the inclusion of an approximate treatment of all the physics implemented. This aspect is expected to produce biases and is the topic of specific validation campaigns, ongoing for about two decades, to correct for them. Regarding the first two sources, averages and small scale variability, both the LMD-MGCM and the MCD supply an estimate of these variations. For our purposes, these outputs of the model can be used as an estimate of its numerical uncertainty, and will be used below, labelled as standard deviation.

8.1.2. Global analysis of densities and temperatures

Figure 8.1 shows bulk statistics of CO_2 densities and temperatures at four different tangent heights (130, 140, 150 and 160 km), for both the LMD-MGCM and our CO_2 retrievals, shown in absolute values and as vmr, including our temperature derivation. The figure presents histograms of CO_2 density, CO_2 vmr and temperature, to represent the number of occurrences of different values in the total set of 47 orbits.

As can be seen in Figure 8.1, the retrieved CO_2 is, in general, in good agreement with the model at 130 km, but presents larger densities above that tangent altitude. This difference is ~ 1 histogram bin in the density axis. With five bins per decade and the log scale used, one bin means an increase by $\sim 60\%$ with respect to the previous bin. This is significant as it is twice the total uncertainty in the retrieved CO_2 (see Chapter 7).

The results in vmr show also a kind of OMEGA-GCM good agreement at 130 km but, contrary to the absolute densities, the vmr do not present any clear difference at higher altitudes, which is the result of two factors. First, the combination of retrieved CO_2 and of minor species from the model, as used to build our OMEGA CO_2 vmr; second and more important, the fact that the vmr maintains a relatively high value at all altitudes, which limits its dispersion.

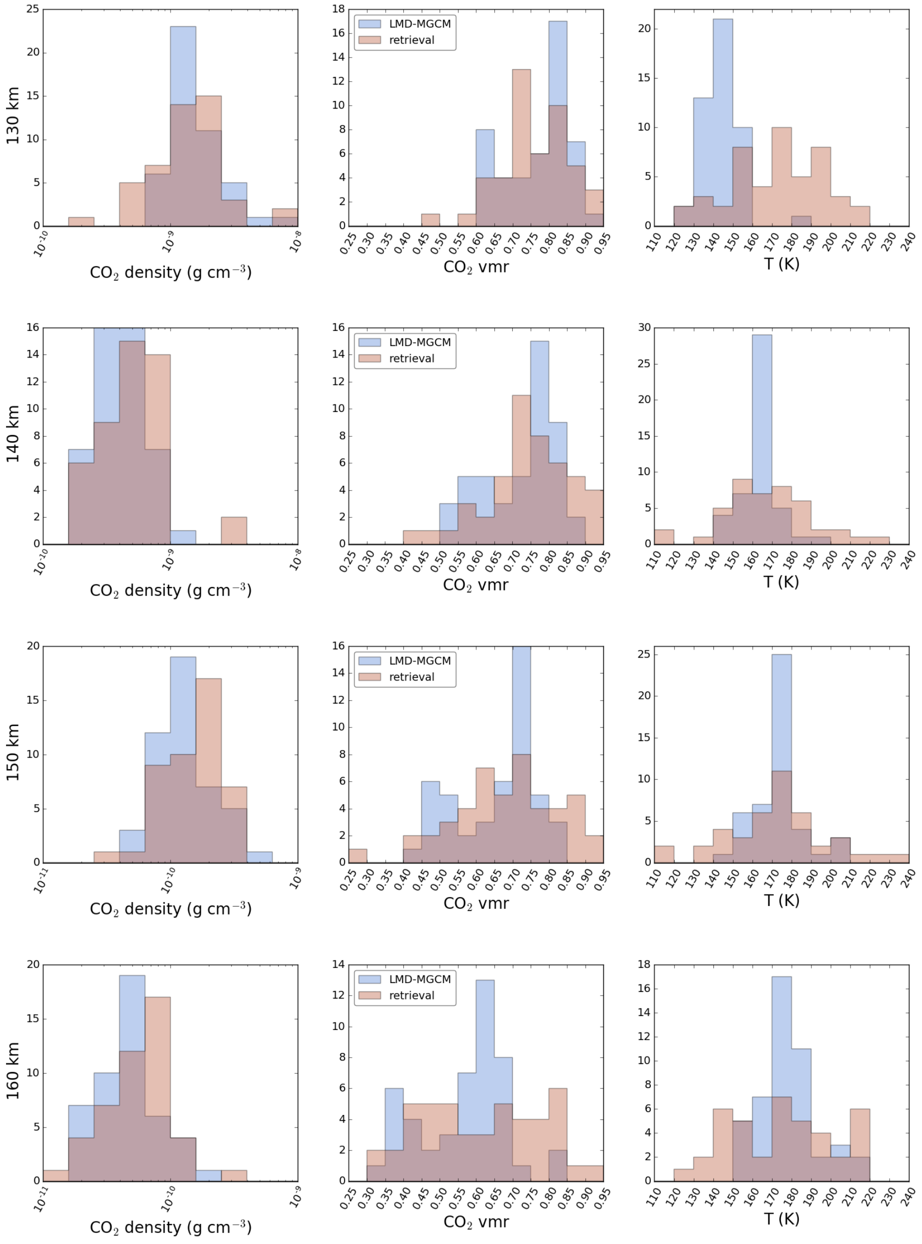

Figure 8.1: Histogram of CO$_2$ densities, CO$_2$ vmr and temperatures from the LMD-MGCM (blue) and our retrievals (red) at four different tangent heights (130, 140, 150 and 160 km). The vertical axis accounts for the number of individual occurrences, of the total 47 OMEGA orbits, in each interval. See text for details.

Regarding the temperature, our retrievals at 130 km are considerably warmer than the model, due to the large gradient introduced by the strong regularisation below 120 km, as shown in Chapter 6. At higher altitudes, the agreement OMEGA-GCM is better, considering our temperature errors, typically 20–30 K. In addition, above 130 km, we observe in the model a clearly dominant temperature bin at each altitude, while this single-bin structure is absent in the OMEGA temperatures. This dispersion in the OMEGA temperatures, much larger than in the GCM, is interesting if we notice the good agreement in the CO_2 densities, both values and dispersion. It is possible that the GCM is capturing well the atmospheric variability in density but not so well in temperature at thermospheric altitudes.

We computed the relative differences between our OMEGA results and the model (data-model, normalised with respect to the model) for the whole OMEGA dataset. The mean results are shown in Table 8.1. As expected, these values coincide with and highlight the previous results and discussion. Starting with the CO_2 absolute densities, there is a positive bias when compared to the LMD-MGCM above 130 km, being, on average, 30%–50% larger. These values are significantly larger than our CO_2 total error, although the small increase, from 30% to 50%, may be related to the larger weight of the error noise at higher altitudes (Chapter 7). The relative differences are smaller in the vmr than in the temperature for the reasons aforementioned. In the case of the temperatures, the 5% difference above 130 km translates to less than 10 K, which is smaller than the temperature errors, and therefore not much can be concluded from this average.

Looking for some additional insight, we made a graphical visualisa-

	$(\rho - \rho_{\mathsf{GCM}})/\rho_{\mathsf{GCM}}$	$(\mathbf{vmr} - \mathbf{vmr}_{\mathsf{GCM}})/\mathbf{vmr}_{\mathsf{GCM}}$	$(\mathbf{T} - \mathbf{T}_{\mathsf{GCM}})/\mathbf{T}_{\mathsf{GCM}}$
130 km	0.08	−0.01	0.19
140 km	0.36	0.04	0.04
150 km	0.46	0.04	0.04
160 km	0.51	0.03	0.05

Table 8.1: Averaged relative differences between the results and the LMD-MGCM at four tangent altitudes (first column), for CO_2 densities (second column), for CO_2 abundances (third column), and for atmospheric temperatures (fourth column).

tion of the OMEGA-GCM comparison in terms of location. From all the possible projections available (see Figure 3.3), we show here the ratios (retrieved/model) as a function of latitude and solar longitude, because most atmospheric variables present their maximum variability with latitude and season. Figures 8.2, 8.3 and 8.4 show the ratios calculated at the aforementioned tangent altitudes, for CO_2 density, CO_2 vmr and temperature, respectively. In this 2-D map, the large dispersion in the 47 orbits creates very large empty spaces, and many orbits, located very close among them, require some careful attention. The inspection of these three figures shows similar results to those found above.

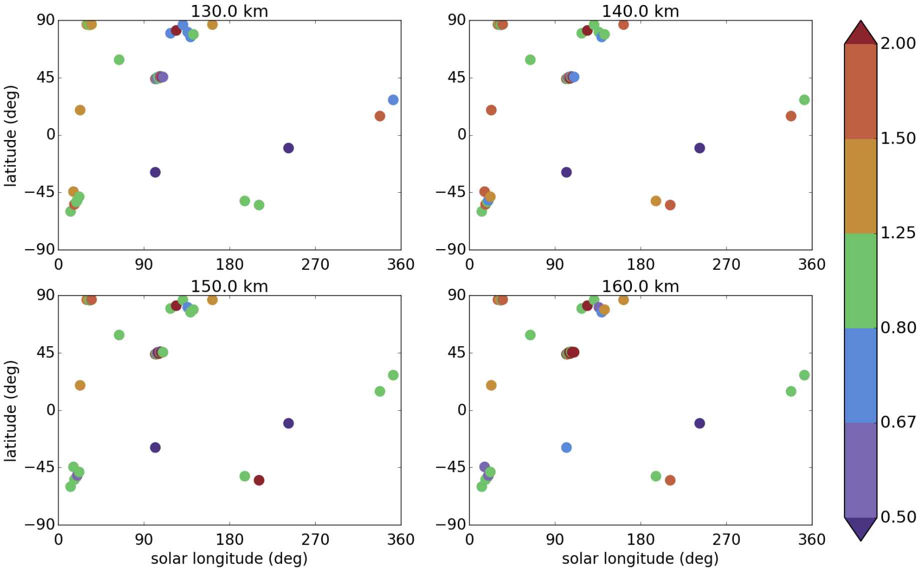

Figure 8.2: CO_2 density ratio (retrieved divided by LMD-MGCM) at four different tangent heights (130, 140, 150 and 160 km) as a function of latitude and solar longitude. Ratios larger than 2 and lower than 1/2 are merged into one colour each.

In addition, in these figures, we see no clear trend in the geographical distribution of the ratios, except, possibly, for the extreme values. The highest ratios tend to appear at high latitudes in northern spring (near aphelion), while the lowest densities (lower than the model) are found at low altitudes. The dispersion in the derived temperature is evident at 160 km, where only a few green points, corresponding to orbits where the derived temperature is within a ±10% interval around the temperature extracted from the model, are found.

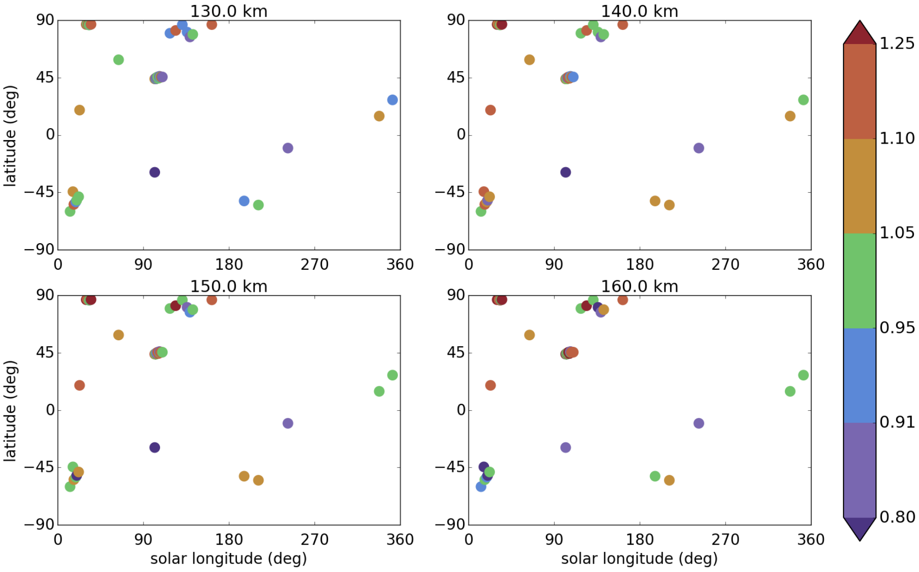

Figure 8.3: Same as Figure 8.2, for the CO_2 relative abundance. Ratios larger than 1.25 and lower than 1/1.25 are merged into one colour each.

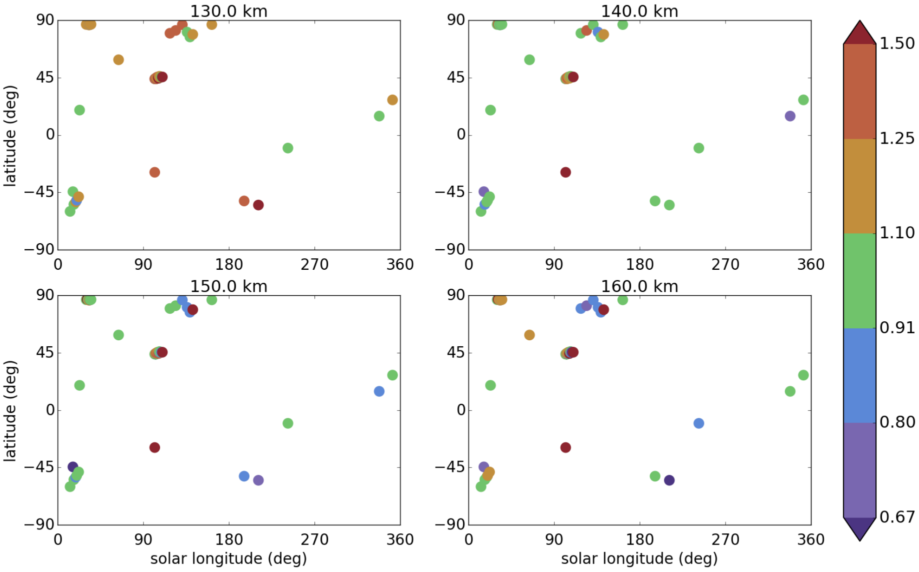

Figure 8.4: Same as Figure 8.2, for the temperature. Ratios larger than 1.5 and lower than 1/1.5 are merged into one colour each. Temperature errors are typically about 15%–25% at most altitudes.

8.1.3. LMD-MGCM and MCD extreme scenarios

In the previous section, we compared the retrieved densities and the derived temperatures presented, respectively, in chapters 5 and 6, to the reference atmospheric profiles from the LMD-MGCM. We now incorporate to the comparison simulations from the LMD-MGCM for extreme solar conditions (*smin* and *smax*), obtaining figures 8.5 and 8.6. A few particular cases were selected to illustrate the heterogeneous casuistry of the complete sample. Orbits 0330_2, 0982_0 and 6126_1 are depicted in Figure 8.5 while 7554_4, 7686_0 and 7718_0 are shown in Figure 8.6. Notice that orbit 0330_2 was already discussed in detail in chapters 5 and 6.

For orbits 0330_2 (Figure 8.5, top) and 7554_4 (Figure 8.6, top) the densities in our nominal retrievals are fairly close to the model, with similar temperatures too. We found, however, profiles with remarkable differences. Some of them are well above model predictions, as is the case of orbits 0982_0 (Figure 8.5, middle), 7686_0 (Figure 8.6, middle) and 7718_0 (Figure 8.6, bottom). On the opposite direction, orbit 6126_1 (Figure 8.5, bottom) shows a density well below that extracted from the model. The differences in the CO_2 density found for both cases (denser and more rarefied atmospheres) are considerable, even comparable to the distance between the *smin* and *smax* profiles. Again, this shows a larger variability in the OMEGA data than in the model, specially in the thermal structure. The *wavy* signatures observed in some temperature plots could be caused by gravity waves, as will be addressed in Section 8.2, where our results are compared to those of other instruments.

Notice the error bars used in figures 8.5 and 8.6 for the OMEGA results represent the standard error of the mean. This quantity was chosen, instead of the standard deviation of the retrievals, because the profiles are almost collocated and the average of the CO_2 densities and of the temperature are expected to reduce the noise. However, the dispersion observed for several orbits is much larger. For example, for orbits 6126_1 (Figure 8.5, bottom) and 7686_0 (Figure 8.6, middle), the density profiles show a large dispersion about 200 km (see Appendix B). Because the density profiles are closer around 160 km (for both orbits), the differences in the density gradient among profiles at these altitudes translate into a large dispersion in temperatures, producing differences as large as 100 K between the minimum and the maximum temperature profiles at 160 km.

Figures 8.5 and 8.6 also bring two interesting issues up. First, the atmospheric conditions extracted from the model for the orbit location

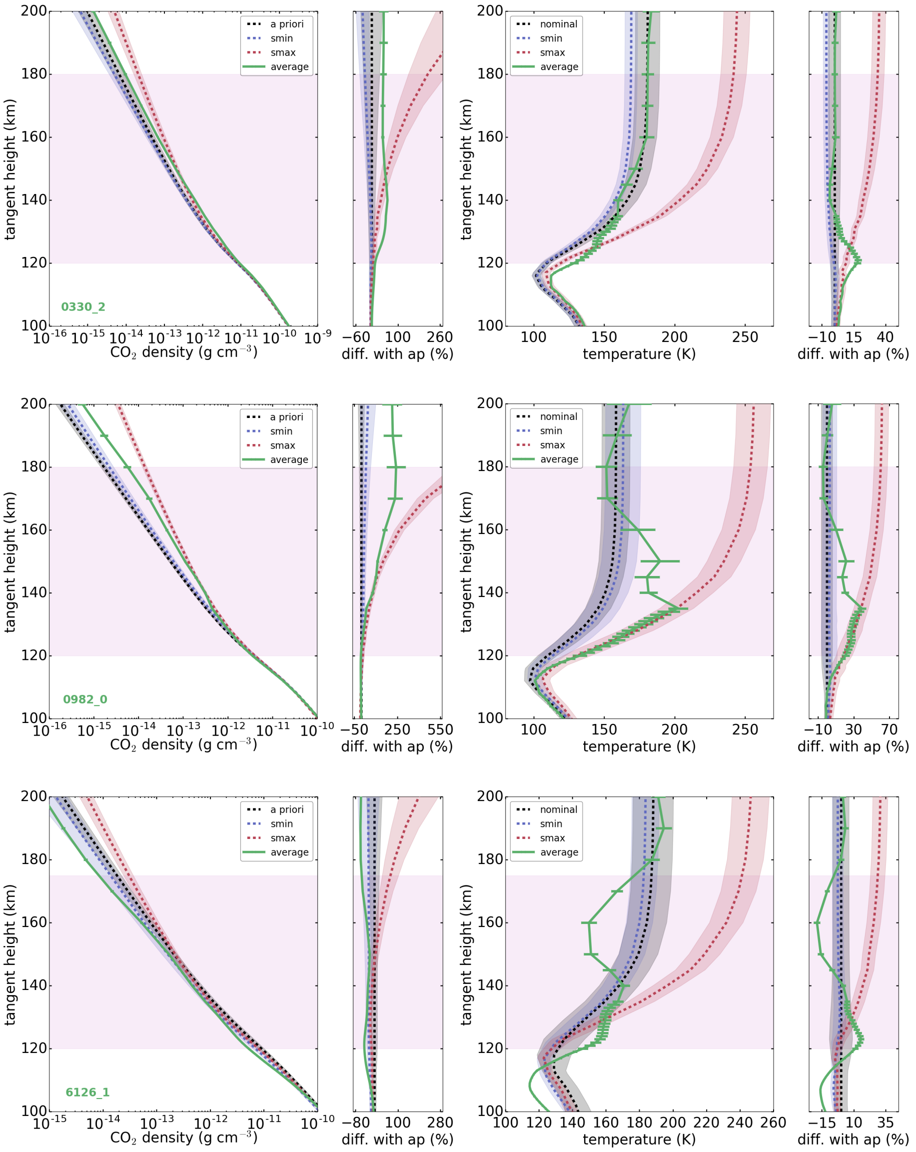

Figure 8.5: *Top left*: Average of all the CO$_2$ density profiles retrieved for orbit 0330_2 compared to the *a priori* of the orbit and to those corresponding to the solar minimum and solar maximum scenarios of the LMD-MGCM. All the profiles from the model include their standard deviation, while the retrieved densities are shown with their standard error. *Top right*: Same for derived temperatures. *Middle*: Same for orbit 0982_0. *Bottom*: Same for orbit 6126_1. See text for details.

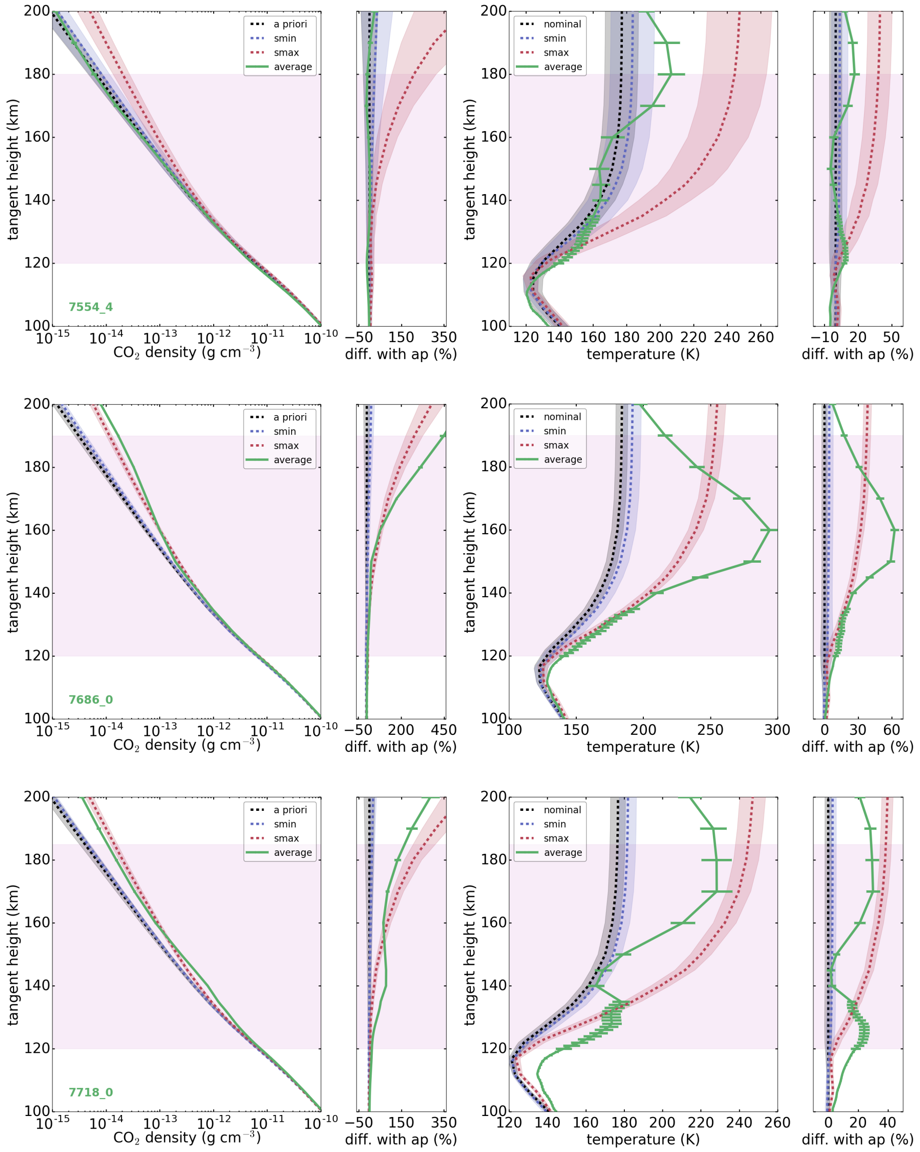

Figure 8.6: Same as Figure 8.5, for orbits 7554_4 (top), 7686_0 (middle) and 7718_0 (bottom).

(dashed black lines) are always closer to the *smin* (dashed blue) than to the *smax* (dashed red). This is a situation expected for the whole selection of orbits, as the datasets analysed in this Thesis (MY26–MY30) correspond to a solar minimum. Secondly, for four of the *qubes* depicted (0982_0, 7554_4, 7686_0 and 7718_0) both the temperature and the density profiles from the model are below the ones corresponding to *smin* conditions. Although this effect is small, or comparable to the model uncertainties, this behaviour was not expected and we analyse it next.

To evaluate how extreme are the *smin* and *smax* scenarios of the LMD-MGCM, we turned to the Mars Climate Database (MCD), version 5.3 (Forget et al., 1999; Millour et al., 2018), through its web interface. The MCD is a climatology derived from two Mars GCMs, the LMD-MGCM and the Oxford Mars GCM, both sharing the same physical package, and both run for a diversity of geophysical scenarios. The results of the MCD should be similar to the LMD-MGCM runs used in this work, and are appropriate for the comparison at hand. In addition, we also looked at other

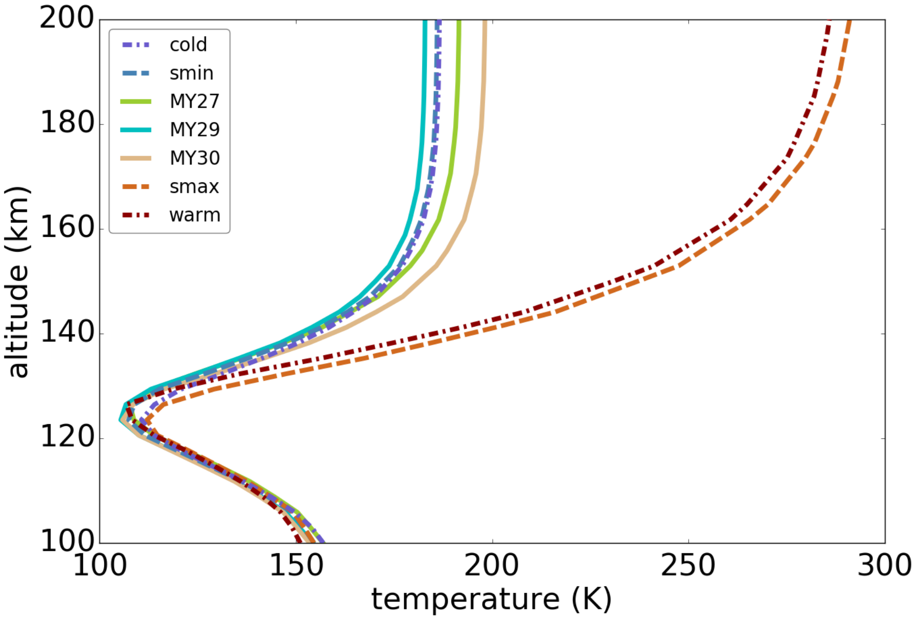

Figure 8.7: Temperatures from the Mars Climate Database, version 5.3. The temperatures computed for years 27, 29 and 30 are shown in solid lines, the MCD scenarios for solar maximum and minimum conditions in dashed lines, and the *cold* and *warm* MCD scenarios in dash-dotted lines.

scenarios of the MCD. Figures 8.7 and 8.8 show the temperature and density profiles, respectively, corresponding to seven MCD runs: three Martian years (27, 29 and 30), the climatology for minimum and maximum solar conditions (*smin* and *smax*), and two scenarios, named *cold* and *warm*, intended to be extreme situations. The *cold* scenario assumes an extremely clear atmosphere with a minimum solar forcing, while the *warm* scenario considers a dusty atmosphere with a maximum solar forcing. All the profiles were extracted for a fixed location, matching none of the selected OMEGA orbits, corresponding to summer in the southern hemisphere, with solar longitude 290 deg, latitude −60 deg, longitude 150 deg, and local time 14 h.

According to figures 8.7 and 8.8, the *smin* and *smax* scenarios in the MCD seem to be slightly more extreme than the *cold* and *warm* scenarios at this specific location. Even the temperature and CO_2 density profiles for Martian Year 29 are below those of the *smin* and *cold* scenarios. This unexpected result, obtained at some locations of the planet, shows the importance of taking into account the standard deviation when performing comparisons.

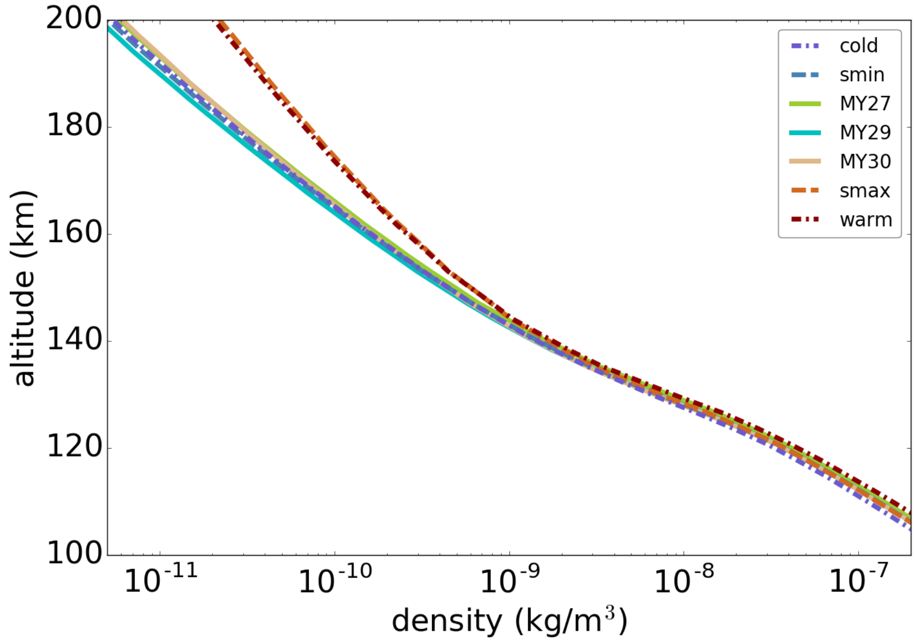

Figure 8.8: Same as Figure 8.7, for densities

8.1.4. Regions of particular interest

As stated before, the poor geographical and temporal coverages of our retrievals impose a strong limitation when investigating for possible trends or when comparing the results with a Global Circulation Model. Ideally, to study the variability with respect to a given parameter, we should compare the retrievals obtained for datasets which are (approximately) homogeneous for the rest of variables. In this section, we focus on locations where observations sharing at least one of their spatial or temporal coordinates are available. These regions are selected in order to focus on those geophysical variables expected to produce the largest variability or, at least, to permit a separate study of the impact of these variables on the retrievals and on their comparison with the Global Circulation Model.

Figure 8.9 shows the six regions selected for this study: longitudinal variability at latitudes ~ 45 deg (a) and ~ 90 deg (b); seasonal variability at latitude ~ -60 deg (c); and latitudinal variability at local time ~ 9 h (d) and at solar longitudes ~ 0 deg (e) and ~ 90 deg (f).

Longitudinal variability (a, b)

First, we evaluated the variations in the retrievals due to changes in longitude. For this, we selected two different fringes with observations sharing a similar latitude (Figure 8.9, a) latitude ~ 45 deg, b) latitude ~ 90 deg). In the upper atmosphere, the dependence of the densities with longitude is normally smaller than the latitudinal and seasonal effects (González-Galindo et al., 2009), with the exception of year-to-year variability, or in the presence of planetary-scale waves (England et al., 2016).

For the first case (latitude ~ 45 deg), the 19 *qubes* are also close in solar longitude (102–110 deg) and local time (~ 9 h), and belong to the same Martian year (MY27). Figure 8.10 shows (i) the densities and (ii) the temperatures extracted from the LMD-MGCM and these obtained from our retrievals, and (iii) their density and (iv) their temperature differences (data-model). The dominant basic variation of the CO_2 density observed in this figure is with altitude, as expected, with lower values at higher altitudes, for both model and measurements, being the variation with altitude similar for both, as discussed in previous sections. Regarding the longitudinal changes, a slowly varying trend with the form of an oscillation is observed in the two density sequences, data and model (i), with two maximum values, around 90 and 270 deg, and two minimum values, around

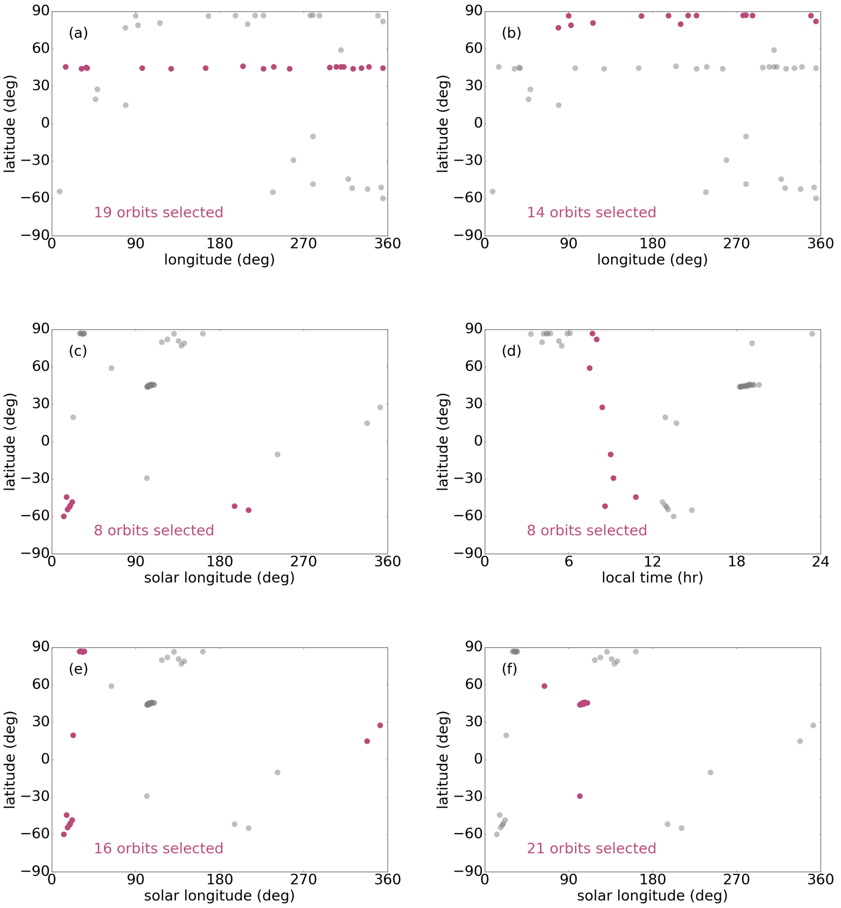

Figure 8.9: Selected orbits for the study of particular regions (non-selected orbits are shown in grey). Notice the distribution of points apparently changes between plots due to the representation of a different horizontal dimension. See text for details.

0 and 180 deg. The temperatures (ii) are affected by a similar pattern, being the OMEGA temperatures, in general, above the climatological ones (iv). According to the data-model differences, we usually obtain lower densities (iii) and larger temperatures (iv) than in the model in the 90 and 250 deg longitude range. Outside this range, the variability found in the data-model differences is too large to obtain any reliable conclusion. On average, a positive bias is obtained for both density and temperature in this case, as can be seen in Table 8.2 at the end of this section.

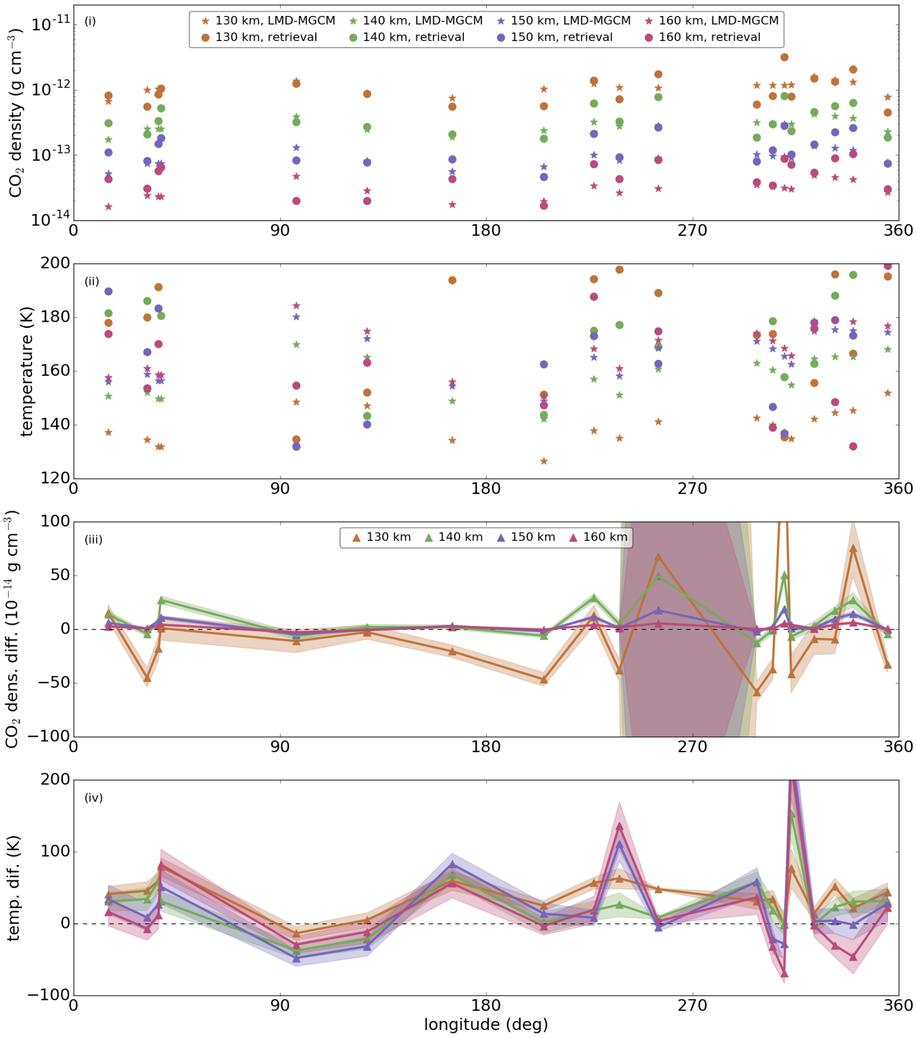

Figure 8.10: Longitudinal variability at latitude ∼ 45 deg in the LMD-MGCM and in the retrievals, for (i) CO$_2$ density, (ii) temperature, (iii) CO$_2$ density difference (data-model), and (iv) temperature difference (data-model). The shaded region in panels (iii) and (iv) represent errors of the differences (summation of the standard deviation for the LMD-MGCM and the standard error for the results). The huge error found at 255 deg longitude in panel (iii) is due to an enormous uncertainty in the pressure of the LMD-MGCM for orbit 0961_0.

The second case (latitude ∼ 90 deg) is formed by 14 orbits and is shown in Figure 8.11. Unfortunately, they are distributed between spring and summer in the northern hemisphere, with very diverse local times, and correspond to Martian years 27, 29 and 30, making their comparison a hard task. Similar oscillatory trends to those around latitude 45 deg are observed in Figure 8.11. In this case, the OMEGA temperatures are equally and quasy-randomly distributed above and below the climatology.

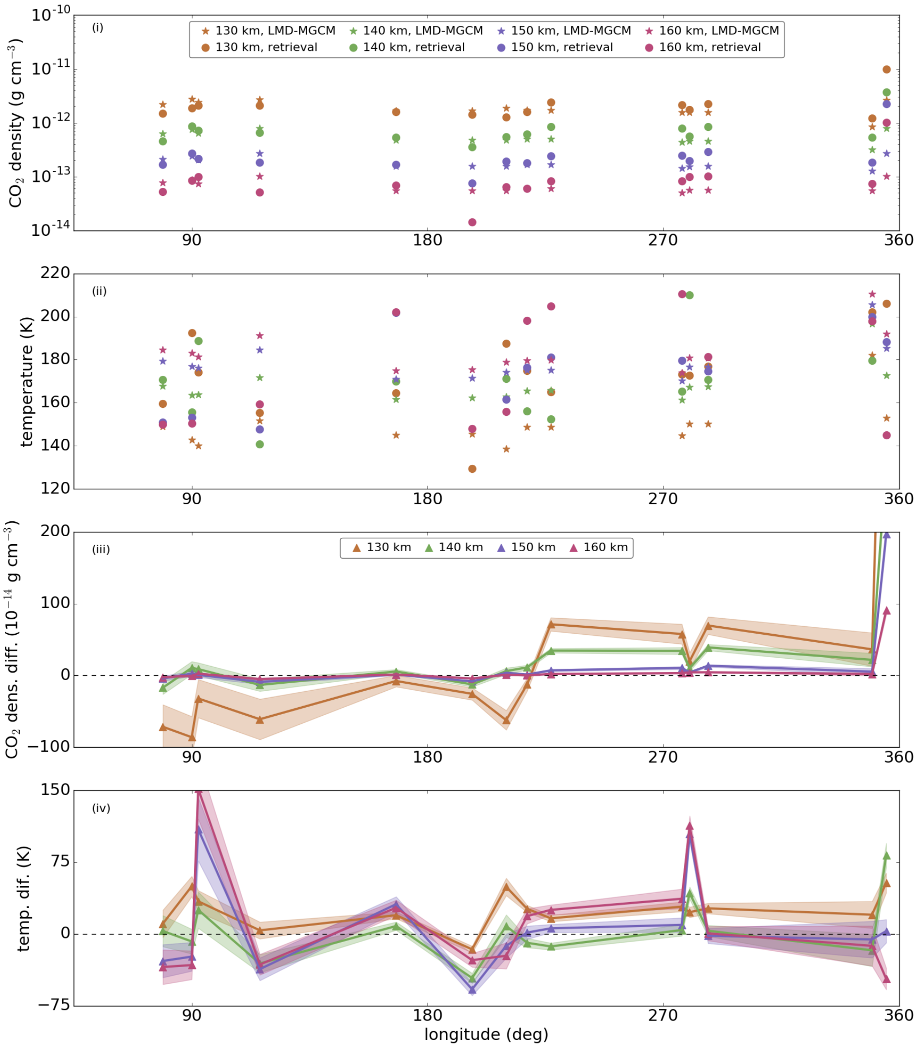

Figure 8.11: Same as Figure 8.10, for the longitudinal variability at latitude ∼ 90 deg.

Seasonal variability (c)

For this analysis, we selected 8 orbits located at similar latitudes (~ -60 deg) in the southern hemisphere, but at different seasons, 6 of them during fall and the other 2 during spring. Figure 8.9 (c) shows the location of the 8 measurements. The local time of the observations varies from 8.6 to 14.8 h.

The data-model comparison of this case study is shown in Figure 8.12, where the x-axis is broken to focus on the two relevant seasons. Again, there is a good overall agreement for the CO_2 abundances (i), once their errors are considered. In particular, the altitude variation seems to match very well. Regarding the seasonal variation, the densities in the southern spring are above those during fall, for both model and retrievals, by about 50%. This is not, however, a large effect, specially compared to our density error and the model uncertainties, and to the variations obtained within each season, also about 50%. In addition, the number of points in the spring side is unfortunately small for a robust statistical conclusion. With respect to the temperature (ii), the agreement is not as good as for the CO_2 density, but is, in general, within the uncertainty brackets. No clear trend can be observed for the seasonal effect, given the large dispersion of one of the only two orbits available in spring.

Latitudinal variability (d)

Here we chose the latitude as the varying geographical parameter, isolating the measurements observed at a similar local time ($\sim$ 9 h). The selection can be seen in Figure 8.9 (d). The 8 orbits selected do not correspond to any delimited longitudinal or seasonal location, and hence the observed variability cannot be linked to latitudinal changes with certainty.

Figure 8.13 shows densities and temperatures along the latitudinal dimension. First, data and model agree very well, both in absolute values and in the altitude and latitude variations. Regarding these ones, it is difficult to draw any clear trend, as the differences are not very large, given the data and model uncertainties. Also, the coverage is not very good, with just 8 points available.

Latitudinal variability (e, f)

We studied the variability in latitude, considering observations taken at a similar time of the Martian year, making tow groups: solar longitude

~ 0 deg in Figure 8.9 (e), and solar longitude ~ 90 deg in Figure 8.9 (f).

Unfortunately, the 16 orbits contained in the first latitudinal group (with solar longitude ~ 0 deg) do not have any other temporal or spatial overlap, i.e., they have a diversity of local times, longitudes and Martian

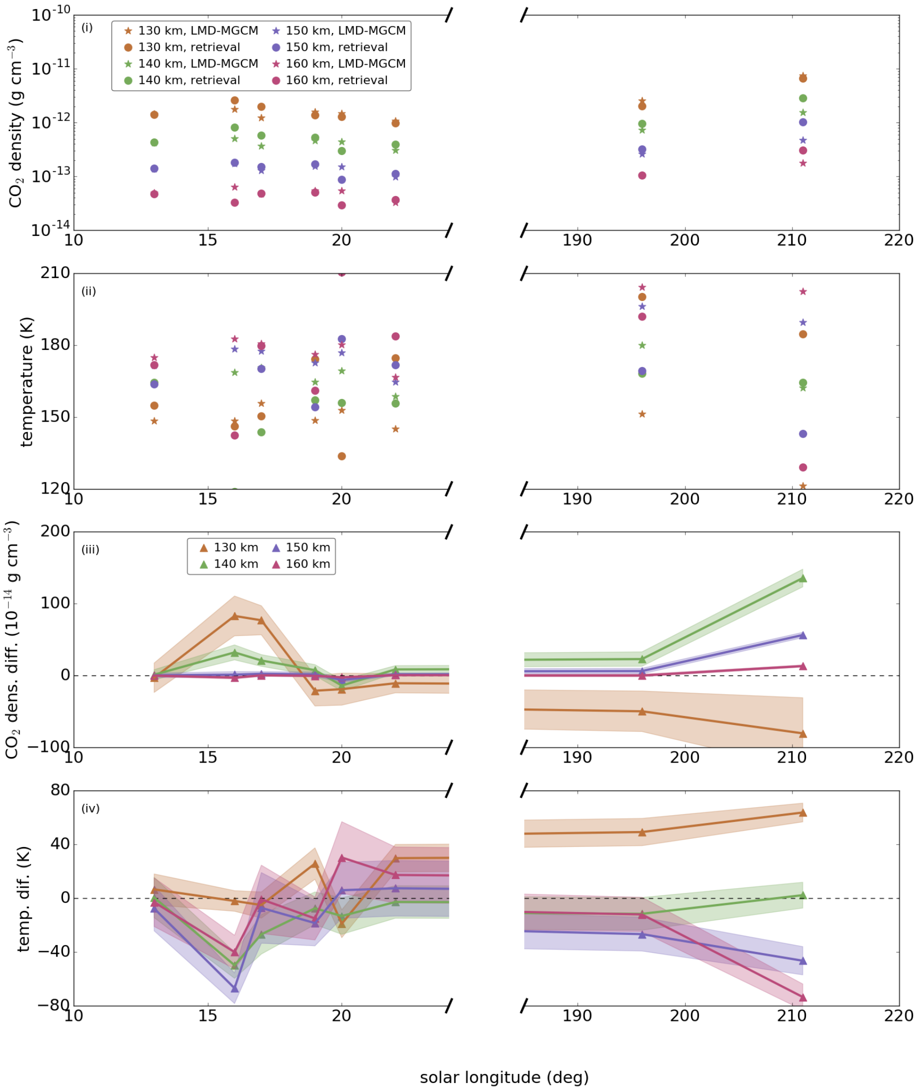

Figure 8.12: Same as Figure 8.10, for the seasonal variability at latitude ~ -60 deg. Data corresponding to fall and spring in the southern hemisphere are located, respectively, left and right of the broken x-axis.

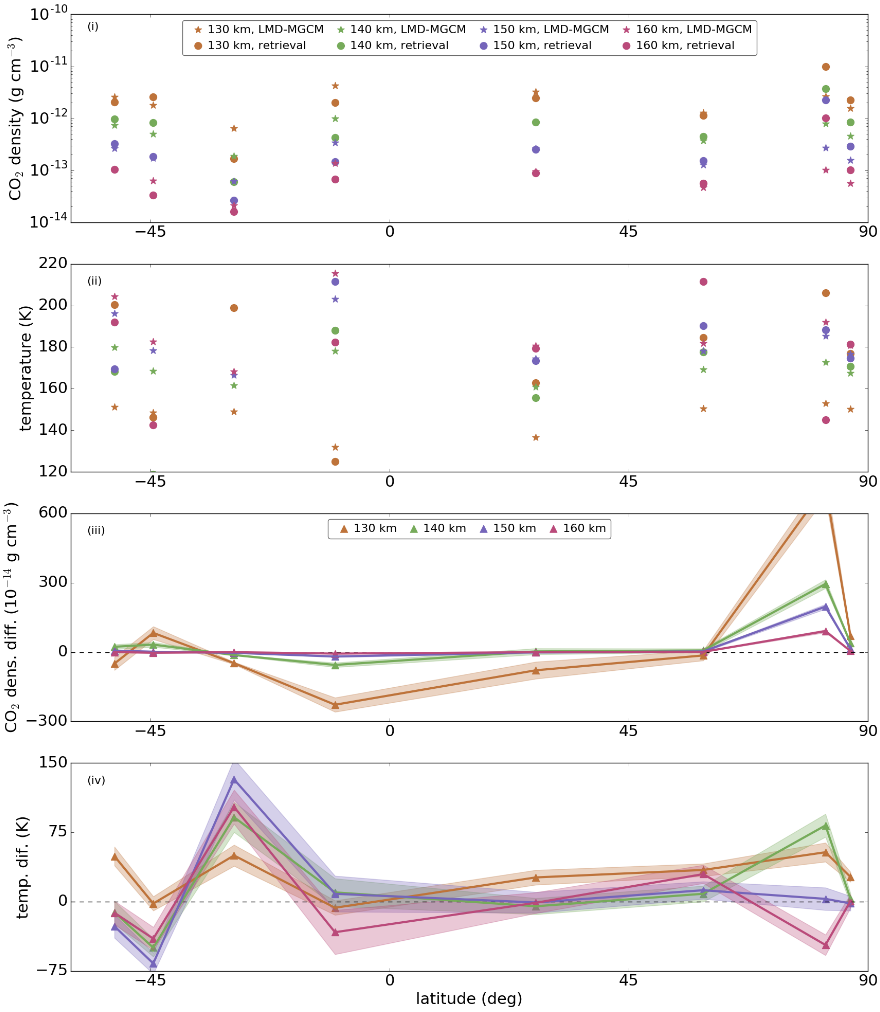

Figure 8.13: Same as Figure 8.10, for the latitudinal variability at local time ∼ 9 h.

Years. As can be seen in Figure 8.14 (ii), the agreement between the OMEGA and the model temperatures is not as good as with the CO_2 densities (i). At 130 km, we observe a warmer region, which surely is the bias in the inversion previously discussed. Above 130 km, the OMEGA temperatures are in general warmer than in the model close to the northern polar region (iv).

The second group (with solar longitude ∼ 90 deg) is composed of 21 orbits and is mainly populated by observations in the vicinity of latit-

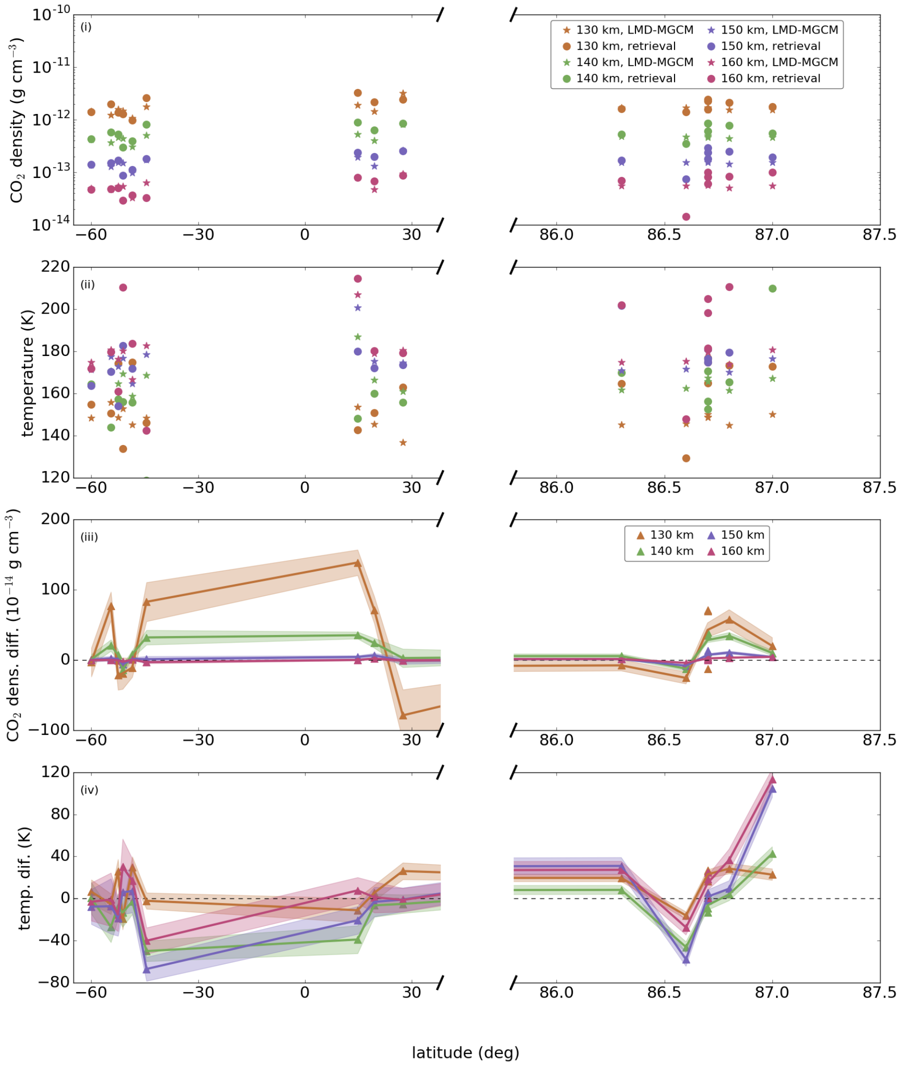

Figure 8.14: Same as Figure 8.10, for the latitudinal variability at solar longitude ~ 0 deg. When more than one point is available for the same latitude, like at 86 deg, the average is used.

ude 45 deg. This subset is entirely similar to the longitudinal variability study (a), except for the addition of two more profiles here. Figure 8.15 shows the results for this group. Starting with the CO$_2$ densities (i), and beyond the good agreement data-model aforementioned, the OMEGA CO$_2$ densities are larger in the northern hemisphere (summer) than in the

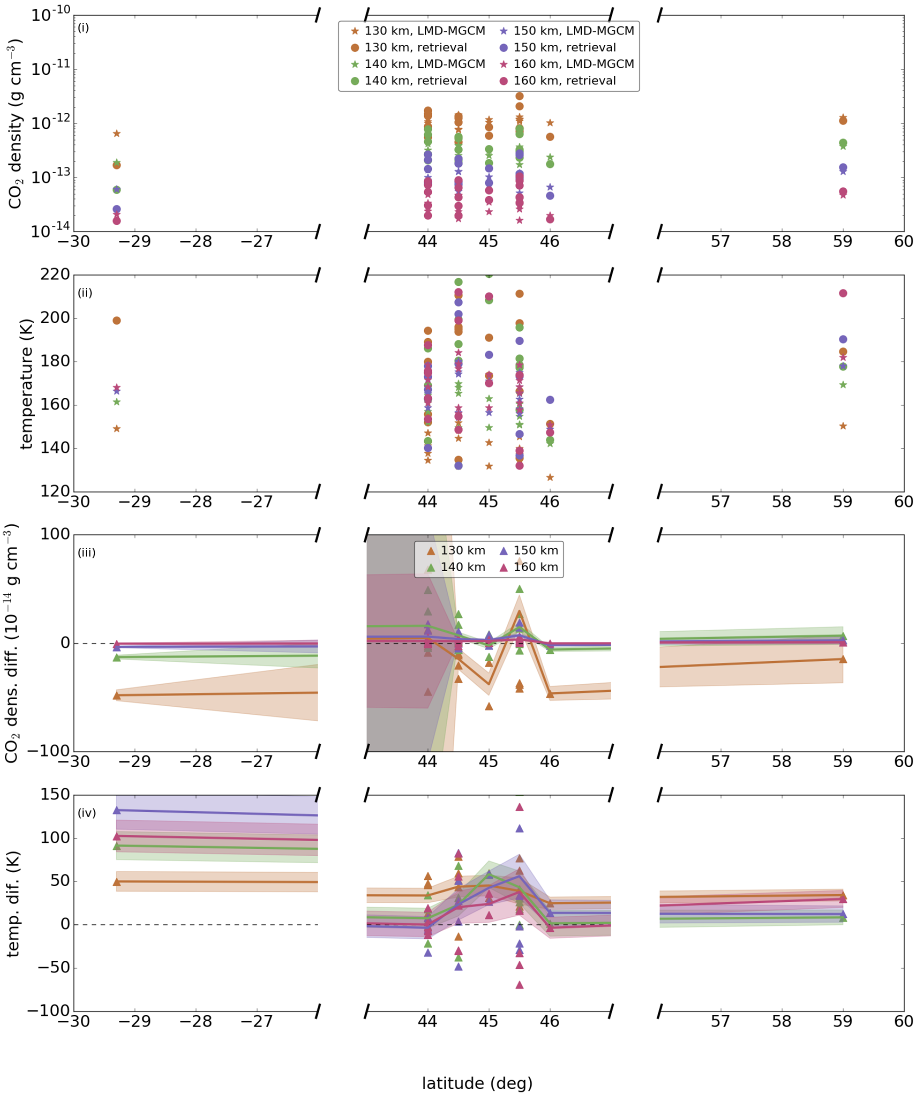

Figure 8.15: Same as Figure 8.10, for the latitudinal variability at solar longitude ∼ 90 deg. The huge error found at 44 deg latitude in panel (iii) is due to an enormous uncertainty in the pressure of the LMD-MGCM for orbit 0961_0. When more than one point is available for the same latitude, like at 86 deg, the average is used.

southern hemisphere (winter), by about 30%, which is in agreement with the model predictions. Unfortunately, the number of points in the southern hemisphere (one) is not enough to derive any conclusions on large inter-hemispheric trends. Instead, we can only examine with some confidence the small latitudinal variation around latitude 45 deg (iii, iv), where no clear trends are observed either.

As a summary, considering the entire set of regions of particular interest, no specific trends or additional differences to the global comparison data-model were found. Therefore, the conclusions deduced from the global inspection may apply to these particular cases. Table 8.2 summarises the averages on the differences data-model found for all the cases (a-f), for both CO_2 densities and temperatures. As can be seen in the table, there is a clear positive bias in the derived temperatures at 130 km, as previously discussed. Above this altitude, the averaged CO_2 densities are always above the model. The drop of the CO_2 differences with altitude from 140 to 160 km in all the cases is due to the large decrease of the density profile with altitude. Regarding the temperature, above 130 km, we obtained warmer temperatures for all the regions, with two exceptions: the study of the seasonal variability at latitude ~ -60 deg (c), where the OMEGA temperatures are clearly colder, by 10–20 K; and the study of the latitudinal variability at solar longitude ~ 0 deg (e), where the derived temperature is colder at 140 km, and, slightly, at 150 km. Above 150 km the temperature is also warmer.

	(a)		**(b)**		**(c)**		**(d)**		**(e)**		**(f)**	
	ρ_{avg}	T_{avg}	ρ_{avg}	T_{avg}	ρ_{avg}	T_{avg}	ρ_{avg}	T_{avg}	ρ_{avg}	T_{avg}	ρ_{avg}	T_{avg}
130 km	0.4	39	44	25	−3.1	18	56	29	26	11	−2.7	39
140 km	10	28	31	3.7	27	−14	41	16	15	−10	9	30
150 km	5	28	16	7	8	−20	25	7	2.5	−1.3	4.5	32
160 km	2.2	20	7	12	0.9	−12	11	−0.2	0.5	12	2.0	24

Table 8.2: Average differences between results and model for the regions of interest presented in Figure 8.9, identified by the letter in the first row. The columns labelled as ρ_{avg} refer to the mean density differences, with units $10^{-14}\,\mathrm{g\,cm^{-3}}$, while the columns labelled as T_{avg} refer to the mean temperature differences, with units K.

8.2. Comparison with other instruments

In this section, we compare the results of the retrievals with the observations carried out by other instruments, both from remote sounding of the Martian thermosphere and from *in situ* measurements during close approaches to the planet itself. We analyse them taking into account the comparison with the LMD-MGCM discussed above. The most recent and extensive datasets of the Martian dayside thermosphere were performed by different instruments on board the Mars Atmosphere and Volatile EvolutioN (MAVEN) mission (Jakosky et al., 2015). Here we describe some of the recent findings of these instruments.

Gravity wave activity with NGIMS/MAVEN

Starting with CO_2 densities, the Neutral Gas Ion Mass Spectrometer (NGIMS) has been measuring *in situ* along-track abundances of several atmospheric species, like CO_2, above 150–170 km, the usual lower layer sampled during periapsis. In a few occasions, during the so called Deep Dip (DD) campaigns, this altitude is lowered down to 120–135 km (Bougher et al., 2017). The measurements are not 1-D vertical profiles, but contain simultaneous vertical and horizontal drifts along the spacecraft track, which require a model for a proper interpretation. The vertical resolution is 5 km. These along-track measurements are not coincident nor directly comparable with our OMEGA 1-D profiles. An example of these DD observations will be shown later in Figure 8.19 (red solid line). A result from NGIMS important to us is the report of small-scale perturbations with apparent (as seen along the orbit track) wavelengths of several tens to hundreds of kilometres. The relative density amplitudes of these perturbations has typical values $\leq 40\%$, and, occasionally, waves with amplitudes in the 50–70% were observed. The amplitudes were found to be anticorrelated with the background temperature (England et al., 2017; Terada et al., 2017). Figure 8.16 shows the relative density amplitude of the waves measured (left panel) and the distribution of their occurrence (right panel).

England et al. (2017) concluded, studying the temperatures derived from the NGIMS CO_2 scale heights (assuming hydrostatic equilibrium), that gravity wave-induced heating/cooling may significantly affect the thermal structure of the Martian thermosphere, as was initially predicted by the general circulation modelling study of Medvedev and Yiğit (2012).

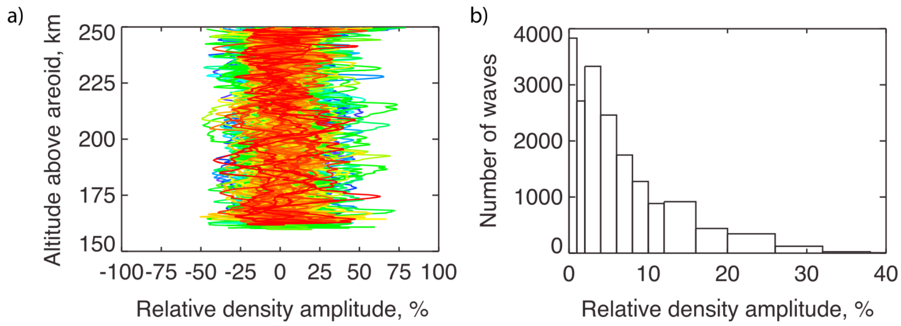

Figure 8.16: Properties of the waves observed during May 2015 by NGIMS/MAVEN. *Left*: A reconstruction of all waves identified in the CO_2 observations, where each orbit is shown in a different colour. *Right*: Occurrence of waves detected with different relative density amplitude. Note the non-uniform bin size used. Reprinted from England et al. (2017).

Non-orographic (i.e. non-zero phase velocity) gravity waves (and the effect of their breakdown) are not included in the LMD-MGCM and could (partly) explain the data-model differences observed in some of the peculiar density and temperature profiles shown in figures 8.5 and 8.6. Given the heating/cooling associated to the dissipation of these waves, their impact is usually better seen on the atmospheric temperatures. The impact of gravity waves in the predicted thermal structure of the LMD-MGCM above 50 km is currently under investigation (Gilli et al., 2017). In the same direction, simulations performed with the Max Planck Institute GCM, suggest that the gravity wave-induced cooling can alone result in up to 40 K colder temperatures in the lower thermosphere (Medvedev et al., 2015).

Another result from NGIMS measurements, although again not directly comparable with the OMEGA observations of this Thesis due to differences in the sampling locations and in the solar activity, point to a standard deviation up to ±20 K in the temperatures at an altitude of about 150 km, and a density standard deviation about ±25% at these same altitudes (Bougher et al., 2017).

Solar occultations with EUVM/MAVEN

The MAVEN Extreme Ultraviolet Monitor (EUVM) performed some observations for solar occultations (Thiemann et al., 2018). Again, the available sample makes very hard a direct comparison with the OMEGA dataset analysed in this Thesis. However, measurements of both the thermospheric temperature and the density near aphelion and perihelion obtained by EUVM have an uncertainty of about ±30%, similar to the precision achieved with our retrievals. In addition, the temperature and density curves in Figure 7 of Thiemann et al. (2018), corresponding to measurements at dusk, describe similar variations to those we found during our study of latitudinal variability at a constant local time (Figure 8.13).

UV dayglow measurements with IUVS/MAVEN

A remote sounding experiment on board MAVEN in the UV part of the spectrum, using a limb geometry and hence more analogous to the research presented in this Thesis can be found in Evans et al. (2015). CO_2 and N_2 density profiles were retrieved from the limb dayglow observations by the Image Ultraviolet Spectrograph (IUVS) and, from them, temperature profiles were then derived. This is an ongoing work in the IUVS team and promises to be an excellent dataset for comparisons with our results, but only 82 vertical profiles were included in that study, with the vertical sampling of IUVS, of about 5 km. Only one vertical CO_2 profile is shown in Figure 1 of that work, which compares well with the M-GITM, within a factor 2–3, in the altitude range from 120 to 200 km. Figure 8.17 shows their retrieved CO_2 densities at 170 km (top panel) and the single temperature value they derived from CO_2 profiles, from 170 to 220 km (bottom panel). Comparing this plot with the OMEGA temperatures in figures 8.10 and 8.11 (only pink dots, which correspond to 160 km), a similar shape is obtained for both CO_2 densities and temperatures. CO_2 densities from both instruments present minimum values around longitude 180 and 360 deg, with variations by a factor 4 with respect to the maximum (compared with the factor 2.5 found by Evans et al. (2015)). Regarding the temperature variability with longitude, observations from both instruments lead to similar shapes, with a minimum around latitude 200 deg, and a maximum about latitude 360 deg.

Stellar occultations with IUVS/MAVEN

Also from IUVS observations, Gröller et al. (2015) and Gröller et al. (2018) performed CO_2, O_2 and O_3 inversions, but now in the nighttime hemisphere, from stellar occultation measurements, as well as derivation of temperature profiles from the retrieved densities. These authors retrieved CO_2 and other species from 12 stellar occultation campaigns. Their CO_2

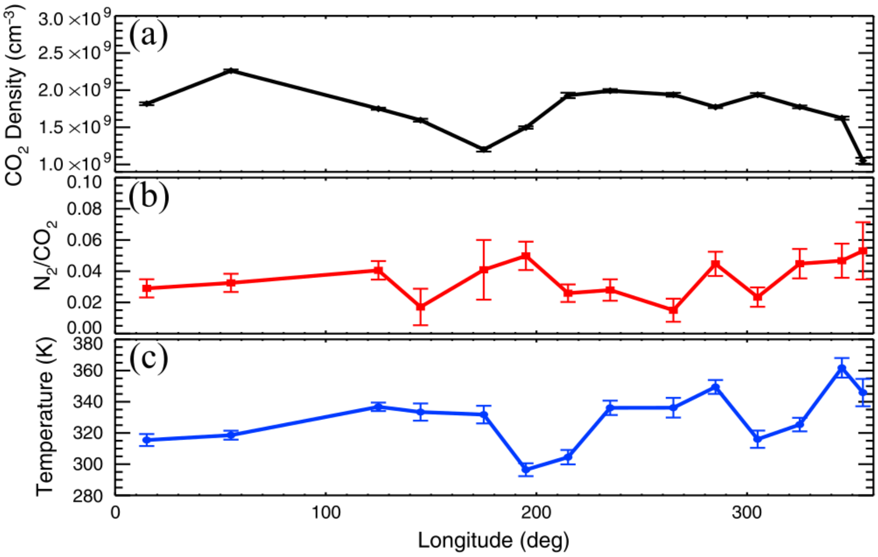

Figure 8.17: *Top*: Retrieved CO_2 density at an altitude of 170 km for 23 (out of 82) limb scans from 18 October 2014 to 18 November 2014. *Middle*: Same for N_2/CO_2. *Bottom*: Upper atmospheric temperature derived from fits to retrieved CO_2 density profiles over altitudes from 170 to 220 km. Reprinted from Evans et al. (2015).

profiles extend from 20 to about 160 km altitude. They compared them to MCD data (version 5.3) extracted from several Mars Years scenarios, according to the EUV flux, to match the measured flux values during those campaigns. They paid particular attention to the solar longitude variation obtained at 100 km, shown in Figure 8.18. Although we do not have results at that altitude, the seasonal variation obtained, as well as that from SPICAM (shown in the same figure), do agree with our results higher up, in the shape and phase of the variation.

Figure 8.19 shows their derived temperatures for two observations corresponding to the first campaign of stellar occultations with IUVS. In these two cases, important differences with the Mars Climate Database can be seen, specially a second minimum in temperature, up to 50 K colder, is obtained around 140–150 km. We found a few profiles with very cold patches, also about 50 K colder than the model and also at about the same tangent altitude. One example is OMEGA orbit 7708_0, shown in Figure 6.4. Our data *qube* corresponds to observations for a local time (4.2 h) and for a solar zenith angle (77 deg) similar to those for the α Lyr occultation (6 h and 95 deg, respectively), with no other geographical or seasonal similarit-

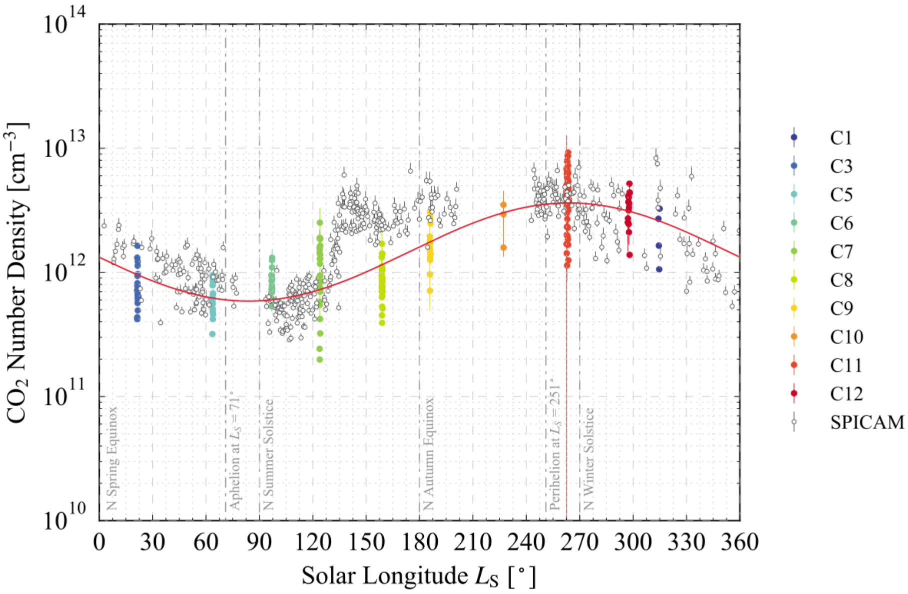

Figure 8.18: Solar longitude dependence of the CO$_2$ number density at 100 km. Colours represent the number densities for a different stellar occultation campaign. The solid red line shows the sinusoidal least squares fit to the measured densities. In addition, the CO$_2$ number densities from Mars Express/SPICAM stellar occultations shown in Forget et al. (2009) are included as gray open circles. The Imaging UltraViolet Spectrograph and SPICAM data shown here include measurements at latitudes below 50 deg and all available longitudes and local times. Reprinted from Gröller et al. (2018).

ies. There are no common coordinates between orbit 7708_0 and the λ Sco occultation.

The vertical temperature profiles derived from the 12 IUVS stellar occultation campaigns reported by these authors reveal substantial disagreement with models, with observed temperatures both warmer and colder than the MCD. Concretely, IUVS temperatures near 120 km can be up to 40–50 K cooler than predicted, while, at about 130 km, several temperatures appear to be warmer by tens of kelvins. In addition, the altitude profiles of density perturbations (defined by the authors as the difference between the local measurement and the mean in longitude at that altitude, divided by the longitude mean) and their variation with longitude show structured atmospheric perturbations at altitudes above 100 km, with relative amplitudes as large as 45%, that are interpreted as atmospheric non-migrating tides (Gröller et al., 2018).

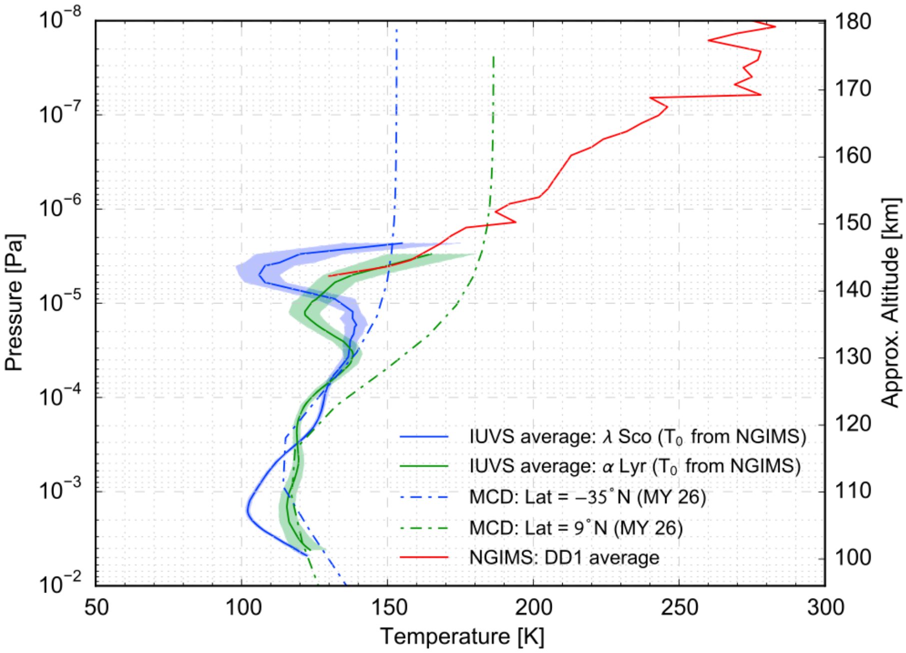

Figure 8.19: Average temperature profiles for two stellar occultations (blue and green) calculated using NGIMS to define the upper boundary temperature, along with the average of the MCD, version 5.2, profiles (dashed) for this set of occultations. The blue and green shaded areas represent the uncertainties calculated as the standard deviation of the mean. NGIMS results are shown in red. Reprinted from Gröller et al. (2015).

Measurements with MAVEN accelerometer

To conclude this section, we briefly comment on some *in situ* measurements from the accelerometer on board MAVEN, during the Deep Dip campaigns, where the spacecraft reaches lower altitudes above the planet, below 140 km. Zurek et al. (2017) studied six Deep Dip campaigns, finding complex variations dependent on season, local time, location, and lower atmosphere activity (dust storm and wave propagation). They also compared the accelerometer measurements with the M-GITM. Some general agreement was found but important discrepancies arose, especially near the terminators, i.e., for high solar zenith angles. The authors pointed to deficiencies in the computed circulation, probably due to the absence in the model of gravity wave drag and an inadequate treatment of the non-LTE radiative cooling by CO_2. The discrepancy in the density, with respect to the model, found by the authors ranges from $\sim 30\%$ (for low solar zenith angle, best case) to $\sim 2000\%$ (near the terminator, worst case), at 130–150 km. They also suggested that the largest discrepancies may be due to a particularly variable upper atmosphere in the pre-dawn hours, a part of the Martian day sampled with aerobraking for the first time during these campaigns.

The comparison to previous results obtained with other instruments did not intend to be exhaustive, but to focus on the most recent studies available. In addition, the comparison with most of them is far from straightforward, as there is no coincidence on the location or time of acquisition. Nevertheless, and making the discussion extensive to comparisons of OMEGA observations with models, the main differences found can be attributed to one or more of the following reasons:

- The thermal structure below 120 km.
- The amount and distribution of suspended dust.
- Gravity waves and tides, not implemented in the LMD-MGCM.

In this Thesis, the gravity waves are pointed to as a possible candidate of the *wavy* trends observed in several OMEGA profiles obtained for CO_2 density and temperature. Unfortunately, these OMEGA profiles do not provide oscillations clear enough to claim a detection and/or to characterise the parameters of gravity waves.

8.3. Solar occultation with ExoMars TGO

The work included in this section contributed to section 3.1 of López-Valverde et al. (2018), .

Trace Gas Orbiter (TGO) carries on board, among others, two instruments: Nadir and Occultation for MArs Discovery (NOMAD) and Atmospheric Chemistry Suite (ACS). Since April 2018, these instruments are sounding the Martian limb and will supply measurements of CO_2 density at high altitude. This is done with the solar occultation technique, mainly using the strong ro-vibrational band of CO_2 around $2.7\,\mu$m. NOMAD also offers the possibility to sound the limb using a flip mirror during the dayside tracks, which has been used to perform a few observations of the infrared solar fluorescence in the same CO_2 band. Both solar occultation and emission datasets will offer, when properly calibrated and inverted, excellent possibilities for comparison with OMEGA retrievals, hopefully in the full altitude range studied in this Thesis, 120–180 km. We briefly review these two measurements in turn, and the work performed in preparation of their full exploitation, which will make use of the same inversion technique applied to OMEGA.

8.3.1. Solar occultation

Solar occultation is the most precise remote observation strategy that can be used to sound as high as possible in an atmosphere. The combination of a strong source and a limb grazing path permits the maximum sensitivity to weak absorption bands and trace species, more difficult to observe otherwise. Regular observations at the terminator, from both NOMAD and ACS, on board ExoMars TGO, are supplying observations during one sunset and one sunrise each orbit, i.e., each two hours approximately. With these measurements, we expect to learn a lot about the atmospheric density and thermal structure in the important altitude range from 80 km up to the upper thermosphere. The precise uppermost altitude expected from each TGO instrument can be evaluated before the full inversion by using a detailed line-by-line calculation of atmospheric transmittances together with a realistic estimation of the instrumental noise.

Figure 8.20 shows such a calculation in the infrared, specifically in the 2.5–2.9 μm region, for an arbitrary reference atmosphere extracted from the LMD-MGCM. The line-by-line transmittances were convolved with an approximate instrumental response at 0.15 cm^{-1} resolution, to mimic the NOMAD SO signal. An analogous exercise was done by Vandaele et al. (2015) in similar transmittance calculations at tangent heights below 50 km. Using a conservative estimation of the SNR of 2500 for the SO channel (Robert et al., 2016), all the spectral features visible in Figure 8.20, even at 170 km altitude (about 0.05 nbar in this reference atmosphere), should be detected in the SO signal. Since the ACS MIR has a spectral resolution about three times better than the SO channel, but a lower sensitivity by about the same factor, a similar conclusion applies to its solar occultation with ACS/MIR.

Figure 8.21 shows that these sensitivity levels are excellent to detect hot bands of CO_2; the first hot band of the major isotope (626), in particular, should be clearly seen at altitudes well above 130 km (at least

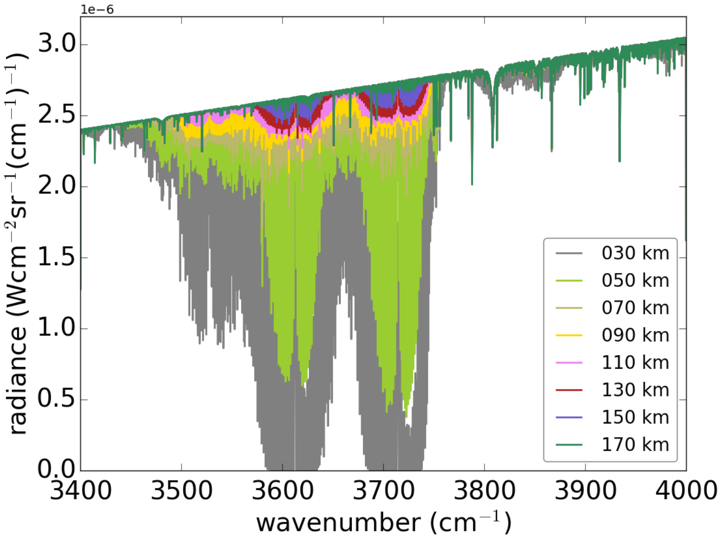

Figure 8.20: Simulation of the solar radiance expected in the NOMAD LNO and ACS MIR channels at different tangent altitudes, and for a typical Martian reference atmosphere. Reprinted from López-Valverde et al. (2018).

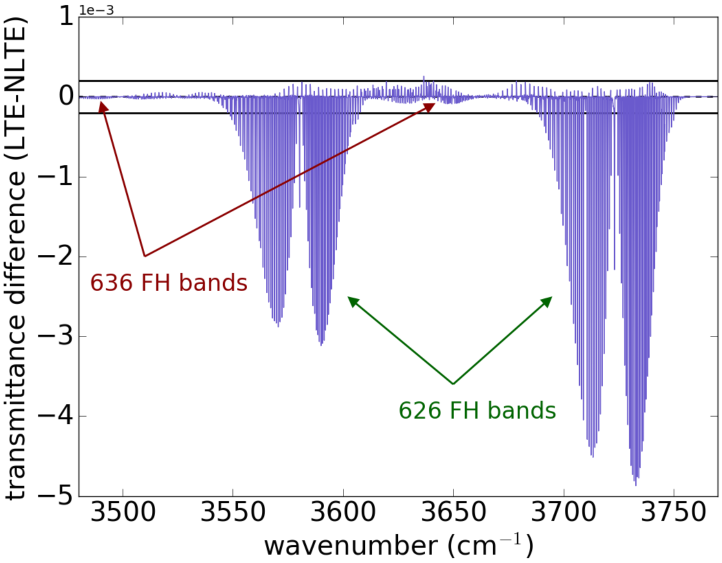

Figure 8.21: Simulation of the atmospheric transmittance differences LTE–NLTE by the first hot (FH) band of the two main CO_2 isotopes, 626 and 636, at a tangent altitude of 130 km, for the reference atmosphere used. A line for SNR = 5000 is indicated for reference. See text for details. Reprinted from López-Valverde et al. (2018).

up to about 150 km, or equivalently to CO_2 number densities around 10^{10} cm^{-3}, for this model atmosphere and the assumed SNR value). This is very interesting for non-LTE studies. Emission spectroscopy is very useful to study the excited states of molecules like CO_2, which may present strong non-LTE populations, but is subject to diverse uncertainties. These include collisional rate coefficients poorly constrained in laboratory and which therefore require assumptions and approximations (López-Valverde and López-Puertas, 1994b; López-Puertas and Taylor, 2001). Absorption spectroscopy, on the contrary, sounds the lower state of the transitions and is more free from those modelling uncertainties. The lower state is the ground state in the fundamental bands, but, for hot bands, it is an excited state.

Figure 8.21 shows LTE–NLTE differences of simulated transmittances to illustrate how the NOMAD SO measurements should permit the study of the population of the lower state of the first hot band, the (0,1,0) state. This is expected to separate from LTE in the upper mesosphere and the whole thermosphere during daytime (López-Valverde and López-Puertas, 1994a), and these data combined with the total density of CO_2 would supply a direct measurement of the (0,1,0) state population, a direct test for the non-LTE models.

Figure 8.22 shows this detection capability more clearly with simulations in a narrow region around 2.83 μm, where the CO_2 636 isotope has its strongest absorption lines. In this figure the irradiance shown is not the actual flux level to be observed, but the difference from the flux at the top of the atmosphere. Individual lines from diverse CO_2 bands and isotopes show a funny shape due to the logarithmic scale used. If the expected noise level is confirmed, the isotopic 636 lines should be detected below about 150 km. We can also see lines of the first hot band of the main CO_2 isotope (626) in the upper mesosphere and below.

Other CO_2 and CO ro-vibrational bands in the near-infrared range (1.0–2.0 μm), which can be covered by the ACS-NIR instrument, will also be useful for sounding, although up to lower altitudes. The strongest CO_2 band in this range, at 1.43 μm, about 1000 times weaker than the 2.7 μm bands, was used to derive CO_2 up to 90 km by Fedorova et al. (2009) during solar occultations with SPICAM. Similar altitudes have been achieved with NIR, due to its better SNR and spectral resolution (Fedorova, private communication). The interest of using this band is the simultaneous derivation of H_2O from the nearby band at 1.38 μm, as exploited by SPICAM (Fedorova et al., 2009). The CO overtone band at

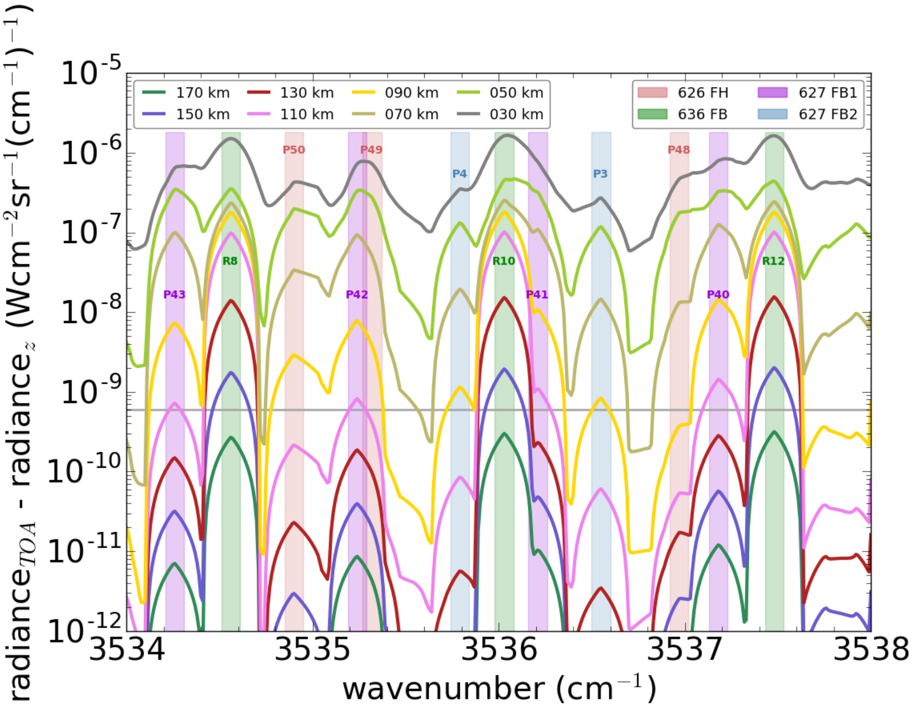

Figure 8.22: Simulation of the difference between the solar spectral irradiance at each tangent altitude and that at the top of the atmosphere (TOA). Different colours are used to visualise the different tangent altitudes. The grey line is the nominal noise of the NOMAD SO channel. Positions of individual lines and bands are indicated with coloured shades. FH and FB stand for first hot and fundamental band, respectively. See text for details. Reprinted from López-Valverde et al. (2018).

2.3 μm has also been detected in single CO measurements by NOMAD and ACS, up to about 90 km, with one single solar occultation (Korablev et al., 2018, 2019b; Erwin et al., 2019).

8.3.2. Limb emissions with NOMAD-LNO

Only a few measurements of the 2.7 μm emission band of CO_2 have been performed in this special mode of operation of the NOMAD-LNO channel, and its analysis is ongoing by our team. The emissions have a much lower intensity than the solar occultation signals, and large averages are necessary.

Figure 8.23 shows an example of the spectra obtained by NOMAD-

LNO channel in the limb, at a few tangent altitudes, after large averages in the vertical. This averaging was done with a running box of 20 km width. The data show strongest signal in the center of the window, as determined by the optical filter function for this particular dispersion order. The number of spectra averaged in each altitude box is shown. Despite this large averaging, the signal is still relatively noisy, but the strongest CO_2 lines in the band can be clearly seen, with a maximum or peak emission around 90 km tangent height.

These are non-LTE emissions in a different spectral region to the OMEGA $4.3\,\mu$m band, but the NOMAD-LNO signal is emitted by the same set of CO_2 upper vibrational states which are responsible for the $4.3\,\mu$m second hot band, the largest contribution to the OMEGA signals below about 140 km. This is an excellent opportunity to combine, complement and mutually validate both OMEGA and NOMAD-LNO channels, and a specific campaign of quasi-simultaneous observations has been scheduled.

Our team is currently working on the application of exactly the same inversion technique presented in this Thesis to the NOMAD-LNO limb emission measurements.

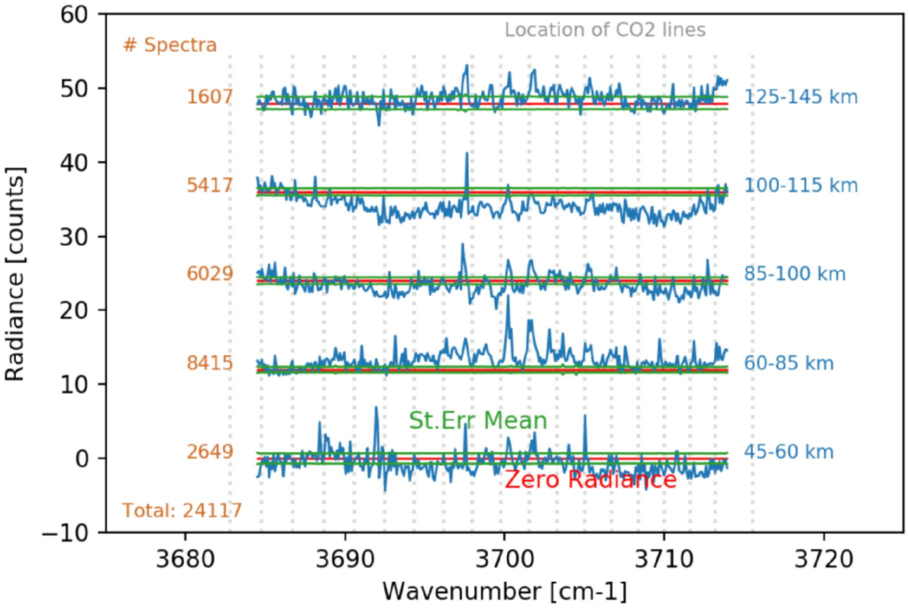

Figure 8.23: Five averaged spectra of Mars measured by NOMAD/LNO around 2.7 μm (dispersion order 164) in a limb geometry in the dayside, at five tangent altitudes, obtained during a *limb emission* campaign of 9 orbits in April and May 2018. The averages were obtained by gathering a large number of individual spectra in boxes of 15 km width in altitude. The five altitude boxes are indicated on the right hand side and the number of binned spectra on the left hand side, and the spectra are shifted in the vertical for clarity. The spectral location of the ro-vibrational lines of the CO_2 fundamental band at 2.7 μm are shown with dashed lines (data from Hitran 2016). The zero radiance and the standard error of the mean are also shown. Measurements, expressed in counts, are level 0.3A. No correction for spectral shifts, nor for bending of the baseline (or zero radiance) were applied. See text for details.

For someone who was never meant for this world, I must confess I'm suddenly having a hard time leaving it.

Andrew Niccol

9

Summary, conclusions and future work

Abstract

This chapter summarises the scientific research and results in this Thesis, before presenting the major global conclusions and the improvements envisaged for the future extension of this research.

9.1. Summary

This work was conducted as part of the project UPWARDS-633127 under the European Union's Horizon 2020 research and innovation Programme. The IAA team was supported by the Spanish Ministry of Economy, Industry and Competitiveness and by FEDER funds under grant ESP2015-65064-C2-1-P (MINECO/FEDER). OMEGA data are publicly available via the ESA Planetary Science Archive (PSA, 2019).

9.1.1. Calibration and cleaning of the OMEGA limb data

We analysed a total of 47 limb observations taken by OMEGA on board Mars Express, in its SWIR L channel, corresponding to Martian

Years 26, 27, 29 and 30. The observations are presented in *qubes*, i.e., 3-D data packs containing one spectrum measured in each pixel of the 2-D detector, with usually one *qube* per orbit. For every data *qube*, we downloaded the level 0 observations, publicly available at the ESA Planetary Science Archive (PSA, 2019) and calibrated them. We needed to change the calibration pipeline used by the OMEGA team to generate Level 1 radiances, in order to avoid a previously unnoticed hard cut introduced at an arbitrary radiance value, and we also corrected the nominal altitude registration of the SWIR L channel, following Piccialli et al. (2016).

A number of preprocessing and data cleaning steps were performed. One of them was the revision of the spectral calibration. For this purpose, the measurements of one profile per orbit were compared to a simulation with our forward model, KOPRA (Stiller, 2002) with the GRANADA non-LTE module (Funke et al., 2012), for the atmospheric conditions corresponding to the *qube* geolocation, as extracted from the LMD-MGCM (González-Galindo et al., 2015). This comparison allowed us to decide the sign of the correction applied to the SWIR L channel altitude registration, and to obtain a first evaluation of the fit between observations and simulations prior to the inversion process. Then we corrected in wavelength by comparing the OMEGA measurements with expected spectral shapes (López-Valverde and López-Puertas, 2001). Finally, we performed a cluster analysis to easily detect singular spectra and discard acquired data exhibiting non-physical shapes.

The 2-D projection of the data *qubes* on the limb needs to be converted into actual 1-D vertical profiles of radiances, which are the basic input required by our inversion method. So, once the data were calibrated and cleaned, we proceeded with the building of such radiance vertical profiles by a careful binning on a given grid. Between 6 and 30 profiles were produced for each data *qube* (16 on average), depending on the 2-D limb projection of the dataset. The vertical profiles we generated extend, in general, from 50 km up to a limit imposed by the available observations and the model calculations. There is no interest in going below 50 km, since model simulations indicate that the limb emissions become saturated, i.e., so optically thick that no information on the tangent point can be obtained. The vertical binning was chosen to be 2 km, except for 7 of the orbits, where the altitude step was widened to 4 km to avoid convergence problems. Our latitude binning varies between 0.02 and 0.4 deg, guaranteeing the spectra averaged in each cell are sufficiently close in the horizontal dimension. For each of the 1-D radiance profiles generated this way, we used the measurements in the uppermost layers of the atmosphere to compute a space offset. We also calculated the noise equivalent spectral radiance for every altitude bin and for every spectral point from the standard error of the averages of the spectra in the bin.

9.1.2. Inversion of CO_2 density profiles

We adapted a non-LTE retrieval scheme, extensively used for Earth's atmosphere, to Martian conditions for the first time (Stiller, 2002; Funke et al., 2012; López-Valverde and López-Puertas, 1994a). This inversion scheme was then used to retrieve CO_2 abundances from the radiance vertical profiles, previously generated from OMEGA limb daytime measurements around $4.3\,\mu$m.

We presented the results of the retrievals of all the radiance vertical profiles formed for one particular data *qube*, 0330_2, as an example of the inversion process applied to the entire dataset. The application of the scheme was limited in tangent altitude from 120 to 180 km for individual profiles. Below 120 km the retrieval process is strongly regularised, in order to avoid complex non-linearities that arise in a very optically thick regime, from a double dependence of the non-LTE limb emission on the local density of the emitting gas. In the uppermost layers, we obtained a density threshold, $10^{-14}\,\mathrm{gcm}^{-3}$, below which the OMEGA measurements noise dominates over the atmospheric emission. This typically occurs above about 180 km, depending on the orbit.

The retrievals were obtained with a very high degree of convergence (94%), with an average of 4–5 iterations needed. The data-model best fits achieved are on average within the measurement noise and do not show any systematics in their spectral shape. The vertical resolution obtained from the FWHM of the averaging kernels is about 15 km between 120 and 160 km. This is larger than the vertical binning used, 2–4 km, which indicates that a thicker binning, up to 5–7 km (about half the width of the averaging kernels) of the data is possible, in order to increase the signal-to-noise ratio. At higher altitudes, the averaging kernels are wider, as expected, since the non-LTE source function of all major bands is constant with altitude in the optically thin regime. Consequently, the emission only depends on the density of CO_2, which strongly decreases with altitude. The trace of the averaging kernel matrix gives the number of independent pieces of information, i.e., the degrees of freedom. This was forced to be about 4 for all the inverted profiles, by adjusting the regularisation strength. This was done for internal consistency, in order to homogenise the different *qubes*, i.e., to make all retrieved CO_2 density profiles comparable among them.

The CO_2 densities obtained show a standard and physically meaningful behaviour, that is, an exponential decrease with altitude, and with a slightly variable scale height, never too far from the *a priori* (within a 50% of the climatology at most altitudes).

9.1.3. Temperatures from CO_2 profiles

Vertical profiles of thermospheric temperatures were obtained from each of the retrieved densities, assuming hydrostatic equilibrium. We developed our own algorithm, which not only integrates the hydrostatic equilibrium equation downwards, from the top of the atmosphere (TOA), using a minimum of assumptions there, but also is able to compute the errors in the temperatures. These are evaluated from the density uncertainties, using a Monte-Carlo type approach, from the envelope of a high number of applications of the routine to random density profiles within those uncertainty brackets.

Most of the ~ 750 temperature profiles obtained in this work present a systematic bias at 120 km, more or less prominent depending on the orbit. This is an artefact produced by an excessive gradient in the retrieved density profiles, due to the strong regularisation introduced at and below the retrieval boundary, located at that altitude. The intra-orbit dispersion found for temperature profiles is significantly larger than in the densities, and increases with altitude from 120 to about 160 km, and then decreases at higher altitudes, due to the selection of the temperature at TOA, T_0. Because this temperature is calculated from the CO_2 density gradient at the two highest altitudes in each profile, the values of T_0 for every profile in the same orbit tend to be close to each other.

For 28 out of the 47 orbits (60%), a second minimum in the temperature profile is found between 140 and 150 km. This minimum is often strong, up to 50 K colder. This very cold thermosphere is not reproducible under usual climatic scenarios by the LMD-MGCM. On the opposite side, 14 orbits (30%) exhibit a temperature much warmer than the model around 150 km. These severe discrepancies between OMEGA and the model (beyond the temperature uncertainties of both results and model) do not show any clear spatial or temporal distribution. Since the temperatures tend to usual values higher up, this result points to a transition from the lower to the upper thermosphere more variable than in the model. This change from the positive thermal gradient typical in the lower thermosphere to the isothermal regime higher up is normally due to the region where the EUV solar radiation by CO_2 peaks. We have to conclude that either there is a large variability in CO_2 density at these altitudes (perhaps due to waves propagating from below or to unusual thermal regimes in the lower atmosphere), or the location of this EUV absorption layer is shifted in altitude for some unidentified reason.

We also applied this algorithm to derive thermospheric temperature profiles from dayglow emissions (González-Galindo et al., 2019). For this, we extracted profiles of the CO_2^+ UV doublet and the Cameron bands, together with CO_2 number density profiles, from the LMD-MGCM, and derived temperature profiles from the three of them. The actual temperature profile in the model was very well reproduced by the temperatures derived from the CO_2 densities, a result which validates our approach. However, the profiles derived from the CO_2^+ UV doublet showed a systematic and small deviation, smaller than 5 K between about 160 and 230 km, and smaller than 2.5 K between 175 and 225 km. The temperature derived from the Cameron bands was at all altitudes significantly warmer than the actual one, with differences larger than 15 K.

This study demonstrates that the application of the traditional derivation of temperatures, from the scale height of UV emissions, to the Cameron bands is incorrect, giving a significant bias towards too warm values. Even the derivation of temperatures from the CO_2^+ UV doublet is not very precise, with small positive biases from 175 to 225 km range, and larger errors outside this altitude range.

9.1.4. Sensitivity studies

An extensive number of internal consistency and sensitivity tests were done in order to (i) confirm the stability and robustness of our scheme to retrieve CO_2 abundances from Mars limb emission data, and (ii) perform a complete error analysis, by combining all relevant sources of uncertainty. We perturbed the main parameters in the forward model, within their respective uncertainties, and quantified the impact of these perturbations on the inversion results. We compared the new retrieved densities with the nominal ones at four different altitudes (120, 140, 160 and 180 km) for all the test cases to compute the different error components. The we combined their contributions in a quadratic way, assuming independence of every term from each other.

The impact of the CO_2 *a priori* uncertainty on the retrievals was also tested on one particular orbit, 0330_2, which is considered as typical in this Thesis. This was done by performing two inversions with two *a priori* density profiles very different to the nominal one. One of the atmospheres selected was denser, while the other was more rarefied, corresponding to simulations of the LMD-MGCM for conditions of orbits 0044_1 and 0647_1, respectively. The two density profiles obtained were quite close to the nominal one, within their uncertainty levels, at all altitudes, except for the denser atmosphere in the uppermost layers. Following a common practice in atmospheric remote sounding, the sensitivity to the *a priori* was not included in the total error budget.

The addition of all error components gave a total uncertainty of about 25% in the retrieved CO_2, slightly increased with altitude to about 30% at 180 km. The uncertainties on the instrumental Gain and on the pointing turned to be the two major terms in the lower thermosphere (below 150 km), while the upper thermosphere densities were mostly dependent on the retrieval noise error and, again, on the instrumental Gain.

9.1.5. Validation with models and other instruments

In order to validate our results, we performed comparisons of the retrieved densities and the derived temperatures with predictions from the LMD-MGCM and with observations taken by other instruments sounding the upper atmosphere of Mars.

We first compared our results with the LMD-MGCM (Forget et al., 1999; González-Galindo et al., 2015) obtaining an overall good agreement. However, our retrieved CO_2 density is systematically larger than the model above 130 km, by 30–50%. The temperatures obtained above 130 km present a larger dispersion than the model, globally speaking. For completeness, extreme scenarios from the LMD-MGCM and the Mars Climate Database (MCD, Forget et al. (1999); Millour et al. (2018)) were included in the comparison. We found that, for some locations in the Martian atmosphere, the so called *smin* and *smax* scenarios of the MCD, which correspond to the minimum and maximum solar fluxes during a typical solar cycle, seem to be more extreme than the so called *cold* and *warm* scenarios, which, in principle, include the extreme solar cycle conditions in addition to extreme dust conditions. Similarly, individual temperature profiles from the MCD for MY29 were slightly below the *smin* and *cold* scenarios, within the numerical uncertainties and the standard deviation of the extracted profiles. The differences found between our retrieved densities and the *a priori* profiles are usually minor compared to the differences between extreme solar conditions of the model, which were extracted for the same location of the orbit.

Thereafter we examined the results after grouping together orbits approximately sharing one or more location parameters, in order to look for possible correlations of the data-model differences with those variables. In general, no clear correlations were observed neither from a global study nor from subsets of data for more homogeneous conditions. The only exception was the solar zenith angle. As expected, the larger it is, the weaker the solar irradiation, and thus the measured emission, leading to noisier profiles.

We also reviewed the main results obtained from measurements by other instruments sounding the Martian upper atmosphere, from the perspective of our OMEGA results. Most of the recent observations in the diurnal thermosphere were performed by instruments on board the MAVEN mission (Jakosky et al., 2015), namely NGIMS, EUVM and IUVS. First, starting with the reported uncertainties from these experiments, they are of the order of those presented in this work. Secondly, all the measurements reported important differences when compared to the LMD-MGCM or other global circulation models (Medvedev and Yiğit, 2012; Medvedev et al., 2015; Evans et al., 2015; Gröller et al., 2015; England et al., 2017; Terada et al., 2017; Gilli et al., 2017; Bougher et al., 2017; Zurek et al., 2017; Thiemann et al., 2018; Gröller et al., 2018).

This points to some needs in the validation of the current GCMs at thermospheric altitudes. Possible biases in the model include a poor representation of gravity waves, although the problem is harder than that, since most, if not all, the datasets available nowadays for model validation share an important limitation. They do not cover the lower atmosphere, whose state has to be assumed, as it is not well determined. This is a serious limitation for reaching a convincing framework for mutual validation.

9.2. Conclusions

The main conclusions of this work are listed next:

1. This research successfully tackled and completed two ambitious tasks of the UPWARDS H2020 project: Task T1.3, related to the develop-

ment of innovative data analysis tools, concretely, the development of a non-LTE inversion scheme for Mars limb infrared emissions; and Task 7.1, related to the scientific exploitation of a unique dataset from OMEGA/Mars Express (its observations of infrared emissions in a limb geometry at thermospheric altitudes), in order to derive for the first time CO_2 density profiles from such a complex dataset.

2. A total of 47 OMEGA SWIR L limb *qubes* were analysed in detail, including corrections in the calibration pipeline of the OMEGA Team. Radiance vertical profiles, or Level 1 OMEGA limb spectra, were built from the unevenly spaced projection of the instrument's 2-D detector on the limb. These profiles exploited the excellent vertical resolution of OMEGA and incorporated the calibration improvements. The 1-D profiles are the basic input of our inversion scheme and can also be useful for other future studies. They were released to the ESA Planetary Science Archive, where they are open to the scientific community, as a data-product of the UPWARDS project.

3. The non-LTE scheme for Mars is entirely based on the KOPRA-GRANADA-RCP scheme used for inversion of limb infrared emissions of Earth's upper atmosphere with MIPAS/Envisat, although some adaptation was needed for Martian conditions. One of the key ingredients of the foward model is the non-LTE model for CO_2 vibrational populations. We used the GRANADA code, after its comparison and fine-tuning with a specific non-LTE model for Mars and Venus, also developed by our team and applied to Mars in numerous previous studies. Comparisons of the best fit spectra with the data indicate no biases (within measurement noise), which gives us confidence on this code's adaptation to OMEGA and Mars' atmosphere. This non-LTE model is now ready for further application to remote sounding of any CO_2 atmosphere, like Mars' or Venus'.

4. The application of the non-LTE retrieval scheme to the 47 OMEGA data *qubes* was successful, after tuning and experimenting with numerous internal parameters. The altitude range of the inversion was fixed at 120–180 km, where a high degree of convergence with a small number of iteration steps was achieved. The iteration started from a first guess profile extracted from simulations of the LMD-MGCM for the locations and Mars Year (dust and solar flux conditions) cor-

responding to every data profile. This was also used as *a priori*. The vertical resolution of the inverted profile was typically about 15 km, as calculated from the full width at half maximum of the averaging kernels, which critically depends on the spectral resolution and on the sensitivity of the instrument. The retrieval code is now ready for direct application to similar datasets, like measurements by the instrument PFS on board Mars Express, the recent limb emission measurements by NOMAD-LNO on board ExoMars, or an entirely similar set of limb measurements also at 4.3 μm of Venus' upper atmosphere taken by the instrument VIRTIS/Venus Express.

5. The extensive error analysis performed, including sensitivity to non-LTE parameters, indicates that the total uncertainty in the retrieved CO_2 densities varies between 20% and 35%, at 120 and 180 km, respectively. The principal contributions to this uncertainty come from the instrumental Gain calibration and from the propagation of the measurement noise error. The individual sensitivities to other parameters uncertainties are significantly smaller. In particular, the sensitivity to the thermal structure extracted from the LMD-MGCM is about a third of the total error in density. This study, together with the description of the non-LTE retrieval scheme, was included in a manuscript led by the author of this Thesis and submitted to a special issue of Icarus, and is currently under revision by the authors once the reviewers submitted their comments.

6. The total number of 742 individual CO_2 profiles in the Mars thermosphere were retrieved and are presented. They correspond to an average of 16 profiles per OMEGA orbit. All of them have a physically meaningful shape, not far from the *a priori*, although on average the retrieved densities are larger than the model climatology, between 125 and 150 km, with largest differences of 75% around 135 km tangent altitude.

7. The distribution of the retrieved densities follows that of the instrument limb orbits, which is very patchy and irregular in a latitude/solar longitude/Mars Year frame. Within each orbit, the profiles obtained present a small dispersion, as expected given their close location and the same acquisition time. This dispersion increases with altitude as the measurement noise component dominates. On a larger scale, the variations in the CO_2 density coincide with those

in the LMD-MGCM. The study of the data-model biases does not show any global trend, nor seem to be correlated with any of the temporal or spatial dimensions, except for the solar zenith angle, as expected, since the weaker the solar irradiation the noisier are the retrieved profiles.

8. An algorithm was developed in this Thesis to derive temperature profiles from the retrieved densities, by assuming hydrostatic equilibrium, and it was presented and validated using densities and temperatures from the LMD-MGCM. The temperature profiles cover the same altitude range than the CO_2 retrievals and include an error calculation based on the CO_2 retrieved errors. The temperatures obtained from the OMEGA CO_2 retrievals present a larger dispersion than the densities above 130 km, and much larger than the LMD-MGCM collocated temperatures. This dispersion is particularly large around 150 km. A significant number of OMEGA orbits (60%) show a local minimum between 140 and 150 km, with very cold temperatures, which are not reproducible under usual climatic scenarios by the LMD-MGCM. On the opposite side, about 30% of the orbits exhibit a larger value of the temperature around 150 km. No correlation with location or time was found in these variations. Potential candidates to explain these differences include propagation of gravity waves from below, variations in dust content from the climatological values, deviations from hydrostatics due to wave activity, and model deficiencies in the local absorption of solar EUV radiation.

9. The hydrostatic algorithm developed in this Thesis is being currently applied to determine thermospheric temperatures from UV dayglow measurements by SPICAM/Mars Express, as part of an ongoing research by our team at IAA. The fist part of such project is the application to those dayglow emissions as simulated by the LMD-MGCM. This application demonstrated that the traditional derivation of temperatures from the scale height of the UV emissions is incorrect in the case of the CO Cameron bands, producing too warm values. A similar warning applies to the temperatures derived from the CO_2^+ UV doublet, affected by a small positive bias in the 175–225 km range, but larger errors outside these altitudes. This result may require a revision of results from diverse previous experiments.

10. Very recent and precise determinations of densities and temperatures from the MAVEN suite of instruments (NGIMS, EUVM and IUVS) are starting to be available. The different geometries, mode of sounding and altitude explored do not permit a proper collocation of observations with our OMEGA limb data though. However, some variations of the IUVS CO_2 densities with latitude at a fixed local time show similar trends than those in our dataset. A very indirect evaluation is also possible via their reported comparison with the LMD-MGCM, which they also used as first guess and ultimate theoretical source for comparison. All these experiments presented a larger variability than the model, which is consistent with our results. Their tentative explanations also coincide with our potential candidates, as they include gravity wave propagation (or deficiencies in their implementation into the LMD-MGCM), and unknown thermal structure of the Martian lower atmosphere. Another aspect of agreement is their reported total error. All those experiments reported uncertainties entirely similar to our more complex inversion technique, around 30% errors in the CO_2 density. These comparisons, together with the complete dataset of CO_2 and temperatures from OMEGA is part of a second manuscript led by the author of this Thesis, currently in preparation.

9.3. Future work

A few improvements are foreseen to extend the work presented in this Thesis:

1. *Extension of the retrievals below* 120 *km.* Extending the retrievals below 120 km may be possible, at least for a couple of scale heights. This would have two scientifically interesting benefits, in addition to the obvious advantage of extending the exploitation of these measurements in the vertical. The first one is to cover the upper mesosphere, 90–120 km, a particularly difficult region for sounding, well below the capability of MAVEN Deep Dip campaigns, and above the sounding region of MCS/MRO. Secondly, covering the homopause is of particular importance for extremely cold atmospheres. This extension will require an in-depth analysis of the non-linearity on density at these altitudes. We already did steps in that direction, by designing a tabulation of the non-LTE dependence on a few CO_2

profiles. Such a tabulation should give correct results close to these profiles and, far from them, at least reduce this effect below the level of other retrieval uncertainties.

2. *Increase of the signal-to-noise ratio to reduce oscillations.* Once the variability study is completed, one possibility is to reduce the spatial and temporal resolutions. Grouping some or all the 1-D radiance vertical profiles within each *qube* in future processing, and/or enlarging the binning in the vertical (from 2 km up to 5–7 km, about half the width of the averaging kernels) would produce an increase in the signal-to-noise ratio. This shall reduce the impact of the total CO_2 and temperature errors, and therefore smooth the derived profiles, at the expense of loosing some vertical resolution. This would be particularly beneficial for reducing the current dispersion in our hydrostatic temperatures, although we do not expect large impacts on the results presented here.

3. *Inclusion of the temperature as a retrieval parameter.* Performing joint retrievals of densities and temperatures is a capability of our non-LTE retrieval suite, which has been exploited in the past in thermospheric remote sounding on Earth (Bermejo-Pantaleón, 2011). In our CO_2 retrievals, the degrees of freedom are large enough to allow for such a possibility. This joint inversion may not produce more precise temperatures than the hydrostatic method, because the dependence of the spectral fit on the temperature is small. However, this would provide a direct measurement of the temperature free from the hydrostatic approximation, and could also improve the density retrieval itself. For example, the double-peak shape of the residuals observed around 4.30 μm should soften if the temperature is modified towards colder values during the retrieval iterative process.

4. *Expansion to other instruments and/or observational geometries.* An exciting application is to process a number of datasets available from other instruments sounding limb emissions, which remain unexploited. This is the case of PFS on board Mars Express and the VIRTIS instrument on board Venus Express. Our scheme is specially suited to apply an optimal estimator to vertical profiles. Measurements performed in very different geometries, like along track limb-pointing measurements, the case of some of the PFS limb datasets, cannot benefit from this capability, and will present larger uncer-

tainties due to the lack of constraints in the vertical. However, the few PFS nearly-vertical profiles should be particularly interesting. In addition, the LNO channel of the NOMAD spectrometer on board ExoMars Trace Gas Orbiter is obtaining limb infrared non-LTE emissions by CO_2, which are being calibrated and analysed by our team, and which will welcome a direct application of our inversion scheme. This is an ongoing research, whose first results will be presented in the EPSC-DPS Joint Meeting 2019, in Geneve.

A

CO_2 vibrational bands included in the model

Table A.1: Vibrational bands included in the model for the most abundant isotopologues of CO_2 (626, 636, 628, 627, 638, 637).

CO_2 vibrational bands included in the model					
Isotope	**Band**	**Upper level**	**Lower level**	$\tilde{\nu}_0$ **(cm^{-1})**	A **(s^{-1})**
626	FB	(9) $00^{0}1$	(1) $00^{0}0$	2349.14	423.8
626	FH	(16) $01^{1}1$	(2) $01^{1}0$	2336.63	413.2
626	SH	(23) $02^{0}1$	(3) $02^{0}0$	2327.43	403.3
626	SH	(24) $02^{2}1$	(4) $02^{2}0$	2324.14	400.6
626	SH	(25) $10^{0}1$	(5) $10^{0}0$	2326.60	401.0
626	TH	(36) $03^{1}1$	(6) $03^{1}0$	2315.23	393.7
626	TH	(37) $03^{3}1$	(7) $03^{3}0$	2311.67	386.2
626	TH	(38) $11^{1}1$	(8) $11^{1}0$	2313.77	390.7

continued on next page

Table A.1 – continued from previous page

Isotope	Band	Upper level	Lower level	$\tilde{\nu}_0$ (cm^{-1})	A (s^{-1})
626	FrH	(43) $04^{0}1$	(10) $04^{0}0$	2305.26	385.0
626	FrH	(44) $04^{2}1$	(11) $04^{2}0$	2302.97	380.4
626	FrH	(47) $04^{4}1$	(13) $04^{4}0$	2299.21	370.2
626	FrH	(48) $12^{0}1$	(12) $12^{0}0$	2306.70	379.5
626	FrH	(49) $12^{2}1$	(14) $12^{2}0$	2301.06	378.4
626	FrH	(50) $20^{0}1$	(15) $20^{0}0$	2302.52	380.0
626	FiH	(54) $05^{1}1$	(17) $05^{1}0$	2293.61	364.5
626	FiH	(56) $05^{3}1$	(18) $05^{3}0$	2290.68	368.4
626	FiH	(57) $05^{5}1$	(20) $05^{5}0$	2286.80	352.8
626	FiH	(58) $13^{1}1$	(19) $13^{1}0$	2293.41	370.7
626	FiH	(59) $13^{3}1$	(21) $13^{3}0$	2288.39	364.5
626	FiH	(60) $21^{1}1$	(22) $21^{1}0$	2289.90	369.5
626	SiH	(64) $06^{0}1$	(26) $06^{0}0$	2283.30	367.9
626	SiH	(65) $06^{2}1$	(27) $06^{2}0$	2281.67	364.5
626	SiH	(66) $06^{4}1$	(28) $06^{4}0$	2278.39	353.2
626	SiH	(68) $14^{0}1$	(29) $14^{0}0$	2285.37	360.5
626	SiH	(69) $06^{6}1$	(31) $06^{6}0$	2274.42	333.4
626	SiH	(70) $14^{2}1$	(30) $14^{2}0$	2280.62	359.7
626	SiH	(71) $22^{0}1$	(32) $22^{0}0$	2283.58	358.7
626	SiH	(73) $14^{4}1$	(33) $14^{4}0$	2275.84	349.1
626	SiH	(74) $22^{2}1$	(34) $22^{2}0$	2277.17	357.4
626	SiH	(75) $30^{0}1$	(35) $30^{0}0$	2277.98	359.8
626	FHv_3	(39) $00^{0}2$	(9) $00^{0}1$	2324.18	413.6
626	FHv_3FH	(51) $01^{1}2$	(16) $01^{1}1$	2311.70	806.5
626	FHv_3SH	(61) $02^{0}2$	(23) $02^{0}1$	2302.37	787.4
626	FHv_3SH	(62) $02^{2}2$	(24) $02^{2}1$	2299.24	781.8

continued on next page

Table A.1 – continued from previous page

Isotope	Band	Upper level	Lower level	$\tilde{\nu}_0$ (cm^{-1})	A (s^{-1})
626	FHv_3SH	(63) $10^{0}2$	(25) $10^{0}1$	2301.91	782.2
626	FHv_3TH	(76) $03^{1}2$	(36) $03^{1}1$	2290.25	768.4
626	FHv_3TH	(77) $03^{3}2$	(37) $03^{3}1$	2286.80	753.6
626	FHv_3TH	(78) $11^{1}2$	(38) $11^{1}1$	2289.08	762.0
626	SHv_3	(79) $00^{0}3$	(39) $00^{0}2$	2299.26	1211.0
626	SHv_3FH	(93) $01^{1}3$	(51) $01^{1}2$	2286.80	1177.0
626	other	(9) $00^{0}1$	(3) $02^{0}0$	1063.73	0.5
626	other	(9) $00^{0}1$	(5) $10^{0}0$	960.96	0.4
626	other	(16) $01^{1}1$	(8) $11^{1}0$	927.16	0.4
626	other	(23) $02^{0}1$	(5) $10^{0}0$	2224.66	0.4
626	other	(23) $02^{0}1$	(12) $12^{0}0$	941.70	0.4
626	other	(24) $02^{2}1$	(14) $12^{2}0$	898.55	0.3
626	other	(25) $10^{0}1$	(3) $02^{0}0$	2429.37	0.2
626	other	(25) $10^{0}1$	(12) $12^{0}0$	1043.64	0.6
626	other	(25) $10^{0}1$	(15) $20^{0}0$	917.65	0.6
626	other	(54) $05^{1}1$	(19) $13^{1}0$	2135.72	0.3
626	other	(56) $05^{3}1$	(21) $13^{3}0$	2089.09	0.09
626	other	(58) $13^{1}1$	(17) $05^{1}0$	2451.30	0.05
626	other	(58) $13^{1}1$	(22) $21^{1}0$	2132.09	0.3
626	other	(59) $13^{3}1$	(18) $05^{3}0$	2489.98	0.05
626	other	(64) $06^{0}1$	(29) $14^{0}0$	2133.44	0.4
626	other	(65) $06^{2}1$	(30) $14^{2}0$	2095.77	0.2
626	other	(68) $14^{0}1$	(26) $06^{0}0$	2435.24	0.08
626	other	(68) $14^{0}1$	(32) $22^{0}0$	2163.64	0.9
626	other	(70) $14^{2}1$	(34) $22^{2}0$	2091.17	0.2
626	other	(71) $22^{0}1$	(29) $14^{0}0$	2405.31	0.3

continued on next page

Table A.1 – continued from previous page

Isotope	Band	Upper level	Lower level	$\tilde{\nu}_0$ (cm^{-1})	A (s^{-1})
626	other	(71) $22^{0}1$	(35) $30^{0}0$	2122.76	0.3
636	FB	(9) $00^{0}1$	(1) $00^{0}0$	2283.49	376.6
636	FH	(16) $01^{1}1$	(2) $01^{1}0$	2271.76	367.4
636	SH	(23) $02^{0}1$	(3) $02^{0}0$	2261.91	359.6
636	SH	(24) $02^{2}1$	(4) $02^{2}0$	2260.05	356.4
636	SH	(25) $10^{0}1$	(5) $10^{0}0$	2262.85	355.5
636	TH	(36) $03^{1}1$	(6) $03^{1}0$	2250.69	330.2
636	TH	(37) $03^{3}1$	(7) $03^{3}0$	2248.36	343.8
636	TH	(38) $11^{1}1$	(8) $11^{1}0$	2250.60	346.7
636	FrH	(43) $04^{0}1$	(10) $04^{0}0$	2240.54	344.1
636	FrH	(44) $04^{2}1$	(11) $04^{2}0$	2239.30	340.5
636	FrH	(47) $04^{4}1$	(13) $04^{4}0$	2236.68	329.8
636	FrH	(48) $12^{0}1$	(12) $12^{0}0$	2242.32	337.6
636	FrH	(49) $12^{2}1$	(14) $12^{2}0$	2238.57	336.1
636	FrH	(50) $20^{0}1$	(15) $20^{0}0$	2240.76	336.0
636	other	(9) $00^{0}1$	(3) $02^{0}0$	1017.66	0.2
636	other	(9) $00^{0}1$	(5) $10^{0}0$	913.43	0.4
636	other	(16) $01^{1}1$	(6) $03^{1}0$	1023.70	0.3
636	other	(23) $02^{0}1$	(5) $10^{0}0$	2157.68	0.2
636	other	(25) $10^{0}1$	(3) $02^{0}0$	2367.08	0.09
628	FB	(9) $00^{0}1$	(1) $00^{0}0$	2332.11	418.7
628	FH	(16) $01^{1}1$	(2) $01^{1}0$	2319.74	408.8
628	SH	(23) $02^{0}1$	(3) $02^{0}0$	2311.71	398.2
628	SH	(24) $02^{2}1$	(4) $02^{2}0$	2307.38	795.2
628	SH	(25) $10^{0}1$	(5) $10^{0}0$	2309.29	397.8
628	other	(9) $00^{0}1$	(5) $10^{0}0$	966.27	0.3

continued on next page

Table A.1 – concluded from previous page

Isotope	Band	Upper level	Lower level	$\tilde{\nu}_0$ (cm^{-1})	A (s^{-1})
628	other	(16) 01^11	(8) 11^10	932.77	0.3
627	FB	(9) 00^01	(1) 00^00	2340.01	409.1
627	FH	(16) 01^11	(2) 01^10	2327.58	399.0
627	SH	(23) 02^01	(3) 02^00	2318.96	388.8
627	SH	(24) 02^21	(4) 02^20	2322.79	788.8
627	SH	(25) 10^01	(5) 10^00	2317.32	387.5
627	other	(9) 00^01	(5) 10^00	963.99	0.3
638	FB	(9) 00^01	(1) 00^00	2265.97	369.4
637	FB	(9) 00^01	(1) 00^00	2274.09	380.6

end of the table

Isotopologues are sorted according to their relative abundances ($^{12}C^{16}O_2$, $^{13}C^{16}O_2$, $^{16}O^{12}C^{18}O$, $^{16}O^{12}C^{17}O$, $^{16}O^{13}C^{18}O$, $^{16}O^{13}C^{17}O$). FB stands for fundamental band, FH for first hot ($v_d = 1$), SH for second hot ($v_d = 2$), TH for third hot ($v_d = 3$), FrH for fourth hot ($v_d = 4$), FiH for fifth hot ($v_d = 5$), SiH for sixth hot ($v_d = 6$), FHv_3 for v_3-FH ($v_3 = 2$), FHv_3FH for v_3-FH v_d-FH ($v_3 = 2$, $v_d = 1$), FHv_3SH for v_3-FH v_d-SH ($v_3 = 2$, $v_d = 2$), FHv_3TH for v_3-FH v_d-TH ($v_3 = 2$, $v_d = 3$), SHv_3 for v_3-SH ($v_3 = 3$), and SHv_3FH for v_3-SH v_d-FH ($v_3 = 3$, $v_d = 1$). Energy levels are given with the HITRAN identifier number (in parenthesis) and the Herzberg notation. $\tilde{\nu}_0$ is the band center. A is the Einstein-A coefficient of the transition, independent of isotopologue abundances (Rothman et al., 2013).

B

CO_2 density retrievals

Here we show the radiance vertical profiles at 4.30 μm and the retrieved CO_2 densities for the entire set of 47 OMEGA orbits. For individual cases of study and a general discussion of the profiles formation and the CO_2 density retrievals, please refer to sections 4.3 and 5.3.

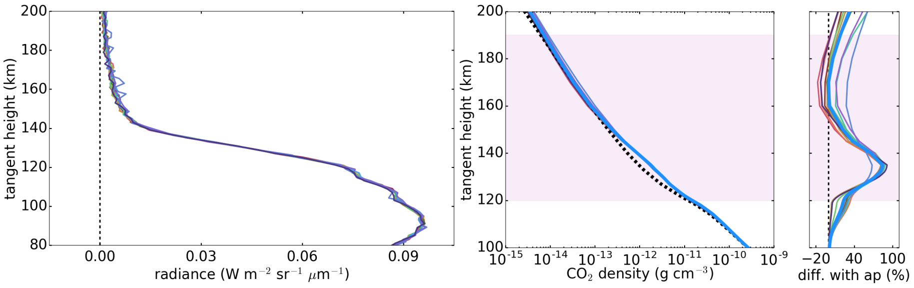

Figure B.1: *Left*: Radiances of all the vertical profiles generated for orbit 0044_1 at 4.30 μm. Each colour corresponds to an individual profile. *Right*: Densities retrieved for all the profiles of the same orbit, each of them with a different colour (solid). Their relative differences with the *a priori* density (dashed) are also shown. The average density of all the profiles in the orbit is represented by a thick blue line. The retrieved quantities contain measurements information only in the shaded region.

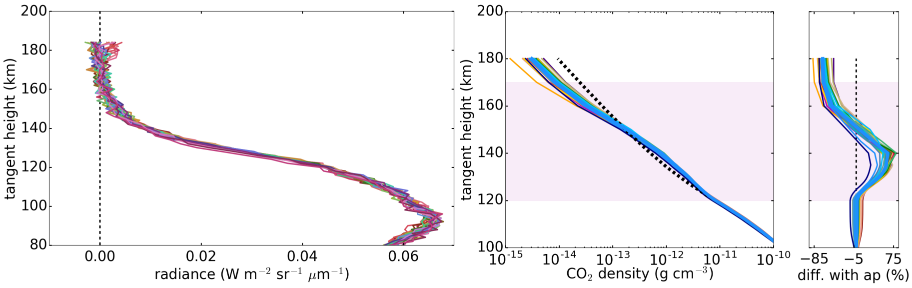

Figure B.2: Same as Figure B.1, for orbit 0285_0.

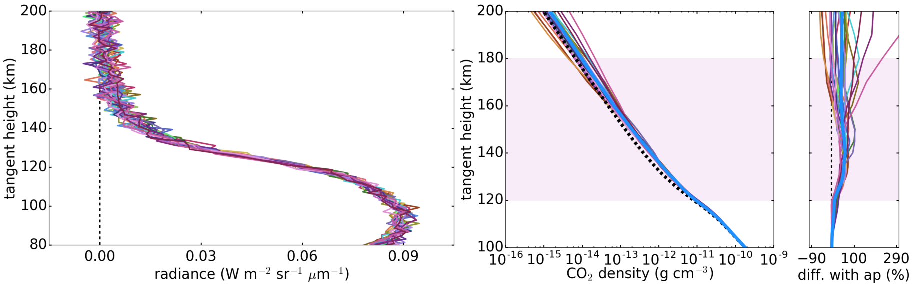

Figure B.3: Same as Figure B.1, for orbit 0330_2.

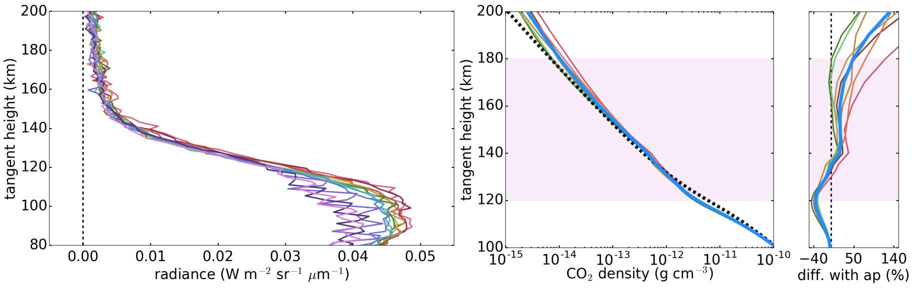

Figure B.4: Same as Figure B.1, for orbit 0647_1.

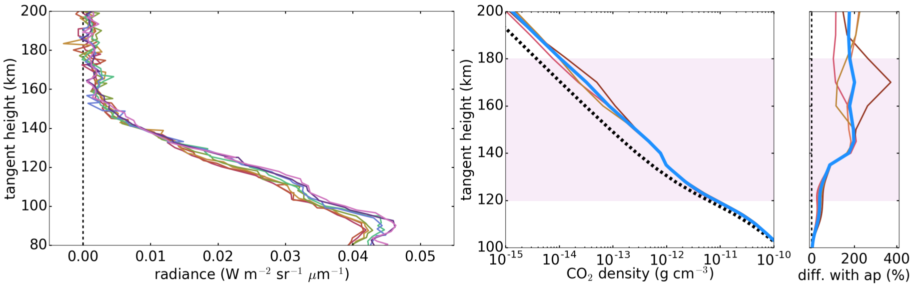

Figure B.5: Same as Figure B.1, for orbit 0961_0.

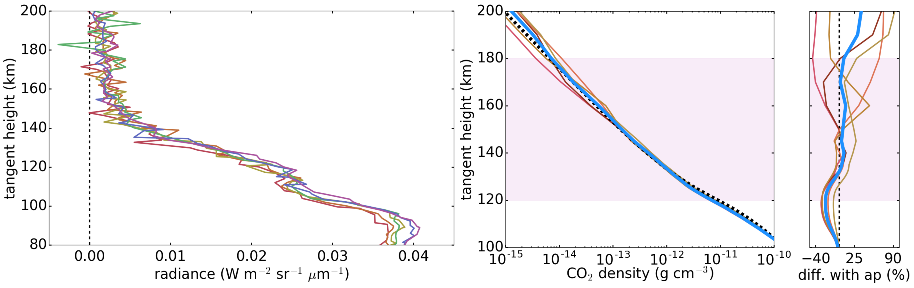

Figure B.6: Same as Figure B.1, for orbit 0964_0.

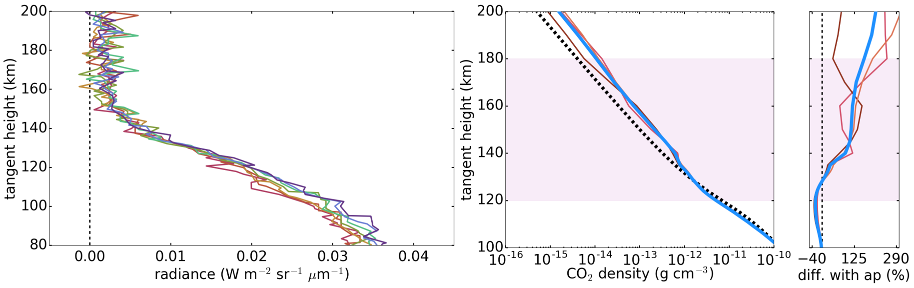

Figure B.7: Same as Figure B.1, for orbit 0965_0.

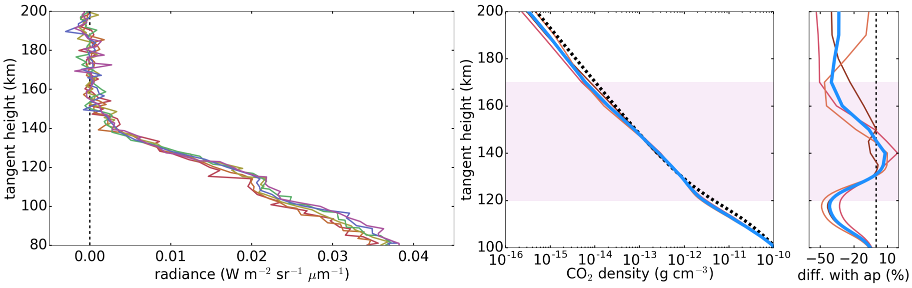

Figure B.8: Same as Figure B.1, for orbit 0966_0.

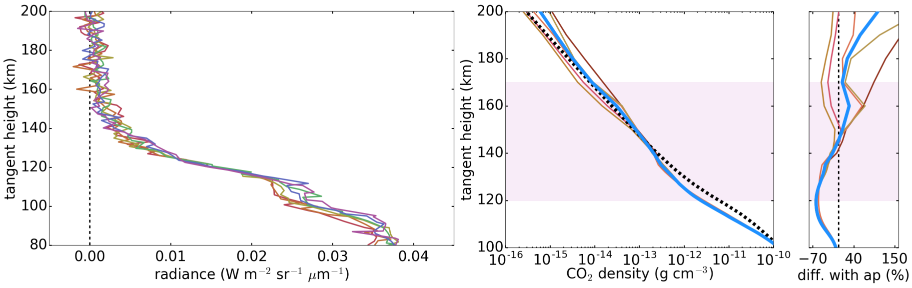

Figure B.9: Same as Figure B.1, for orbit 0967_0.

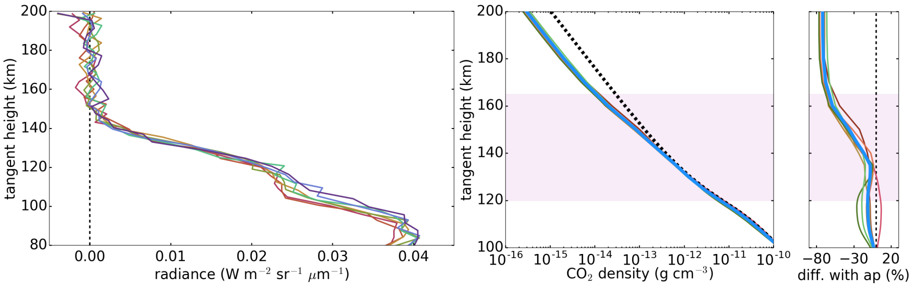

Figure B.10: Same as Figure B.1, for orbit 0970_0.

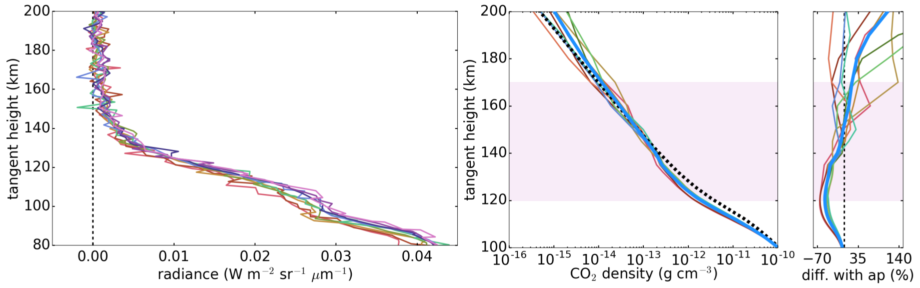

Figure B.11: Same as Figure B.1, for orbit 0971_0.

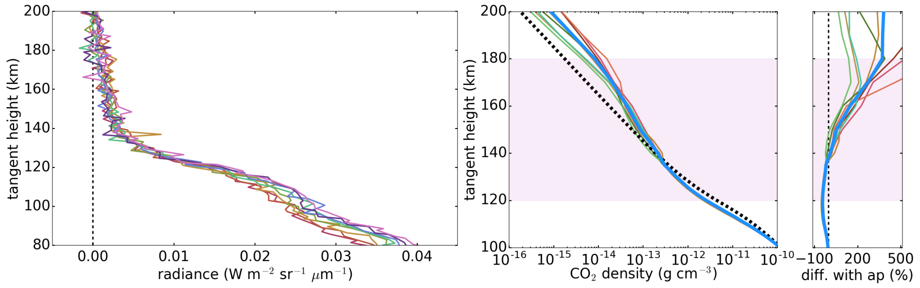

Figure B.12: Same as Figure B.1, for orbit 0973_0.

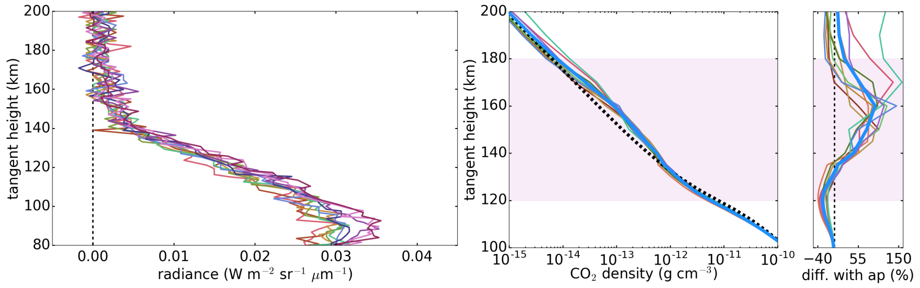

Figure B.13: Same as Figure B.1, for orbit 0975_0.

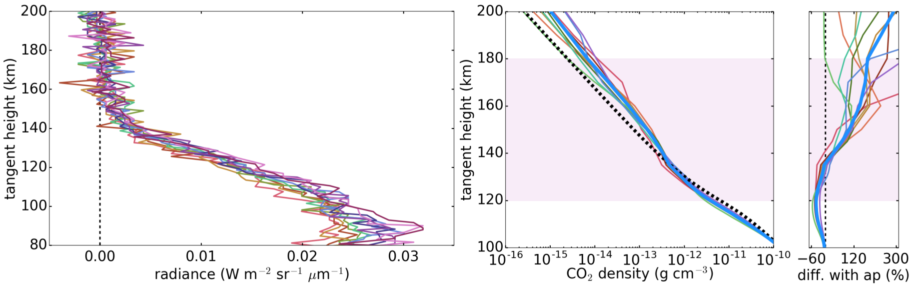

Figure B.14: Same as Figure B.1, for orbit 0978_0.

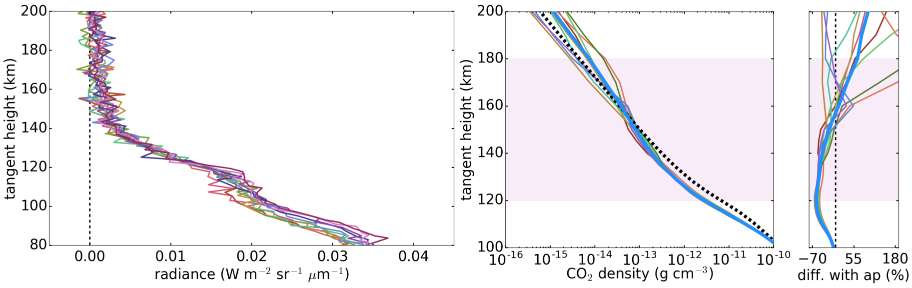

Figure B.15: Same as Figure B.1, for orbit 0979_0.

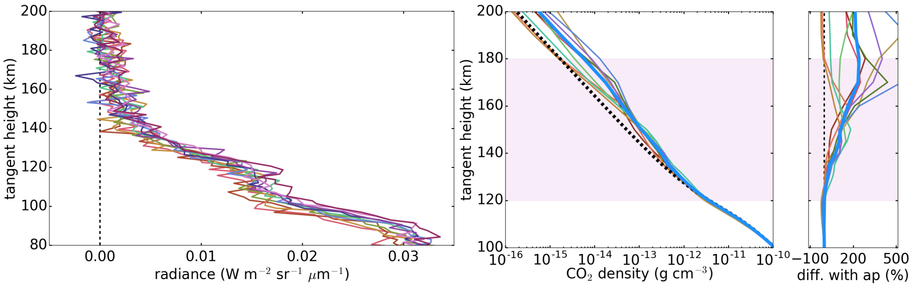

Figure B.16: Same as Figure B.1, for orbit 0982_0.

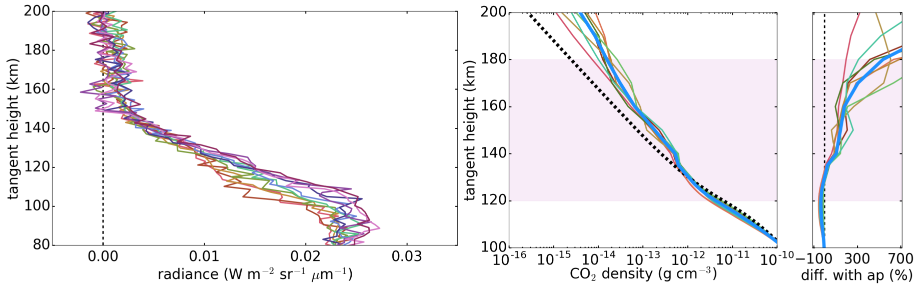

Figure B.17: Same as Figure B.1, for orbit 0989_0.

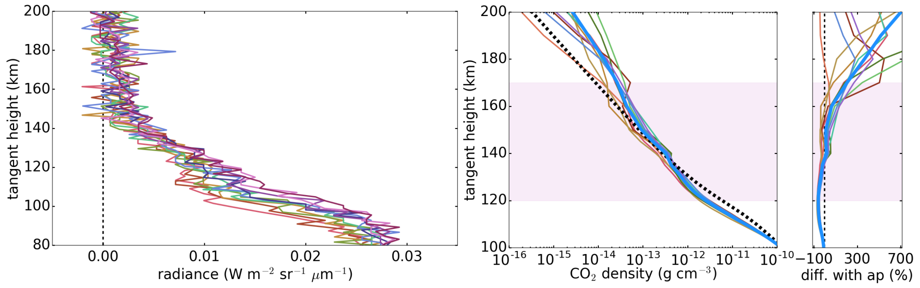

Figure B.18: Same as Figure B.1, for orbit 0998_0.

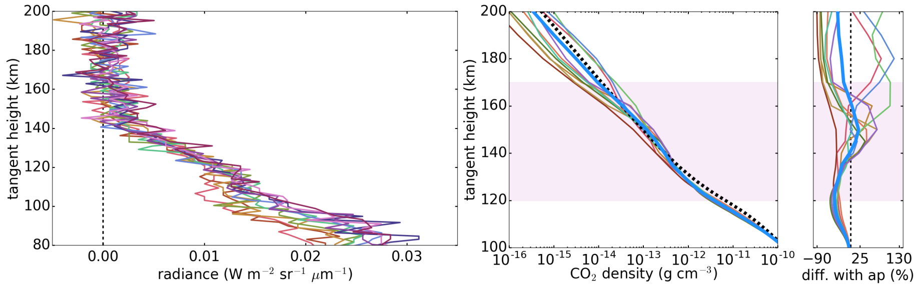

Figure B.19: Same as Figure B.1, for orbit 1001_0.

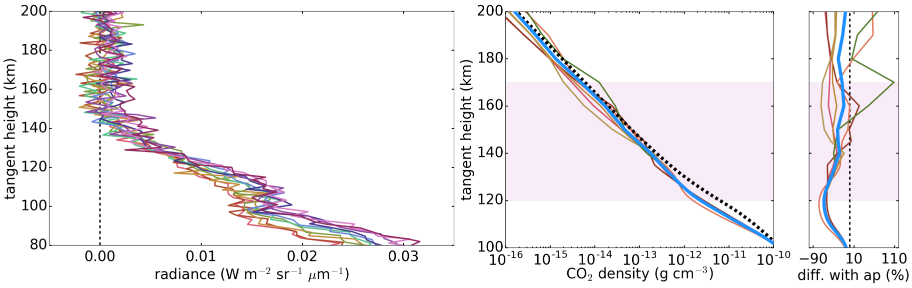

Figure B.20: Same as Figure B.1, for orbit 1002_0.

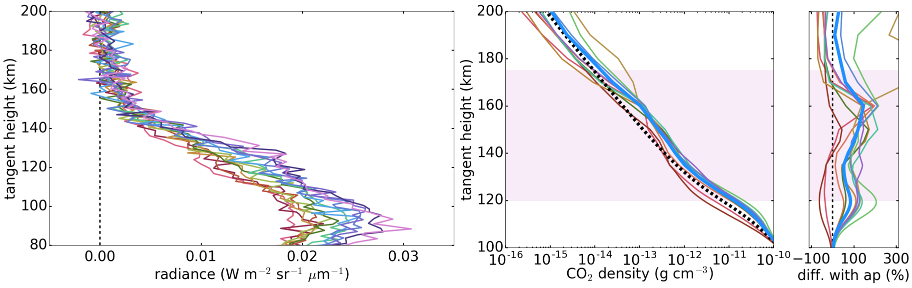

Figure B.21: Same as Figure B.1, for orbit 1008_0.

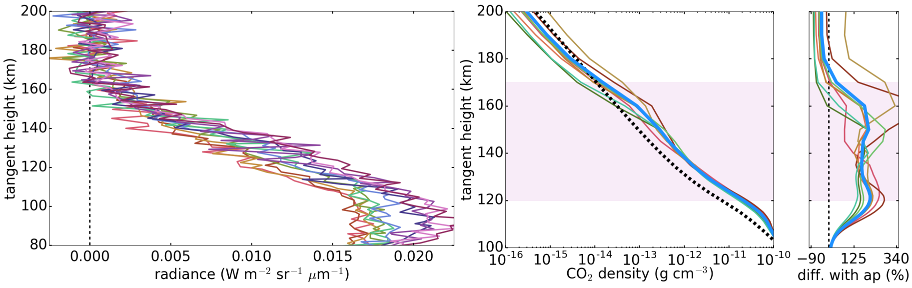

Figure B.22: Same as Figure B.1, for orbit 1012_0.

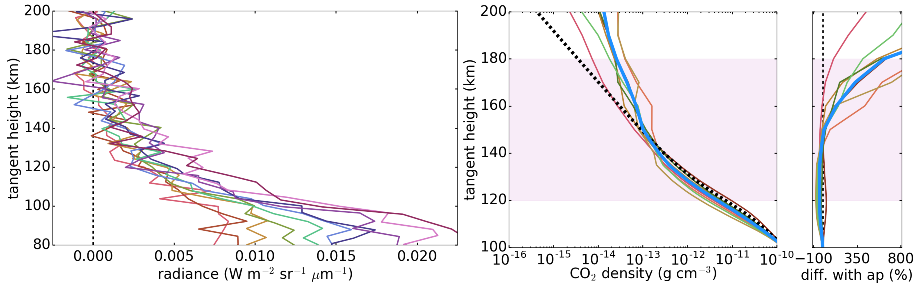

Figure B.23: Same as Figure B.1, for orbit 1023_0.

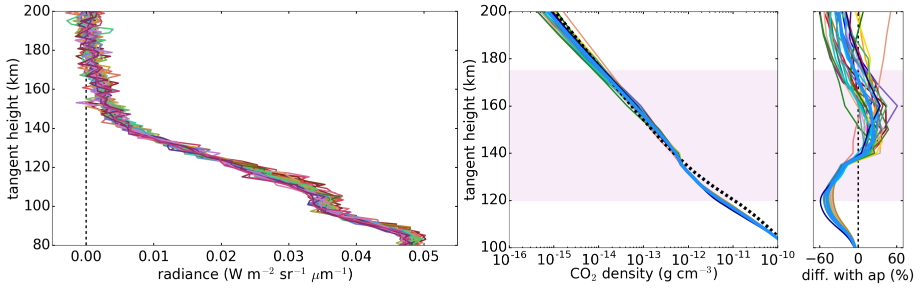

Figure B.24: Same as Figure B.1, for orbit 1084_0.

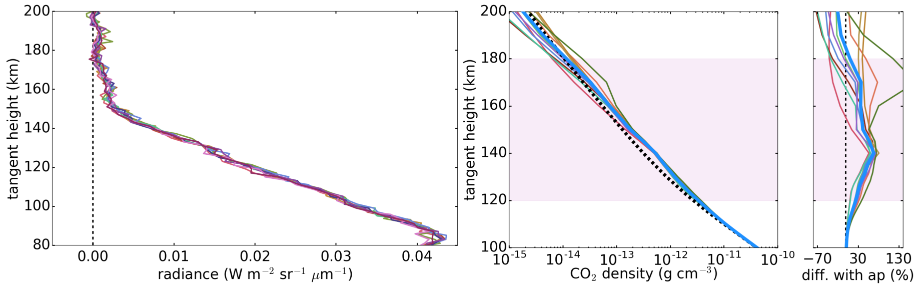

Figure B.25: Same as Figure B.1, for orbit 1402_0.

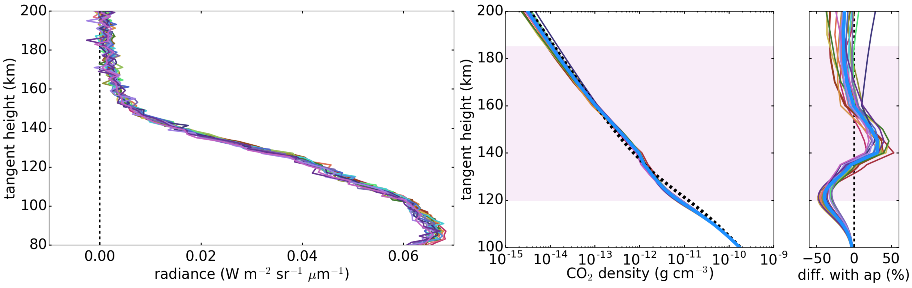

Figure B.26: Same as Figure B.1, for orbit 1619_4.

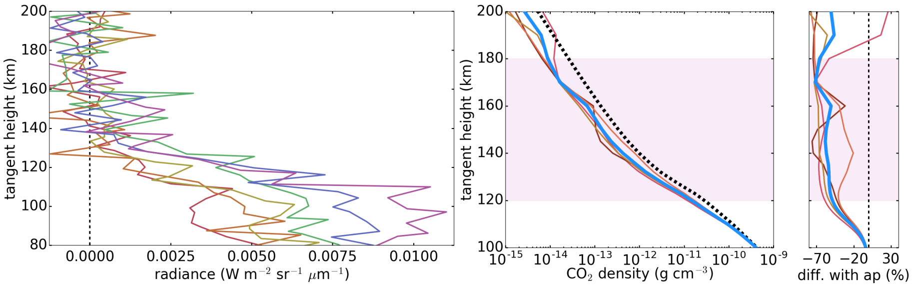

Figure B.27: Same as Figure B.1, for orbit 1880_1.

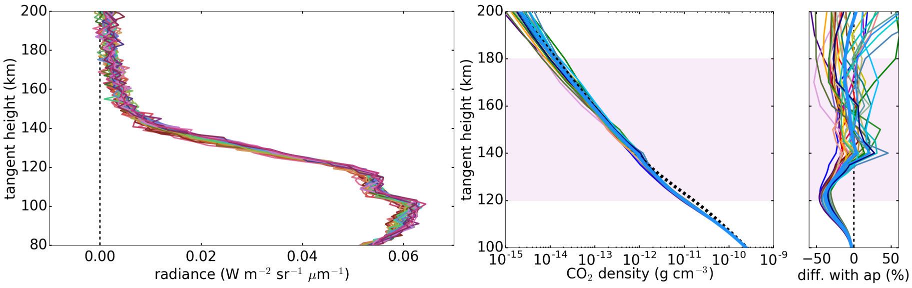

Figure B.28: Same as Figure B.1, for orbit 2547_2.

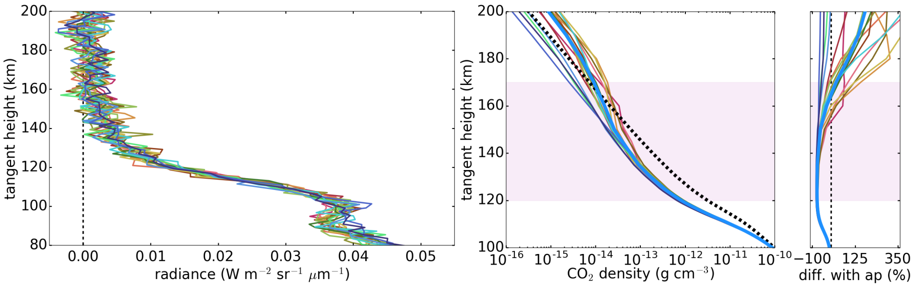

Figure B.29: Same as Figure B.1, for orbit 5851_0.

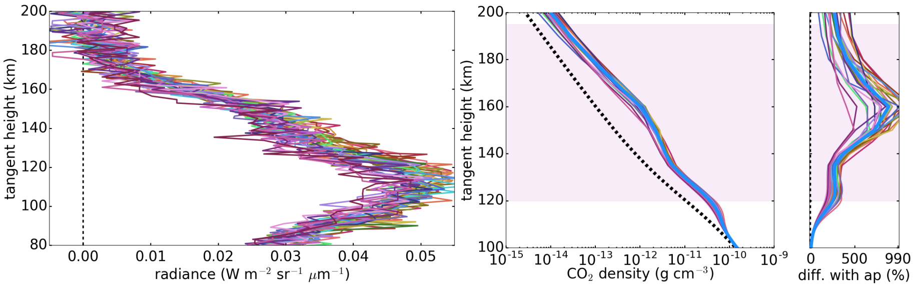

Figure B.30: Same as Figure B.1, for orbit 6020_1.

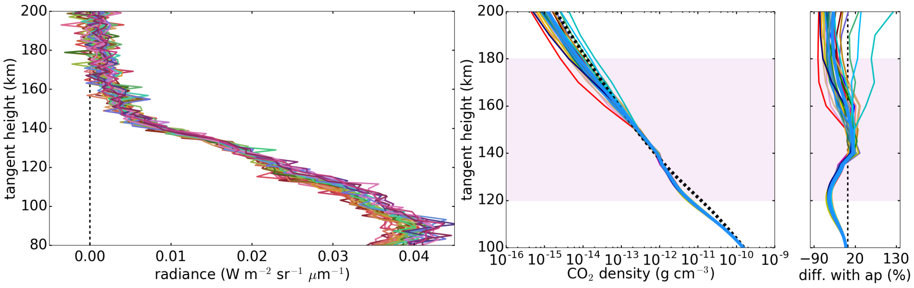

Figure B.31: Same as Figure B.1, for orbit 6071_1.

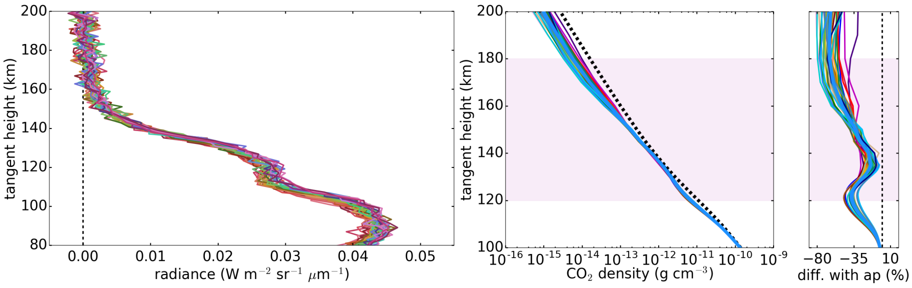

Figure B.32: Same as Figure B.1, for orbit 6104_1.

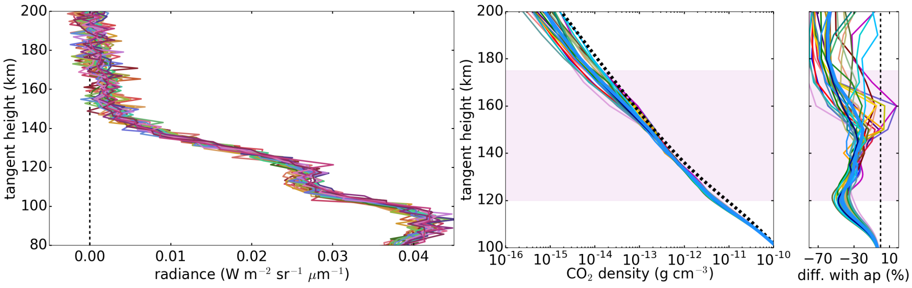

Figure B.33: Same as Figure B.1, for orbit 6126_1.

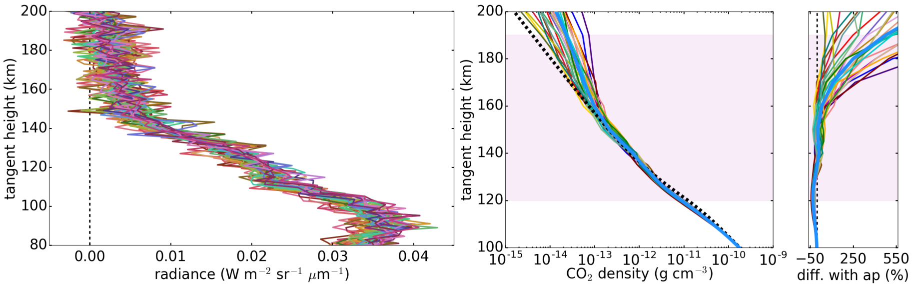

Figure B.34: Same as Figure B.1, for orbit 6146_0.

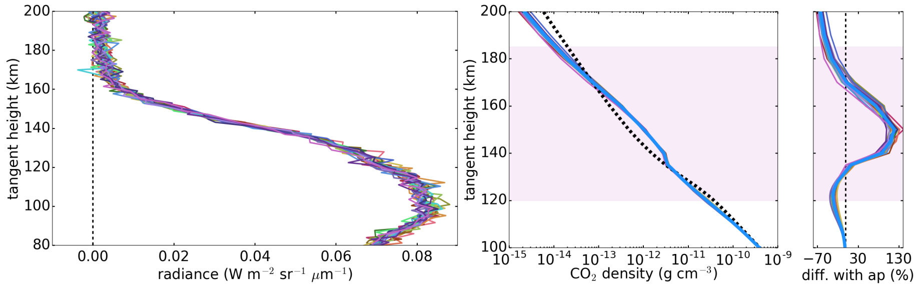

Figure B.35: Same as Figure B.1, for orbit 6586_0.

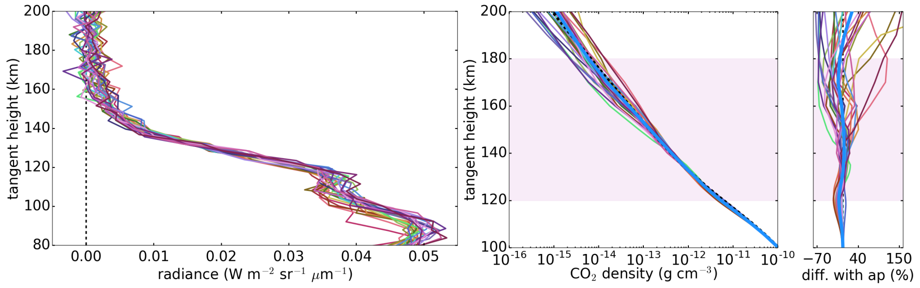

Figure B.36: Same as Figure B.1, for orbit 7554_4.

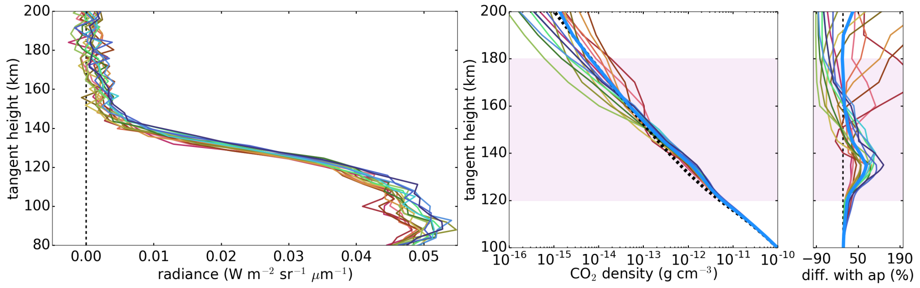

Figure B.37: Same as Figure B.1, for orbit 7586_4.

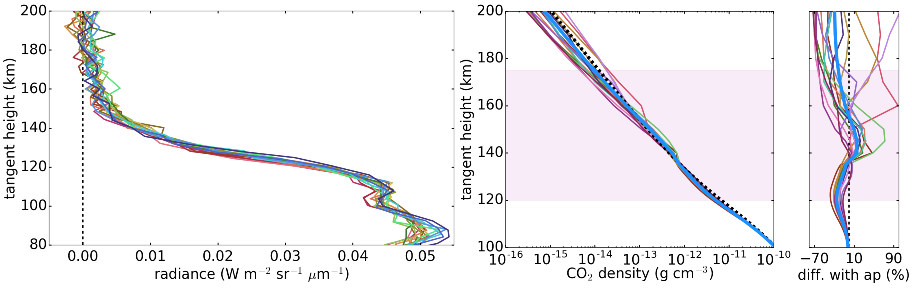

Figure B.38: Same as Figure B.1, for orbit 7597_4.

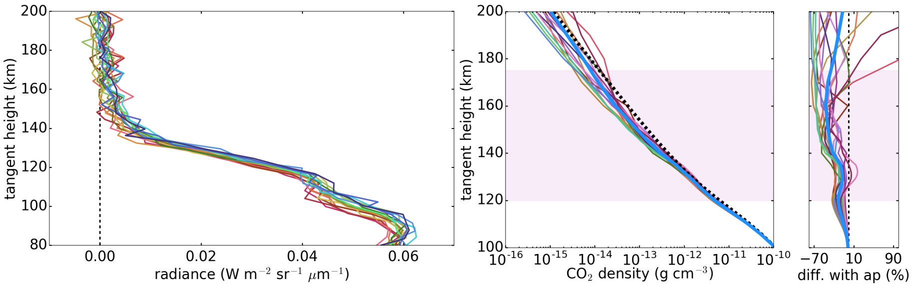

Figure B.39: Same as Figure B.1, for orbit 7604_4.

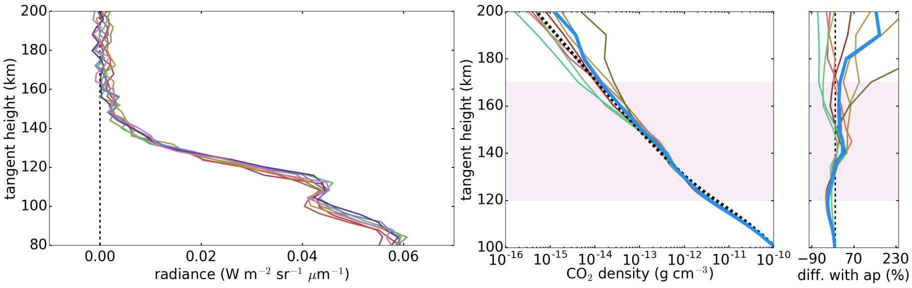

Figure B.40: Same as Figure B.1, for orbit 7619_4.

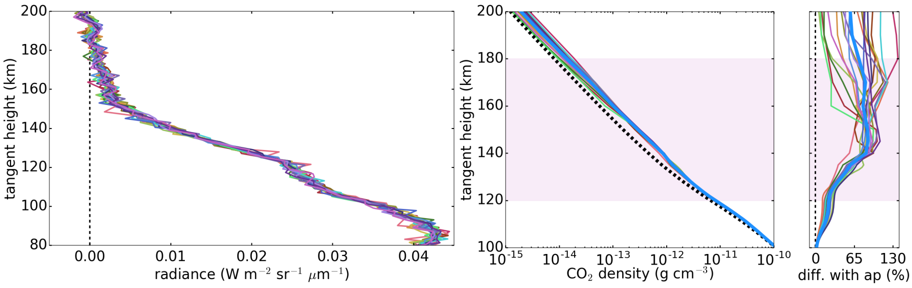

Figure B.41: Same as Figure B.1, for orbit 7679_0.

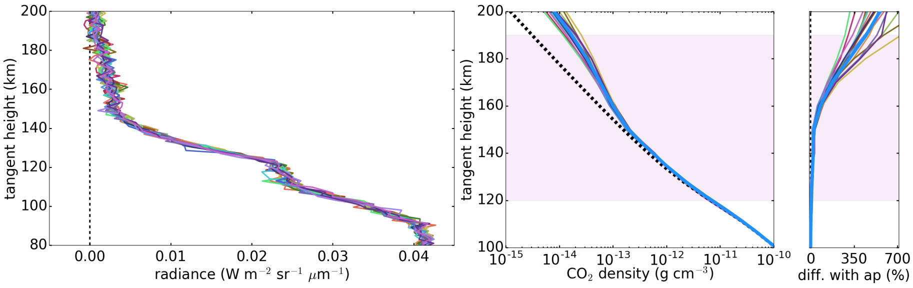

Figure B.42: Same as Figure B.1, for orbit 7686_0.

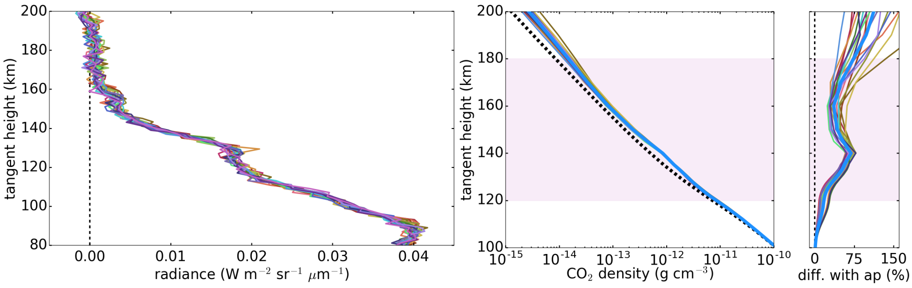

Figure B.43: Same as Figure B.1, for orbit 7697_0.

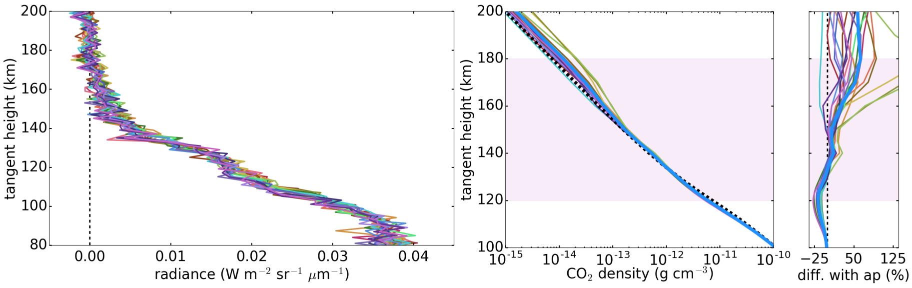

Figure B.44: Same as Figure B.1, for orbit 7701_0.

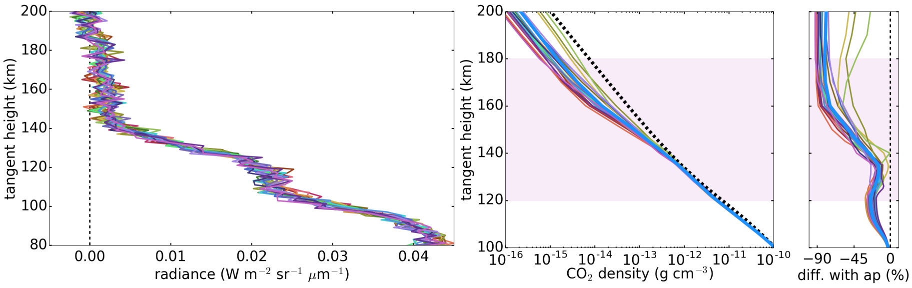

Figure B.45: Same as Figure B.1, for orbit 7708_0.

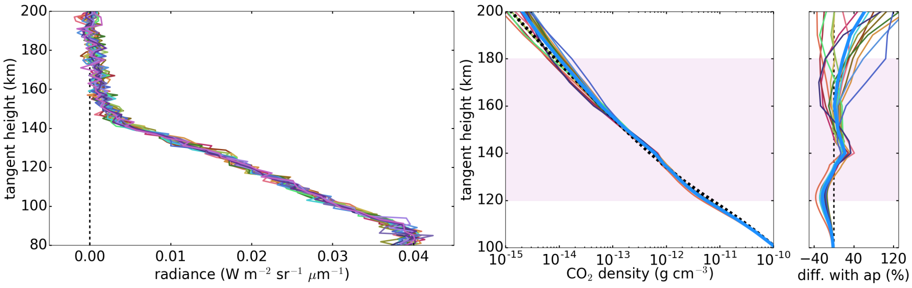

Figure B.46: Same as Figure B.1, for orbit 7715_0.

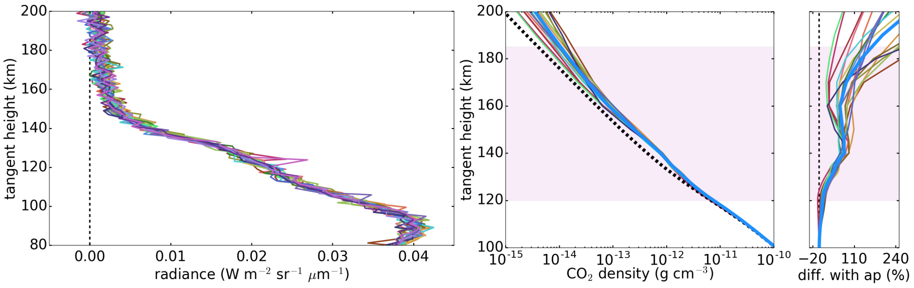

Figure B.47: Same as Figure B.1, for orbit 7718_0.

C

Software summary

Here we show a list of the relevant software utilised for the elaboration of this Thesis, grouped according to the purpose of its use:

- *Operating System*: Canonical ubuntu (Sobell, 2015).
- *OMEGA orbital data correction and calibration*: IDL (`https://www.harrisgeospatial.com/Software-Technology/IDL`).
- *Data inspection*: Meld (`https://meldmerge.org/`), GNU Octave (Eaton et al., 2016).
- *Preprocessing and clustering*: python (van Rossum, 1995), with special contributions from the NumPy (Oliphant, 2006) and scikit-learn (Pedregosa et al., 2011) packages, Jupyter (Kluyver et al., 2016).
- *Routines or scripts to automate processes*: C (Kernighan, 1988), GNU Bash (GNU, 2007).
- *Image processing*: GIMP (The GIMP Development Team, 2019), INKSCAPE (`https://inkscape.org/`).
- *Inversion of radiance vertical profiles*: GRANADA (Funke et al., 2012), KOPRA (Stiller, 2002), RCP (von Clarmann et al., 2003). All three computational codes were programmed in fortran (Backus and Heising, 1964).

- *Data post-processing and visualization*: python (van Rossum, 1995), with special contributions from the NumPy (Oliphant, 2006) and matplotlib (Hunter, 2007) packages, Jupyter (Kluyver et al., 2016).
- *Scientific reports and Thesis*: LaTeX (Lamport, 1986).

Bibliography

A. Adriani, B. M. Dinelli, M. López-Puertas, M. García-Comas, M. L. Moriconi, and B. Funke. Distribution of HCN in Titan's atmosphere from non-LTE emission from CASSINI/VIMS observations at 3 μm. *Icarus*, 214:584–595, 2011. doi:10.1016/j.icarus.2011.04.016. URL `http://dx.doi.org/10.1016/j.icarus.2011.04.016`.

A. L. Albee, R. E. Arvidson, F. Palluconi, and T. Thorpe. Overview of the Mars Global Surveyor mission. *JGR*, 106(E10):23291–23316, Oct 2001. doi:10.1029/2000JE001306.

D. G. Andrews. *An Introduction to Atmospheric Physics*. Cambridge University Press, 2010.

J. C. Andrews-Hanna, R. J. Phillips, and M. T. Zuber. Meridiani Planum and the global hydrology of Mars. *Nature*, 446(7132):163–166, Mar 2007. doi:10.1038/nature05594.

F. Anguita. *Historia de Marte. Mito, exploración, futuro*. Editorial Planeta, 1998.

J. Audouard, F. Poulet, M. Vincendon, J.-P. Bibring, F. Forget, Y. Langevin, and B. Gondet. Mars surface thermal inertia and heterogeneities from OMEGA MEX. *Icarus*, 233:194–213, May 2014. doi:10.1016/j.icarus.2014.01.045.

J. W. Backus and W. P. Heising. Fortran. *IEEE Transactions on Electronic Computers*, (4):382–385, 1964.

C. N. Banwell. *Fundamentals of Molecular Spectroscopy*. McGraw-Hill Book Company, 1972.

S. Basu, M. I. Richardson, and R. J. Wilson. Simulation of the Martian dust cycle with the GFDL Mars GCM. *Journal of Geophysical Research (Planets)*, 109(E11):E11006, Nov 2004. doi:10.1029/2004JE002243.

J. K. Beatty, C. C. Petersen, and A. Chaikim. *The New Solar System*. Cambridge University Press, 1999.

G. Bellucci, F. Altieri, J. P. Bibring, G. Bonello, Y. Langevin, B. Gondet, and F. Poulet. OMEGA/Mars Express: Visual channel performances and data reduction techniques. *Planet. Space Sci.*, 54:675–684, 2006. doi:10.1016/j.pss.2006.03.006.

D. Bermejo-Pantaleón. *Nitric oxide and Temperature in the Thermosphere: MIPAS observations*. PhD thesis, Universidad de Granada, 2011.

J.-P. Bibring, Y. Langevin, F. Poulet, A. Gendrin, B. Gondet, M. Berthé, A. Soufflot, P. Drossart, M. Combes, G. Bellucci, V. Moroz, N. Mangold, B. Schmitt, OMEGA Team, S. Erard, O. Forni, N. Manaud, G. Poulleau, T. Encrenaz, T. Fouchet, R. Melchiorri, F. Altieri, V. Formisano, G. Bonello, S. Fonti, F. Capaccioni, P. Cerroni, A. Coradini, V. Kottsov, N. Ignatiev, D. Titov, L. Zasova, P. Pinet, C. Sotin, E. Hauber, H. Hoffman, R. Jaumann, U. Keller, R. Arvidson, J. Mustard, T. Duxbury, and F. Forget. Perennial water ice identified in the south polar cap of Mars. *Nature*, 428(6983):627–630, Apr 2004a. doi:10.1038/nature02461.

J.-P. Bibring, A. Soufflot, M. Berthé, Y. Langevin, B. Gondet, P. Drossart, M. Bouyé, M. Combes, P. Puget, A. Semery, G. Bellucci, V. Formisano, V. Moroz, V. Kottsov, G. Bonello, S. Erard, O. Forni, A. Gendrin, N. Manaud, F. Poulet, G. Poulleau, T. Encrenaz, T. Fouchet, R. Melchiori, F. Altieri, N. Ignatiev, D. Titov, L. Zasova, A. Coradini, F. Capacionni, P. Cerroni, S. Fonti, N. Mangold, P. Pinet, B. Schmitt, C. Sotin, E. Hauber, H. Hoffmann, R. Jaumann, U. Keller, R. Arvidson, J. Mustard, and F. Forget. OMEGA: Observatoire pour la Minéralogie, l'Eau, les Glaces et l'Activité. In A. Wilson and A. Chicarro, editors, *Mars Express: the Scientific Payload*, volume 1240 of *ESA Special Publication*, pages 37–49, Aug. 2004b.

G. Bonello, J. Pierre Bibring, A. Soufflot, Y. Langevin, B. Gondet, M. Berthé, and C. Carabetian. The ground calibration setup of OMEGA and VIRTIS experiments: description and performances. *Planetary and Space Science*, 53 (7):711–728, Jun 2005. doi:10.1016/j.pss.2005.02.002.

S. Bougher, M. Benna, E. Y. it, Y. Lee, M. Lopez-Valverde, F. Gonzalez-Galindo, P. Mahaffy, and K. Roeten. Comparisons Between MAVEN/NGIMS Thermospheric Winds and M-GITM Model Simulations: Processes Driving Winds. In *42nd COSPAR Scientific Assembly*, volume 42, pages C3.2–13–18, Jul 2018.

S. W. Bougher, J. M. Bell, J. R. Murphy, M. A. Lopez-Valverde, and P. G. Withers. Polar warming in the Mars thermosphere: Seasonal variations owing to changing insolation and dust distributions. *GRL*, 33(2):L02203, Jan 2006. doi:10.1029/2005GL024059.

S. W. Bougher, D. Pawlowski, J. M. Bell, S. Nelli, T. McDunn, J. R. Murphy, M. Chizek, and A. Ridley. Mars Global Ionosphere-Thermosphere

Model: Solar cycle, seasonal, and diurnal variations of the Mars upper atmosphere. *Journal of Geophysical Research (Planets)*, 120(2):311–342, Feb 2015. doi:10.1002/2014JE004715.

S. W. Bougher, K. J. Roeten, K. Olsen, P. R. Mahaffy, M. Benna, M. Elrod, S. K. Jain, N. M. Schneider, J. Deighan, E. Thiemann, F. G. Eparvier, A. Stiepen, and B. M. Jakosky. The structure and variability of mars dayside thermosphere from maven ngims and iuvs measurements: Seasonal and solar activity trends in scale heights and temperatures. *Journal of Geophysical Research: Space Physics*, 122(1):1296–1313, 2017. doi:10.1002/2016JA023454. URL `https://agupubs.onlinelibrary.wiley.com/doi/abs/10.1002/2016JA023454`.

S. Chandrasekhar. *Radiative transfer*. 1960.

A. R. Curtis. A statistical model for water–vapour absorption. *Q. J. Roy. Meteorol. Soc.*, 78:638–640, 1952.

A. R. Curtis. The computation of radiative heating rates in the atmosphere. *Proc. Royal Society of London, Ser. A*, 236:156–159, 1956.

J. W. Eaton, D. Bateman, S. Hauberg, and R. Wehbring. *GNU Octave version 4.2.0 manual: a high-level interactive language for numerical computations*, 2016. URL `http://www.gnu.org/software/octave/doc/interpreter`.

T. Encrenaz and C. Sotin. *Planetary and Space Science. Special issue on First results of the Planetary Fourier Spectrometer aboard the the Mars Express Mission*, volume 53 (10). August 2005. URL `https://science.sciencemag.org/content/307/5715#special-issue`.

Encyclopædia Britannica. Encyclopædia Britannica, 2019. URL `https://www.britannica.com/place/Mars-planet`. Online.

S. L. England, G. Liu, P. Withers, E. Yiğit, D. Lo, S. Jain, N. M. Schneider, J. Deighan, W. E. McClintock, P. R. Mahaffy, M. Elrod, M. Benna, and B. M. Jakosky. Simultaneous observations of atmospheric tides from combined in situ and remote observations at Mars from the MAVEN spacecraft. *Journal of Geophysical Research (Planets)*, 121(4):594–607, Apr 2016. doi:10.1002/2016JE004997.

S. L. England, G. Liu, E. Yiğit, P. R. Mahaffy, M. Elrod, M. Benna, H. Nakagawa, N. Terada, and B. Jakosky. MAVEN NGIMS observations of atmospheric gravity waves in the Martian thermosphere. *Journal of Geophysical Research (Space Physics)*, 122(2):2310–2335, Feb 2017. doi:10.1002/2016JA023475.

J. T. Erwin, S. Aoki, I. R. Thomas, L. Trompet, A. C. Vandaele, S. Robert, F. Daerden, B. Ristic, G. L. Villanueva, G. Liuzzi, J. J. Lopez-Moreno, G. Bellucci, and M. R. Patel. Martian Atmospheric Vertical Profiles: Results from the First Year of TGO/NOMAD Operations. *LPI Contributions*, 2089:6219, Jul 2019.

J. S. Evans, M. H. Stevens, J. D. Lumpe, N. M. Schneider, A. I. F. Stewart, J. Deighan, S. K. Jain, M. S. Chaffin, M. Crismani, A. Stiepen, W. E. McClintock, G. M. Holsclaw, F. Lefèvre, D. Y. Lo, J. T. Clarke, F. G. Eparvier, E. M. B. Thiemann, P. C. Chamberlin, S. W. Bougher, J. M. Bell, and B. M. Jakosky. Retrieval of CO_2 and N_2 in the Martian thermosphere using dayglow observations by IUVS on MAVEN. *GRL*, 42(21):9040–9049, Nov 2015. doi:10.1002/2015GL065489.

A. A. Fedorova, O. I. Korablev, J. L. Bertaux, A. V. Rodin, F. Montmessin, D. A. Belyaev, and A. Reberac. Solar infrared occultation observations by SPICAM experiment on Mars-Express: Simultaneous measurements of the vertical distributions of $H\ _2O$, $CO\ _2$ and aerosol. *Icarus*, 200(1):96–117, Mar 2009. doi:10.1016/j.icarus.2008.11.006.

F. Forget, F. Hourdin, R. Fournier, C. Hourdin, O. Talagrand, M. Collins, S. R. Lewis, P. L. Read, and J.-P. Huot. Improved general circulation models of the Martian atmosphere from the surface to above 80 km. *JGR*, 104(E10): 24155–24176, Oct 1999. doi:10.1029/1999JE001025.

F. Forget, F. Costard, and P. Lognonné. *Planet Mars: Story of Another World.* 2008.

F. Forget, F. Montmessin, J.-L. Bertaux, F. González-Galindo, S. Lebonnois, E. Quémerais, A. Reberac, E. Dimarellis, and M. A. López-Valverde. Density and temperatures of the upper Martian atmosphere measured by stellar occultations with Mars Express SPICAM. *Journal of Geophysical Research (Planets)*, 114(E1):E01004, Jan 2009. doi:10.1029/2008JE003086.

V. Formisano, S. Atreya, T. Encrenaz, N. Ignatiev, and M. Giuranna. Detection of Methane in the Atmosphere of Mars. *Science*, 306(5702):1758–1761, Dec 2004. doi:10.1126/science.1101732.

V. Formisano, A. Maturilli, M. Giuranna, E. D'Aversa, and M. A. López-Valverde. Observations of non-LTE emission at 4 5 microns with the planetary Fourier spectrometer abord the Mars Express mission. *Icarus*, 182:51–67, May 2006. doi:10.1016/j.icarus.2005.12.022.

B. Funke, M. López-Puertas, M. García-Comas, G. P. Stiller, T. von Clarmann, M. Höpfner, N. Glatthor, U. Grabowski, S. Kellmann, and A. Linden. Carbon monoxide distributions from the upper troposphere to the mesosphere inferred from 4.7μm non-local thermal equilibrium emissions measured by MIPAS on Envisat. 9(7):2387–2411, 2009.

B. Funke, M. López-Puertas, M. García-Comas, M. Kaufmann, M. Höpfner, and G. P. Stiller. GRANADA: A Generic RAdiative traNsfer AnD non-LTE population algorithm. *Journal of Quantitative Spectroscopy and Radiative Transfer*, 113:1771–1817, Sept. 2012. doi:10.1016/j.jqsrt.2012.05.001.

M. García-Comas, M. López-Puertas, B. Funke, B. Dinelli, M. L. Moriconi, A. Adriani, A. Molina, and A. Coradini. Analysis of Titan CH_4 3.3 μm upper atmospheric emission as measured by Cassini/VIMS. *Icarus*, 214:571–583, 2011. doi:10.1016/j.icarus.2011.03.020. URL `http://dx.doi.org/10.1016/j.icarus.2011.03.020`.

J. C. Gérard, S. W. Bougher, M. A. López-Valverde, M. Pätzold, P. Drossart, and G. Piccioni. Aeronomy of the Venus Upper Atmosphere. *SSR*, 212(3-4): 1617–1683, Nov 2017. doi:10.1007/s11214-017-0422-0.

G. Gilli, M. A. López-Valverde, P. Drossart, G. Piccioni, S. Erard, and A. Cardesín-Moinelo. Limb observations of CO_2 and CO non-LTE emissions in the Venus atmosphere by VIRTIS/Venus Express. *J. Geophys. Res.*, 114, 2009. doi:10.1029/2008JE003112.

G. Gilli, M. A. López-Valverde, J. Peralta, S. Bougher, A. Brecht, P. Drossart, and G. Piccioni. Carbon monoxide and temperature in the upper atmosphere of Venus from VIRTIS/Venus Express non-LTE limb measurements. *Icarus*, 248:478–498, Mar. 2015. doi:10.1016/j.icarus.2014.10.047.

G. Gilli, F. Forget, A. Spiga, T. Navarro, L. Montabone, and E. Millour. On the Impact of Non-Orographic Gravity Waves in the LMD Mars Global Climate Model. In *The Mars Atmosphere: Modelling and observation*, page 2104, Jan 2017.

P. GNU. Free software foundation. bash (3.2.48) [unix shell program], 2007.

W. L. Godson. The evaluation of infrared radiative fluxes due to atmospheric water vapour. *Q. J. R. Meteorol. Soc.*, 79:367–379, 1953.

F. González-Galindo. *Modelos energéticos, químicos y dinámicos de la alta atmósfera de Marte*. PhD thesis, Universidad de Granada, June 2006.

F. González-Galindo, F. Forget, M. Angelats I Coll, and M. A. López-Valverde. *The Martian upper atmosphere*, volume 3, pages 151–162. 2008.

F. González-Galindo, F. Forget, M. A. López-Valverde, M. Angelats i Coll, and E. Millour. A ground-to-exosphere Martian general circulation model: 1. Seasonal, diurnal, and solar cycle variation of thermospheric temperatures. *Journal of Geophysical Research (Planets)*, 114(E4):E04001, Apr 2009. doi:10.1029/2008JE003246.

F. González-Galindo, S. W. Bougher, M. A. López-Valverde, F. Forget, and J. Murphy. Thermal and wind structure of the Martian thermosphere as given by two General Circulation Models. *Planetary and Space Science*, 58(14-15): 1832–1849, Dec 2010. doi:10.1016/j.pss.2010.08.013.

F. González-Galindo, M. A. López-Valverde, F. Forget, M. García-Comas, E. Millour, and L. Montabone. Variability of the Martian thermosphere during eight Martian years as simulated by a ground-to-exosphere global circulation model. *Journal of Geophysical Research (Planets)*, 120:2020–2035, Nov. 2015. doi:10.1002/2015JE004925.

F. González-Galindo, J.-Y. Chaufray, F. Forget, M. García-Comas, F. Montmessin, S. K. Jain, and A. Stiepen. UV dayglow variability on Mars: Simulation with a Global Climate Model and comparison with SPICAM/MEx data. *Journal of Geophysical Research: Planets*, 123(7):1934–1952, 2018. doi:10.1029/2018JE005556. URL `https://agupubs.onlinelibrary.wiley.com/doi/abs/10.1029/2018JE005556`.

F. González-Galindo, S. Jiménez-Monferrer, M. A. López-Valverde, F. Forget, F. Montmessin, and J.-L. Bertaux. On the derivation of thermospheric temperatures from dayglow emissions on Mars: GCM study and application to SPICAM/MEx observations. *Icarus*, 2019. In preparation.

R. M. Goody and Y. L. Yung. *Atmospheric radiation : theoretical basis*. 1989.

H. Gröller, R. V. Yelle, T. T. Koskinen, F. Montmessin, G. Lacombe, N. M. Schneider, J. Deighan, A. I. F. Stewart, S. K. Jain, M. S. Chaffin, M. M. J. Crismani, A. Stiepen, F. Lefèvre, W. E. McClintock, J. T. Clarke, G. M. Holsclaw, P. R. Mahaffy, S. W. Bougher, and B. M. Jakosky. Probing the Martian atmosphere with MAVEN/IUVS stellar occultations. *GRL*, 42(21): 9064–9070, Nov 2015. doi:10.1002/2015GL065294.

H. Gröller, F. Montmessin, R. V. Yelle, F. Lefèvre, F. Forget, N. M. Schneider, T. T. Koskinen, J. Deighan, and S. K. Jain. MAVEN/IUVS Stellar Occultation Measurements of Mars Atmospheric Structure and Composition. *Journal of Geophysical Research (Planets)*, 123(6):1449–1483, Jun 2018. doi:10.1029/2017JE005466.

J. P. Grotzinger, D. Y. Sumner, L. C. Kah, K. Stack, S. Gupta, L. Edgar, D. Rubin, K. Lewis, J. Schieber, N. Mangold, R. Milliken, P. G. Conrad, D. DesMarais, J. Farmer, K. Siebach, F. Calef, J. Hurowitz, S. M. McLennan, D. Ming, D. Vaniman, J. Crisp, A. Vasavada, K. S. Edgett, M. Malin, D. Blake, R. Gellert, P. Mahaffy, R. C. Wiens, S. Maurice, J. A. Grant, S. Wilson, R. C. Anderson, L. Beegle, R. Arvidson, B. Hallet, R. S. Sletten, M. Rice, J. Bell, J. Griffes, B. Ehlmann, et al. A Habitable Fluvio-Lacustrine Environment at Yellowknife Bay, Gale Crater, Mars. *Science*, 343(6169):1242777, Jan 2014. doi:10.1126/science.1242777.

O. A. Gusev and A. A. Kutepov. Non-LTE Gas in Planetary Atmospheres. In I. Hubeny, D. Mihalas, and K. Werner, editors, *Stellar Atmosphere Modeling*, volume 288 of *Astronomical Society of the Pacific Conference Series*, page 318, Jan 2003.

R. M. Haberle. Estimating the power of Mars' greenhouse effect. *Icarus*, 223(1): 619–620, Mar 2013. doi:10.1016/j.icarus.2012.12.022.

R. M. Haberle, C. B. Leovy, and J. B. Pollack. Some effects of global dust storms on the atmospheric circulation of Mars. *Icarus*, 50(2-3):322–367, Jun 1982. doi:10.1016/0019-1035(82)90129-4.

R. M. Haberle, M. M. Joshi, J. R. Murphy, J. R. Barnes, J. T. Schofield, G. Wilson, M. Lopez-Valverde, J. L. Hollingsworth, A. F. C. Bridger, and J. Schaeffer. General circulation model simulations of the Mars Pathfinder atmospheric structure investigation/meteorology data. *JGR*, 104(E4):8957–8974, Apr 1999. doi:10.1029/1998JE900040.

P. Hartogh, A. S. Medvedev, T. Kuroda, R. Saito, G. Villanueva, A. G. Feofilov, A. A. Kutepov, and U. Berger. Description and climatology of a new general circulation model of the Martian atmosphere. *Journal of Geophysical Research (Planets)*, 110(E11):E11008, Nov 2005. doi:10.1029/2005JE002498.

G. Herzberg. *Molecular spectra and molecular structure. Vol.2: Infrared and Raman spectra of polyatomic molecules*. 1945.

J. T. Houghton. *The physics of atmospheres*. Cambridge: Cambridge University Press, 1977.

D. M. Hunten, R. O. Pepin, and J. C. G. Walker. Mass fractionation in hydrodynamic escape. *Icarus*, 69(3):532–549, Mar 1987. doi:10.1016/0019-1035(87)90022-4.

J. D. Hunter. Matplotlib: A 2D graphics environment. *Computing in Science & Engineering*, 9(3):90–95, 2007. doi:10.1109/MCSE.2007.55.

S. K. Jain, A. I. F. Stewart, N. M. Schneider, J. Deighan, A. Stiepen, J. S. Evans, M. H. Stevens, M. S. Chaffin, M. Crismani, W. E. McClintock, J. T. Clarke, G. M. Holsclaw, D. Y. Lo, F. Lefèvre, F. Montmessin, E. M. B. Thiemann, F. Eparvier, and B. M. Jakosky. The structure and variability of Mars upper atmosphere as seen in MAVEN/IUVS dayglow observations. *GRL*, 42(21): 9023–9030, Nov 2015. doi:10.1002/2015GL065419.

B. M. Jakosky, R. P. Lin, J. M. Grebowsky, J. G. Luhmann, D. F. Mitchell, G. Beutelschies, T. Priser, et al. The Mars Atmosphere and Volatile Evolution (MAVEN) Mission. *SSR*, 195(1-4):3–48, Dec 2015. doi:10.1007/s11214-015-0139-x.

B. M. Jakosky, D. Brain, M. Chaffin, S. Curry, J. Deighan, J. Grebowsky, J. Halekas, F. Leblanc, R. Lillis, J. G. Luhmann, et al. Loss of the Martian atmosphere to space: Present-day loss rates determined from MAVEN observations and integrated loss through time. *Icarus*, 315:146–157, Nov 2018. doi:10.1016/j.icarus.2018.05.030.

JGR. *Special issue on Observations of the Atmosphere of Mars with SPICAM Spectrometers on board Mars Express*. February 2018. URL `https://agupubs.onlinelibrary.wiley.com/doi/toc/10.1002/(ISSN)2169-9100.SPICAM1`.

S. Jiménez-Monferrer, M. A. López-Valverde, B. Funke, F. González-Galindo, A. Piccialli, M. García-Comas, M. López-Puertas, B. Gondet, and J.-P. Bibring. CO2 retrievals in the Mars daylight thermosphere from its 4.3 um limb emission measured by OMEGA/MEx. *Icarus*, 2019. Submitted.

D. Jouglet, F. Poulet, Y. Langevin, J.-P. Bibring, B. Gondet, M. Vincendon, and M. Berthe. OMEGA long wavelength channel: Data reduction during non-nominal stages. *Planetary and Space Science*, 57(8-9):1032–1042, Jul 2009. doi:10.1016/j.pss.2008.07.025.

A. A. Jurado-Navarro. *Retrieval of CO2 and collisional parameters from the MIPAS spectra in the Earth atmosphere*. PhD thesis, Universidad de Granada, 2015.

A. A. Jurado-Navarro, M. López-Puertas, B. Funke, M. García-Comas, A. Gardini, F. González-Galindo, G. P. Stiller, T. von Clarmann, U. Grabowski, and A. Linden. Global distribution of CO2 volume mixing ratio in the middle and upper atmosphere from MIPAS high resolution spectra. *Atmospheric Measurements Techniques, Discuss.*, 2016, 2016.

M. A. Kahre, J. R. Murphy, and R. M. Haberle. Modeling the Martian dust cycle and surface dust reservoirs with the NASA Ames general circulation model. *Journal of Geophysical Research (Planets)*, 111(E6):E06008, Jun 2006. doi:10.1029/2005JE002588.

M. Kaufmann, O. A. Gusev, K. U. Grossmann, R. G. Roble, M. E. Hagan, C. Hartsough, and A. A. Kutepov. The vertical and horizontal distribution of CO_2 densities in the upper mesosphere and lower thermosphere as measured by CRISTA. *J. Geophys. Res.*, 107(D23):8182, 2002. doi:10.1029/2001JD000704.

B. W. Kernighan. *The C Programming Language*. Prentice Hall Professional Technical Reference, 2nd edition, 1988. ISBN 0131103709.

T. Kluyver, B. Ragan-Kelley, F. Pérez, B. E. Granger, M. Bussonnier, J. Frederic, K. Kelley, J. B. Hamrick, J. Grout, S. Corlay, P. Ivanov, D. Avila, S. Abdalla, C. Willing, and et al. Jupyter notebooks - a publishing format for reproducible computational workflows. In *ELPUB*, 2016.

O. Korablev, F. Montmessin, A. Trokhimovskiy, A. A. Fedorova, A. V. Shakun, A. V. Grigoriev, B. E. Moshkin, N. I. Ignatiev, F. Forget, F. Lefèvre, et al. The Atmospheric Chemistry Suite (ACS) of Three Spectrometers for the ExoMars 2016 Trace Gas Orbiter. *SSR*, 214(1):7, Feb 2018. doi:10.1007/s11214-017-0437-6.

O. Korablev, A. C. Vandaele, F. Montmessin, A. A. Fedorova, A. Trokhimovskiy, F. Forget, F. Lefèvre, F. Daerden, I. R. Thomas, L. Trompet, J. T. Erwin, S. Aoki, S. Robert, L. Neary, S. Viscardy, A. V. Grigoriev, N. I. Ignatiev, A. Shakun, A. Patrakeev, D. A. Belyaev, J.-L. Bertaux, K. S. Olsen, L. Baggio, J. Alday, Y. S. Ivanov, B. Ristic, J. Mason, Y. Willame, C. Depiesse, L. Hetey, S. Berkenbosch, R. Clairquin, C. Queirolo, B. Beeckman, E. Neefs, M. R. Patel, G. Bellucci, J.-J. López-Moreno, C. F. Wilson, G. Etiope, L. Zelenyi, H. Svedhem, J. L. Vago, and ACS and NOMAD Science Teams. No detection of methane on Mars from early ExoMars Trace Gas Orbiter observations. *Nature*, 568(7753):517–520, Apr 2019a. doi:10.1038/s41586-019-1096-4.

O. I. Korablev, F. Montmessin, A. A. Fedorova, A. Trokhimovskiy, M. Luginin, N. I. Ignatiev, F. Lefèvre, A. Shakun, A. Patrakeev, D. A. Belyaev, J. L. Bertaux, K. S. Olsen, L. Baggio, J. Alday, C. F. Wilson, S. Guerlet, R. M. B. Young, E. Millour, F. Forget, A. V. Grigoriev, I. Maslov, D. Patsaev, G. Arnold, and D. Grassi. One Year of ACS/TGO Observations of the Mars Atmosphere. *LPI Contributions*, 2089:6416, Jul 2019b.

R. P. Kornfeld, M. D. Garcia, L. E. Craig, S. Butman, and G. M. Signori. Entry, Descent, and Landing Communications for the 2007 Phoenix Mars Lander. *Journal of Spacecraft and Rockets*, 45(3):534–547, May 2008. doi:10.2514/1.33789.

A. A. Kutepov, D. Kunze, D. G. Hummer, and G. B. Rybicki. The solution of radiative transfer problems in molecular bands without the LTE assumption by accelerated lambda iteration methods. *JQRST*, 46:347–365, Nov 1991. doi:10.1016/0022-4073(91)90038-R.

A. A. Kutepov, O. A. Gusev, and V. P. Ogibalov. Solution of the non-LTE problem for molecular gas in planetary atmospheres: superiority of accelerated lambda iteration. *JQSRT*, 60(2):199–220, Aug 1998. doi:10.1016/S0022-4073(97)00167-2.

L. Lamport. Latex: A document preparation system, 1986.

F. Leblanc, J. Y. Chaufray, J. Lilensten, O. Witasse, and J. L. Bertaux. Martian dayglow as seen by the SPICAM UV spectrograph on Mars Express. *Journal of Geophysical Research (Planets)*, 111(E9):E09S11, Aug 2006. doi:10.1029/2005JE002664.

M. T. Lemmon, M. J. Wolff, I. Bell, James F., M. D. Smith, B. A. Cantor, and P. H. Smith. Dust aerosol, clouds, and the atmospheric optical depth record over 5 Mars years of the Mars Exploration Rover mission. *Icarus*, 251:96–111, May 2015. doi:10.1016/j.icarus.2014.03.029.

C. Leovy and Y. Mintz. Numerical Simulation of the Atmospheric Circulation and Climate of Mars. *Journal of Atmospheric Sciences*, 26(6):1167–1190, Nov 1969. doi:10.1175/1520-0469(1969)026<1167:NSOTAC>2.0.CO;2.

K. Levenberg. A method for the solution of certain nonlinear problems in least squares. *Quarterly of Applied Mathematics*, 2:164–168, 1944.

S. R. Lewis, M. Collins, P. L. Read, F. Forget, F. Hourdin, R. Fournier, C. Hourdin, O. Talagrand, and J.-P. Huot. A climate database for Mars. *J. Geophys. Res.*, 104:24,177–24,194, 1999.

M. López-Puertas and F. W. Taylor. Carbon dioxide 4.3-μm emission in the earth's atmosphere: A comparison between Nimbus 7 SAMS measurements and non-local thermodynamic equilibrium radiative transfer calculations. *JGR*, 94(D10):13045–13068, Sep 1989. doi:10.1029/JD094iD10p13045.

M. López-Puertas and F. W. Taylor. *Non-LTE radiative transfer in the atmosphere*. Singapore: World Scientific, 2001.

M. López-Puertas, R. Rodrigo, J. J. López-Moreno, and F. W. Taylor. A non–LTE radiative transfer model for infrared bands in the middle atmosphere. II. CO_2 (2.7 and 4.3 μm) and water vapour (6.3 μm) bands and $N_2(1)$ and $O_2(1)$ vibrational levels. *Journal of Atmospheric and Terrestrial Physics*, 48 (8):749–764, 1986.

M. A. López-Valverde and M. López-Puertas. A non-local thermodynamic equilibrium radiative transfer model for infrared emissions in the atmosphere of Mars. 1: Theoretical basis and nighttime populations of vibrational levels. *Journal of Geophysical Research*, 99:13093–13115, June 1994a. doi:10.1029/94JE00635.

M. A. López-Valverde and M. López-Puertas. A non-local thermodynamic equilibrium radiative transfer model for infrared emission in the atmosphere of Mars. 2: Daytime populations of vibrational levels. *J. Geophys. Res.*, 99: 13117–13132, June 1994b. doi:10.1029/94JE01091.

M. A. López-Valverde and M. López-Puertas. A fast computation of radiative heating rates under non-LTE in a CO_2 atmosphere. In Smith, W. and T. Eds., editors, *IRS 2000: Current Problems in Atmospheric Radiation*, 2001.

M. A. López-Valverde, D. P. Edwards, M. López-Puertas, and C. Roldán. Non-local thermodynamic equilibrium in general circulation models of the Martian atmosphere 1. Effects of the local thermodynamic equilibrium approximation on thermal cooling and solar heating. *Journal of Geophysical Research*, 103: 16799–16812, July 1998. doi:10.1029/98JE01601.

M. A. López-Valverde, E., Lellouch, and A. Coustenis. CO fluorescence from Titan's atmosphere. *Icarus*, 175:503–521, 2005. doi:10.1016/j.icarus.2004.12.015.

M. A. López-Valverde, G. Gilli, M. García-Comas, F. González-Galindo, P. Drossart, and G. Piccioni. *The upper atmosphere of Venus observed by Venus Express*, volume 3, pages 13–32. 2008.

M. A. López-Valverde, M. López-Puertas, B. Funke, G. Gilli, M. García-Comas, P. Drossart, G. Piccioni, and V. Formisano. Modeling the atmospheric limb emission of CO $_2$ at 4.3 μm in the terrestrial planets. *Planetary and Space Science*, 59:988–998, Aug. 2011. doi:10.1016/j.pss.2010.02.001.

M. A. López-Valverde, L. Montabone, M. Sornig, and G. Sonnabend. On the Retrieval of Mesospheric Winds on Mars and Venus from Ground-based Observations at 10 μm. *The Astrophysical Journal*, 816:103, Jan. 2016. doi:10.3847/0004-637X/816/2/103.

M. A. López-Valverde, J.-C. Gerard, F. González-Galindo, A.-C. Vandaele, I. Thomas, O. Korablev, N. Ignatiev, A. Fedorova, F. Montmessin, A. Määttänen, S. Guilbon, F. Lefevre, M. R. Patel, S. Jiménez-Monferrer, M. García-Comas, A. Cardesin, C. F. Wilson, R. T. Clancy, A. Kleinböhl, D. J. McCleese, D. M. Kass, N. M. Schneider, M. S. Chaffin, J. J. López-Moreno, and J. Rodríguez. Investigations of the Mars Upper Atmosphere with ExoMars Trace Gas Orbiter. *SSR*, 214(1):29, Feb 2018. doi:10.1007/s11214-017-0463-4.

J. MacQueen. Some methods for classification and analysis of multivariate observations. In *Proceedings of the Fifth Berkeley Symposium on Mathematical Statistics and Probability, Volume 1: Statistics*, pages 281–297, Berkeley, Calif., 1967. University of California Press. URL `https://projecteuclid.org/euclid.bsmsp/1200512992`.

D. W. Marquardt. An algorithm for least-squares estimation of nonlinear parameters. *Journal of the Society for Industrial and Applied Mathematics*, 11(2): 431–441, 1963.

Mars Express. European Space Agency. Mars Express, 2019. URL `http://sci.esa.int/mars-express`. Online.

L. J. Martin. The Major Martian Dust Storms of 1971 and 1973. *Icarus*, 23(1): 108–115, Sep 1974. doi:10.1016/0019-1035(74)90108-0.

A. S. Medvedev and E. Yiğit. Thermal effects of internal gravity waves in the Martian upper atmosphere. *GRL*, 39(5):L05201, 2012. doi:10.1029/2012GL050852.

A. S. Medvedev, F. González-Galindo, E. Yiğit, A. G. Feofilov, F. Forget, and P. Hartogh. Cooling of the Martian thermosphere by CO_2 radiation and gravity waves: An intercomparison study with two general circulation models. *Journal of Geophysical Research (Planets)*, 120(5):913–927, May 2015. doi:10.1002/2015JE004802.

C. J. Mertens, J. M. Russell III, M. G. Mlynczak, C.-Y. She, F. J. Schmidlin, R. A. Goldberg, M. López-Puertas, P. P. Wintersteiner, R. H. Picard, J. R. Winick, and X. Xu. Kinetic temperature and carbon dioxide from broadband infrared limb emission measurements taken from the TIMED/SABER instrument. *Adv. Space Res.*, 43(1):15–27, 2009. doi:10.1016/j.asr.2008.04.017.

E. Millour, F. Forget, A. Spiga, M. Vals, V. Zakharov, L. Montabone, F. Lefèvre, F. Montmessin, J. Y. Chaufray, M. A. López-Valverde, F. González-Galindo, S. R. Lewis, P. L. Read, M. C. Desjean, F. Cipriani, and MCD Development Team. The Mars Climate Database (version 5.3). In *From Mars Express to ExoMars*, page 68, Feb 2018.

E. A. Milne. *Thermodynamics of the Stars*, pages 65–255. Springer Berlin Heidelberg, Berlin, Heidelberg, 1930. ISBN 978-3-642-90705-0. doi:10.1007/978-3-642-90705-0_2.

Y. Moudden and J. C. McConnell. A new model for multiscale modeling of the Martian atmosphere, GM3. *Journal of Geophysical Research (Planets)*, 110 (E4):E04001, Apr 2005. doi:10.1029/2004JE002354.

I. Müller-Wodarg, R. V. Yelle, M. Mendillo, L. A. Young, and A. D. Aylward. The thermosphere of Titan simulated by a global three-dimensional time-dependent model. *JGR*, 105(A9):20833–20856, Jan 2000. doi:10.1029/2000JA000053.

NASA. NASA Science. Mars Exploration Program, 2019. URL `https://mars.nasa.gov`. Online.

G. Neukum, R. Greeley, H. Hiesinger, and P. Pinet. *Special issue on Mars Express after 6 Years in Orbit: Mars Geology from Three-Dimensional Mapping by the High Resolution Stereo Camera (HRSC) Experiment*, volume 294 (3-4). June 2010.

T. E. Oliphant. *A guide to NumPy*, volume 1. Trelgol Publishing USA, 2006.

R. Orosei, R. L. Jordan, D. D. Morgan, M. Cartacci, A. Cicchetti, F. Duru, D. A. Gurnett, E. Heggy, D. L. Kirchner, R. Noschese, W. Kofman, A. Masdea, J. J. Plaut, R. Seu, T. R. Watters, and G. Picardi. Mars Advanced Radar for Subsurface and Ionospheric Sounding (MARSIS) after nine years of operation: A summary. *PLANSS*, 112:98–114, Jul 2015. doi:10.1016/j.pss.2014.07.010.

T. J. Parker, D. S. Gorsline, R. S. Saunders, D. C. Pieri, and D. M. Schneeberger. Coastal Geomorphology of the Martian northern plains. *JGR*, 98(E6):11061–11078, Jun 1993. doi:10.1029/93JE00618.

F. Pedregosa, G. Varoquaux, A. Gramfort, V. Michel, B. Thirion, O. Grisel, M. Blondel, P. Prettenhofer, R. Weiss, V. Dubourg, J. Vanderplas, A. Passos, D. Cournapeau, M. Brucher, M. Perrot, and E. Duchesnay. Scikit-learn: Machine learning in Python. *Journal of Machine Learning Research*, 12:2825–2830, 2011.

J. Peralta, M. A. López-Valverde, G. Gilli, and A. Piccialli. Dayside temperatures in the Venus upper atmosphere from Venus Express/VIRTIS nadir measurements at 4.3 μm. *Astronomy and Astrophysics*, 585:A53, Jan. 2016. doi:10.1051/0004-6361/201527191.

A. Piccialli, M. A. López-Valverde, A. Määttänen, F. González-Galindo, J. Audouard, F. Altieri, F. Forget, P. Drossart, B. Gondet, and J. P. Bibring. CO_2 non-LTE limb emissions in Mars' atmosphere as observed by OMEGA/Mars Express. *Journal of Geophysical Research (Planets)*, 121:1066–1086, June 2016. doi:10.1002/2015JE004981.

PSA. European Space Agency's Planetary Science Archive, 2019. URL `https://archives.esac.esa.int/psa/`. Online, PSA 5.6.8.

N. E. Putzig, R. J. Phillips, B. A. Campbell, M. T. Mellon, J. W. Holt, and T. C. Brothers. SHARAD soundings and surface roughness at past, present, and proposed landing sites on Mars: Reflections at Phoenix may be attributable to deep ground ice. *Journal of Geophysical Research (Planets)*, 119(8):1936–1949, Aug 2014. doi:10.1002/2014JE004646.

P. L. Read, S. R. Lewis, S. J. Bingham, and C. E. Newman. Predicting Weather Conditions and Climate for Mars Expeditions. *Journal of the British Interplanetary Society*, 57:75–86, Jan 2004.

S. Robert, A. C. Vandaele, I. Thomas, Y. Willame, F. Daerden, S. Delanoye, C. Depiesse, R. Drummond, E. Neefs, L. Neary, B. Ristic, J. Mason, J. J. López-Moreno, J. Rodríguez-Gómez, M. R. Patel, G. Bellucci, A. C. Vandaele, J. J. Lopez Moreno, G. Bellucci, M. Patel, et al. Expected performances of the NOMAD/ExoMars instrument. *planss*, 124:94–104, May 2016. doi:10.1016/j.pss.2016.03.003.

C. D. Rodgers. Inverse Methods for Atmospheric Sounding - Theory and Practice. *Inverse Methods for Atmospheric Sounding - Theory and Practice. Series: Series on Atmospheric Oceanic and Planetary Physics, ISBN: 9789812813718. World Scientific Publishing Co. Pte. Ltd., Edited by Clive D. Rodgers, vol. 2*, 2, 2000. doi:10.1142/9789812813718.

C. Roldán, M. A. López-Valverde, M. López-Puertas, and D. P. Edwards. Non-LTE infrared emissions of CO_2 in the atmosphere of Venus. *Icarus*, 147:11–25, Sept. 2000. doi:10.1006/icar.2000.6432.

L. S. Rothman, I. E. Gordon, Y. Babikov, A. Barbe, D. Chris Benner, P. F. Bernath, M. Birk, L. Bizzocchi, V. Boudon, L. R. Brown, A. Campargue, K. Chance, E. A. Cohen, L. H. Coudert, V. M. Devi, B. J. Drouin, A. Fayt, J.-M. Flaud, R. R. Gamache, J. J. Harrison, J.-M. Hartmann, C. Hill, J. T. Hodges, D. Jacquemart, A. Jolly, J. Lamouroux, R. J. Le Roy, G. Li, D. A. Long, O. M. Lyulin, C. J. Mackie, S. T. Massie, S. Mikhailenko, H. S. P. Müller, O. V. Naumenko, A. V. Nikitin, J. Orphal, V. Perevalov, A. Perrin, E. R. Polovtseva, C. Richard, M. A. H. Smith, E. Starikova, K. Sung, S. Tashkun, J. Tennyson, G. C. Toon, V. G. Tyuterev, and G. Wagner. The HITRAN2012 molecular spectroscopic database. *JQSRT*, 130:4–50, Nov. 2013. doi:10.1016/j.jqsrt.2013.07.002.

G. B. Rybicki and D. G. Hummer. An accelerated lambda iteration method for multilevel radiative transfer. *AAP*, 245:171–181, May 1991.

A. Sánchez-Lavega. *An Introduction to Planetary Atmospheres.* Taylor and Francis Group, 2011.

A. Sánchez-Lavega, H. Chen-Chen, I. Ordoñez-Etxeberria, R. Hueso, T. del Río-Gaztelurrutia, A. Garro, A. Cardesín-Moinelo, D. Titov, and S. Wood. Limb clouds and dust on Mars from images obtained by the Visual Monitoring Camera (VMC) onboard Mars Express. *Icarus*, 299:194–205, Jan 2018. doi:10.1016/j.icarus.2017.07.026.

Science. *Special issue on Mars Express: OMEGA*, volume 307 (5715). 2005. URL `https://science.sciencemag.org/content/307/5715#special-issue`.

M. G. Sobell. *A practical guide to Ubuntu Linux.* Pearson Education, 2015.

A. Spiga, F. González-Galindo, M. Á. López-Valverde, and F. Forget. Gravity waves, cold pockets and CO_2 clouds in the Martian mesosphere. *GRL*, 39(2): L02201, Jan 2012. doi:10.1029/2011GL050343.

G. Stiller. Sensitivity of trace gas abundances retrievals from infrared limb emission spectra to simplifying approximations in radiative transfer modelling. *Journal of Quantitative Spectroscopy and Radiative Transfer*, 72:249–280, Feb. 2002. doi:10.1016/S0022-4073(01)00123-6.

F. W. Taylor. *Planetary Atmospheres.* Oxford University Press, 2010.

N. Terada, F. Leblanc, H. Nakagawa, A. S. Medvedev, E. Yiğit, T. Kuroda, T. Hara, S. L. England, H. Fujiwara, K. Terada, K. Seki, P. R. Mahaffy, M. Elrod, M. Benna, J. Grebowsky, and B. M. Jakosky. Global distribution and parameter dependences of gravity wave activity in the Martian upper thermosphere derived from MAVEN/NGIMS observations. *Journal of Geophysical Research (Space Physics)*, 122(2):2374–2397, Feb 2017. doi:10.1002/2016JA023476.

The GIMP Development Team. GIMP, 2019. URL `https://www.gimp.org`.

J. S. Theon and W. Nordberg. On the determination of pressure and density profiles from temperature profiles in the atmosphere. *National Aeronautics and Space Administration, Technical Note*, 1965.

E. M. B. Thiemann, F. G. Eparvier, S. W. Bougher, M. Dominique, L. Andersson, Z. Girazian, M. D. Pilinski, B. Templeman, and B. M. Jakosky. Mars Thermospheric Variability Revealed by MAVEN EUVM Solar Occultations: Structure at Aphelion and Perihelion and Response to EUV Forcing. *Journal of Geophysical Research (Planets)*, 123(9):2248–2269, Sep 2018. doi:10.1029/2018JE005550.

R. N. Thomas. *Some aspects of non-equilibrium thermodynamics in the presence of a radiation field*. 1965.

UPWARDS. Understanding Planet Mars With Advanced Remote-sensing Datasets and Synergistic studies, 2019. URL `http://upwards-mars.eu`. Online.

G. van Rossum. Python reference manual. Technical report, Amsterdam, The Netherlands, 1995.

A. C. Vandaele, E. Neefs, R. Drummond, I. R. Thomas, F. Daerden, J. J. López-Moreno, J. Rodriguez, M. R. Patel, G. Bellucci, M. Allen, F. Altieri, D. Bolsée, T. Clancy, S. Delanoye, C. Depiesse, E. Cloutis, A. Fedorova, V. Formisano, B. Funke, D. Fussen, A. Geminale, J. C. Gérard, M. Giuranna, N. Ignatiev, J. Kaminski, O. Karatekin, F. Lefèvre, M. López-Puertas, M. López-Valverde, A. Mahieux, J. McConnell, M. Mumma, L. Neary, E. Renotte, B. Ristic, S. Robert, M. Smith, S. Trokhimovsky, J. Vander Auwera, G. Villanueva, J. Whiteway, V. Wilquet, and M. Wolff. Science objectives and performances of NOMAD, a spectrometer suite for the ExoMars TGO mission. *planss*, 119: 233–249, Dec 2015. doi:10.1016/j.pss.2015.10.003.

A. C. Vandaele, O. Korablev, F. Daerden, S. Aoki, I. R. Thomas, F. Altieri, M. López-Valverde, G. Villanueva, G. Liuzzi, M. D. Smith, J. T. Erwin, L. Trompet, A. A. Fedorova, F. Montmessin, A. Trokhimovskiy, D. A. Belyaev, N. I. Ignatiev, M. Luginin, K. S. Olsen, L. Baggio, et al. Martian dust storm impact on atmospheric H_2O and D/H observed by ExoMars Trace Gas Orbiter. *Nature*, 568(7753):521–525, Apr 2019. doi:10.1038/s41586-019-1097-3.

M. Vincendon, J. Audouard, F. Altieri, and A. Ody. Mars Express measurements of surface albedo changes over 2004-2010. *Icarus*, 251:145–163, May 2015. doi:10.1016/j.icarus.2014.10.029.

T. von Clarmann, N. Glatthor, U. Grabowski, M. Höpfner, S. Kellmann, M. Kiefer, A. Linden, G. M. Tsidu, M. Milz, T. Steck, G. P. Stiller, D. Y. Wang, H. Fischer, B. Funke, S. Gil-López, and M. López-Puertas. Retrieval of temperature and tangent altitude pointing from limb emission spectra recorded from space by the Michelson Interferometer for Passive Atmospheric Sounding (MIPAS). *Journal of Geophysical Research (Atmospheres)*, 108:4736, Dec. 2003. doi:10.1029/2003JD003602.

J. T. Wilson, V. R. Eke, R. J. Massey, R. C. Elphic, W. C. Feldman, S. Maurice, and L. F. A. Teodoro. Equatorial locations of water on Mars: Improved resolution maps based on Mars Odyssey Neutron Spectrometer data. *Icarus*, 299: 148–160, Jan 2018. doi:10.1016/j.icarus.2017.07.028.

C. Zeitlin, W. Boynton, I. Mitrofanov, D. Hassler, W. Atwell, T. F. Cleghorn, F. A. Cucinotta, M. Dayeh, M. Desai, S. B. Guetersloh, K. Kozarev, K. T. Lee, L. Pinsky, P. Saganti, N. A. Schwadron, and R. Turner. Mars Odyssey measurements of galactic cosmic rays and solar particles in Mars orbit, 2002-2008. *Space Weather*, 8:S00E06, Nov 2010. doi:10.1029/2009SW000563.

V. N. Zharkov. The Internal Structure of Mars: A Key to Understanding the Origin of Terrestrial Planets. *Solar System Research*, 30(6):456, Jan 1996.

R. W. Zurek, R. A. Tolson, S. W. Bougher, R. A. Lugo, D. T. Baird, J. M. Bell, and B. M. Jakosky. Mars thermosphere as seen in MAVEN accelerometer data. *Journal of Geophysical Research (Space Physics)*, 122(3):3798–3814, Mar 2017. doi:10.1002/2016JA023641.